Carnegie Mellon University
MELLON COLLEGE OF SCIENCE

THESIS

SUBMITTED IN PARTIAL FULFILLMENT OF THE REQUIREMENTS
FOR THE DEGREE OF

DOCTOR OF PHILOSOPHY IN THE FIELD OF PHYSICS

TITLE: "Revealing the structural and molecular basis of retroviral assembly and endolysin PlyC membrane translocation using surface plasmon resonance and neutron reflectometry"

PRESENTED BY: Marilia Cabral Do Rego Barros

ACCEPTED BY THE DEPARTMENT OF PHYSICS

MATHIAS LOESCHE	02/16/16
MATHIAS LOESCHE, CHAIR PROFESSOR	DATE

STEPHEN GAROFF	02/16/16
STEPHEN GAROFF, DEPT HEAD	DATE

APPROVED BY THE COLLEGE COUNCIL

FRED GILMAN	02/22/16
FRED GILMAN, DEAN	DATE

Revealing the structural and molecular basis of retroviral assembly and endolysin PlyC membrane translocation using surface plasmon resonance and neutron reflectometry

Marilia Barros

Submitted in partial fulfillment of the
requirements for the degree of
Doctor of Philosophy

at

Carnegie Mellon University
Department of Physics
Pittsburgh, Pennsylvania 15213

Thesis Committee:
Mathias Lösche (Chair)
Frank Heinrich
Markus Deserno
Kris Dahl

February 2016

Abstract

In this thesis we focus on the mechanistic understanding of two membrane mediated biological processes: retroviral assembly and endolysin PlyC plasma membrane translocation. Retroviral Gag polyprotein is the structural determinant that assembles in a protein lattice on the hosts plasma membrane to trigger formation of the viral protein/membrane shell. In this process, it employs multiple signals - electrostatic, hydrophobic and lipid-specific interactions conferred by the matrix domain (MA) - to recruit the protein to the proper cellular location and assist protein-protein interactions located on full-length Gag in lattice formation. In this thesis I address the interaction of non-lipidated and myristoylated (+myr) HIV-1 Gag matrix domains with model membranes, sparsely tethered bilayer membranes (tBLMs), to dissect these complex membrane signals and quantify their contributions to the overall interaction. SPR on well-defined membrane models is used to quantify binding affinities and amounts of protein and yields free binding energy contributions, ΔG, of the various signals. Charge-charge interactions in the absence of the phosphatidylinositide PI(4,5)P_2 attract the protein to acidic membrane surfaces, and myristoylation increases the affinity by a factor of 10, arguing against a PI(4,5)P_2-trigger of myristate exposure. Lipid-specific interactions with PI(4,5)P_2, the major signal lipid in the inner plasma membrane, increase membrane attraction at a similar level as the protein lipidation. Cholesterol augments protein affinity strongly, apparently by enabling efficient myristate insertion and PI(4,5)P_2 binding. We thus observe that the isolated matrix protein, in the absence of protein-protein interaction conferred by the full-length Gag, binds the membrane with sub-micromolar affinities. These studies resulted in a detailed understanding of the thermodynamic aspects that determine membrane association, preferential lipid recruitment to the viral shell, and aspects of Gag assembly into the membrane-bound protein lattice that are driven by its matrix domain

We also report the difficulties in the assessment of protein-membrane complex structures that involved HIV-1 +myrMA. While myrMA is well behaved, and protein-membrane complexes could be readily characterized by neutron reflection (NR) on stBLMs , this was not possible for +myrMA because of membrane reconstruction that prevented the interpretation of NR data after protein incubation of the bilayer. We confirm the hypothesis of membrane reconstruction with electron microscopy and screen for experimental conditions that would allow the maintainance of planar bilayers - needed for NR - after +myrMA incubation. We are able to identify a pH range near pH = 8 where membrane reconstruction is minimal.

The mechanisms by which full-length Gag proteins interact with membranes were also investigated. Rous sarcoma virus (RSV) Gag protein, and Murine leukemia virus (MLV) had their biophysical properties and membrane interactions in tBLMs studied by SPR and NR. We correlated solution and membrane-bound structures of the Gag proteins from various retroviral species and compare to mutants lacking the linker that connects MA and CA, MLV ΔP12 and RSV Δflex. MLV wild-type and ΔP12 mutant shows similar affinities to anionic membranes. However, structural characterization by NR found significant differences, ΔP12 extended 200 $\AA$ away from the bilayer surface while the wild-type extended only 100 $\AA$. RSV Gag was found to have 10 and 100 fold higher affinity for charged membranes compared to wild-type MLV and RSV MA, respectively. We also demonstrate that RSV wild-type and Δflex mutant have similar affinity and conformation at anionic membranes with the interaction between RSV Gag and membranes being strongly cooperative. The NR studies indicate that RSV Gag in the membrane-

bound state is also back-folded, similar to HIV Gag which was investigated earlier.

The last part of the thesis was dedicated to PlyC, a bacteriophage-encoded endolysin, that lyses Streptococcus pyogenes (Spy) on contact. It was demonstrate that the PlyC enzyme, mediated by its PlyCB subunit, crosses epithelial cell membranes and clears intracellular Spy. Here we demonstrate through quantitative studies using stBLMs that PlyCB interacts strongly with phosphatidylserine (PS) whereas its interaction with other lipids is weak, suggesting specificity for PS as its cellular receptor. Membranes that contain small amounts of PS (5 mol% or less) also bind PlyCB strongly if other anionic lipids provide an low electrostatic potential to attract the cationic protein. Two distinct protein-membrane complexes are characterized in which PlyCB is either interfacially associated with the bilayer at low PS concentration or is inserted into the membrane at high PS concentration Neutron reflection data showed that PlyCB binding to the membrane surface is followed by penetration into the hydrophobic membrane core, while impedance spectroscopy confirms that the membrane integrity is not affected during PlyCB exposure. Those findings provided insights towards mechanistic understanding of how PlyCB binds and initiates membrane translocation.

Acknowledgments

I would like to thank my advisor Prof. Mathias Lösche for all the guidance, support, for teaching me how to do research and for the many important lessons in life which will always guide me throughout my career. I especially thank Frank Heinrich. I am indebted for his constant assistance, encouragement, guidance, dedication and the tremendous support and opportunities he provided throughout my doctoral studies. I thank Hirsh Nanda who advised me during the first years of my PhD. I would like to thank my committee members Profs Markus Deserno and Kris Dahl for all the suggestions and input on my research. I want to express my appreciation to all my collaborators whose efforts and support made my research possible. Alan Rein and Sid Datta for providing feedback on the retroviral assembly project. Rob Dick and Prof. Volker Vogt for the fruitful collaboration on the RSV Gag project. Ioannis Karageorgos for helping me to give continuity to the HIV-1 matrix experiments. Daniel Nelson for giving me the opportunity to work on the PlyC project.

Muito obrigada a minha família por me apoiar na minha busca por novos desafios. Tio Mauricio, Mari, mãe, pai obrigada por investirem na minha educação, por me permitirem viver meus sonhos, por respeitarem minhas decisões, por acreditarem no meu potencial e por nunca duvidarem da minha capacidade. Tenho vocês como meus grandes exemplos de vida, superação, disciplina, determinação e humildade. Meus amigos e minhas amigas-irmãs obrigada pela amizade de anos, pela paciência, pelas piadas, pelas risadas, pelas viagens, pelos dramas e pelas visitas inesperadas. Sem vocês nao teria chegado onde cheguei.

"If you're going to try, go all the way. Otherwise, don't even start. This could mean losing girlfriends, wives, relatives and maybe even your mind. It could mean not eating for three or four days. It could mean freezing on a park bench. It could mean jail. It could mean derision. It could mean mockery–isolation. Isolation is the gift. All the others are a test of your endurance, of how much you really want to do it. And, you'll do it, despite rejection and the worst odds. And it will be better than anything else you can imagine. If you're going to try, go all the way. There is no other feeling like that. You will be alone with the gods, and the nights will flame with fire. You will ride life straight to perfect laughter. It's the only good fight there is." - Charles Bukowski

List of Publications

TL. Yap, Z. Jiang, F. Heinrich, JM. Gruschus, CM. Pfefferkorn, M. Barros, JE. Curtis, E. Sidransky, JC. Lee *"Structural Features of Membrane-bound Glucocerebroside and α-Synuclein Probed by Neutron Reflectometry and Fluorescence Spectroscopy"*, J. Biol. Chem. 2014

Chapter 6:

M. Barros, F. Heinrich, I. Karageorgos, AKS. Datta, A. Rein, M. Lösche *"Membrane Binding of HIV-1 Matrix Protein: Dependence on Bilayer Composition and Protein Lipidation"*, submitted to J. Virol. 2015

Chapter 8:

RA. Dick, M. Barros, D. Jin, M. Lösche, V. Vogt *"Membrane Binding of the Rous Sarcoma Virus Gag Protein is Cooperative and Dependent on the SPA Domain"*, in press J. Virol 2016

RA. Dick, AKS. Datta, H. Nanda, X. Fang, Y. Wen, M. Barros, YX. Wang, A. Rein, V. Vogt *"Hydrodynamic and membrane binding properties of Rous sarcoma virus Gag protein"*, J. Virol 2015

Chapter 9:

Y. Shen, M. Barros, T. Vennemann, TD. Gallagher, Y. Ying, SB. Linden, RD. Heselpoth, DJ. Spencer, DM. Donovan, J. Moult, VA. Fischetti, F. Heinrich, M. Lösche, DC. Nelson *"PlyC, A Bacteriophage Endolysin that Internalizes in Epithelial Cells and Retains Bacteriolytic Activity Against intracellular streptococci"*, submitted to e-Life 2015

Contents

List of Publications **vii**

1 Introduction **1**
1.1 Retroviral assembly . . . 3
1.1.1 Objectives . . . 3
1.2 Endolysin PlyC plasma membrane translocation . . . 5
1.2.1 Objectives . . . 5

2 Methodology: Lipid-protein Interactions studied using Model Membranes **7**
2.1 Lipid Bilayer Membranes . . . 7
2.1.1 Overview . . . 7
2.2 Biomimetic Model Membranes . . . 11
2.2.1 Langmuir Monolayers . . . 11
2.2.2 Lipid Vesicles . . . 11
2.2.3 Solid Supported Membranes . . . 12
2.2.4 Sparsely tethered bilayer lipid membranes (stBLMs) . . . 12
2.3 Proteins: structure-function relationship . . . 14
2.3.1 Membrane binding . . . 14
2.3.2 Membrane-bound structure . . . 15

3 Experimental Techniques **17**
3.1 Electrochemical Impedance Spectroscopy (EIS) . . . 17
3.1.1 Introduction . . . 17
3.1.2 Theory . . . 17
3.1.3 Instrumentation . . . 19
3.1.4 Data Analysis . . . 20
3.2 Surface Plasmon Resonance (SPR) . . . 22
3.2.1 Introduction . . . 22
3.2.2 Theory . . . 23
3.2.3 Instrumentation . . . 26
3.2.4 Data Acquisition . . . 27
3.2.5 Data Analysis . . . 28
3.3 Neutron Reflectometry (NR) . . . 30
3.3.1 Introduction . . . 30

3.3.2 Theory . . . 31
3.3.3 Data Acquisition . . . 34
3.3.4 Instrumentation . . . 35
3.3.5 Data Analysis . . . 36

4 Multi-component Defect-free Tethered Bilayer Lipid Membranes by Vesicle Fusion 41
4.1 Introduction . . . 41
4.2 stBLM Preparation . . . 42
4.2.1 Self Assembled Monolayer (SAM) . . . 42
4.2.2 stBLM Completion . . . 43
4.3 Single-component stBLMs . . . 44
4.4 Multi-component stBLMs . . . 46
4.4.1 Influence of Surface Charge and Ionic Strength on Planar Membrane Formation . . . 46
4.4.2 Effect of cholesterol on multi-component stBLMs . . . 47
4.4.3 Impact of PI(4,5)P_2 on stBLM completion . . . 48
4.5 Discussion . . . 50

5 Membrane Coupling and Dynamic Reorganization of Gag in Retroviral Assembly 53
5.1 Introduction . . . 53
5.2 Human Immunodeficiency Virus type I (HIV-1) . . . 54
5.2.1 MA structure and binding mechanisms . . . 54
5.2.2 Conformational Reorganization of HIV-1 Gag at the membrane . . . 58
5.3 A comparison between HIV-1, MLV and RSV Gag protein properties . . . 58
5.3.1 Gag assembly with RNA and packing in immature virus . . . 58
5.3.2 Solution properties of Gag . . . 60

6 Membrane Binding of HIV-1 Matrix Protein: Dependence on Bilayer Composition and Protein Lipidation 61
6.1 Synopsis . . . 61
6.2 Materials . . . 62
6.2.1 Lipids . . . 62
6.2.2 Protein expression and purification . . . 62
6.3 Results . . . 63
6.3.1 Myristoylation increases the MA membrane affinity by over an order of magnitude on PS-containing sstBLMs . . . 63
6.3.2 Cholesterol affects +myrMA targeting to charged membranes . . . 66
6.3.3 Cholesterol and PI(4,5)P_2 enhance MA membrane affinity cooperatively . 69
6.3.4 +myrMA binds preferentially to PS-containing membranes as compared to PI-containing membranes . . . 70
6.4 Discussion . . . 71
6.5 Conclusions . . . 75

7 pH Dependent Membrane Reorganization Induced upon HIV-1 MA Binding 77
7.1 Background . . . 77
7.2 Evidence for membrane remodeling . . . 79
7.2.1 +myrMA binding correlates with membrane impairment . . . 79
7.2.2 Membrane remodeling observed on DOPS vesicles . . . 80
7.3 Targeting the origin of membrane reshaping . . . 81
7.3.1 Ionic strength effect . . . 81
7.3.2 pH effect . . . 81
7.4 Discussion . . . 85

8 Conformational Differences in Membrane Bound Retroviral Gag 87
8.1 Background . . . 87
8.2 Rous Sarcoma Virus (RSV) . . . 87
8.2.1 Constructs . . . 87
8.2.2 Membrane binding . . . 88
8.2.3 Membrane-bound structure . . . 93
8.3 Murine Leukemia Virus (MLV) . . . 95
8.3.1 Constructs . . . 95
8.3.2 Membrane binding . . . 96
8.3.3 Membrane-bound structure . . . 98
8.4 Discussion . . . 99

9 Endolysin PlyC Mechanism for Plasma Membrane Translocation: Entry Point Revealed 103
9.1 Introduction . . . 103
9.1.1 PlyCB electrostatic map . . . 105
9.2 Results . . . 105
9.2.1 PlyCB binding to stBLMs containing anionic lipids shows specificity for PS . . . 105
9.2.2 PlyCB membrane affinity depends on PS concentration . . . 106
9.2.3 Membrane response to PlyCB binding . . . 109
9.2.4 PlyCB localization at PS-containing membranes depends on PS concentration . . . 110
9.3 Discussion . . . 112

List of Figures

1.1 **HIV-1 assembly at the plasma membrane of a host cell.** The Gag polyprotein (multi-colored) targets the inner face of the PM (2) with its MA domain (purple) where it reorganizes from its solution structure (1), extending upon binding of viral RNA (black lines) to NC (orange). Budding into immature virions requires lateral contacts between the extended Gag (3), presumably mediated by CA (green). Dynamic sorting of PM lipids recruits a viral membrane composition that differs substantially from that of the parent membrane (3). A complex process completes budding of immature viruses (4) which mature further (5). . . 2

2.1 **Lipid bilayer bimolecular sheet structure.** The hydrocarbon chains of the lipids form the hydrophobic core of the membrane while the polar lipid headgroups are exposed to the aqueous environment 8

2.2 **Plasma membrane phospholipid asymmetry** The outer leaflet of the plasma membrane is predominantly neutral and enriched in sphingomyelin (SM) and phosphatidylcholine (PC). Phosphatidylethanolamine (PE) and phosphatidylinositol (PI) reside mainly in the inner leaflet, while phosphatidylserine (PS) is located almost exclusively in the inner leaflet of the plasma membrane. Figure adapted from [174] 10

2.3 **Model membrane systems.** Solid supported bilayer, lipid monolayer and liposome mimic of biomembranes [139]. 12

2.4 **Sparsely tethered bilayer lipid membrane.** Lipid bilayer coupled to the solid support through a synthetic lipid diluted on the surface using a spacer to create a submembrane hydration layer adjacent to the substrate-proximal leaflet 13

3.1 **Schematic of a three electrode electrochemical cell.** The reaction takes place at the Au substrate, working electrode. A periodic voltage signal of variable frequency is applied between the working and reference electrodes across the sample, stBLM. The auxiliary electrode, along with the working electrode, completes the circuit over which current is measured 18

3.2 **Equivalent circuit model for a SAM**. The SAM is represented by an RC parallel circuit with the capacitance-like behavior being captured by a constant-phase element, CPE_{SAM}, and resistance R_{def} 20

3.3 **Equivalent circuit model for a stBLM** The bilayer is represented by a constant-phase element, CPE_{mem}, parallel to a branch that represents membrane defects characterized by their resistance, R_{def}, and a constant-phase element, CPE_{def}, which reflects the electrical conductivity of the submembrane space 21

3.4 **Representative Cole-Cole plot**. Raw EIS spectra of a mixed HC18:βME 30:70 SAM and stBLM. The diameter of the semi-circle gives the value of C' ≈ 6 μFcm^{-2} for the SAM and C' ≈ 0.8 μFcm^{-2} for the DOPC lipid bilayer 22

3.5 **Refraction of plane a wave at a dielectric interface.** The incident electromagnetic wave travels between two media 1 and 2 with refractive indices n_1 and n_2, respectively, at an incident angle α. The y direction is perpendicular to the surface. Figure from [152] 24

3.6 **Dispersion relation for photon in air and in a dielectric compared to surface plasmon dispersion relation.** Excitation of plasmons is not possible through air, since photon dispersion relation does not intercept the surface plasmon dispersion relation. However, in a dielectric k_{photon} can be increased and thus intersect SPP dispersion other than at the origin, generating the surface plasmons. Figure from [4] 26

3.7 **Surface plasmon resonance in the kretschmann configuration.** stBLM is coupled to a prism. The incident beam goes through total internal reflection at the prism-gold interface. Light passing from one interface to another generates an evanescent wave that interacts with the free electrons of the gold layer, resulting in plasmon wave excitation at the stBLM-gold interface. When the momentum and energy of the photons of the incident beam light matches the energy and momentum of the surface plasmons, resonance is achieved. 27

3.8 **SPR data acquisition.** Protein binding response is monitored over time at different protein concentrations(right panel). The increase in signal due to protein adsorption shows the shift in the minimum position of the resonance angle (left panel). Reflected light intensity is measured and at a certain angle, surface plasmon resonance occurs, resulting in a dip in the intensity. A change in the refractive index due protein adsorption at the neat bilayer interface alters the resonance angle. Those changes are monitored in real time and observed as a raise in the SPR signal. 28

3.9 **An exemplary SPR binding curve.** SPR response as a function of protein concentration is fitted to a sigmoid curve. From this fit, two parameters may be determined, the dissociation equilibrium constant, K_d, as the concentration of protein at which half of the binding sites are occupied and saturation response, R_∞, which corresponds to the maximum amount of protein that can be adsorbed at the interface at infinite protein concentration 29

3.10 **Illustration of neutron reflectometry at lipid membrane interface.** The technique involves shining a highly collimated beam of neutrons onto an extremely flat surface and measuring the intensity of reflected beam as a function of angle . 31

3.11 **Specular reflection, $\theta_i = \theta_r$.** Plane wave reflection at a flat interface between two bulk media of refractive indices n_0 and n_1 showing incident and reflected waves at an angle θ_i and the transmitted wave at an angle θ_t along with the normal component of the momentum transfer vector, q_z 32

3.12 **Reflection and refraction on a layered material.** Slab view of a reflectivity sample consisting of m layers of thickness d_m and scattering length density ρ_m. The incident beam will be reflected and refracted at the interfaces between each of the layers. The reflection and refraction coefficients for each pair of adjacent media is calculated by a sum of amplitudes of the reflected and refracted rays. . . 35

3.13 **Neutron reflection reduced data.** DOPC tBLM on HC18:βME 30:70 SAM. The measurements utilized three different solvent contrasts: D_2O, H_2O and Contrast Mixture 4 (CM4, a mixture of D_2O and H_2O with a scattering length density of 4×10^6 Å^2). Curves were shifted for better visualization 36

3.14 **Typical neutron scattering length density profile for tBLMs** nSLD obtained from the NR best-fit of a DOPC tBLM on HC18:βME 30:70 SAM in three different isotopic constrasts: D_2O, CM4 and H_2O. Solid substrate nSLD is unaffected by the contrast variation while the organic layer is contrast sensitive in the areas exposed to solvent 37

3.15 **Continuous distribution model**. Area of submolecular components of DOPC tBLM on HC18:βME 30:70 SAM. The bilayer is defect-free, no water is found in the hydrocarbon region as evidenced by the dashed line, which represents the sum of all the molecular components without water. 38

3.16 **Euler angles.** The xyz system is shown in black, the XYZ rotated system is shown in red. The intersection of the xy and the XY coordinate planes is represented by the N axis. ϕ represents a rotation around the z axis, θ represents a rotation around the N axis, ψ represents a rotation around the Z axis Figure adapted from https://en.wikipedia.org/wiki/Eulerangles 39

4.1 Cole-Cole plot of a mixed HC18:βME 70:30 SAM (black), pure DOPC vesicles before (blue) and after osmotic shock (red). Defect-free DOPC stBLM is formed upon vesicle incubation only. Osmotic shock promotes the break up of the remainder vesicles improving bilayer quality. 44

4.2 **Efficient vesicle fusion requires minimal surface coverage.** Correlation between surface coverage of adsorbed vesicles and formation of defect-free tBLMs. (A) SPR signal of vesicles DOPC:DOPS 70:30 prepared with dispersant buffer of various ionic strengths adsorbing on HC18:βME 30:70 as a function of incubation time. After 2 hours incubation, the SPR response R $\sim$ 300, 250, 70 and 20 pixels decreases with ionic strengths. Higher coverage correlates with better insulating bilayer properties, SAM-like spectrum at 50 mM NaCl and $R_{def} \sim <$ 50, 150, 250 $k\Omega cm^2$ with increasing in salt concentration, as indicated by the EIS measurements shown in (B). 45

4.3 **Effect of charge and cholesterol on membrane electrical properties** (A) EIS spectra of dual component tBLMs DOPC:DOPS on HC18:βME 30:70 at DOPS concentrations ranging from 0 to 40 mol% (B) EIS spectra of a three-component stBLMs DOPC:DOPS:chol on HC18:βME 30:70 at fixed concentration 30 mol% DOPS and cholesterol concentrations ranging from 0 to 30 mol%. Area normalized capacitance and resistance as a function of PS and cholesterol content are shown in panels (C) and (D) 47

4.4 **PI(4,5)P_2 effect on tBLM formation.** (A) vesicle fusion of DOPC:DOPS liposomes containing PI(4,5)P_2 lipids at 5 mol % on HC18:βME 30:70 monitored over time with EIS (B) PI(4,5)P_2- containing membrane formed by vesicle fusion after 1.5h in a gold functionalized substrate with higher tether density HC18:βME 50:50 49

4.5 nSLD profile for stBLMs on HC18:βME-based stBLMs completed by vesicle fusion. (A) DOPC:DOPS 70:30 (B) DOPC:DOPS:PI(4,5)P_2 80:10:05. Bilayer completion is nearly 100% as evidenced by the overlap of the two isotopic contrast, H_2O and D_2O, profiles in the hydrocarbon group region 50

5.1 **HIV-1 Gag polyprotein structured domains.** Matrix (MA) is responsible for targeting Gag to the plasma membrane. Capsid (CA) promotes the lateral interaction between adjacent Gag molecules. Nucleocapsid (NC) binds to the viral genome. MA is formed by α-helices that form a globular structure and a flexible C-terminal region. Biophysical features of MA that mediates targeting to the PM includes basic patch residues, binding pocket specific to PI(4,5)P_2 located close to its N-terminus and a myristate group sequestered in a hydrophobic cleft. . . . 55

5.2 Sedimentation coefficient distribution, c(s), obtained from the sedimentation profiles for +myrMA (left) and -myrMA (right) as a function of pH. -myrMA is monomeric for the pH ranges tested while +myrMA is purely monomeric only at pH 8.0 and exists in a monomer-trimer equilibrium below that pH. Figure adapted from [55] 56

5.3 **Model for MA membrane association based on NMR studies.** Basic residues (blue) interact with acidic phospholpids (red) while PI(4,5)P_2 (yellow) inositol ring packs towards MA. The interaction between PI(4,5)P_2 and MA induces conformational changes that trigger the exposure of myristoyl (green) followed by the flip of the unsaturated chain of PI(4,5)P_2 towards the hydrophobic pocket vacated by the myristate upon membrane insertion. Figure from [149] 57

5.4 **HIV-1 Gag conformational changes**. In the absence of nucleic acid, Gag adopts a compact conformation at the membrane. Once membrane-bound Gag is exposed to RNA it becomes extended. Both membrane and genome binding are required for HIV-Gag adopting an extended conformation. Figure adapted from [39] 59

6.1 Comparison of -myrMA and +myrMA binding to stBLMs that contain DOPC and DOPS. Buffer: 10 mM $NaHPO_4$, 50 mM NaCl, pH 7.4. (A) Representative SPR curves of -myr MA binding, analyzed using the Langmuir model. (B) Representative SPR curves for +myrMA. Binding to 100% DOPS stBLMs showed significant deviations from a Langmuir isotherm and was analyzed with the Hill model, yielding a Hill coefficient of N $\approx$ 2. For low-affinity isotherms, it was not possible to measure full binding curves due to limitations in available amounts of protein. 64

6.2 Free binding energies ΔG determined from binding isotherms from the data shown in Figure 6.1. 65

6.3 Saturation protein surface densities, R_∞. The solid line is a model, indicating saturation of the equilibrium protein load for stBLMs containing more than $\approx$ 40 mol% DOPS. The R_∞ value for +myrMA binding to a 100% DOPS stBLM is excluded from the plot, since it was determined using a different binding model. . 66

6.4 **Myristoylation enhances MA binding to cholesterol-containing membranes.** Cholesterol was incorporated in stBLMs containing DOPC and 30 mol% DOPS, bathed in 50 mM NaCl, 10 mM $NaHPO_4$ pH 7.4. (A) -myrMA adsorption isotherm at 30 mol% cholesterol. (B) +myrMA adsorption isotherms at various cholesterol concentrations between 10 mol% and 30 mol%. 67

6.5 **Cholesterol enhances MA binding in the presence of PI(4,5)P_2.** Exemplary SPR response curves for (A) -myrMA and (B) +myrMA binding to mixed stBLMs containing constant amounts PI(4,5)P_2, bathed in 50 mM NaCl, pH 7.4, in the presence of 15 mol% DOPS and 30 mol% cholesterol 68

6.6 Free binding energies of MA to stBLMs derived from the data such as those shown in Figs. 6.7 and 6.8. 69

6.7 **Myristoylated MA favors interaction with PS-containing membranes over that with PI-containing membranes.** SPR binding curves of +myrMA to stBLMs containing DOPC and PI with or without PI(4,5)P_2 at equivalent surface charge densities of the membranes bathed in 50 mM NaCl, pH 7.4. 71

7.1 NR profile of +myrMA at pH 7.4 shows the presence of overlayers. Simplified molecular distributions for each organic interface layer of the DOPC/DOPS stBLM and +myrMA obtained from the best fit of reflectivity data to the spline fit model. The median protein envelope is shown with its associated 68% confidence intervals (red). Volume occupancy is indicated on the right axis. For comparison, median protein envelope of the hydrocarbon-like material (blue) is also shown. 78

7.2 Membrane undergoes reconstruction upon +myrMA interaction. Cole-Cole plot of DOPC:DOPS 70:30 stBLM on HC18:βME 30:70 as prepared (black) and after +myrMA concentration series ranging from 0.01 to 5 μM (red). Tail length is proportional to defect-density. Upon protein interaction with the membrane, the bilayer capacitance resembled a SAM spectrum. Its resistance decreased to values below the quality standards adopted for defect-free stBLMs ($R_{def} << 100$ kΩcm^2). Other protein incubation experiments on membrane of different lipid compositions showed similar disturbances of the bilayer membrane. 80

7.3 Electron microscopy images of PS containing vesicles remodeled by +myrMA at pH 7.4. (A) DOPS vesicles ([DOPS] = 0.5 mM), upon the addition of (B) 10M +myrMA. (C) POPC:POPS 70:30 vesicles ([POPS] = 0.5mM]) and (D) 10μM +myrMA control. POPC:POPS 70:30 vesicles incubated with 20μM of +myrMA for (E) 20 min and (F) after overnight incubation. Lipid-to-protein molar ratios (L/P) are stated in the individual micrographs. Measurements were performed at RT. Length of the scale bar is 500 nm. Micrographs of pure DOPS vesicles at pH 7.4 for control (right). Deformation and mild tubulation can be observed in pure DOPS vesicles but not in the mixed vesicles. 82

7.4 Binding of +myrMA on POPC:POPS 70:30 stBLM at pH 8.0. (A) Raw SPR data. Each spike indicates an injection with an increased concentration of protein. A final buffer rinse completely removes the adsorbed protein (B) Langmuir isotherm generated from the equilibrium raw data shows +myrMA affinity to PS-containing membrane is weaker at pH 8.0 83

7.5 Lipid membrane is minimally affected by +myrMA binding at pH 8.0. Cole-Cole plots of an stBLM POPC:POPS 70:30 as prepared (red trace) and after being incubated with +myrMA at 5 μM (blue trace). Upon protein interaction with the membrane, the bilayer capacitance increases slightly and its resistance remains the same or slightly improves, $R_{def} > 200$ kΩcm^2. 85

7.6 +myrMA monolayer at pH 8.0. Molecular distributions for each component of the d-31POPC/POPS 70/30 stBLM are zoomed in to emphasize the protein layer distribution. 10 μM +myrMA profile obtained from the best fit of reflectivity data to the spline fit model. The median protein envelope is shown with its associated 68% confidence intervals (red trace). Volume occupancy is indicated on the right axis. No overlayers are detected. A comparison of the median orientation fit using MA NMR structure is shown (black trace). 86

8.1 **Schematic representation of RSV Gag constructs** 88

8.2 Examples of SPR binding curves (raw data) of MA and Gag to DOPC/DOPS (70/30) stBLMs. Neat bilayer is exposed to increasing protein concentrations. Plateaus correspond to equilibrium responses at given protein concentrations, followed by a final rinse. Gag remains bound to the membrane after rinsed with buffer while MA is almost completely removed. 89

8.3 Affinity was quantified in 50mM NaCl at pH 8 to stBLMs at a fixed PS concentration of 30%.Gag (squares) and MA (circles) binding quantification to DOPC/DOPS stBLMS either with (red) or without (black) 2% PI(4,5)P_2. Langmuir isotherm well described MA data. In contrast, Gag data was fitted with Hill equation to model its cooperative membrane binding behavior. Measurements were repeated at least two times 90

8.4 Affinity was quantified in 50mM NaCl at pH 8 to stBLMs at a fixed PS concentration of 30%. Gag (circles) and Δflex (triangles) binding quantification to DOPC:DOPS 70:30 stBLMS. Langmuir isotherm well described the Δflex. In contrast, Gag data was fitted with Hill equation to model its cooperative membrane binding behavior. Measurements were repeated at least two times 91

8.5 nSLD profile of RSV MA profile at 10 μM on DOPC:DOPS 70:30 lipid bilayer as determined by spline method shown in green. Black lines correspond to MBD protein envelope at 50 μM on DOPC:DOPS 70:30 lipid bilayer. Red line represent the best-fit of the nSLD distribution calculated from the MBD crystal structure. 93

8.6 **RSV Gag is compact at the membrane.** Area fraction profile showing the molecular distribution of the lipid layer DOPc:DOPS 70:30 and the RSV Gag protein (solid green curve). 95% confidence bands determined by the fitting procedure are also shown (dashed green curve). An interpretative cartoon is also included. 94

8.7 **Δflex RSV is compact at the membrane.** Area fraction profile showing the molecular distribution of the lipid layer DOPC:DOPS 70:30 and the RSV Gag protein (solid red curve).95% confidence bands determined by the fitting procedure are also shown (dashed red curve). 95

8.8 **Schematic representation of MLV Gag constructs** 95

8.9 **Gag membrane-binding is electrostatically driven**. Comparison of MLV and ΔP12 binding to stBLMs that contain DOPC and DOPS at varying amounts. (A) Representative SPR curves of MLV binding, analyzed with the Langmuir model. (B) Representative SPR curves for ΔP12. 97

8.10 **MLV Gag is compact at the membrane while ΔP12 is extended**. Area fraction profile showing the molecular distribution of the lipid layer DOPC:DOPS 70:30 and the ΔP12 (solid green curve) MLV Gag protein in the absence (solid red curve) and presence of nucleic acid (solid blue curve). 95% confidence bands determined by the fitting procedure are also shown (dashed curves). MLV envelope generated by SAXS is also included. 99

9.1 **PlyC crystal structure**. PlyC is composed by two subunits connected by a flexible linker: PLyCA the catalytic domain and PlyCB the bacteria cell wall biding domain 104

9.2 **Electrostatic surface potential PlyCB binding domain.** The protein surface is color-coded according to electrostatic potential: positive and negative charges are shown in blue and red, respectively. The enlarged view at the right shows a binding pocket structure, which is composed of several cationic residues. The pocket has been identified as crucial for specific phospholipid binding and initiating PlyC internalization into mammalian cells. 105
9.3 Affinity of wt PlycB to negatively charged tethered lipid bilayer membranes containing neutral DOPC and anionic lipids at 30 mol% under physiologically relevant conditions (150 mM NaCl at pH 7.4). The isotherm for DOPC:DOPS = 70:30 is only partially shown. Data at cp $>$ 10 μM were corrected for protein contributions to the optical index of the buffer. Buffer rinses following protein incubations removed bound PlyCB from PG, PI and PA-containing membranes. PlyCB binds poorly to PA, PG and PI (phosphatidic acid, phosphatidylglycerol and phosphatidylinositol - membrane lipids that bear the same charge as phosphatidylserine but have slightly distinct molecular structures). The much stronger protein adsorption to PS shows clearly the specificity of PlyCB to this plasma membrane lipid 106
9.4 Binding of PlyCB to stBLMs with 10 and 20 mol% DOPS, respectively. Each spike indicates an injection with an increased concentration of protein. A final buffer rinse removes the adsorbed protein quantitatively on 10 mol% PS, but only partially on 20 mol% PS, indicating that the association of the protein with the membrane surface may differ depending on PS concentration 107
9.5 Roles of specific interaction of PlyCB with PS and electrostatic interaction in membrane binding. Affinity of PlyCB in 150 mM NaCl at pH 7.4 to stBLMs that contain DOPC and DOPS. (A) wt PlyCB binding to binary membranes with DOPC and various concentrations of DOPS. Inset presents an exemplary data set (20 mol% DOPS) and shows that PlyCB protein remains bound to the membrane after a buffer rinse. A similar resistence to washoff of the protein is observed with 30 mol% PS in the bilayer. 108
9.6 WT PlyCB binding to a ternary membranes composed of DOPC:DOPA:DOPS, systematically replacing PS by PA. Both electrostatic attraction and specific interaction contribute to PlyCB interaction to the membranes. At 2.5 mol% PS PlyCB lost its high affinity 109
9.7 PlyCB-R66E binding to a binary stBLM containing DOPC with 30 mol% DOPS. Data at $c_p > 10$ μM were corrected for protein contributions to the optical index of the buffer 110
9.8 Summary of protein affinities, displayed as differences in Free Energy of membrane binding $\Delta G = k_B T \ln K_d$, for membranes with 30 mol% anionic lipids of various compositions as indicated with respect to WT PlyCB on 30 mol% PS. This graph visualizes that the binding of WT protein to PG, PI or PA is much weaker than to PS (positive deviations of $\Delta\Delta G$ indicate lower affinities) and that a low concentration of PS with a larger concentration of PA restores some of the protein binding. Similarly, the R66E mutant of PlyCB binds to 30 mol% PS with a similarly low affinity as that of WT PlyCB to 30 mol% PI 111

9.9 **PlyCB membrane binding distorts bilayer integrity only minimally.** Raw EIS spectra (Cole-Cole plots) of an stBLM (DOPC:DOPS = 7:3) as prepared (red) and after incubation with 480 nmol/L PlyCB (black trace). While the EIS spectra were measured between 10 kHz and 1 Hz, the spectra shown here cover only the range, 10 kHz to 13.6 Hz in order to visualize the capacitive semi-circles well. Upon protein interaction with the membrane, the bilayer capacitance increases slightly and its resistivity decreases by $\approx 25\%$, as determined by fitting to the ECM shown in the inset. Other protein incubation experiments showed even less disturbances of the bilayer membrane than those in this graph. 113
9.10 Neutron reflectivity raw data for DOPC:DOPS 70:30 neat stBLM (black and red) and in contact with 600 nM of PlyCB (blue and green) in H_2O and D_2O contrasts 114
9.11 **PlyCB forms distinct membraneprotein complexes at high and low PS content of the bilayer.** CVO profiles of membrane-bound PlyCB on DOPC stBLMs containing (a) 15 mol% and (b,c) 30 mol% DOPS. Neutron reflection experiments were performed on neat bilayers and on bilayers in contact with protein-containing solutions (5 μM and 600 nM in panels a and b, respectively), and co-refined. While the CVO profile in (a) shows accumulation of protein outside the bilayer, but no incorporation into the membrane, the protein inserts deeply into the PS-rich bilayer, as indicated by the CVO profiles in panel b. The same stBLM DOPC:DOPS 70:30 as in after a buffer rinse. Only the structures of the stBLMs in the presence of PlyCB protein are shown. The CVO profile shows the protein remains deeply inserted into the PS-rich bilayer even after rinse (red trace). The loosely associated protein from the membrane surface was removed. Comparison of the median orientation fit using PlyCB crystal structure is shown with its associated 68% confidence intervals(black trace) 115
9.12 Probability distribution of PlyCB orientations (θ,ϕ) with respect to the DOPC:DOPS 70:30 bilayer normal. The most likely distribution of PlyCB inclination angle θ is larger than 60 and ϕ is equally distributed along the arc defined by θ, reflecting the symmetry of PlyCB. 116

List of Tables

4.1 Best-fit parameters obtained from the ECM model shown in chapter 3 for the data in Figure 4.3. Capacitance values were corrected by gold roughness ($\beta \approx 1.4$) and by the area of the electrochemical cell. Resistance values were normalized by the area of electrochemical cell ($A_{el} \approx 0.33$ cm^2). Hydrophobic thickness was calculated using equation 4.1, assuming ϵ =2.2 48

6.1 Best-fit parameters obtained from the Langmuir model for data shown in Figs. 6.1, 6.4, 6.5 and 6.7 72

7.1 Summary of +myrMA SPR experiments best-fit parameters obtained from the Langmuir model at 100 mM NaCl salt concentration and pH 8.0. The experiments were just performed once. 84

8.1 Best-fit parameters obtained from the Langmuir model and Hill equation for RSV MA and Gag, respectively, membrane binding at different lipid compositions (50 mM NaCl at pH 8.0) 92

8.2 Best-fit binding parameters estimated from the Langmuir model for MLV Gag wt and ΔP12 mutant on DOPC:DOPS membranes 98

9.1 Best-fit parameters from fitting Hill equation to SPR data shown in Fig. 9.3, 9.5 . 112

Chapter 1

Introduction

Numerous biological processes are either triggered by or result in the formation of protein-lipid complexes at the membrane [186]. The study on the interactions between lipids and proteins is fundamental to gaining insights into the physical aspects of biological processes. Because most proteins in the cell function as part of a complex with other proteins or lipids, an important way to understand their biological roles is to identify their interaction partners. These interactions are often regulated through reversible modifications, through lipid binding or other proteins. To begin to understand these interactions, one must quantify how tightly lipid-proteins associate, how slowly or rapidly those protein-lipid complexes assemble and break down over time, how they impact structure and how external molecular influences can affect these parameters [103].

Biological membranes have a high lipid composition diversity, are asymmetric across the two leaflets and also occur in different lipid phases depending on their structure and environment [174]. The complexity of biomembranes is further increased by the presence of carbohydrates and proteins, which control a variety of roles vital to cell activity. Due to the complexity of biological membranes, simplified model membrane systems have been developed [22] [168] [180] [82] to investigate the biological processes that occur on the membrane surface or within the membrane lipid bilayer. Model membranes allow for a systematic investigation of protein-lipid interactions and for the control and screening of certain parameters, such as lipid composition, pH and ionic strength, whereas in natural systems, the interactions are often complicated by the cell membrane intricate structure and wide variety of components. The use of biomimetic model membranes and biophysical methods, yet simplified, play a big role in the elucidation of the structure and the properties of biomembranes as well as provide a better understanding for biological processes placed at the membrane. Proteins may have different functions when associated with lipid membranes thus the importance of characterizing protein membrane association. The interaction of proteins with the lipid bilayer may involve significant changes within the structure of a protein. Most of the proteins functions may be structurally driven or tied to conformational changes, resulting in the activation of the proteins biological role [104] [77].

Structural properties of isolated proteins rarely reflect the protein's role within the membrane context. Usually they act in synergy with lipid membrane and other protein components. Obtaining structural information of protein-lipid complexes is particularly challenging because such complexes are often dynamic. In particular, partially disordered proteins contain regions that are intrinsically flexible, which permit molecular reorganization that controls molecular interactions

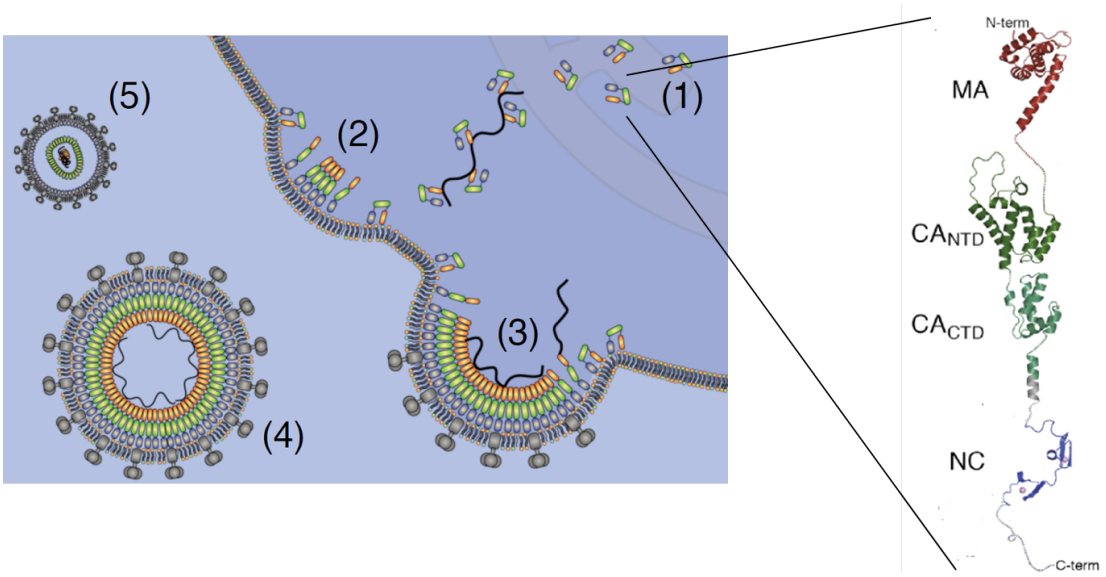

Figure 1.1: HIV-1 assembly at the plasma membrane of a host cell. The Gag polyprotein (multi-colored) targets the inner face of the PM (2) with its MA domain (purple) where it reorganizes from its solution structure (1), extending upon binding of viral RNA (black lines) to NC (orange). Budding into immature virions requires lateral contacts between the extended Gag (3), presumably mediated by CA (green). Dynamic sorting of PM lipids recruits a viral membrane composition that differs substantially from that of the parent membrane (3). A complex process completes budding of immature viruses (4) which mature further (5).

with different cellular components. The structural characterization of full-length partially disordered proteins by using traditional structural methods is challenging and the analysis of deletion variants usually lack essential determinants of protein's function contained in the deleted regions. Even though the structural characterization of proteins when in complex with membranes can be difficult, provided with the right set of complementary tools structural information can be obtained with unprecedented resolution [159] [39]. For proteins associated with lipid membranes, neutron reflectometry is a powerful alternative to reveal the details of the structural reorganization of intrinsically disordered proteins at physiologically relevant conditions.

Complementary surface-sensitive biophysical characterization methods and a repertoire of cutting-edge metrologies for proteins in and on membranes has helped to elucidate the mechanisms underlying biological processes and to establish a clear picture of the individual role of lipids and proteins in the formation of protein-membrane complexes. Two membrane-related biological processes are investigated in this thesis: the mechanisms behind retroviral assembly and endolysin PlyC plasma membrane translocation. It is the purpose of this thesis to understand the dynamics, function and structure of protein-membrane association complexes at molecular scale.

1.1 Retroviral assembly

The retroviral Gag protein is an essential component for the formation of a number of viral pathogens such as Human Immunodeficiency Virus (HIV) and oncoviruses such as Rous Sarcoma Virus (RSV) and Murine Leukemia Virus (MLV). Gag is a polyprotein, composed of multiple structured domains separated by linkers that can either be flexible as for HIV-1 or more rigid as for RSV and MLV. Those domains play specific roles during assembly. From N to C terminus: Matrix (MA), which is myristoylated in HIV-1 and MLV but not in RSV, targets the plasma membrane, capsid (CA) mediates the lateral interaction between adjacent Gag molecules and nucleocapsid (NC) binds and incorporates the viral genome into the immature virus particle (Figure 1.1). The mechanistic events involved in retroviral assembly are still poorly understood.

The basic principles of our current understanding of assembly are summarized in Figure 1.1, the details are rather complex [167] [15] [57]. The viral particles are the result of a series of complex interactions between Gag, the plasma membrane (PM) and the viral RNA genome, which jointly drive the process of viral assembly [1]. Gag is expressed in the cytoplasm, migrates to the cellular periphery and targets the surface of the PM, where assembly of immature virus occurs. Not all retroviral Gag proteins assemble at the PM. Type B and D retroviruses, such as Mouse mammary tumor virus (MMTV) and Mason Pfizer Monkey virus (MPMV) respectively, assemble in the cytoplasm, and then the assembled structure is transported to the PM where they acquire their lipid envelope as they bud out [29] [166]. Gag proteins may interact in small numbers with their genomic RNA (gRNA) in the cytoplasm. Lateral interactions between Gag molecules on the membrane, presumably mediated by nucleic acid, induces ordering and growth of a protein lattice. Eventually, the growing Gag lattice deforms the membrane and leads to the budding of immature viral particles. It is clear that the formation of viral shells include Gag trafficking to the membrane, its multimerization and the incorporation of viral gRNA but the actual pathway taken by Gag is unclear.

Here, we address the general aspects of coupling and structural reorganization of Gag of different retrovirus species at different molecular contexts. The nature and strength of proteins interaction with different lipid components, delineation of the individual contributions of the mechanisms of interactions involved in protein-membrane association and impact of those interactions in the protein structure, orientation and depth of insertion were studied in order to provide a molecular picture of viral assembly which may lead to new therapeutic interventions. Understanding Gag structure-function relationships when bound to the membrane may be a key to understand and prevent the assembly of Gag in vivo.

1.1.1 Objectives

Gag protein regulates assembly at the plasma membrane as an indispensable structural element of the virus core together with lipid and nucleic acid [1]. Quantitative assessment of the interactions that drive the assembly of intermediate Gag complexes is not possible in vivo. Model membranes are thus used to study macromolecular assemblies on the membrane under physiologically relevant conditions. A multitude of molecular interactions involved in protein membrane association result in complex molecular reorganizations which makes understanding these processes difficult. This lack in understanding, in turn, prevents the targeting of this important

step in the reproduction of virus particles with therapeutic interventions. Chapters 5, 6, 7 and 8 focus on the major mechanisms underlying the molecular interactions between Gag, domains or full-length, with lipids at a molecular level and how they affect the those Gag protein constructs conformation at the membrane.

Matrix: Gag-membrane coupling domain

Establish the molecular interactions that control MA association with the membrane

Specific Aims:

1. Quantify MA binding to bilayers.

2. Investigate the role of myristoylation in binding affinity and protein orientation.

3. Understand the mechanisms that lead to the recruitment of specific lipids into the viral shell.

4. Determine individual contributions to the free energy of binding through a comparative study of non-myristoylated (-myr) and myristoylated (+myr) HIV-1 MA.

5. Determine the MA membrane-bound structure and how that is affected by N-terminal lipidation and lipid composition.

6. Characterize and compare the membrane binding of matrix that naturally lacks lipidation, RSV MA, to HIV-1 MA.

Full-length Gag: the principal building-block of retrovirus particles
Characterize the origin and the implications of the conformational reorganization of full-length Gag at the membrane

Specific Aims:

1. Characterize and compare the membrane coupling of distinct Gag species, MLV and RSV, to test whether the conformational flexibility of Gag is important for the assembly of HIV-1 virions.

2. Determine conformation and density of Gag on the membrane in the absence and presence of nucleic acid.

3. Characterize the membrane bound structure of the Gag protein from two different viral species, RSV and MLV, and compare the effect of linker region deletion. How does the linker deletion alter membrane-protein interactions?

4. Understand the complex structural dynamics involved in viral assembly. How does the linker flexibility affect Gag conformation on the membrane?

5. Establish a functional role for the disordered linker regions in retroviral Gag that may rely in preventing unproductive assembly processes in the host cytosol or on the membrane in the absence of viral genome. Are these linkers responsible for regulating Gag multimerization?

1.2 Enzyme PlyC plasma membrane translocation

Endolysins are bacteriophage-encoded murein hydrolases expressed in the late stage of phage replication when they lyse the cell wall of Gram-positive bacterial hosts, thus enabling progeny phage release [53] [54]. However, they can also lyse bacteria when externally administered. As a result, they offer a unique antimicrobial alternative, referred to as enzybiotics. PlyC also has the unique and inherent ability to penetrate into mammalian cells, without inflicting damage, and retain bacteriolytic activity in the intracellular environment.

The entry point of PlyC on mammalian cell is not known, nor is the mechanism by which PlyC translocates the plasma membrane. Bacterial membranes contain negatively charged lipids on the outer leaflet, whereas the outer leaflets of eukaryotic cell membranes are predominantly zwitterionic [174]. In this thesis we investigate the molecular basis of the observation that PlyC can bind and cross the mammalian plasma membrane by examining the details of two-stage interaction - surface adsorption and bilayer insertion - of PlyC with various model membranes.

1.2.1 Objectives

Endolysin PlyC mechanism of translocation
In Chapter 9, we investigate molecular-scale aspects of PlyC binding domain, PlyCB, membrane interactions, seeking a mechanistic understanding of how the binding domain initiates membrane penetration and transfer of the catalytic PlyCA domain across cell membranes.

Specific Aims:

1. Determine the lipid components that contribute to membrane association, the origin of lipid-protein molecular interactions and their relative strengths

2. Establish the mechanisms of interaction that drive PlyC insertion into the membrane

3. Investigate the impact of a point mutation, which affects PlyC ability of internalize eukaryotic cells, on PlyC membrane-association and localization

Chapter 2

Methodology: Lipid-protein Interactions studied using Model Membranes

The complexity of the cell environment makes it difficult to investigate macromolecular assemblies at biological membranes in a systematic way. Model membrane systems are an alternative to investigate protein-lipid interactions under well defined and controlled conditions. The chemical and physical properties of lipid membranes are reviewed in section 2.1 followed by a brief overview of the different kinds of model membranes in section 2.2. Finally, protein-membrane binding and protein structure when in complex with lipid membranes are addressed in section 2.3.

2.1 Lipid Bilayer Membranes

2.1.1 Overview

Biomembranes play an essential role in maintaining the biology of the cell [80]. The plasma membrane, in particular, act as a barrier, regulating the transit of molecules from the extracellular environment to the cytoplasm preventing undesired molecules from entering the cell and maintaining proper ionic composition of the cytosol. While biological membranes are permeable to water, the transport of ions and organic molecules across the membrane typically requires the presence of membrane proteins. Besides defining the cell and its compartments boundaries, the ability of the membrane to reshape itself is indispensable for cell biological function such as cellular division and intracellular membrane trafficking. Furthermore, proteins on or buried in the lipid bilayer mediate communication with other cells and its surroundings.

The first direct observation of the cell membrane as a bimolecular sheet was achieved by electron microscopy [148]. Advances in structural biology resulted in a rapid evolution of lipid membrane models as they are currently understood. The basic plasma membrane model is the fluid mosaic model that treats the lipids as a two-dimensional fluid interspersed with proteins and lipids being able to diffuse freely within the plane of the membrane [165]. Improvements in the original model reflect the subsequent development of biophysical techniques that led to the observation of domains that restricted the lateral diffusion of the membrane components [99] [49].

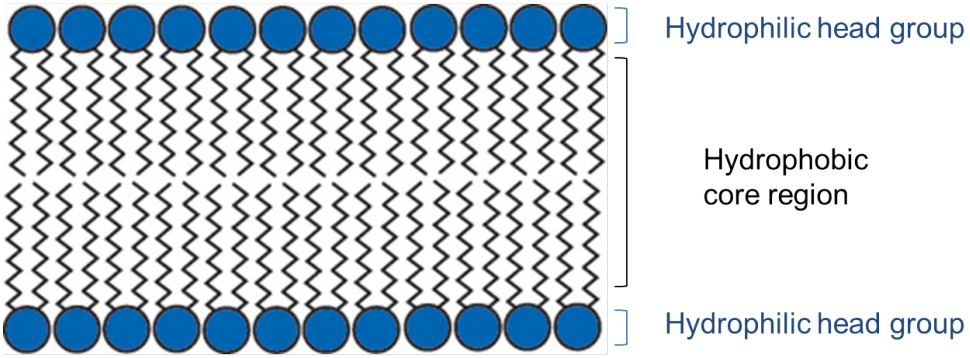

Figure 2.1: Lipid bilayer bimolecular sheet structure. The hydrocarbon chains of the lipids form the hydrophobic core of the membrane while the polar lipid headgroups are exposed to the aqueous environment

Those specialized regions within the membrane were attributed to ordered assemblies composed of specific lipids and proteins that possess in-plane organization [162] [163]. The complex structure of biological membranes is due to a wide variety of lipid components that interact with several proteins influencing membrane dynamics and structure [91] [141]. The interplay between protein and lipids is important for understanding cellular processes that occur in or at the membrane.

Lipid components

Phospholipids are the principal structural lipid constituents of the plasma membrane. They have an amphiphilic nature, and are composed of polar, or hydrophilic, headgroups and a non-polar, or hydrophobic, hydrocarbon chains. The headgroups favorably interact with water while the hydrocarbon region is organized to prevent contact with water. In an aqueous environment, the lipids, depending on their shape, pack as a two-dimensional lipid sheet (see Figure 2.1). The phospholipid bilayer constitutes the basic structure unit of all biomembranes.

The polar groups can be either charged or zwitterionic (neutral) dictating the surface chemistry of the membrane. Charged surfaces can promote protein-membrane association through non-specific and long range electrostatic interactions. Moreover, the headgroup size and geometry can also control local membrane curvature. Finally, the acyl chain structure, saturation and length, can determine the fluidity of the bilayer. Lipid membrane components are not homogeneously distributed in the bilayer membrane of biological cells but rather organized in lateral microdomains.

Cholesterol also constitutes an important lipid component of membranes, being particularly abundant in the plasma membrane of mammalian cells. Due to its very hydrophobic nature it cannot form sheetlike bilayers on its own but can be incorporated to phospholipid bilayers influencing the bilayer fluidity. Plasma membrane also contains sphingomyelin (SM), the most abundant sphingolipid, residing in its majority on the outer leaflet. Indirect methods based on detergent extraction reveal sphingomyelin colocalizes with cholesterol forming lateral microdomains known as rafts [107]. However, the existence of rafts in living cells is still under dispute [119] [96].

Lipid phases

Membranes are in a highly dynamic state [67]. Thermal motion permits lipids to rotate along their long axis and laterally diffuse in the membrane. The mobility of the lipids indicates the non polar interior of these structures is fluid like. Membranes can exist in different physical states, characterized by the lateral mobility and structural organization of the lipid molecules within the bilayer. Membrane-related biological phenomena are affected by the fluidity of the membrane, which largely depends on temperature and lipid composition [62]. The response of lipid bilayer physical state i.e. lipid mobility to changes in the temperature characterizes the phase behavior of the bilayer. Besides the phospholipids structural role in the maintenance of membrane architecture, phospholipid phases that are gel, liquid ordered and liquid disordered, have specific properties that determine the orientation and mobility of lipids and proteins, and therefore affect membrane functionality.

Hydrated lipid bilayers undergo phase transitions which occur at defined temperatures for each lipid species [174]. All the phospholipids in the plasma membrane have a characteristic phase transition temperature, above which the lipid bilayer is best described as a two-dimensional liquid crystal. As in a crystal, the molecules still retain a specific orientation. In this case, the long axes of the molecules tend toward a parallel arrangement, yet individual phospholipids can rotate around their axis or move laterally within the plane of the bilayer. Below the phase transition temperature, the lipids adopt a gel phase. The lipid bilayer is converted from a liquid crystalline phase to a gel phase in which the movement of the phospholipid fatty acid chains is greatly restricted. Gel phase can occur or be induced in synthetic lipid bilayers containing membrane proteins or peptides [97] but most of the biological membranes exist in a fluid phase. The transition temperature of a particular bilayer depends on the packing of the lipid molecules, which depends in turn on the membrane lipid components. Bilayer physical state is greatly influenced by the degree of saturation of hydrophobic chains and also by acyl length. Phospholipids with saturated chains pack together more tightly than those containing unsaturated chains. Consequently, the greater the degree of unsaturation of the fatty acids of the bilayer, the lower the temperature before the bilayer transitions to a gel phase. Another factor that influences bilayer fluidity is fatty acid chain length [136]. The longer the fatty acyl chains of a phospholipid, the lower its melting temperature. Cholesterol also influences the structure and phase behavior of lipid bilayers [75] [135]. Cholesterol induces tighter packing of fluid membrane by decreasing the permeability and flexibility of surrounding lipid chains [174], while it increases fluidity of gel phase membranes by disrupting the packing order [117]. Interactions of cholesterol with multi-component systems are complicated and result in complex phase diagrams.

As mentioned above, the compositional complexity chemical and structural nature of lipids, in and out of plane, influences the properties of the membranes [194] and proteins leading to the coexistence of different types of lipid domains [99]. The domain segregation plays a critical role in protein sorting [164]. Some proteins are preferentially associated with more ordered phases [162]. The molecular interactions that control the phase behavior may be dominated by lipid-lipid, lipid-protein and coupling to the other leaflet [103].

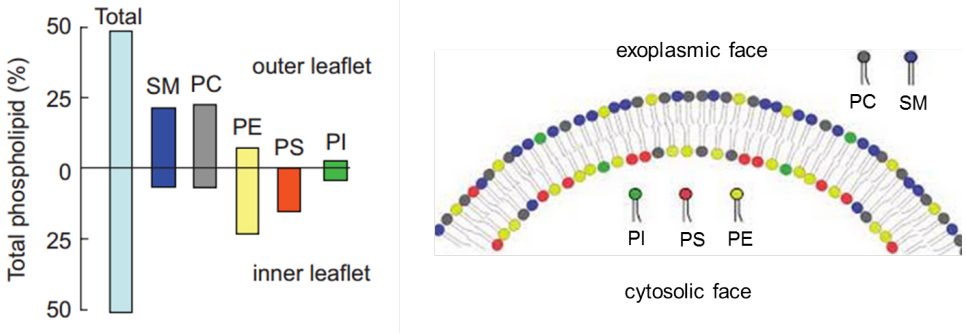

Figure 2.2: Plasma membrane phospholipid asymmetry The outer leaflet of the plasma membrane is predominantly neutral and enriched in sphingomyelin (SM) and phosphatidylcholine (PC). Phosphatidylethanolamine (PE) and phosphatidylinositol (PI) reside mainly in the inner leaflet, while phosphatidylserine (PS) is located almost exclusively in the inner leaflet of the plasma membrane. Figure adapted from [174]

Asymmetry

Biological membranes have distinct lipid composition distribution across the two lipid leaflets [174] [43]. Active enzymes, such as flipases and scramblases, maintain this imbalance by actively transporting specific phospholipids from one monolayer to the opposite one [35]. The outer leaflet of the plasma membrane is largely zwitterionic with phosphatidylcholine (PC) and sphingomyelin (SM) as its main components, while negatively charged lipids, phosphatidylserine (PS) and phosphatidylinositol (PI), are almost exclusively found in the cytosolic face of the cellular membrane, as shown in Figure 2.2. Phosphatidylethanolamine (PE) mostly resides in the inner leaflet. Cholesterol on other hand is evenly distributed among the two leaflets. Disturbance of the asymmetry such as PS exposure to the outer leaflet can trigger immune responses or result in cell death [51].

Maintenance of lipid distribution across the PM leaflets is an essential aspect of the structure and function of biological membranes, and is reflected in the asymmetric distribution of integral membrane proteins. They adopt a specific orientation with respect to the cytosolic and exoplasmic faces of a cellular membrane, contributing to different properties on the two membrane faces. The lipid and protein asymmetry lead to spatial segregation of biological processes associated with different membrane leaflets. Additionally, the difference in lipid component distribution among the leaflets is a substantial contributor to the curvature in biomembranes.

Since model membranes should be representative of natural membranes, they must capture the essential features of the membrane at which the biological process takes place, including lipid composition. Retroviral assembly for example occurs at the inner leaflet of the PM, which is rich in acidic lipids, while the endolysin PlyC initially interacts with the outer leaflet, which is mainly zwitterionic, prior to PM translocation. It is hence important to consider the choice of the lipids, of the complexity of the lipid mixture as well as of the model membrane when investigating biological processes.

2.2 Biomimetic Model Membranes

The complex architecture of biological membranes and vast number of cell components make the characterization of lipid-protein interaction challenging. The necessity of assessing functional and structural features of biomembranes and investigating membrane related processes in a well-controlled environment has pushed the development of biomimetic platforms [150] [34] [102] [180]. Model membranes mimics the lipid arrangement found in natural plasma membranes and although not as complex as the native membrane, they capture their most fundamental aspects. The use of model membranes permits the manipulation of lipid composition and other experimental conditions, which helps to identify the elements that control particular mechanisms and to attribute interactions and their contributions to a specific biological process. Biomimetic membranes are ideal for studying the molecular mechanisms by which proteins interact with membranes.

To reliably examine the interactions of proteins with membranes, experiments with model membranes are designed taking into account the biological context. The lipid composition of the model membrane should resemble the biological membrane at which the protein of interest associates. Therefore, the choice of an adequate membrane platform and biologically relevant conditions (pH, salt, temperature) is critical to investigate the mechanistic details of protein-lipid interactions.

Three systems are widely used: lipid monolayers, supported bilayers and liposomes - as shown in Figure 2.3. While each of these systems exhibits advantages and disadvantages, they all mimic to a certain extent the lipid arrangement of natural cell membranes [47].

2.2.1 Langmuir Monolayers

Monolayers are constituted of one lipid leaflet formed at the air-water interface in a Langmuir trough. They are extensively used to describe lipid-lipid interaction controlled by lateral pressure [11]. Under compression, the Langmuir monolayers can undergo phase transitions, which depend on physical and chemical properties of the lipid and subphase conditions [60] [105]. Compression isotherms, the measurement of surface pressure as a function of the molecular area of the lipid components spread at the interface, reveal the phase behavior of those molecules. Langmuir monolayers are also appropriate to study lipid-protein interaction [118]. By keeping the film area constant, changes in surface pressure are recorded upon addition of biomolecules in the subphase [33] [95]. Since monolayers do not hold the structural complexity of a bilayer, the features obtained from the Langmuir monolayers do not necessarily represent the properties of the lipid bilayer.

2.2.2 Lipid Vesicles

Liposomes are spherical lipid assemblies that form spontaneously due to the amphiphatic nature of the lipids. One of the advantages of using vesicles over monolayers is that liposomes provide a well-defined, native-like environment for incorporation of integral proteins. Lipid vesicles can be prepared at different sizes, ranging from 0.1 to 200 μm, with the largest ones being an

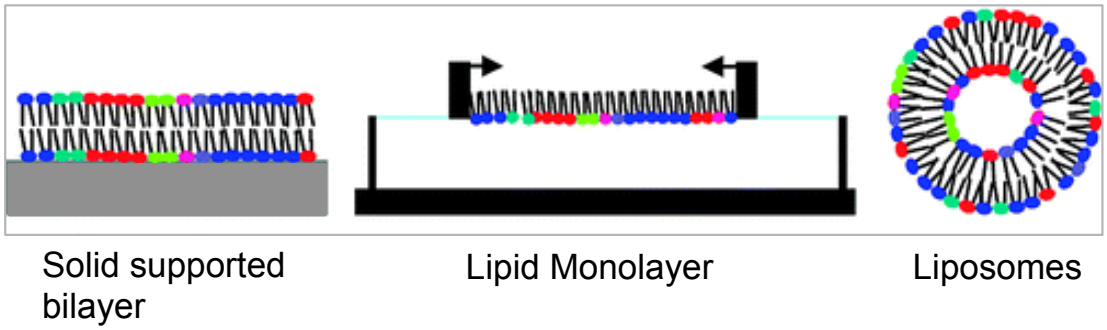

Figure 2.3: Model membrane systems. Solid supported bilayer, lipid monolayer and liposome mimic of biomembranes [139].

ideal model membrane to visualize phase separation and lipid domain formation and membrane remodeling induced by protein interaction through light microscopy studies [185].

2.2.3 Solid Supported Membranes

Lipid bilayers attached to solid substrates, usually glass, mica or silicon oxide, constitute the category of solid supported membranes (SSMs). Planar bilayers are either formed by spontaneous rupture of vesicles on the hydrophilic surface or by Langmuir-Blodgett technique which consists of transferring Langmuir monolayers to the solid substrate. In particular, the planar geometry enables the characterization of membrane structure and dynamics using numerous surface characterization techniques such as quartz crystal microbalance with dissipation monitoring (QCM-D) [46] [155], fluorescence correlation spectroscopy (FCS) [106], atomic force microscopy (AFM) [155], surface plasmon resonance (SPR) [170], electrochemical impedance spectroscopy (EIS) [61] and neutron reflectometry (NR) [14] [114].

The SSMs have certain limitations; membranes in contact with solid substrates, the thickness of the water layer gap for SSMs is estimated to be $<<$10 Å, have their in-plane dynamics affected due to lipid and the solid surface interactions. Also, proteins reconstituted into lipid membranes for functionalization, tend to denature i.e., unfold from their specific three-dimensional structure required for protein function, at the surface [89]. As an alternative, tether molecules can be chemisorbed to the substrate to establish a thicker water reservoir and a more fluid bilayer [157]. Again, the choice of a particular supported membrane system depends highly on the desired information needed from the experiments.

2.2.4 Sparsely tethered bilayer lipid membranes (tBLMs)

To minimize the influence of the substrate on the bilayer properties, tether molecules are chemically adsorbed to the solid substrate. This spacer supports the membrane above a solid substrate, providing the potential for a sub-membrane aqueous reservoir. Such a reservoir enables the incorporation of transmembrane proteins to extend beyond the membrane [114] [113], and also helps to reduce the effects of the solid surface on the membrane. The tethers maintain the robustness and increase the stability of the SSM system. tBLMs are thus resilient in-plane fluid sys-

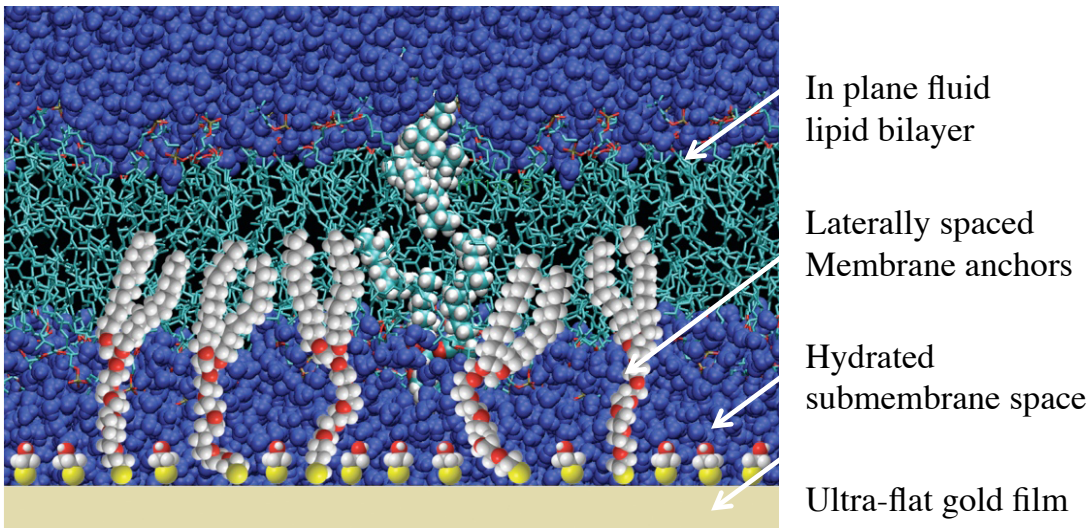

Figure 2.4: Sparsely tethered bilayer lipid membrane. Lipid bilayer coupled to the solid support through a synthetic lipid diluted on the surface using a spacer to create a submembrane hydration layer adjacent to the substrate-proximal leaflet

tems [157] built on metal functionalized substrates [114] [113] [50] that consist of a lipid bilayer decoupled from the coated substrate through a linker or anchor molecules as shown in Figure 2.3. To design a hydrated submembrane reservoir, thiolipids are spaced out on the surface by using β-mercaptoethanol (βME) as the first preparation step for the formation of a self-assembled monolayer (SAM). This method decreases the amount of the tether on the surface, resulting in sparsely tethered bilayer lipid membranes (stBLMs) that comprise aqueous solvent between the bilayer membrane and the substrate. The tethers create a 20 Åwater reservoir between the bilayer and substrate [70]. The in-plane dynamics of the stBLMs, assessed by fluorescence correlation spectroscopy depended on the density of the lipidic anchors in the bilayer leaflet proximal to the substrate as well as on details of the molecular structure of the anchor lipid [157]. These measurements were able to distinguish the diffusivities of the leaflets, revealing the value observed in the distal leaflet to be indistinguishable from that measured in free-standing bilayers [157], such as those forming giant unilamellar vesicles.

The lipid tether used in this work, HC18 [14], was synthesized by David Vanderah at Institute for Bioscience and Biotechnology Research (IBBR). HC18 is a thiolipid composed of three parts: a chemical linker (sulfur) that will form covalent bonds with the gold, a hydrophilic spacer (hexa ethylene oxide) that maintains the separation between the substrate and bilayer creating a hydration layer, and an unsaturated lipid tail (dioleoyl chains) corresponding to the hydrophobic region that controls lipid bilayer self-assembly. In comparison with previously developed tethers [70] [114], HC18 unsaturated hydrocarbon chains provide more fluidity to the membrane. The lipid components of biomembranes have at least one saturated chain, HC18 is thus the best option to build stBLMs that resemble more accurately lipid membranes.

stBLMs have extremely low defect density, preventing non-specific protein association and forming effective barriers to ions (highly electrically sealing) which is a valuable aspect in biosensor applications [150]. Membranes consisting of diverse lipid species can also be formed,

allowing stBLMs to capture the most salient biochemical features of the native membrane. Apart from characterization of lipid physical properties, planar bilayers are used to reveal structural details and mechanisms of interaction of proteins within their native lipid environment. It has been shown that stBLMs are stable in their dielectric properties over the course of months [114]. Not surprisingly, stBLMs prepared from synthetic phospholipids are increasingly used to study protein-membrane interaction [157] [123] [187].

2.3 Proteins: structure-function relationship

2.3.1 Membrane binding

The ability of a protein to bind selectively and with high affinity to a ligand depends on the formation of a set of interactions. Some proteins need to strongly associate to the membrane to carry out their function. Non-specific i.e. electrostatic and hydrophobic, and lipid specific are the predominant forces involved in protein membrane binding and they also govern protein orientation at the membrane.

Electrostatic interactions

Electrostatic is a long-range fundamental force that dominates the initial protein-lipid interactions. The nature of this interplay is typically non-specific. Proteins containing basic patches will be eventually recruited by the anionic lipids to the inner leaflet of the plasma membrane. Surfaces with opposite charges provide the general attraction mechanism for proteins that might further lead to membrane penetration. pH changes, and ionic strength may disrupt the nonspecific electrostatic interactions. Another type of electrostatic interaction is the binding to bilayers containing anionic lipids of negatively charged proteins or peptides mediated by divalent cations bridges [176].

Hydrophobic interactions

Hydrophobic interactions are an entropic-driven effect. The proteins may anchor to the bilayer as a result of hydrophobic interactions between the bilayer core and exposed nonpolar residues at the surface of a protein or by their lipid modification [69]. Partitioning of hydrophobic domains into the non-polar hydrocarbon core favors protein-membrane contact. Proteinmembrane interactions frequently involve a conformational change at the membrane interface that expose a buried hydrophobic surface, which in turn facilitates insertion of a particular domain into the hydrophobic core of the lipid membrane.

Lipid specific interaction

Binding of protein to a specific lipid occurs via specific membrane targeting structural protein domains. Some proteins have specific binding pockets for the headgroups of the lipids to which they bind. Lipid specificity has chemical and structural character. It plays a key role in the

understanding of the penetration and/or activity of endolysin PlyC and the HIV-1 Gag interaction with lipid membranes.

2.3.2 Membrane-bound structure

Structural and functional characterization of membrane-protein complexes are crucial for elucidating the biological processes that occur at the membrane interface. In fact, cellular processes can be mimicked in artificial systems, and their molecular basis can be studied in a controlled environment, while the resulting structures or structural changes are being probed [39] [87]. Neutron reflectometry (NR), in particular, as a surface sensitive technique has the capabilities to characterize such disordered systems [158]. Protein-membrane complexes can be probed on the sub-nanometer scale as a result of model refinement [68]. Molecular dynamics simulations are a good complement to NR. By combining these two methods one gains insight into partially disordered molecular complexes that have so far not been attained by other structural techniques [124] [159]. NR can resolve structural details of membrane-associated proteins at physiological conditions, and it may be unique in its ability to directly resolve details of the membrane-bound protein structure [87] [39].

The sparsely tethered bilayer lipid membrane, stBLM, described in section 2.2.4. is a fine-tuned engineered model membrane compatible with NR experiments. Previous measurements on planar membrane mimics showed that it is indeed possible to resolve at high resolution the spatial association and orientation of proteins on a fluid bilayer [123] [158]. Structural information can be obtained from protein structures determined by NMR and x-ray under the assumption that the crystal structure is conserved in the membrane-bound protein. MD simulations can be used to validate the NR predictions based on the protein crystal structure - as successfully accomplished for the PTEN tumor supressor [159].

Those tools circumvent the complications surrounding the structural characterization of intrinsically disordered systems where atomic structure of protein-membrane complexes on fluid bilayers can be precisely determined, with angstrom precision. This novel strategy complemented by other biophysical techniques enable to scrutinize the molecular origins of diseases, through the quantification of the membrane interactions of proteins with membranes, and provide new insights on the structural basis of protein-membrane complexes.

Chapter 3

Experimental Techniques

Sparsely tethered bilayer lipid membranes (stBLMs) are a robust platform suitable for the study of molecular level interaction and the structure of protein-membrane complexes.The planar geometry of stBLMs makes them amenable to numerous surface sensitive techniques, which allows functional and structural characterization of proteins when adsorbed to the lipid bilayer. In this work, electrochemical impedance spectroscopy (EIS), discussed in section 3.1, is used to investigate electrical properties and thus assess the quality of lipid bilayers before and after protein binds to the interface. Surface plasmon resonance (SPR), described in section 3.2, is employed to probe the molecular level interactions of proteins with membranes and optimize the experimental conditions for neutron scattering experiments. Finally, neutron reflectometry, theoretical and experimental foundations presented in section 3.3, is utilized to reveal structural properties of stBLMs and proteins associated with the membranes.

3.1 Electrochemical Impedance Spectroscopy (EIS)

3.1.1 Introduction

An important feature of model membranes is their resistance to ion flow across the membrane. Highly insulating membranes indicate low defect density of the bilayer which in turn is a prerequisite for studying protein-lipid interaction preventing non-specific association with defect-rich regions. EIS is a powerful tool to determine bilayer integrity, ensuring high membrane quality prior to protein binding measurements [172], and to monitor the effect of protein adsorption on the membrane electrical properties.

3.1.2 Theory

Impedance spectroscopy is an alternating current technique in which a single frequency sinusoidal AC potential is applied to an electrochemical cell and the current through the sample is measured. The EI spectrum is obtained by scanning over a range of frequencies. For detailed theory and applications see [8]. Impedance is a measure of the ability of a circuit element to resist the flow of electrical current. The complex electrical impedance, $Z(\omega)$, is the ratio of ap-

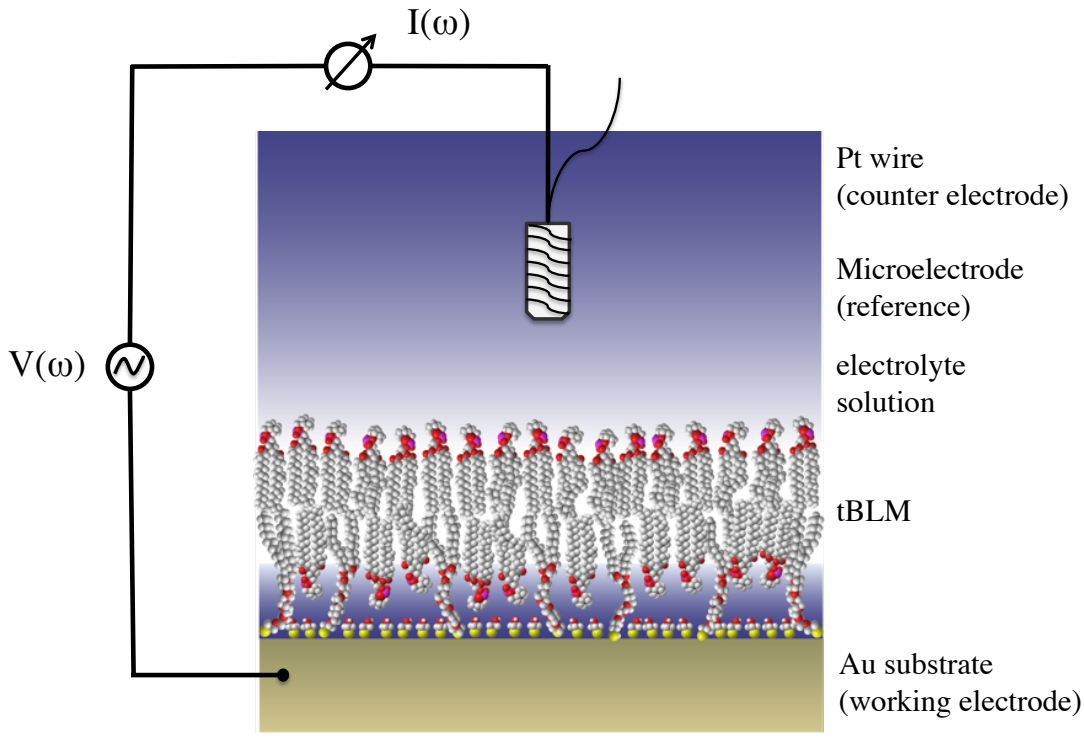

Figure 3.1: Schematic of a three electrode electrochemical cell. The reaction takes place at the Au substrate, working electrode. A periodic voltage signal of variable frequency is applied between the working and reference electrodes across the sample, stBLM. The auxiliary electrode, along with the working electrode, completes the circuit over which current is measured

plied voltage, $V(\omega)$, to the measured current response, $I(\omega)$.

$$Z(\omega) = \frac{V(\omega)}{I(\omega)} \tag{3.1}$$

The excitation signal applied across the interface has the form $V(\omega)$= $V_0 \sin(\omega t)$ where V_0 is the amplitude of the signal and ω is the angular frequency, $\omega = 2\pi f$ and f is the frequency. The current response, $I(\omega)$, of electrochemical cells is non-linear [86] unless the excitation is kept small. In the linear regime, the current response has the same frequency, ω, as the sinusoidal voltage but differs in phase, ϕ.

$$I(\omega) = I_0 \sin(\omega t - \phi(\omega)) \tag{3.2}$$

In Euler notation, the potential and the current have the form:

$$\begin{aligned} V(\omega) &= V_0 e^{j\omega t} \\ I(\omega) &= I_0 e^{j(\omega t - \phi(\omega))} \end{aligned} \tag{3.3}$$

where $j^2 = -1$.
Combining Eqs 2.1 and 2.3 it follows that

$$\begin{aligned} Z(\omega) &= \frac{V_0}{I_0} e^{j\phi(\omega)} \\ &= Z_0 e^{j\phi(\omega)} \\ &= Z_0 \cos\phi(\omega) + j|Z_0| \sin\phi(\omega) \\ &= Z'(\omega) + jZ''(\omega) \end{aligned} \tag{3.4}$$

with $Z'(\omega)$ and $Z''(\omega)$ as the real and imaginary parts of impedance, respectively, and $|Z(\omega)| = \sqrt{Z'^2(\omega) + Z''^2(\omega)}$
The impedance of a capacitor is given by

$$Z(\omega) = \frac{1}{j\omega C} \tag{3.5}$$

which leads to

$$C(\omega) = -\frac{Z''(\omega)}{\omega|Z(\omega)|^2} - j\frac{Z'(\omega)}{\omega|Z(\omega)|^2} = C'(\omega) + jC''(\omega) \tag{3.6}$$

A plot of the imaginary vs real part of $C(\omega)$, $C'(\omega)$ vs $C"(\omega)$, known as Cole-Cole plot, is one of several well established representations of the impedance spectra of circuits and it is not limited to pure capacitive components.

3.1.3 Instrumentation

The EI spectra were generated by applying an AC voltage with an amplitude of 10 mV across the interface. The amplitude of the signal is small enough to ensure a linear response of the system while sufficient in terms of signal to noise ratio. The experiments were performed using a Solartron (Farnborough, UK) 1287A potentiostat and 1260 frequency analyzer. A three-electrode configuration [171] [114] was implemented to study the electrochemical events taking place at the working electrode (WE). The gold-coated substrate served as the WE, a saturated silver-silver chloride (Ag| AgCl|NaCl(aq,sat)) microelectrode (Microelectrodes M-401F, Bedford, NH) was used as a reference electrode and a 0.25 mm diameter platinum wire (99.9 % purity, Aldrich) coiled around the reference electrode acted as the auxiliary (counter) electrode (Figure 3.1). The potentiostat maintains the potential across the reference and working electrode at a constant level by adjusting the current of the counter electrode. The frequency analyzer was used to apply the sinusoidal wave into the electrochemical cell and to measure the amplitude and phase shifts of the current response of the circuit at single frequency, thereby determining the impedance. The measurements were carried out over a frequency range of 1 Hz to 100 kHz. Data acquisition and modeling was obtained using the Zplot and Zview software packages, respectively (Scribner Associates, Southern Pines, NC). The RE was placed on the EIS cell well filled with electrolyte solution and was maintained at a distance of at least 2-3 mm from the WE. The EIS measurements were carried out at room temperature at 0V bias versus the reference electrode over the frequency

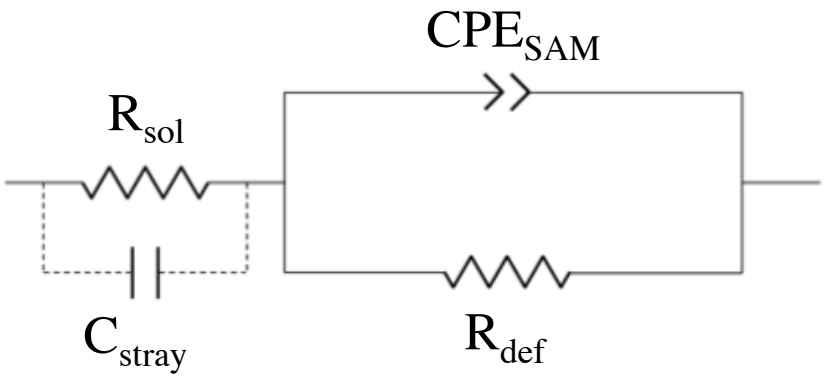

Figure 3.2: Equivalent circuit model for a SAM. The SAM is represented by an RC parallel circuit with the capacitance-like behavior being captured by a constant-phase element, CPE_{SAM}, and resistance R_{def}

range described above.

The custom-designed electrochemical cell allows for the preparation of up to six different samples on the same substrate. Each well holds a volume of 400 μl, confined by Viton O-rings to a geometric area of $A_{el} \approx 0.33$ cm^2. The surface area of the working electrode was determined using the copper contrast method as described in [175]. The roughness of the gold film interface, β, was estimated from the gold surface oxidation/oxide stripping charge. Typical values for β varied from 1.2 to 1.4 for this particular experimental setup.

3.1.4 Data Analysis

Equivalent circuit model (ECM)

Equivalent circuit models (ECMs) were used to quantify the measured impedance spectra. The electrochemical system is described in terms of electrical circuit components. A schematic of the ECMs for SAM and stBLMs are shown in Figures 3.2 and 3.3, respectively. The solution resistance R_{sol} is the resistance of the electrolyte solution between the working and reference electrodes and the stray capacitance, C_{stray}, is associated with the cables and sample cell. The SAM is represented by an RC circuit. The monolayer capacitive behavior is captured by a constant-phase element CPE_{SAM}. The monolayer resistance is characterized R_{def}. For a well-formed monolayer, the increased presence of defects lowers the resistance. The bilayer is represented by CPE_{mem} parallel to a branch that represents membrane defects characterized by their resistance, R_{def}, and a constant-phase element, CPE_{def}, which reflects the electrical conductivity of the submembrane space for isolated defects in the bilayer [93].

The impedance response rarely represents the response of ideal circuit elements. It often reflects variations in surface properties that arise from heterogeneities of the underlying material[6]. The CPE models the behavior of an imperfect capacitor with an impedance characterized by its constant-phase element coefficient, CPE (a capacitance per unit area $\times$ $t^{\alpha 1}$) and its expo-

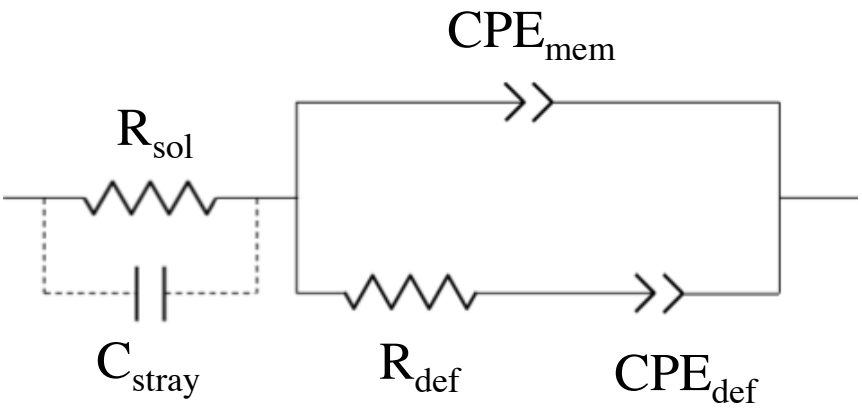

Figure 3.3: Equivalent circuit model for a stBLM The bilayer is represented by a constant-phase element, CPE_{mem}, parallel to a branch that represents membrane defects characterized by their resistance, R_{def}, and a constant-phase element, CPE_{def}, which reflects the electrical conductivity of the submembrane space

nent α, which may vary between 0 and 1.

$$Z(\omega) = (CPE(j\omega)^{\alpha})^{-1} \tag{3.7}$$

Thereby, a CPE becomes a conventional capacitance for $\alpha = 1$.

Earlier studies show that the lipid membranes behave like a nearly-ideal capacitor, $\alpha \sim 1$, despite membrane defects [114] [70]. The choice of CPE or ideal capacitor to model the lipid membrane capacitance does not affect significantly the values obtained for the other parameters. Since $\alpha \sim 1$ $CPE_{mem} \approx C_{mem} = \epsilon\epsilon_0 d$ where ϵ and ϵ_0 are the dielectric constant of the hydrocarbon chains of the membrane and the permittivity of the free space, respectively, and *d* is the thickness of the membrane.

In contrast, α_{def} often deviates significantly from one. According to EIS theory, α_{def}= 0.5 is interpreted as an infinite RC ladder that takes into account the attenuation of the electric field along conducting pores of different geometries, as observed on porous and brush electrodes. For stBLMs with low defect density, α_{def} = 0.5. α_{def} approaches to 1 with increasing defect density [168].

EI spectra were fitted by *ZView* with best-fit model parameters determined by Levenberg-Marquardt algorithm. Resistance and capacitance were normalized by the area of the working electrode, $A_{el} \approx 0.33\ cm^2$ and capacitance was further corrected for gold roughness$\beta \approx 1.4$.

Cole-Cole plots

Impedance spectra are typically represented in a plot of the real and imaginary parts of the capacitance, $C'(\omega)$ vs $C"(\omega)$, referred as Cole-Cole plots. These plots allow efficient visualization and qualitative assessment of bilayer quality prior to any data fitting. For an ideal membrane capacitor with α=1 the impedance data appears as a semicircle. For α <1 the semicircle is flattened. Change in the EI spectra upon tBLM completion were consistent with increase of the

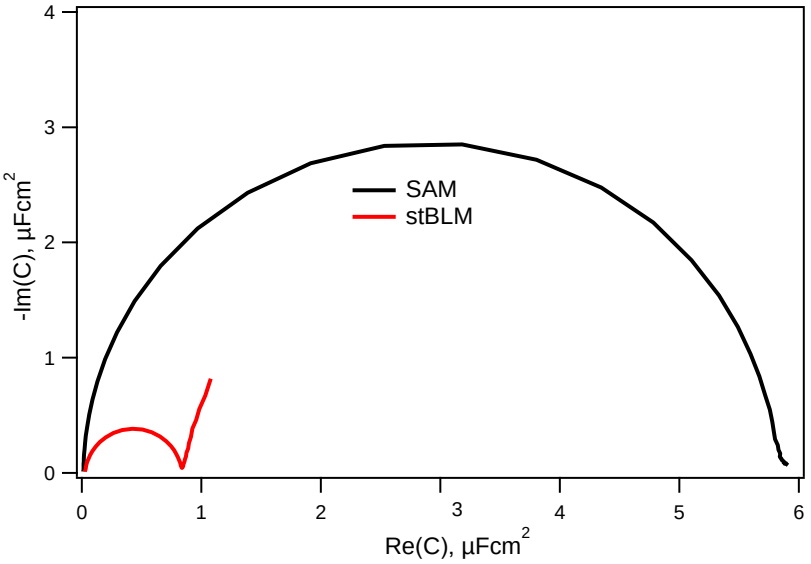

Figure 3.4: Representative Cole-Cole plot. Raw EIS spectra of a mixed HC18:βME 30:70 SAM and stBLM. The diameter of the semi-circle gives the value of C' $\approx$ 6 μFcm^{-2} for the SAM and C' $\approx$ 0.8 μFcm^{-2} for the DOPC lipid bilayer

dielectric surface layer as can be observed in Figure 3.4. The diameter of the semicircle gives the capacitance of the SAM and the lipid bilayer, C'$_{tBLM}$ < C'$_{SAM}$, from which the thickness may be estimated. The tail shown in the stBLM spectrum is a measure of membrane defect-density. Shorter tails indicate low defect-density.

3.2 Surface Plasmon Resonance (SPR)

3.2.1 Introduction

SPR is a surface-sensitive analytical method that is largely used to observe the formation of molecular assemblies at solid surfaces, and to investigate ligand-receptor interactions [153]. SPR was used to characterize protein interactions with stBLMs of various compositions. Complementary information of the changes in the interfacial properties of the membrane surface can be obtained by simultaneously measuring the EIS, described in section 2.1. Optical excitation of surface plasmons was first demonstrated by Otto [134] and Kretschmann and Raether [92] [71]. Their work used the attenuated total reflection (ATR) technique to couple radiation to a surface plasmon at a metal/air interface in the evanescent field of photons which are total internally reflected at a prism surface. The interaction of an electromagnetic wave with a metal-dielectric interface generates electronic excitations, or plasmon waves, in the thin metal film [151]. The plasmon resonance is sensitive to changes in the dielectric properties near the interface. Thereby, changes in SPR signal reflect the changes of the refractive index at the metal-dielectric interface. Even small change in the refractive index affects the resonance condition, which allows the detection of adsorbed molecules at the surface in real time with high sensitivity.

3.2.2 Theory

The electromagnetic theory of reflection, refraction and transmission of light at a dielectric metal interface may be used to describe basic SPR principles, as illustrated in Figure 3.5 and detailed in [152]. Evanescent waves, which arise from total internal reflection are fundamental to understanding SPR theory. Consider an electromagnetic plane wave travelling in a medium with refractive index, *n*

$$\mathbf{E}(\mathbf{r},t) = E_0 e^{j(\omega t - \mathbf{k}\cdot\mathbf{r})} = E_0 e^{j(\omega t - k_x x - k_y y - k_z z)} \tag{3.8}$$
$$\mathbf{B}(\mathbf{r},t) = \frac{c}{\omega}\mathbf{k} \times \mathbf{E}(\mathbf{r},t)$$

where E_0 is the amplitude of the electric field, ω is angular frequency, **r** is the position vector and **k** is the wavevector with direction parallel to the wave propagation and magnitude

$$|k| = \sqrt{k_x^2 + k_y^2 + k_z^2} = n\frac{2\pi}{\lambda} = n\frac{\omega}{c} \tag{3.9}$$

where λ and *c* are wavelength and speed of light in vacuum.

Total Internal Reflection and Evanescent Wave

Now consider the refraction of the electromagnetic wave at the interface between media 1 and 2 with refractive indices n_1 and n_2, respectively (Figure 3.5). The conservation of in plane momentum, i.e. Snell's law, holds

$$k_{x1} = k_{x2} \tag{3.10}$$
$$n_1 \sin\alpha = n_2 \sin\beta$$

For $n_1 > n_2$, there is a critical angle of incidence, θ_c, given by

$$\sin\theta_c = \frac{n_2}{n_1} \tag{3.11}$$

below which total internal reflection occurs and no wave can propagate into medium 2. Even though radiation coming from medium 1 is totally reflected, evanescent waves from the oscillating charges at the interface penetrate medium 2. These fields have the same frequency as the incident wave but decay in amplitude in a direction normal to the interface.

At the interface between the two media, the tangential component of **E** must be continuous. The boundary conditions at y=0 are given by

$$E_{x1} = E_{x2} \tag{3.12}$$
$$E_{z1} = E_{z2}$$

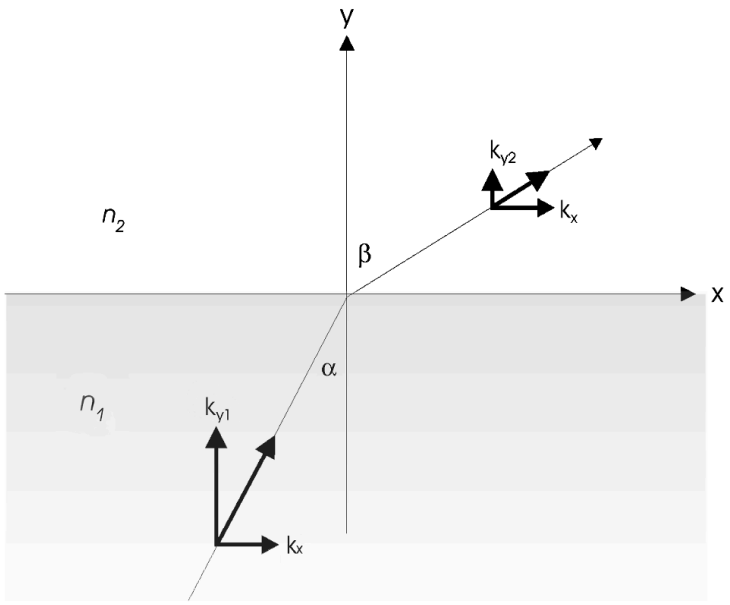

Figure 3.5: Refraction of plane a wave at a dielectric interface. The incident electromagnetic wave travels between two media 1 and 2 with refractive indices n_1 and n_2, respectively, at an incident angle α. The y direction is perpendicular to the surface. Figure from [152]

Thus from equation 3.12 follows

$$\begin{aligned} k_{x1} &= k_{x2} = k_x \\ k_{z1} &= k_{z2} = k_z \end{aligned} \tag{3.13}$$

By using equations 3.9 and 3.13, the expression for the wavevector perpendicular to the interface is given by

$$k_{y2}^2 = n_1^2(\frac{2\pi}{\lambda})^2((\frac{n_2}{n_1})^2 - \sin^2\alpha) \tag{3.14}$$

For the case where $n_1 > n_2$, the right side of equation 3.14 is negative when $\sin\theta > \frac{n_2}{n_1}$ and thus k_{y2} is purely imaginary, generating a travelling wave in medium 2 parallel to the interface

$$E_2 = E_0 e^{k_{y2}y} e^{j(\omega t - k_x x - k_z z)} \tag{3.15}$$

with amplitude of the electric field decaying along the y-direction, perpendicular to the surface. This field is designated as evanescent field. A change in the dielectric properties in the vicinity of the media boundaries will disturb this field, which leads to the interfacial sensitivity of the SPR method.

Surface Plasmons

The presence of free electrons at the interface is essential for the generation of surface plasmons. Good conductors, eg. metals, contain free electrons. Suppose one of the media is a metal. The free electrons of the metal can perform coherent oscillations, known as surface plasmons, when excited by the evanescent field. Only an electric field with a component perpendicular to the interface can induce a surface charge density and only p-polarized light has an electric field component perpendicular to the surface. The electromagnetic waves associated with the free electrons motion in the metal are generated when both momentum and energy of the incoming photons match the surface plasmons. The plasmonic waves are confined at the metal-dielectric boundary. The oscillation frequency, ω_{sp}, is tied to the wavevector by the dispersion relation shown in equation 3.16a. The dispersion relation for a surface plasmon may be calculated from first principles via Maxwells equations together with continuity relations, for detailed calculations, see [152]. Relation 3.13 and equation 3.14, rewritten in terms of dielectric constants of the media, yield

$$\begin{aligned} k_x &= \frac{\omega}{c}(\epsilon_1 \frac{\epsilon_1}{\epsilon_1 + \epsilon_2}) \\ k_{yi} &= \frac{\omega}{c}(\frac{\epsilon_i^2}{\epsilon_1 + \epsilon_2}) \end{aligned} \tag{3.16}$$

When medium 2 is a metal, the dielectric constant will be negative at angular frequency $\omega < \omega_p$:

$$\epsilon_2(\omega) = 1 - \frac{\omega_p}{\omega} \tag{3.17}$$

ω_p is the plasma frequency below which no electromagnetic wave can propagate in the metal. For $\epsilon_2 < 0$ and $|\epsilon_2| > \epsilon_1$, k_x and k_{yi} become complex. A gold water interface meets these conditions. The fields have their maxima in the surface ($y = 0$) and decay in both y direction exponentially, characterizing an evanescent field, that excites the surface plasmons.
When the momentum of the incoming photons match the momentum of the plasmon wave, a drop in the intensity of the reflected light is observed, indicating resonance. Surface plasmon excitation requires

$$k_{photon} = k_{SP} \tag{3.18}$$

The wave vector of the photons parallel to the metal/dielectric interface is given by (Figure 3.5)

$$k_{photon} = \frac{\omega}{c} n_1 \sin\alpha = \frac{\omega}{c}\sqrt{\epsilon_1}\sin\alpha \tag{3.19}$$

and $k_{SP} = k_x$, the wave vector of the surface plasmon at the metal-dielectric interface. The SPR resonance condition is thus met when

$$\sin\theta_{SPR} = \sqrt{\epsilon_1}\frac{\epsilon_1\epsilon_2}{\epsilon_1 + \epsilon_2} \tag{3.20}$$

where $\sin\theta_{SPR}$ is the resonance angle at which the intensity of reflected light reaches a minimum.

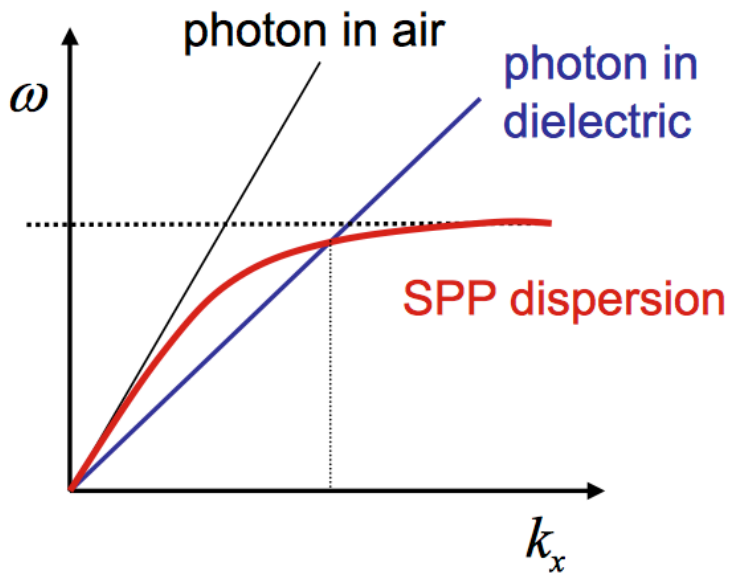

Figure 3.6: Dispersion relation for photon in air and in a dielectric compared to surface plasmon dispersion relation. Excitation of plasmons is not possible through air, since photon dispersion relation does not intercept the surface plasmon dispersion relation. However, in a dielectric k_{photon} can be increased and thus intersect SPP dispersion other than at the origin, generating the surface plasmons. Figure from [4]

The excitation of surface plasmons by photons at an air-metal interface is not feasible because k_{photon} is always $< k_{sp}$. The dispersion relations for light and surface plasmons do not intersect $(k_x > \frac{\omega}{c})$, implying that in this configuration light cannot simultaneously provide the correct energy and momentum to excite a surface plasmon. This limitation can be overcome by an attenuated total reflection setup in the Kretschmann configuration [23], which features a prism directly coupled to gold-coated substrate. In a dielectric, k_{photon} can be increased and thus equation 3.18 can be satisfied. Figure 3.6 shows the dispersion relations of photons and surface plasmons. The evanescent wave of the electromagnetic field generated at the gold-prism interface decreases exponentially in the metal and excites the surface plasmons at the gold-dielectric interface.

3.2.3 Instrumentation

A custom-built SPR instrument (SPR Biosystems, Germantown, MD) assembled in the Kretschmann configuration was used for the experiments. SAM-covered gold-coated ($\sim$ 45 nm) glass slides are optically coupled to the prism by use of an appropriate refractive index, n=1.5200$\pm$0.0002, matching fluid (Cargile, Cedar Grove, NJ). Gold is suitable for biophysical experiments due to its inertness. In the optical set-up, a superluminescent LED (EXS7510 Exalos AG, Switzerland) fan of monochromatic light at $\lambda = 763.8$ nm hits the sample at a range of incident angles, and a 2D-CCD detector (Hamamatsu C10990, Hamamatsu City, Japan) records the intensity of the reflected light as a function of reflected angles. The position of the intensity minimum on the CCD

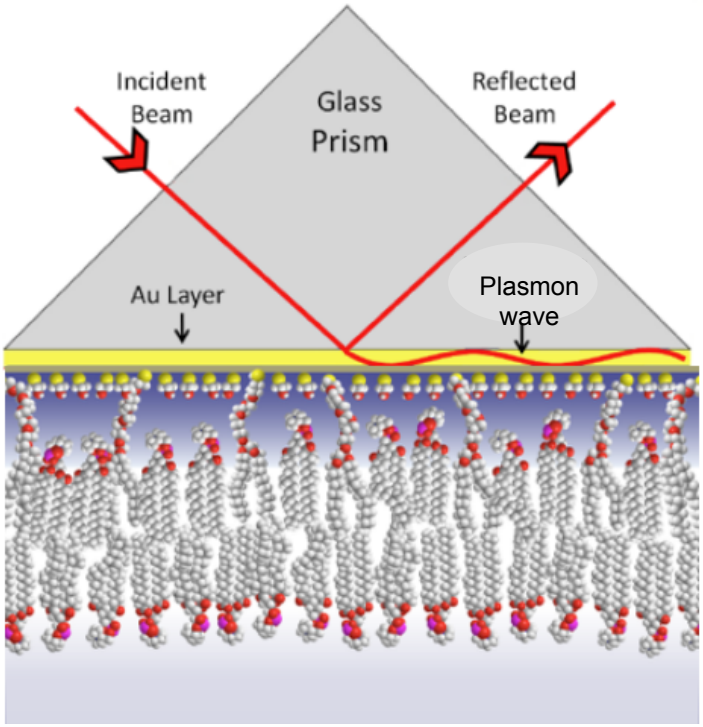

Figure 3.7: Surface plasmon resonance in the kretschmann configuration. stBLM is coupled to a prism. The incident beam goes through total internal reflection at the prism-gold interface. Light passing from one interface to another generates an evanescent wave that interacts with the free electrons of the gold layer, resulting in plasmon wave excitation at the stBLM-gold interface. When the momentum and energy of the photons of the incident beam light matches the energy and momentum of the surface plasmons, resonance is achieved.

defines the resonance angle, recorded as a function of time. The system has a time resolution of 0.1 s with a sensitivity of 5×10^{-7} reflectivity units (RU (pixels); 1 RU1 pg of adsorbed protein per mm^2) or better. The temperature controller (Wavelength Electronics LFI-3751, Bozeman, MT), typically set to 25 $^{\circ}C$, maintains the temperature within $\pm$ 0.01 $^{\circ}C$. The software package SPR Aria (SPR Biosystems) was used for real-time data recording. The SPR setup was designed to allow for simultaneous EIS measurements so that the integrity of the lipid membranes can be assessed before each protein binding experiment.

3.2.4 Data Acquisition

When performing SPR experiments, two sets of data are generated and recorded: reflected intensity as a function of SPR resonance angle and resonance angle as a function of time which allows to monitor the protein membrane adsorption at different concentrations. As a first step, the resonance angle corresponding to the neat bilayer is measured as a reference and its change recorded as increasing concentrations of protein added to the stBLM. The SPR response, *R*, is measured as a displacement of the reflection minimum on the CCD detector. Time courses of R at each protein concentration, c_p, were either recorded until equilibrated i.e. resonance angle stops

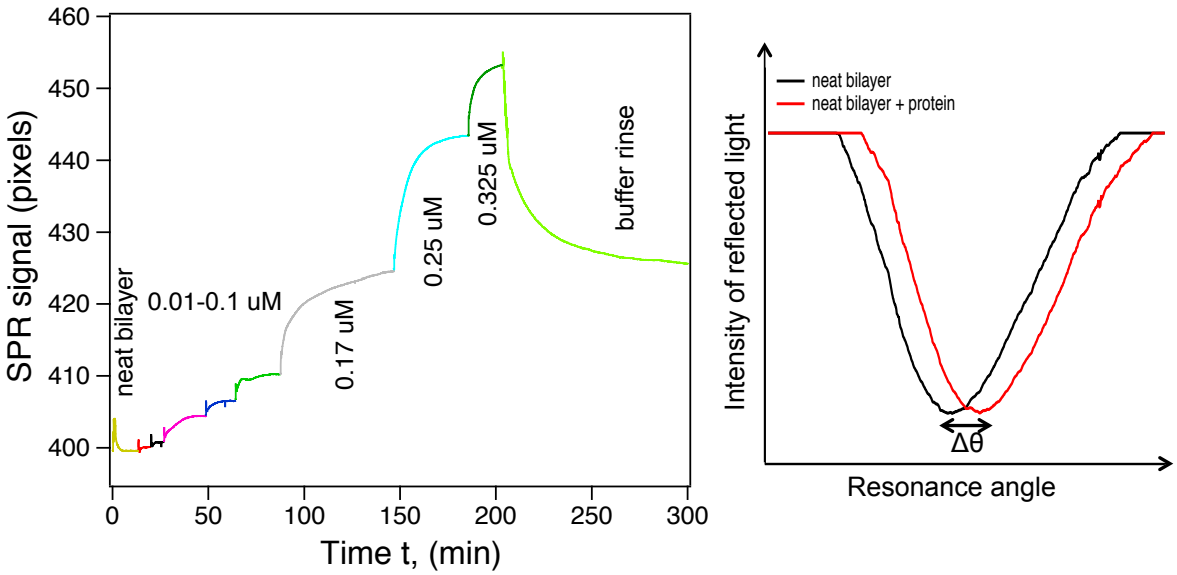

Figure 3.8: SPR data acquisition. Protein binding response is monitored over time at different protein concentrations(right panel). The increase in signal due to protein adsorption shows the shift in the minimum position of the resonance angle (left panel). Reflected light intensity is measured and at a certain angle, surface plasmon resonance occurs, resulting in a dip in the intensity. A change in the refractive index due protein adsorption at the neat bilayer interface alters the resonance angle. Those changes are monitored in real time and observed as a raise in the SPR signal.

varying or fitted to an exponential function for determination of the equilibrium SPR response, R_{eq}. The sensitivity of the SPR depends strongly on the metal thickness. To obtain maximum sensitivity and therefore a more accurate determination of the SPR minimum, the optimal gold layer thickness used is of approximately 45 nm. The SPR minimum becomes broad below and shallow above the optimal thickness.

3.2.5 Data Analysis

SPR was used to measure dissociation equilibrium constant, K_d, of protein-membrane interactions. The protein binding is assumed to be either a Langmuir-type or a Hill cooperative process.

Quantification of low protein affinities requires high protein concentrations in the buffer. At large concentrations in solution, protein affects the bulk optical index, n, of the medium in contact with the sensor surface, increasing the signal. In such cases, measurements were corrected as follows. The refractive index increment for protein is $dn/dc \approx 0.185$ ml/g [158] [9] [7]. At high protein concentrations, SPR response is affected by the bulk solvent refractive index. The bulk solvent contribution to the SPR signal was estimated for the proteins at a range of concentration using $dn/dc \times \rho = \Delta n$ where Δn corresponds to the variation in the refractive index, $\Delta n = (6.4 \pm 0.3) \times 10^5$ per response unit (pixel), and ρ corresponds to the protein mass concentration. To validate this calculation, the SPR response of the protein binding to zwitterionic tBLM was measured under the assumption that the protein does not adsorb to neutral lipid bilayers. The results were consistent with the calculated bulk solvent contributions to the SPR signal

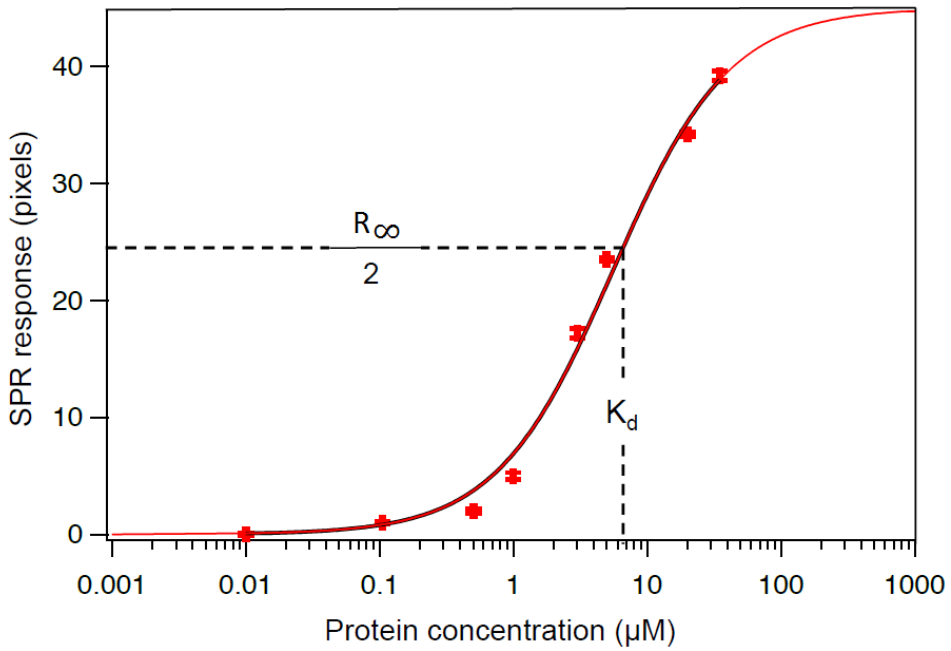

Figure 3.9: An exemplary SPR binding curve. SPR response as a function of protein concentration is fitted to a sigmoid curve. From this fit, two parameters may be determined, the dissociation equilibrium constant, K_d, as the concentration of protein at which half of the binding sites are occupied and saturation response, R_∞, which corresponds to the maximum amount of protein that can be adsorbed at the interface at infinite protein concentration

dn/dc = 0.186 $\pm$ 0.011 ml/g for PlyCB and for HIV-1 MA the protein concentration range used in the SPR experiments did not have any significant effect on the bulk refractive index. SPR response at high c_p ($>$ 10 μM for PlyCB and $>$ 50 μM for HIV-1 MA) are corrected for bulk refractive index effect accordingly.

Binding Model

To quantify the protein affinity to the membranes in terms of its equilibrium binding constant K_d and surface density of bound protein at infinite concentration, R_∞, SPR equilibrium response as a function of concentration was fitted to a Langmuir isotherm.

Langmuir Isotherm Basic Assumptions:

There are no interaction among adsorbed molecules on adjacent binding sites. All binding sites are equivalent. Each binding site only binds one molecule. These assumptions are valid in the case of a 1:1 molecular interaction where the binding sites are well-distinguishable. The adsorbate binding is treated as a chemical reaction between the adsorbate molecule A (protein) and empty site, B (lipid). This reaction yields an adsorbed complex, AB, with an associated

equilibrium constant $K_d = k_{off}/k_{on}$.

$$A + B \underset{k_{off}}{\overset{k_{on}}{\rightleftharpoons}} AB \tag{3.21}$$

The rate equations are given by

$$\frac{d[AB]}{dt} = k_{on}[A][B] - k_{off}[AB] \tag{3.22}$$

$$\frac{d[AB]}{dt} = -k_{off}[AB] \tag{3.23}$$

At equilibrium the association and dissociation rates are the same

$$k_{on}[A][B] = k_{off}[AB] \tag{3.24}$$

Plugging in $[B]=[AB]_{max}-[AB]$ in equation 3.24, where $[AB]_{max}$ is the concentration of the bound complex at saturation, the Langmuir equation then becomes

$$[AB] = \frac{c_p R_\infty}{c_p + K_d} \tag{3.25}$$

where $[AB]_{max}=R_\infty$ is the saturation SPR response and $c_p=[A]$. For the cases where the Langmuir model was not suitable to describe protein adsorption to the stBLMs, the Hill equation was used [184] [73].

$$R_{eq} = \frac{c_p^N R_\infty}{c_p^N + K_d^N} \tag{3.26}$$

where N reflects the degree of cooperativity and N = 1 corresponds to the Langmuir adsorption isotherm [152]. Hill binding implies simultaneous ligand binding and it was used to describe binding where the binding was clearly beyond Langmuir-type. Protein binding free energies, ΔG, were calculated from the dissociation constants, K_d, measured by SPR:

$$\Delta G = RT \ln(K_d/c_{ref}) \tag{3.27}$$

where c_{ref} is an arbitrary reference concentration, taken here to be 55 M, the concentration of the solvent [183], to directly compare our results with other values in the literature. In summary, the information derived from equilibrium binding studies is the strength of the interaction (K_d) or binding free energy (ΔG) and evidence relating to the nature of the interaction.

3.3 Neutron Reflectometry (NR)

3.3.1 Introduction

The marked difference in scattering contrast, between hydrogeneous materials containing ^{2}H or ^{1}H makes neutron scattering a powerful probe of the structure of biological samples [140]. The contrast variation, replacement of hydrogen by deuterium, has minimal effect on the sample but

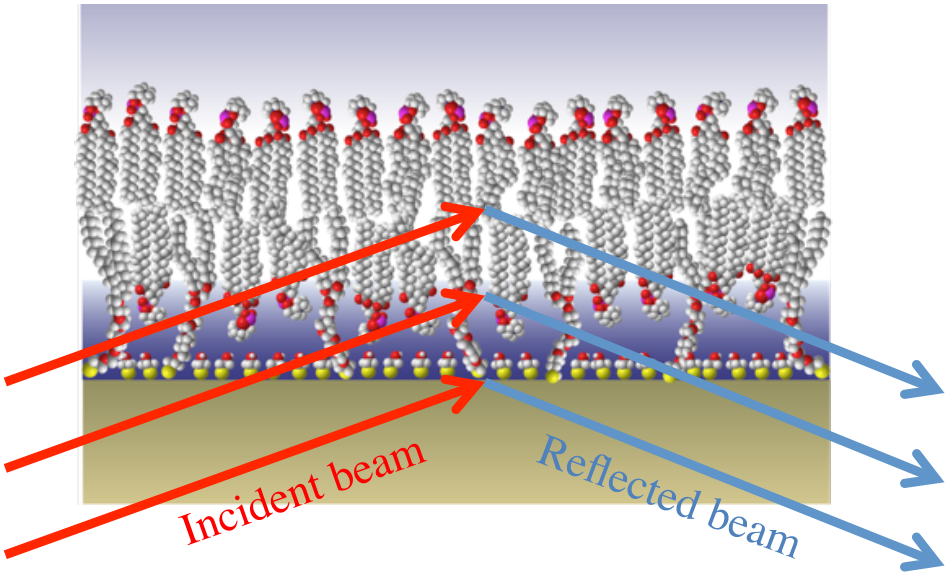

Figure 3.10: Illustration of neutron reflectometry at lipid membrane interface. The technique involves shining a highly collimated beam of neutrons onto an extremely flat surface and measuring the intensity of reflected beam as a function of angle

has dramatic effects on the scattering. The high sensitivity of neutrons towards hydrogen isotopes can be used to highlight specific regions of a molecule and gives neutron reflectometry (NR) an edge over x-ray reflectometry.

3.3.2 Theory

Reflectivity Formalism

As neutrons carry no charge, their interaction with matter, both nuclear and magnetic, is short ranged. As a result of this overall weak interaction they penetrate deeply into condensed matter, which makes neutrons optimal for revealing the structure of buried interfaces. This technique is sensitive to refractive index profile across the surfaces which is related to the neutron scattering length density ρ

$$n = 1 - \rho\frac{\lambda^2}{2\pi} = 1 - \frac{4\pi\rho}{k_0^2} \tag{3.28}$$

where $\lambda = 2\pi/k$ is the neutron wavelength and ρ is defined as

$$\rho = \sum_{i=1}^{n} N_i b_i \tag{3.29}$$

b is the scattering length, which measures the strength of interaction between the neutron and the nucleus. b does not vary in a systematic way as function of atomic number. N is the number density of the nuclei within a volume.

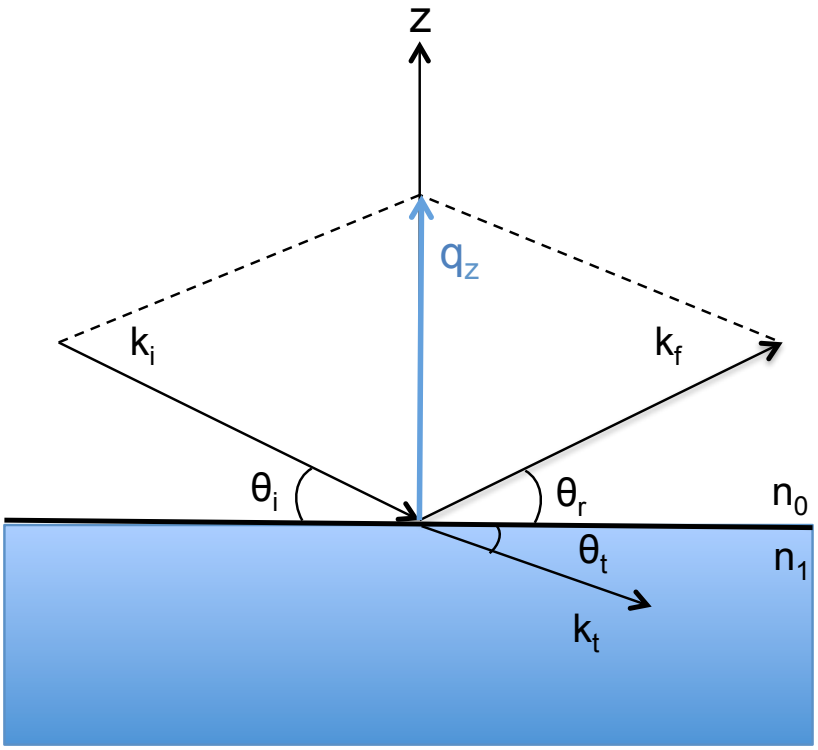

Figure 3.11: Specular reflection, $\theta_i = \theta_r$. Plane wave reflection at a flat interface between two bulk media of refractive indices n_0 and n_1 showing incident and reflected waves at an angle θ_i and the transmitted wave at an angle θ_t along with the normal component of the momentum transfer vector, q_z

Figure 3.11 shows the neutron beam represented as plane wave in air (medium 0) with incident wavevector k_i ($|k_i| = k_0 = 2\pi/\lambda$), reflected wave vector k_f and transmitted wavevector k_t. The coherent (in phase), elastic (no energy transfer) reflection of neutrons at the interface of a flat thin film can be either specular and non-specular. For elastic scattering $|k_i| = |k_f| = |k_0|$. Specular reflection occurs when $\theta_i = \theta_r$ and the momentum transfer, q_z, is in the direction normal to the interface

$$q_z = \frac{4\pi}{\lambda} \sin\theta \tag{3.30}$$

Consider a 1-D potential, $V(z)$, that varies along the surface normal, z, and therefore does not affect the neutron wavevector parallel to the interface. To calculate the reflectivity of an interface we use Schrödinger equation:

$$\left[\frac{\hbar}{2m_n}\frac{\partial^2}{\partial y^2} + V(y)\right]\Psi(y) = E\Psi(y) \tag{3.31}$$

with the interaction potential

$$V = \frac{2\pi\hbar^2}{m}\rho(y) \tag{3.32}$$

The solution for the wave function representing the neutron wave in medium 1 and in medium 0

of the reflecting sample follows as

$$\begin{aligned} \psi_0(z) &= e^{+ik_0 z} + re^{-ik_0 z} \\ \psi_1(z) &= te^{+ik_1 z} \end{aligned} \tag{3.33}$$

where k_i is the perpendicular component of the vector $\mathbf{k}_i$. Conservation of momentum requires that $\Psi(z)$ and its derivative, $\partial\Psi/\partial z$, be continuous at the media boundaries

$$\begin{aligned} \Psi_0(0) &= \Psi_1(0) \\ \frac{\partial \Psi_0}{\partial y}\Big|_{z=0} &= \frac{\partial \Psi_1}{\partial z}\Big|_{z=0} \end{aligned} \tag{3.34}$$

Applying the wave functions, equation 3.33, on interfacial boundary conditions, equation 3.34, yields

$$\begin{aligned} 1 + r &= t \\ ik_0(1 - r) &= ik_1 t \end{aligned} \tag{3.35}$$

The neutron reflectivity,R, is the ratio of reflected to incident intensity measured as a function of q_z. R is related to the reflection amplitude, r, by

$$R = rr^* = |r^2| \tag{3.36}$$

where r^* is the complex conjugate. Solving equations 3.35 for r, the reflection amplitude of a single interface between two media of infinite extent, gives

$$r = \Big(\frac{k_0 - k_1}{k_0 + k_1}\Big) \tag{3.37}$$

from which the reflectivity of a single interface is derived as

$$R = rr^* = \Big(\frac{k_0 - k_1}{k_0 + k_1}\Big)\Big(\frac{k_0 - k_1}{k_0 + k_1}\Big)^* \tag{3.38}$$

Equation 3.38 shows the fact that the phase information is lost. As a function of q_z, R can be written as

$$R = \Big[\frac{1 - \sqrt{1 - (\frac{4\pi\rho}{q_z})^2}}{1 + \sqrt{1 - (\frac{4\pi\rho}{q_z})^2}}\Big]^2 \tag{3.39}$$

At the critical edge neutrons are perfectly reflected from a smooth surface, $R = 1$. Equation 3.39 shows the critical edge position is thus given by

$$k_1 = nk_0 = \sqrt{1 - \frac{4\pi\rho}{k_0^2}}k_0 = 2\sqrt{\pi\rho} \tag{3.40}$$

The reflected and transmitted amplitudes can also be calculated from the classical Fresnel equation, where the incident light is treated as a plane wave under the assumption that the interface between the homogeneous media is flat.

Reflection from perfectly flat stratified media

For the case of reflection from a single perfect interface, there is no additional information that can be obtained beyond that provided by the position of the critical edge. More interesting and realistic cases involve reflection from stratified media. The reflected intensity from multiple layers is the result of interference from reflections at all interfaces of the multi-layered system and can be calculated directly by the sum of amplitudes of the reflected and refracted rays. In this case, the scattering length density is not constant with depth, and abrupt changes of the scattering length density, such as those produced by buried interfaces, modulate the reflectivity. The reflection coefficient, r, for the sample is calculated by first considering the coefficient between the substrate and bottom layer, $r_{m,m+1}$, between $(m+1)^{th}$ and m^{th} layer [138].

$$r'_{m-1,m} = \frac{r_{m-1,m} + r_{m,m+1}e^{2i\beta_m}}{1 + r_{m-1,m}r_{m,m+1}e^{2i\beta_m}} \tag{3.41}$$

This value is then used to calculate $r_{m,m-1}$ and process goes on until $r_{0,1}$ is evaluated. Finally the reflectivity of the sample is calculated using equation 3.38.

Reflection from a Rough Interface

The calculations presented in the subsection above assume that the multiple interfaces have no roughness. Rough interfaces lead to attenuation of the reflectivity curve. The attenuation increases with q_z, as a consequence the interface roughness will limit the accessible region of wavevector transfer and the sensitivity of reflectometry to changes of the scattering length density profile over thin layers. The attenuation of the reflectivity with roughness is a function of roughness σ and q_z. For a single interface reflectivity is modified by

$$R(q) = R_0(q)e^{-q_0 q_1 \sigma^2} \tag{3.42}$$

More information can be extracted from samples with smooth interfaces than those with rough interfaces. For many experiments, useful information can be obtained from samples with root mean square (rms) interface roughness on the order of 10Å.

3.3.3 Data Acquisition

The neutron reflectometry experiments were performed in a specular regime. Collimated neutron beam at grazing angles incident on the sample is reflected by a ultraflat, smooth ($\sigma_{rms} < 5$ Å) stratified layer architecture. Reflectivity measurements were conducted over a range of angles, $q_z, 0.008 - 0.250 \AA^{-1}$. The reflected intensity is recorded as a function of momentum transfer, q_z, the direction normal to the surface. In the case where in-plane height fluctuations, domains, holes are present, the specular component of the reflected intensity is the result of the laterally averaged

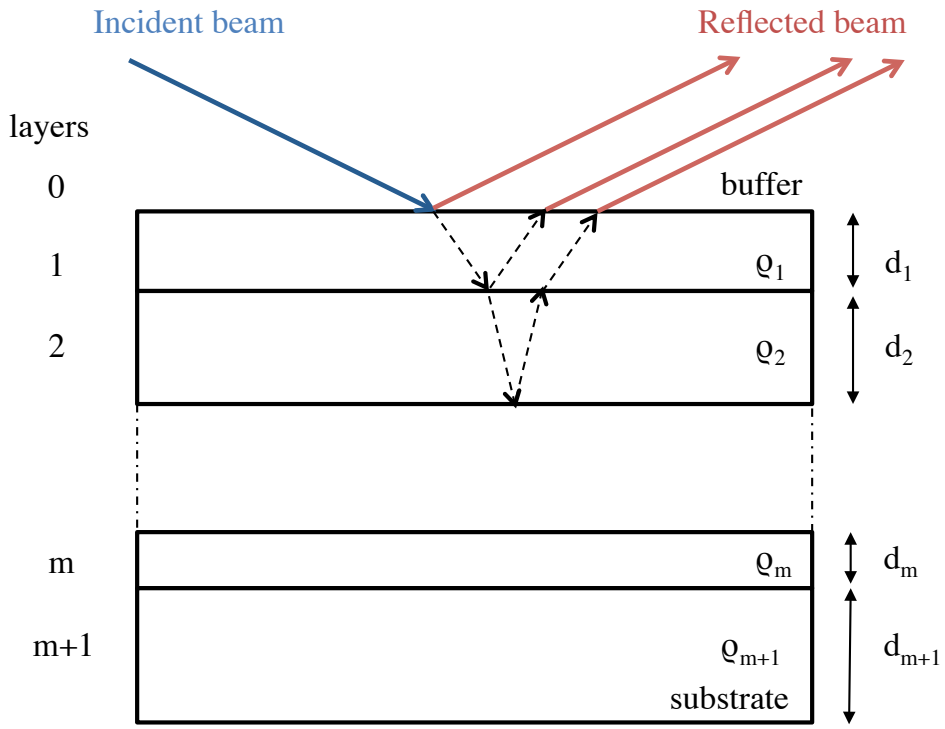

Figure 3.12: Reflection and refraction on a layered material. Slab view of a reflectivity sample consisting of m layers of thickness d_m and scattering length density ρ_m. The incident beam will be reflected and refracted at the interfaces between each of the layers. The reflection and refraction coefficients for each pair of adjacent media is calculated by a sum of amplitudes of the reflected and refracted rays.

scattering length density,$\rho(z)$, at a given depth, over the inplane area for which the neutron plane wavefront is coherent, typically μm. Background scattering is also measured and subtracted from the averaged reflected intensity. The neutron reflectivity is calculated from the measured specular raw data, the background data and normalized by the incident beam intensity. Typically, protein-free and protein-loaded membranes are measured in at least two solvent isotopic contrasts consisting of aqueous buffer prepared with D_2O, H_2O, or mixtures of the two. For each contrast, acceptable counting statistics are typically obtained after 6 h.

3.3.4 Instrumentation

NR measurements were performed at the NG7 horizontal plane reflectometer and NGD-Magik vertical reflectometers at the NIST Center for Neutron Research. The incident neutron wavelength is λ = 4.75 and 5.00 Åfor NG7 and MagiK respectively. The reflectivity was collected over a momentum transfer, q_z, between 0.008 and 0.250 $Å^{-1}$. Independent movement of both sample and detector allows measurement of off-specular scattering, out of the scope of this work. Adequate sample format smooth, flat surface, preferably several cm^2 in area is essential to minimize diffuse scattering. stBLMs are prepared on a SAM gold-coated ($\sim$ 15 nm) circular silicon wafer (El-Cat, Ridgefield Park, NJ) and assembled in a flow cell. An O-ring creates a small vol-

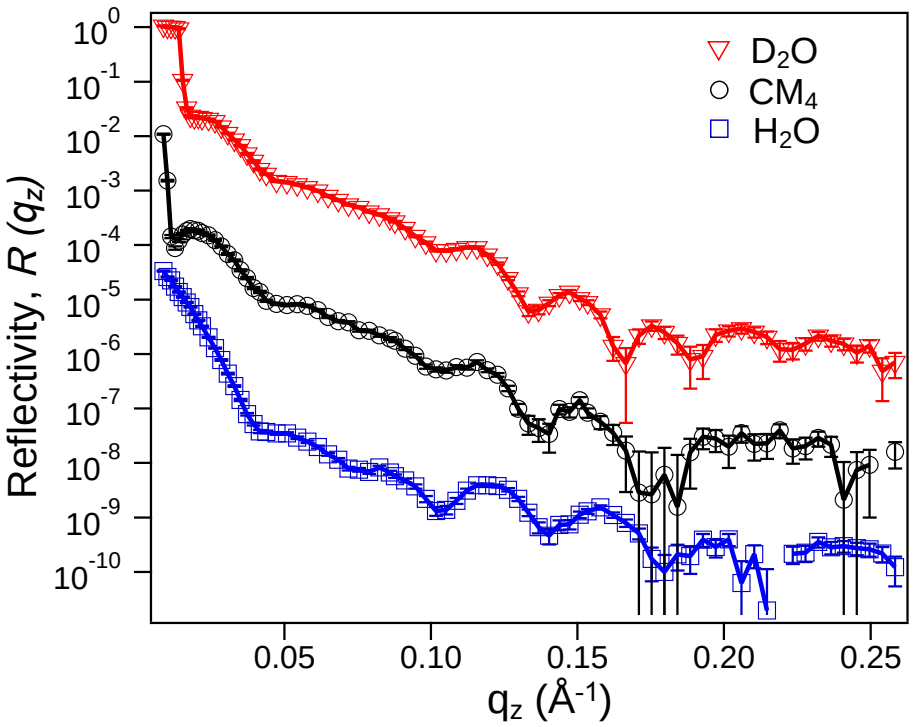

Figure 3.13: Neutron reflection reduced data. DOPC tBLM on HC18:βME 30:70 SAM. The measurements utilized three different solvent contrasts: D_2O, H_2O and Contrast Mixture 4 (CM4, a mixture of D_2O and H_2O with a scattering length density of 4×10^6 Å^2). Curves were shifted for better visualization

ume aqueous reservoir of $\sim$100 μm thickness, reducing the background scattering from water. The wet cell [108] design allows for in situ buffer exchange on the instrument. This ensures that the structure of the inorganic substrate is the same for all the measurements.

3.3.5 Data Analysis

Although the loss of phase information is a general problem in scattering that prevents direct data inversion, robust modeling strategies have been developed for already known structures which circumvent this problem [69]. Since NR probes the structural profile along the membrane normal, any in-plane information has to be inferred from a 1D profile. However, complementing information such as volumetric data, chemical connectivity, high-resolution structures or MD simulations aid greatly to fill that gap [156] [158].

Continuous Distribution Model

The box model was successfully used for the neutron reflectivity data analysis. Also known as slab model, it describes the various layers of material as a box of constant scattering length density, ρ_i. The interface between two adjacent layers is smoothed by error functions. This representation constrained each sample element in a distinct box, preventing the accurate description of overlapping molecules and resulting in a unrealistic modeling of the interfacial regions. The

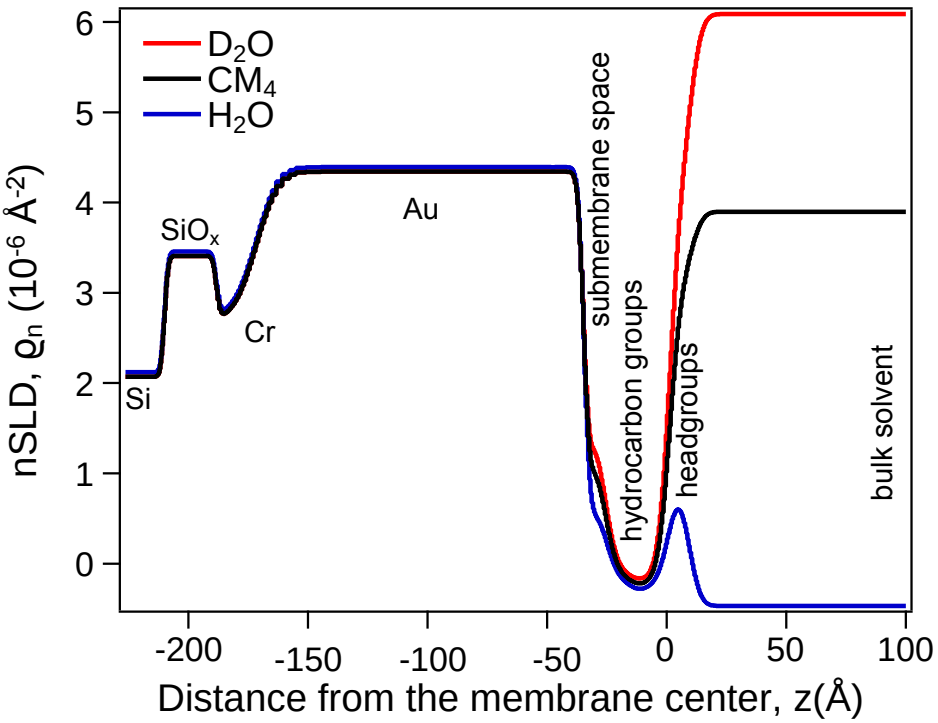

Figure 3.14: Typical neutron scattering length density profile for tBLMs nSLD obtained from the NR best-fit of a DOPC tBLM on HC18:βME 30:70 SAM in three different isotopic constrasts: D_2O, CM4 and H_2O. Solid substrate nSLD is unaffected by the contrast variation while the organic layer is contrast sensitive in the areas exposed to solvent

continuous distribution (CD) model [156] was thus developed in order to fill those gaps. The composition space approach uses a sum of two error-functions to describe the spatial distribution or component volume occupancy (CVO) of the individual molecular components of the complex layered structure. In the CD model, the structural information of a molecule is represented by their cross-sectional area along the membrane normal. Auxiliary information about the sample, such as chemical connectivities, molecular propensities for self-organization and volumetric data, is used to constrain the scattering length density distributions. This approach increases the precision with which molecular components may be localized within the sample, with a minimal use of free parameters.

Catmull-Rom splines

In the context of neutron reflectometry modeling, protein modeling depends on the structural information available. If NMR or crystal structures are known, those can be directly used in the data modeling. For proteins with unknown structure and partially disordered proteins, model-independent parametrization is available. The modeling strategy adopted by our group implements the CD model to describe lipid bilayer membranes and splines to describe membrane-associated proteins. The splines are defined by a set of control points, usually set 15 Åapart on average, allowing smooth transition between points they connect. Hermite splines [19], in partic-

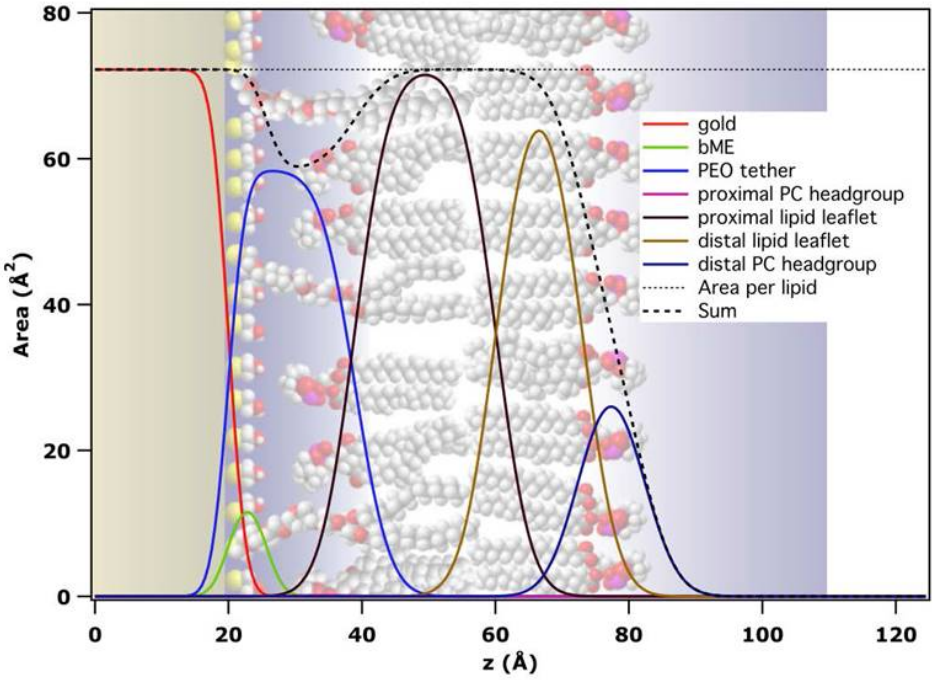

Figure 3.15: Continuous distribution model. Area of submolecular components of DOPC tBLM on HC18:βME 30:70 SAM. The bilayer is defect-free, no water is found in the hydrocarbon region as evidenced by the dashed line, which represents the sum of all the molecular components without water.

ular, go through the control points and were chosen for being simpler and for avoiding technical complications such as unphysical overshooting in the vicinity of the control points [58]. The traditional Hermite spline that describes the CVO of the protein along the bilayer normal has a fixed neutron scattering length density (nSLD). In the case where the protein forms a complex with a molecule of distinct scattering length-density, the nSLD of the complex is a function of z, nSLD(z) [189]. The complex is therefore described by two splines functions, nSLD$_p rot$(z) and nSLD$_e xtra$(z), with nSLD(z) allowed to vary between the nSLD values of the protein and the extra molecule. The individual profiles for the components of the complex are obtained using a linear decomposition of nSLD(z) spline [189].

High-resolution protein structure and rigid body modeling

High-resolution protein crystal structure can be used to determine the protein contribution to the overall nSLD profile, providing the relative spatial arrangement of the protein in a fixed orientation with respect to the membrane [123] [69]. In most refined model, we obtain information about the molecular association of the protein with the membrane in terms of orientation and membrane penetration. The protein orientation is defined by two Euler angles, θ and ϕ. Because neutron reflection is invariant against rotational symmetry around the z axis, the third Euler angle, Ψ, is irrelevant and does not contribute to the NR profile along the z axis. Orientation is obtained by rotating the protein around the axes of the bilayer coordinate system. First rotating

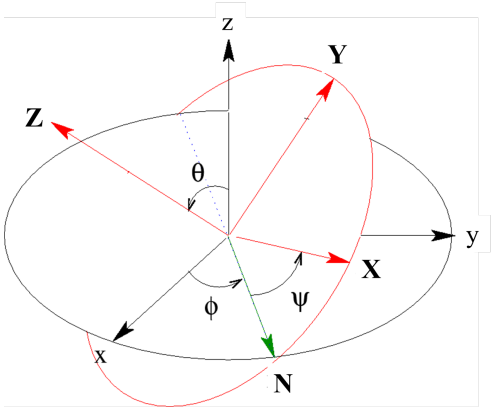

Figure 3.16: Euler angles. The xyz system is shown in black, the XYZ rotated system is shown in red. The intersection of the xy and the XY coordinate planes is represented by the N axis. ϕ represents a rotation around the z axis, θ represents a rotation around the N axis, ψ represents a rotation around the Z axis Figure adapted from https://en.wikipedia.org/wiki/Eulerangles

by θ about the z axis (membrane normal) followed by ϕ rotation about the x axis (in the plane of the membrane). The nSLD is compared to the neutron reflectivity data in order to assess the potential of a given orientation suit the experimental data. An uncertainty analysis, described in the subsection below, was extended to the euler angles (θ, ϕ) and a probability plot consistent with the reflectivity data was thus generated and used to determine the most probable orientation of membrane-bound protein. The initial ($\theta = 0°, \phi = 0°$) orientation of the protein on the membrane is the one predicted by the crystal structure.

Monte-Carlo based uncertainty analysis

Free-form modeling of unknown structures uses a large number of free parameters when compared to the other models. Monte Carlo (MC) resampling [143] and more recently Monte Carlo Markov Chain [90] were thus used to determine the uncertainties and correlation between model fit parameters. Besides providing accurate median model parameter values and their confidence intervals, a robust uncertainty analysis also avoids overparametrization of the model. Data modeling and optimization of model parameters were performed using the Refl1D software package developed at the NCNR [90].

Chapter 4

Multi-component Defect-free Tethered Bilayer Lipid Membranes by Vesicle Fusion

For this work, it was essential to reproducibly prepare defect-free bilayers. Vesicle fusion protocol was optimized to low-defect-density membranes. EIS, SPR and NR were used to assess the quality of the stBLMs. The structural and electrical properties of the stBLMs are described in this chapter starting with single component membranes in section 4.2 and followed by a systematic increase in the chemical and structural complexity of the stBLMs components, as discussed in section 4.3.

4.1 Introduction

stBLMs are resilient in-plane fluid systems that allow precise control of their lipid composition. An important characteristic of a membrane model is its defect density. The quality criterion established for the stBLMs used in this work is of $R_{def} \sim 100\ k\Omega cm^2$ which implies surface coverage $> 95\%$. If membrane quality criterion is not reached, the lipid bilayer is not considered for protein binding experiment. Defect-rich regions could lead to non-specific interaction between the protein and the SAM-coated substrate, contributing to protein-membrane binding. Previous work confirmed optical homogeneity and the fluidity of the stBLMs to be similar to free standing bilayers [157]. It is important that as the stBLMs systems become more complex they preserve the essential structural and dynamic features of biological membranes. We prove here that the formation of multi-component, defect-free stBLMs can be achieved through careful control of the vesicle fusion process.

Here, we investigate how complex lipid compositions can change the physical and chemical properties of the membrane making planar bilayer formation more difficult. Surface chemistry of the solid substrate and vesicle surface coverage play a critical role in vesicle fusion. Despite the fact that POPC vesicles adsorbed to pure gold substrate do not rupture and form an intact liposome layer, AFM imaging and force spectroscopy measurements showed that increasing the number of functional groups in single lipid component vesicles, and thereby increasing the

chemical affinity between vesicles and substrate surfaces, lowers the required force to initiate stBLM formation [181]. Likewise, increasing the ionic strength of the buffer used to prepare the vesicles containing functional lipids [46] [82] accelerates the transition from adsorbed vesicle to lipid bilayer, possibly by increasing vesicle surface coverage.

Systematic increase in the chemical and structural complexity of the stBLMs composition affects vesicle fusion and membrane quality in different ways. For example, the presence of anionic lipids can reduce vesicle surface coverage due to electrostatic repulsion between the liposomes. Cholesterol, known to affect liposome membrane elasticity, does not impact vesicles fusogenic properties but influences stBLM structural features improving bilayer quality. An increase in the diversity of lipid species retarded vesicles rupture and resulted in the formation of incomplete membranes. Elaborate lipids such as PI(4,5)P_2 may have their own peculiarities. These complications were circumvented by increasing the tether density and thus the hydrophobicity of the substrate which led to the completion of electrically sealed bilayers.

The work presented here shows how parameters that control vesicle fusion can be optimized by implementing high ionic strength, longer incubation times or high tether density. Intact bilayers that capture the essential features of native membranes can thus be formed without resorting to fusion peptides. In another scenario, this study can be relevant to facilitate the mechanisms of drug delivery by helping the development of multi-component liposomes and improving their fusogenic character to certain tissues. More broadly stBLMs assembled interfaces can be used in the construction of biosensors based on membrane components and exploiting their exquisite sensitivity and selectivity [22].

4.2 stBLM Preparation

Reproducible protocols have been established to form robust and long term stable simple lipid systems. When preparing any model membrane, it is important that the lipids remain well mixed throughout the sample preparation procedure. Among the most popular are rapid solvent exchange (RSE), first described in [32], and vesicle fusion.

4.2.1 Self Assembled Monolayer (SAM)

Self-assembled monolayers (SAMs) are formed on gold coated microscopy glass slides initially cleaned with a mixture of sulphuric acid and Nochromix (Godax Laboratories, Cabin John, MD), followed by rinses with ultrapure water (EMD Millipore) and pure ethanol (Pharmco-Aaper), and dried in a nitrogen flow. The clean substrates are loaded into a magnetron (ATC Orion; AJA International) and coated with a $\sim$ 2 nm Cr adhesion layer followed by a $\sim$ 45 nm Au layer for surface plasmon resonance and impedance spectroscopy measurements and 15 nm for neutron reflectometry experiments. Substrates are incubated in a 0.2 mM ethanolic solution (total concentration) of HC18 and β-mercaptoethanol (βME) in a molar ratio of 30:70, unless otherwise stated, for at least 12 hours immediately after the deposition of the gold layer. The long-term stable SAM forms on the gold electrode via covalent bonds with the thiol linkers. After incubation, the substrates are thoroughly rinsed with ethanol and dried in a nitrogen flow before mounting in the measuring cell apparatus where stBLM completion will take place.

4.2.2 stBLM Completion

Rapid solvent exchange (RSE)

This method consists of displacing a lipid solution with a large amount of buffer, resulting in the precipitation of lipids and thereby bilayer formation on the substrate. Lipids are dissolved in the appropriate organic solvents (ethanol, chloroform, methanol or a chloroform/methanol/water mixture) and lipid mixtures with concentration of 10 mg/ml are prepared and left to incubate in the SAM-covered substrate for 5 to 10 min, followed by a low-salt buffer flush. That results in the direct transfer of lipids from the organic solvent to the SAM. Different solubility of the mixture components can cause deviation from the molar ratio desired. Thus it is not guaranteed that multi-component bilayer deposition preserves the inital molar ratio in the organic solvent mixture. Although RSE reliably forms bilayers on SAMs of low hydrophobicity, stBLM formation is challenging when charged lipids are introduced. The standard procedure adopted by our lab was to add small percentages of cholesterol ($\sim$ 5%) to augment the completion of the stBLM. Furthermore, the reproducibility of stBLMs formed by RSE is easily affected by uncontrolled external parameters. For example buffer flow can introduce air-bubbles that result in incomplete bilayer formation

Vesicle fusion

Vesicles first adhere to the SAM-coated substrate, followed by rupture, yielding a planar bilayer structure. The procedure starts by mixing stock solutions of the lipids in chloroform to obtain targeted lipid compositions. The organic solvent is then evaporated by placing the lipid mixtures under vacuum for 12 h, to ensure complete removal of the organic solvent. Dried lipid films are hydrated afterwards in a high salt aqueous buffer (500 mM NaCl, 10 mM $NaPO_4$ at pH 7.4) at a lipid concentration of $\sim$5 mg/ml and sonicated until clear suspensions are obtained. These are extruded through a polycarbonate membrane (Avanti) with a pore size of 100 nm at least 21 times to obtain narrow distributions of unilamellar vesicles. Upon removal from the HC18:βME incubation solution, the SAM-covered slides are immediately incubated with the vesicle suspension at high ionic strength for at least 2 hours, followed by a rinse with of low ionic strength (50 mM NaCl at pH 7.4) that completes stBLM formation by rupturing adhering vesicles under osmotic shock.

As opposed to RSE, vesicle fusion facilitates control of stBLM composition, allowing for complex heterogeneous lipid mixtures to be tethered to the substrate. The use of unilamellar liposomes, though, depends on the surface properties of the substrate. Alpha-helical fusion peptides can make vesicle fusion more efficient by destabilizing the lipid vesicle structure, inducing vesicle-bilayer transformation [26] [28]. On the other hand, the fusion peptides binds and partitions into the lipid bilayer headgroup altering its fluidity and causing membrane thinning [27]. To speed up the vesicle fusion process and increase rates of planar membrane formation, parameters such as ionic strength and tether density were adjusted to ensure defect-free stBLM. In this work, all the stBLMs used in the experiments were formed by vesicle fusion.

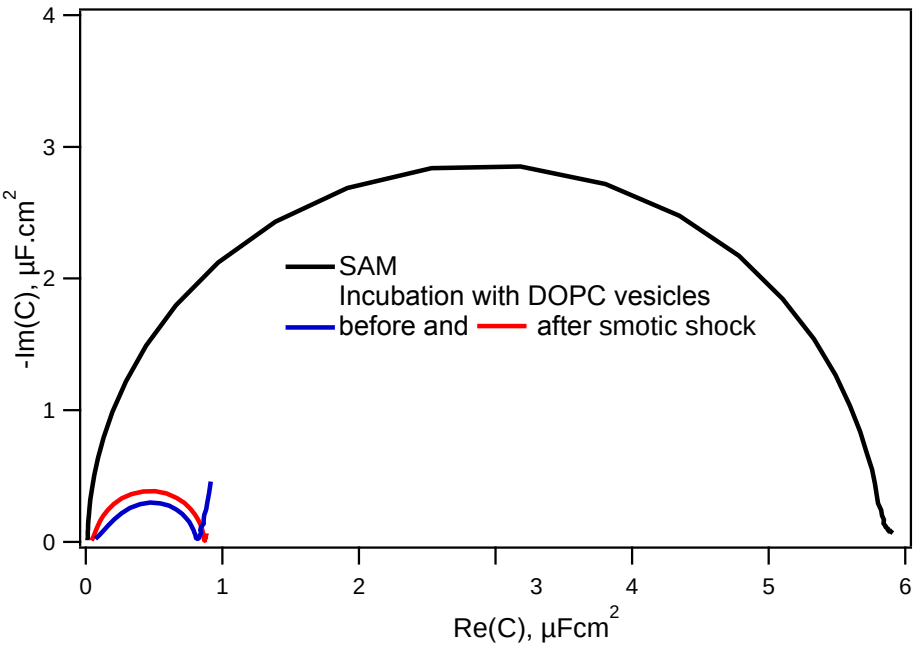

Figure 4.1: Cole-Cole plot of a mixed HC18:βME 70:30 SAM (black), pure DOPC vesicles before (blue) and after osmotic shock (red). Defect-free DOPC stBLM is formed upon vesicle incubation only. Osmotic shock promotes the break up of the remainder vesicles improving bilayer quality.

4.3 Single-component stBLMs

The majority component of the bilayers in this work was phosphatidylcholine (PC), which together with phosphatidylethanolamine (PE) constitutes the main components of the plasma membrane. PC is predominantly present in the outer leaflet while PE resides mainly in the inner leaflet. However, PE at physiological concentration ($\sim 50\%$) does not form stable stBLMs in our hands. For DOPC membranes, in particular, the formation of overlayers can be a concern. These may manifest in the EIS spectra as a decrease in the semi-circle radius, suggesting membrane thickening. Extensive rinsing with buffer or low percentage of ethanol-water ($< 30\%$ ethanol) mixtures can remove the extra lipid layers. stBLMs are stable under experimental manipulation such as buffers exchange without compromising membrane quality as attested by neutron reflectometry. The lipid composition complexity was increased in a way to resemble the plasma membrane inner leaflet composition as a basis for the binding studies involving retroviral Gag protein discussed in chapter 5.

Formation of planar membranes on solid substrates with zwitterionic DOPC has been previously characterized on hydrophilic surfaces where a rapid transfer of lipids to silicon oxide [144] and mica [6] resulted in complete lipid coverage. DOPC has also been characterized in stBLM systems using a range of tethering compounds, including HC18 [114] [70] [14]. Adsorbed vesicles are exposed to a drastically lower salt concentration than the internal aqueous environment thus inducing vesicle rupture. Osmotic shock was initially thought to be the primary mechanism behind vesicle fusion, however EIS shows high quality tBLMs are achieved prior to low salt buffer rinse (see Figure 4.1) which indicates another interaction triggers the vesicles rupture. For

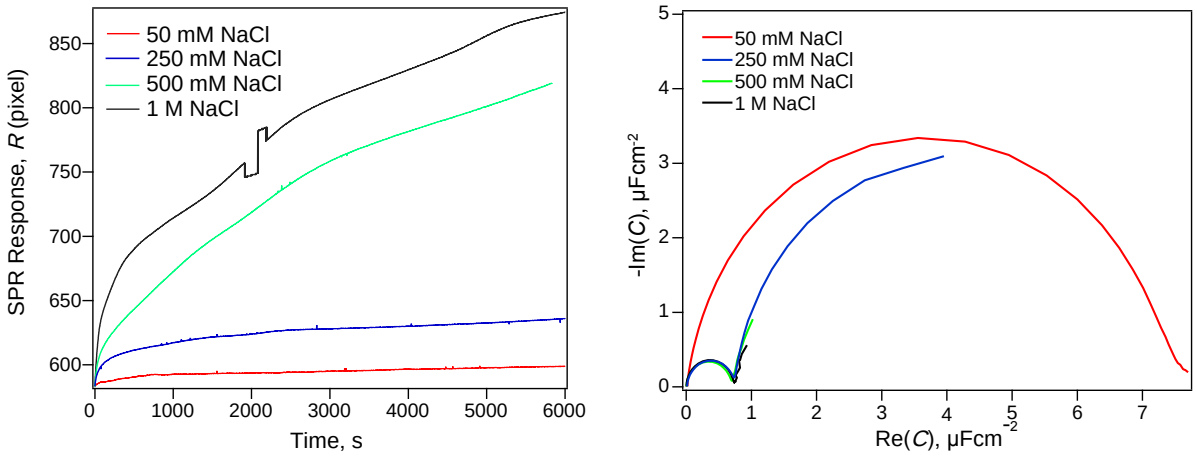

Figure 4.2: Efficient vesicle fusion requires minimal surface coverage. Correlation between surface coverage of adsorbed vesicles and formation of defect-free tBLMs. (A) SPR signal of vesicles DOPC:DOPS 70:30 prepared with dispersant buffer of various ionic strengths adsorbing on HC18:βME 30:70 as a function of incubation time. After 2 hours incubation, the SPR response R $\sim$ 300, 250, 70 and 20 pixels decreases with ionic strengths. Higher coverage correlates with better insulating bilayer properties, SAM-like spectrum at 50 mM NaCl and $R_{def} \sim <$ 50, 150, 250 $k\Omega cm^2$ with increasing in salt concentration, as indicated by the EIS measurements shown in (B).

a single-component DOPC membrane we compared the difference between membrane quality before and after osmotic shock to vesicles adsorbed to a 7:3 mol:mol βME:HC18 SAM. EIS was then used to measure the electrical properties of the formed planar membrane and determine defect density before and after the low-salt rinse. Figure 4.1 shows the complex capacitance, Cole-Cole plot of the hydrated SAM layer, DOPC membrane after vesicle incubation and the membrane after low-salt rinse. The resulting stBLMs had resistance in the order of $M\Omega cm^2$ and their capacitances C_{mem} were one order of magnitude lower than the C_{SAM}, consistent with the formation of high-quality stBLMs, as reported earlier [114] [70] [14].

Even though the formation of pure DOPC membranes by vesicle fusion on hydrophilic and hydrophobic interfaces has already been previously characterized, important information could be inferred from this study. The impedance measurements of the bilayer before and after buffer change showed that osmotic shock improves membrane quality but it is not the primary driving force of the vesicle fusion. A high quality membrane, $R_{def} \sim 400\ k\Omega cm^2$), was formed prior to the low-salt buffer exchange which implies the vesicle-substrate and vesicle-vesicle interaction triggered the fusion process. Vesicle and substrate related parameters were thus fine-tuned to promote efficient formation of more elaborated membranes.

4.4 Multi-component stBLMs

4.4.1 Influence of Surface Charge and Ionic Strength on Planar Membrane Formation

The incorporation of anionic lipid into DOPC vesicles makes stBLM formation by vesicle fusion more challenging [70]. Preparation of charged membranes by rapid solvent exchange, for example, require the incorporation of at least 5% cholesterol for the formation of defect-free bilayer. Vesicles containing 30% negatively charged phosphatidylserine (PS) were prepared in buffer of varied ionic strength ranging from 50 mM to 1 M NaCl. The adsorption was monitored in real time by SPR as shown in Figure 4.2 (A). After 2 hours of incubation, the SPR response (R $\sim$ 300, 250, 70 and 20 pixels) decreases with ionic strengths. Increase in the ionic strength correlates with the formation of higher quality stBLMs. Figure 4.2 (B) shows the EIS spectra corresponding to the different ionic strengths 50 mM NaCl yielded an EIS spectrum that resembles a SAM indicating an incomplete lipid surface coverage. At 250 mM NaCl the characteristic stBLM spectrum was observed, however, the long tail implies a low resistance to ion mobility and therefore indicates the presence of defect-rich regions ($R_{def} < 50\ k\Omega cm^2$). A highly insulating bilayer was formed at 500 mM NaCl with defect density within the standard quality established ($R_{def} \sim 150\ k\Omega cm^2$), still 1M NaCl resulted in an even better sealed stBLM as indicated by the short tail ($R_{def} \sim 250\ k\Omega cm^2$). Higher ionic strength buffers efficiently screen the negative charges which diminishes the repulsion between vesicles, resulting in an increase in the amount of vesicles adsorbed at the lipid membrane interface as shown by SPR (Figure 4.2A). The net surface charge densities on lipid vesicles may promote vesicle repulsion due to the high anionic content, reducing the number of vesicles adsorption and thus inhibiting liposome to reach a substrate surface coverage threshold that will lead to fusion and formation of defect-free stBLMs. The SPR and EIS measurements combined show that the ionic strength of the dispersing buffer has a huge impact on the adsorption and fusion of vesicles containing anionic lipids.

Using buffer conditions optimal for vesicle fusion (1 M NaCl) with anionic membranes we systematically determined the effect DOPS concentration has on membrane formation and structure. The DOPS content was varied from 0 to 40 mol% and the formed stBLMs were characterized by EIS. The Cole-Cole plot, Figure 4.3 (A), shows a slight increase in the radius of the semi-circle with increasing PS amounts as well as a lengthening of the low-frequency tail. Thus PS leads to higher membrane capacitance suggesting membrane thinning. This effect is more noticeable at 40 mol% PS when the bilayer capacitance, 0.936 $\mu F/cm^2$, is larger than the pure DOPC membrane, 0.882 μFcm^2 by a considerable amount. Following an opposite trend, the stBLM resistance systematically decreases with increasing PS content ranging from 1.2 - 0.2 $M\Omega cm^2$, see Table 4.1.

The defect-density of a bilayer can be estimated based on the R_{def} obtained from the EIS spectrum. Modeling the defects as a cylinder of radius 1 nm and length 3 nm and water resistance as being 100 Ω cm the estimated defect density for the lowest resistance bilayer measured (0.2 $M\Omega cm^2$) was $\sim 1.8 \times 10^4 cm^{-2}$ [114] . This value corresponds to volume fraction of solvent in the membrane less than 1% which is within the quality criterion established for stBLMs required to carry on protein-membrane binding experiments.

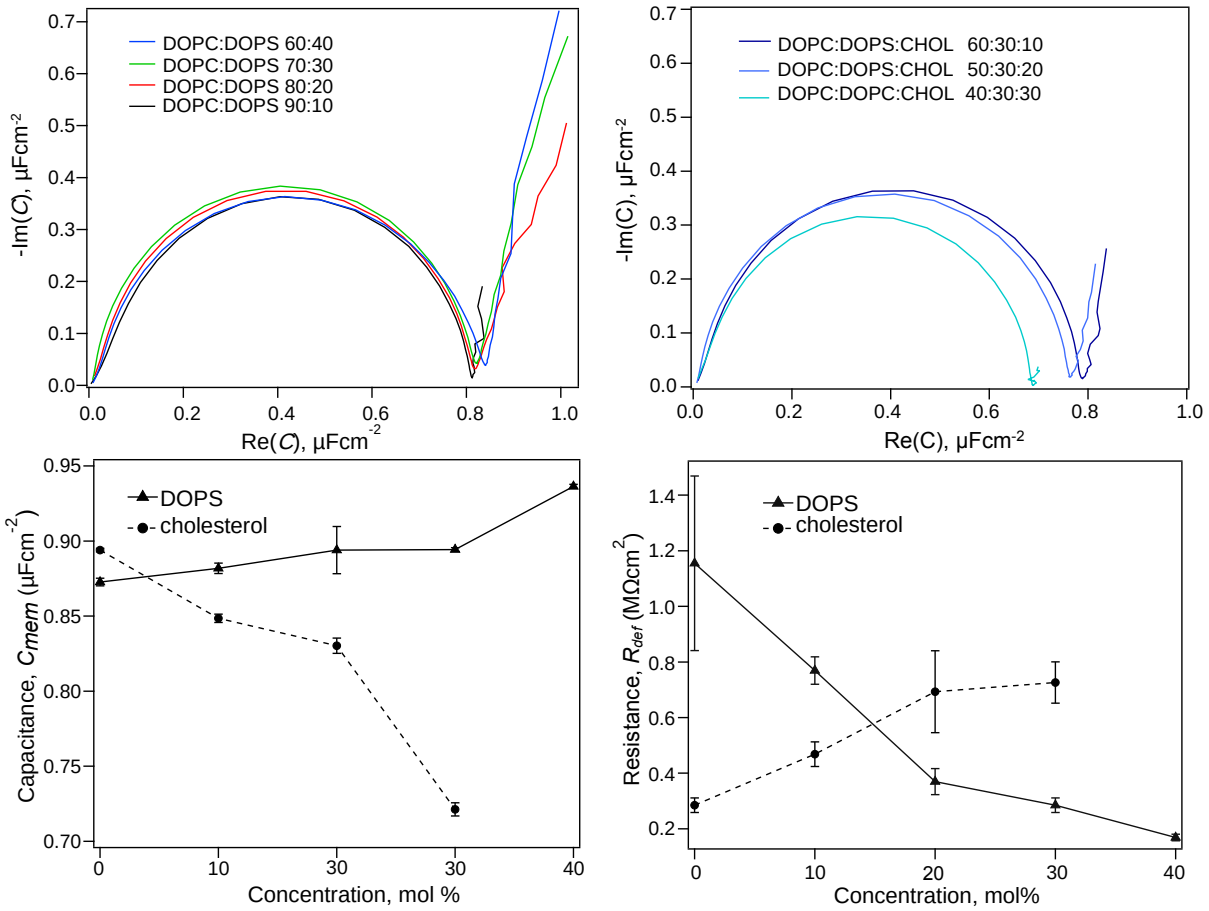

Figure 4.3: Effect of charge and cholesterol on membrane electrical properties (A) EIS spectra of dual component tBLMs DOPC:DOPS on HC18:βME 30:70 at DOPS concentrations ranging from 0 to 40 mol% (B) EIS spectra of a three-component stBLMs DOPC:DOPS:chol on HC18:βME 30:70 at fixed concentration 30 mol% DOPS and cholesterol concentrations ranging from 0 to 30 mol%. Area normalized capacitance and resistance as a function of PS and cholesterol content are shown in panels (C) and (D)

4.4.2 Effect of cholesterol on multi-component stBLMs

Cholesterol is an essential structural component found in large quantities in the plasma membrane. When incorporated into artificial membranes, it alters the lipid bilayer mechanical properties, making them less fluid and less permeable to water soluble small molecules and ions. The influence of cholesterol on DOPC:DOPS membrane formation was thus investigated. The mol-fraction of DOPS was maintained at 30% while the neutral DOPC lipids were replaced by increasing amounts of cholesterol from 10 to 30%.

The Cole-Cole plot, Figure 4.3 (C), shows an increase in the capacitance from 0.84 to 0.72 $\mu F/cm^2$ with increasing concentrations of cholesterol, indicating membrane thickening which is consistent with cholesterol's ability to promote order of the acyl chains. The capacitance values found are slightly smaller than for DOPC:DOPS 70:30 $\sim$ 0.89 $\mu F/cm^2$. The R_{def} improves considerably with cholesterol concentration, ranging from 0.3 - 0.7 $M\Omega cm^2$ as the cholesterol

content is increased. The addition of cholesterol resulted in stBLMs with smaller capacitances (Figure 4.3 C) and higher resistances (Figure 4.3D), i.e. membrane thickness increased, when compared to the 30% anionic lipid membranes.

Based on the parallel plate capacitor model and assuming ϵ = 2.2 for a fluid lipid bilayer, we can roughly estimate the hydrophobic thickness of the membranes (see Table 4.1) from the initial capacitances obtained by equivalent circuit fitting and using the relation $C = \frac{\epsilon A}{d}$.

Comparison between capacitance and resistance of the PS and cholesterol containing membranes show two opposite trends (Figure 4.3 C-D). While the capacitance of cholesterol containing stBLMs shrinks and thus the membrane thickness increases with higher concentrations of cholesterol the capacitance of PS containing membranes increases and therefore membrane thins with higher concentrations of PS. stBLM resistance shows a reverse trend, it increases with cholesterol concentration and decreases with PS concentration. Overall, increase of charge content compromises the bilayer integrity while incorporation of cholesterol reduces membrane defects, thereby improving bilayer quality

Table 4.1: Best-fit parameters obtained from the ECM model shown in chapter 3 for the data in Figure 4.3. Capacitance values were corrected by gold roughness ($\beta \approx 1.4$) and by the area of the electrochemical cell. Resistance values were normalized by the area of electrochemical cell ($A_{el} \approx 0.33$ cm^2). Hydrophobic thickness was calculated using equation 4.1, assuming ϵ =2.2

stBLM composition	$C_{mem}(\mu$F/cm$^2)$	$R_{def}(k\Omega$ cm$^2)$	hydrophobic thickness(nm)
100% DOPC	0.873 ± 0.002	1,155 ± 313	2.231 ± 0.010
DOPC:DOPS 90:10	0.882 ± 0.003	768.9 ± 49.5	2.208 ± 0.014
DOPC:DOPS 80:20	0.893 ± 0.016	369.6 ± 46.5	2.178 ± 0.062
DOPC:DOPS 70:30	0.894 ± 0.001	285.1 ± 26.0	2.177 ± 0.005
DOPC:DOPS 60:40	0.936 ± 0.001	168.6 ± 12.1	2.079 ± 0.005
DOPC:DOPS:chol 60:30:10	0.848 ± 0.003	486.6 ± 44.4	2.295 ± 0.011
DOPC:DOPS:chol 50:30:20	0.830 ± 0.005	693 ± 147	2.345 ± 0.022
DOPC:DOPS:chol 40:30:30	0.721 ± 0.004	726 ± 111	2.700 ± 0.021

4.4.3 Impact of PI(4,5)P_2 on stBLM completion

Although PI(4,5)P_2 is a minor phospholipid component in cell membranes, it is characteristic for the plasma membrane and plays a central role in cell signaling pathways and in retroviral assembly. Given its relevance in the biological scenario, PI(4,5)P_2 lipids were incorporated into vesicles and assembled in stBLMs in a systematic way. The same standard procedure used for the previous mixtures was followed, see Section 4.2. Vesicles were prepared with 1 M NaCl salt buffer and incubated in a SAM-coated slide for 1 hour.

Figure 4.4 shows a three-component system DOPC:DOPS:PI(4,5)P_2 80:15:05 where the overall charge density was kept constant at $\sim$ 30 mol%, assuming an effective charge between -3e and -4e for PI(4,5)P_2 at pH 7.4, for comparison with PS-only containing membranes. After 1 hour of incubation, the bilayers failed to form and its EI spectrum resembled that of a SAM (data not shown). Vesicles were then incubated for longer periods and monitored in intervals of

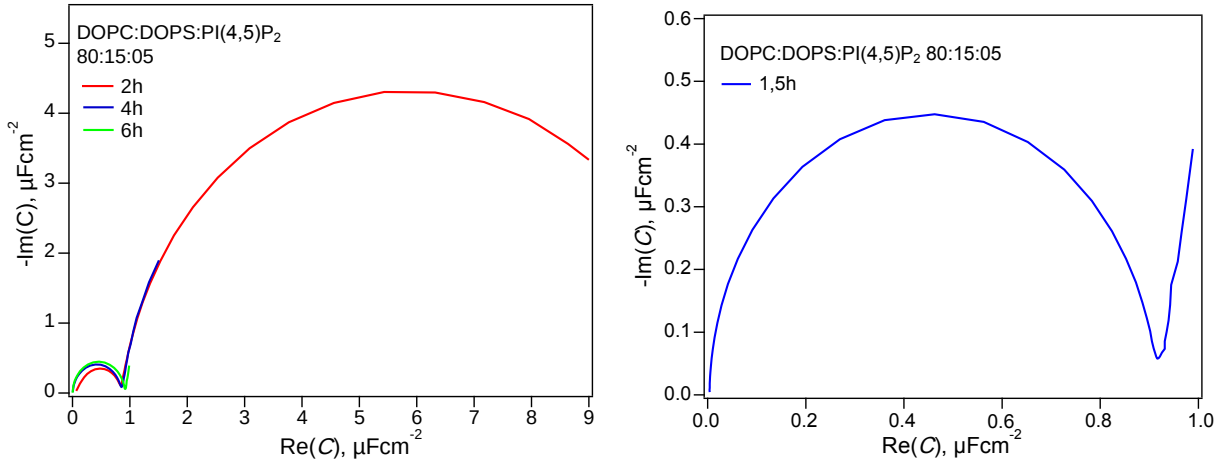

Figure 4.4: PI(4,5)P_2 effect on tBLM formation. (A) vesicle fusion of DOPC:DOPS liposomes containing PI(4,5)P_2 lipids at 5 mol % on HC18:βME 30:70 monitored over time with EIS (B) PI(4,5)P_2-containing membrane formed by vesicle fusion after 1.5h in a gold functionalized substrate with higher tether density HC18:βME 50:50

2h with EIS before carrying out osmotic shock, as shown in Figure 4.4A. Two hours later the stBLM spectrum still partially resembled that of a SAM rather than a good quality lipid bilayer. Within four hours, the length of tail shrank, but the resistance was still below the quality criterion adopted($R_{def} < 100\ k\Omega cm^2$). After incubating for six hours, the ruptured vesicles formed a complete and electrically insulating membrane ($R_{def} \sim 0.2\ M\Omega cm^2$). We thus conclude that prolonged incubation of the liposomes generates less defective membranes.

The formation of stBLMs containing PI(4,5)P_2 ($\sim$ 5 mol%) compared to PS-only containing stBLMs, at similar surface charge densities, was more challenging and time demanding. To eliminate the time constraint and build defect-free bilayers, the hydrophobicity of the substrate was raised by augmenting the lipid tether molar percentage from 30 to 50 mol%. Increasing HC18 density from 30 to 50 mol%does not hinder the capability of stBLMs for the study of transmembranes proteins or drastically alters membrane fluidity.

Incubation of PI(4,5)P_2 containing vesicles on the higher density tethered substrate resulted in defect-free tBLM formation within 1.5h. Resistances were similar to those stBLMs obtained when the vesicles were incubated for 6h, $R_{def} \sim 0.4 M\Omega cm^2$, Figure 4.4B. Moreover, cholesterol up to 30 mol% incorporated into PI(4,5)P_2 containing lipid vesicles increased lipid membrane resistance resulting in defect-free stBLMs (data not shown).

stBLM characterization by neutron reflectivity

SPR and EIS experiments alone cannot distinguish between the presence of unruptured vesicles adsorbed at the bilayer interface and lipid bilayer overlayers. A detailed structural characterization of the tethered lipid membrane was then provided by neutron reflectivity measurements. From those experiments it is possible to infer the structure of multi-component stBLMs that were shown with other methods to be defect-free and highly insulating. In full agreement with EIS, NR measurements showed completion above 95% of well-structured bilayers, validating vesicle

fusion as a reliable and efficient method to obtain stBLMs with minimal defect density. The corresponding nSLD profiles are consistent with structures in which the membrane is decoupled from the gold substrate by a nanometer thick hydration layer. NR detects no sign of water-filled defects in the hydrophobic bilayer core by the virtue of isotopic contrast variation. In Figure 4.5, note that the profiles shown only differ in nSLD in the regions containing aqueous buffer, i.e. tether, headgroups and bulk solvent, for the all the other regions the profiles overlap. That includes the hydrocarbon core which implies no aqueous material is detected in that region and therefore defect-free stBLM structure prevails.However, neutron reflectometry in general is not as sensitive to water-filled pores as EIS. Even small number of defects would lead to an EIS spectrum resembling that of a SAM but still show stBLM completion above 95% if probed with neutrons.

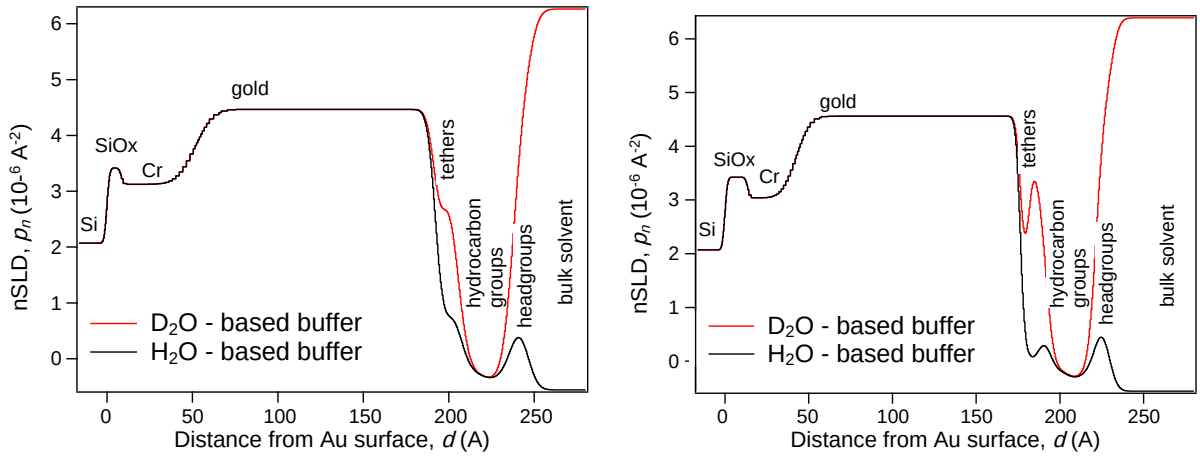

Figure 4.5: nSLD profile for stBLMs on HC18:βME-based stBLMs completed by vesicle fusion. (A) DOPC:DOPS 70:30 (B) DOPC:DOPS:PI(4,5)P_2 80:10:05. Bilayer completion is nearly 100% as evidenced by the overlap of the two isotopic contrast, H_2O and D_2O, profiles in the hydrocarbon group region

4.5 Discussion

In this chapter, several aspects important for an efficient vesicle fusion and how they influence the formation of multi-component defect-free bilayers were highlighted.

Zwitterionic membranes. A systematic study of single-component liposomes showed that pure PC vesicles naturally form highly sealed lipid membranes when in contact with a SAM-covered surface, even before osmotic shock. These measurements suggest that the spontaneous rupture of the vesicles is promoted by the interaction between the liposomes and the hydrophobic SAM-coated substrate. The osmotic shock induced by the low ionic strength aqueous solution plays a secondary role improving stBLM completion and resistance by rupturing remaining intact vesicles.

Charge effect Adsorption of vesicles containing 30 mol% of anionic lipids were monitored at different ionic strengths. Anionic lipids reduce the vesicles coverage due to electrostatic repulsion. High ionic strength of the buffer reduces the electrostatic repulsion between the charged vesicles and increases the vesicle surface coverage which ultimately evolves into a complete planar bilayer. Adsorption kinetics is surface specific [84], the population of vesicles at the interface stimulates vesicle-vesicle interaction which leads to rupture at critical surface coverage [145]. SPR experiments suggest that a critical coverage needs to be reached in order to induce vesicle rupture and thereby promote the formation of high quality bilayers, as observed for hydrophilic substrates [181]. The results indicate that vesicles adsorb intact at low salt conditions and do not form a bilayer spontaneously. Defect-free lipid bilayer completion is observed at high ionic strength after a critical coverage is surpassed, consistent with increase of the SPR signal and EIS measurements, see Figure 4.2.

Evolution of the capacitance and resistance of stBLMs with PS concentrations between 10 and 40 mol%, Figure 4.3C,D shows a modest increase in capacitance that can be explained by the charged nature of the anionic lipid species included in the system. The repulsion between the headgroups contributes to a more disordered distribution of lipids within the lipid bilayer. The lipids may adopt a tilted orientation [182] [79], inducing membrane thinning and thus resulting in the increasing in capacitance. Likewise, we see a clear difference in the low frequency region of the EI spectra (Figure 4.3A,B). Tail lengthening due to increasing amounts of PS is associated with higher density of defects. The stBLM resistances were within the range 1.2 - 0.2 $M\Omega cm^2$, where the lowest resistance corresponded to the 40% negatively charged membrane. The resistance loss is again associated with the lipid organization within the bilayer. The lipid tilting [182] [79] contributes to a less compact bilayer structure organization resulting in the creation of water-filled defects and thereby less electrically sealed, defect-rich membranes.

Cholesterol effect. Other factors such as incorporation of cholesterol on 30 mol% anionic vesicles did not affect the fusion process i.e increase the rate of planar bilayer formation but its higher contents had impact on the membrane structure yielding better sealed stBLMs. Cholesterol in the stBLMs induces lipid rearrangement that improves the quality of the bilayers. Higher resistances were observed at the lowest cholesterol concentration, 10 mol%, when compared to the 30 mol% PS-only membranes. The capacitance followed an opposite trend when compared to anionic stBLMs, it decreases with higher contents of cholesterol. Addition of cholesterol to the model membranes induces ordering of the lipids, known as cholesterol condensing effect, and thus thickening of the bilayer. Mechanical stiffening of the liposomes due to cholesterol only impacted bilayer structural properties but did not affect vesicle fusion. Cholesterol in the physiologically relevant fluid state promotes ordering and rigidity. These properties impact on the structure

PI(4,5)P_2 effect Diversity of the liposomes components also play a role in fusion. PI(4,5)P_2 lipids have a more complex chemical structure [116], bulkier headgroup and higher effective charges between +3e or +4e, than other phospholipids. As mentioned before, the initial and dominant force driving rupture is due the vesicle-substrate interaction. Increasing the HC18 tether ratio, augments the hydrophobicity of the mixed SAM [14]which facilitates the rupture of the vesicles. This fact supports the idea that surface interaction is important on the vesicle transfor-

mation to lipid bilayer. Increasing the tether ratio enhances the chemical affinity of the vesicles for the substrate making the pre-adsorbed vesicles to burst more easily. This work demonstrates that many steps of the vesicle fusion protocol and substrate preparation can be optimized. Here, we established the guidelines for preparing robust, multi-component defect-free membranes to be used for the characterization of membrane-protein complexes.

Chapter 5

Membrane Coupling and Dynamic Reorganization of Gag in Retroviral Assembly

In the next three chapters, the molecular and structural basis of retroviral assembly is discussed. The structure and binding mechanisms of HIV-1 Gag and its membrane binding domain, matrix (MA), are reviewed in section 5.2. Interaction between retroviral Gag and MA of different species with membranes is discussed and compared in sections 5.3. In Chapter 6 the factors that control the association of HIV-1 MA with membranes are dissected. Chapter 7 addresses lipid membrane reorganization upon MA binding. Finally, in chapter 8 the structural reorganization of membrane-bound Gag is characterized at intermediate stages of assembly.

5.1 Introduction

Retroviruses are enveloped viruses that have two identical copies of single-stranded RNA as their genome. The envelope is acquired from the host membrane and includes some viral glycoproteins associated to the lipid bilayer exterior. The RNA viruses typically replicate in the cytoplasm [167] [57]. Early steps of viruses life cycle [31] [127] start with virus attachment at the cell surface followed by fusion of the virus with the host cell plasma membrane. Once it gains cell entry, the virus core is taken apart and the viral components are delivered to the cytosol. The dismantling of the virus unit culminates with the release of the nucleic acid into the cytoplasm, followed by reverse transcription of the viral genomic RNA into DNA. The next step in viral infection is integration of DNA into the host genome. The hijacking of the cell machinery is crucial to maintain the progress of the viral replication process. After being generated in the nucleus, RNA is exported back to the cytoplasm where translation occurs. That step directs synthesis of Gag protein, the only retroviral protein required to form a virus particle. In order for a virus to spread to other cells it must form an infectious virus particle. Successful assembly of the virus particle requires the convergence of multiple viral components within the cell. These spatially and temporally controlled events include Gag trafficking to and interaction with the PM, Gag interaction with other Gag proteins, and Gag interaction with viral RNA. After

assembly, the progeny virions bud out from the plasma membranes from which they obtain their lipid envelope. As the virions are released, enzymes cleave the Gag protein into its constituent domains resulting in the conversion of the immature virions into a mature infectious form. By studying Gags of different retroviral species we can characterize the complex molecular interactions involved in the intermediate stages of assembly and provide a clear molecular picture of the assembly process.

The functional structure in viral assembly is a uniform, tightly packed Gag protein lattice on the PM. However, there are multiple pathways by which this structure can form. In vitro assays suggest a central role of nucleic acid in viral like particles (VLPs) assembly. Recombinant Gag is soluble, displaying no propensity to assembly into VLPs, the addition of nucleic acid triggers rapid and spontaneous assembly of Gag into VLPs. All immature retroviral particles studied to date share common structural features [41]. In cells, the immature virus can be formed by expression of Gag only [56], where it is distributed radially as elongated rods, with protein shell thickness of approximately 200 Å. Micrographs also revealed the presence of concentric layers interpreted to be the separated folded domains of Gag: MA, CA and NC [59] [10].

5.2 Human Immunodeficiency Virus type I (HIV-1)

5.2.1 MA structure and binding mechanisms

The N-terminal matrix (MA) domain of Gag is the structural motif that mediates PM targeting [132] and remains bound to viral lipid membrane after maturation. The MA domains of retroviruses share a high degree of structural homology, despite the low sequence similarity [121]. Most of the N-terminal portion of MA, composed of 5-6 alpha helices, adopts a compact globular fold, while the C-terminus is often flexible or unstructured [72].

Distinct molecular mechanisms complement each other in positioning the protein in an orientation productive for assembly: electrostatic interaction between a patch of basic residues and anionic membrane lipids, hydrophobic interaction between MAs myristoylated N-terminus and the membrane, and specific binding of the protein to phosphatidylinositol-4,5-bisphosphate ($PI(4,5)P_2$) selectively enriched in the PM [174] and detected in the HIV-1 membrane envelope after assembly [3] [12]. Basic amino acids are clustered on the surface of MA globular head resulting in a basic patch which interacts electrostatically with the inner leaflet of the PM [120]. The MA domains of different retroviral genera carry different net charge in this basic patch, the net surface charges for RSV MA and HIV-1 MA at neutral pH are +3 and +6, respectively, suggesting different contribution of electrostatics in the membrane protein targeting. Moreover, HIV MA has a defined $PI(4,5)P_2$ binding pocket [149], depletion of this phospholipid from the plasma membrane compromises Gag membrane association. RSV MA, on the other hand, has no known binding site. The matrix domain of HIV-1 has a myristate group attached to its N-terminus while RSV MA has no fatty-acid modification. Both the myristoylation of HIV-1 MA as well as its basic patch are required for correct PM targeting [147] [192] while the remainder of the Gag polyprotein appears not to participate in this process.

The mechanisms that contribute to MA binding are determined by MA structural features and by Gag assembly site location. The plasma membrane inner leaflet, where assembly takes place,

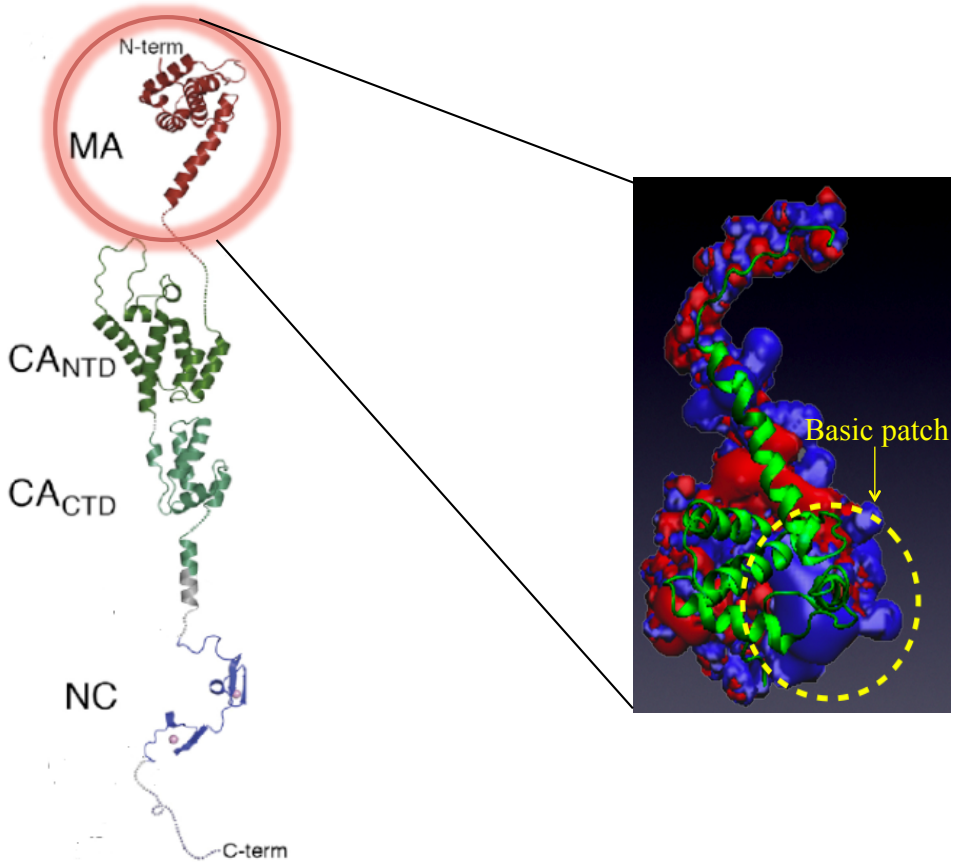

Figure 5.1: HIV-1 Gag polyprotein structured domains. Matrix (MA) is responsible for targeting Gag to the plasma membrane. Capsid (CA) promotes the lateral interaction between adjacent Gag molecules. Nucleocapsid (NC) binds to the viral genome. MA is formed by α-helices that form a globular structure and a flexible C-terminal region. Biophysical features of MA that mediates targeting to the PM includes basic patch residues, binding pocket specific to PI(4,5)P_2 located close to its N-terminus and a myristate group sequestered in a hydrophobic cleft.

is composed of neutral lipids such as phosphatidylcholine (PC) and phosphadylethanolamine (PE), acidic lipids such as PS $\sim$ 30 mol% and PI(4,5)P_2 $\sim$ 1-3 mol%, which is found exclusively at the PM preventing Gag from associating to other membranes and target specifically the PM, and cholesterol. Lipidomic studies also show raft-affine lipids, sphingomyelin and cholesterol enriched in the HIV-1 envelope when compared to the PM [3] [12], supporting the hypothesis that HIV-1 buds from lipid rafts [74] [129] [131]. One of the challenges is to understand how HIV-1 acquires a raft-like lipid composition. Gag interacts directly with the inner leaflet while rafts are known to occur on the outer leaflet of the PM, abundant in sphingomyelin. Comparison between macrophages and T-cells, preferential targets of HIV [81] [109], show similar virion lipid composition [21] even though their global composition are different, which suggests HIV-1 recruits lipids to create a favorable lipidic environment for viral assembly [109].

Our major interest is the molecular interaction of Gag with membranes and more specifically how matrix interact with phospholipids and to bring that knowledge into the context of viral

assembly. The binding mechanisms of MA and phospholipids have been extensively studied in vitro and in vivo [5] [36] [48] [65] [149] but no conclusion has been reached regarding the individual contribution of those interactions to the MA membrane association. None of the previous experimental approaches were able to provide a quantitative assessment of MA affinity to the membrane. In Chapter 6, MA binding free energy is determined and provides a delineation of how the individual bilayer components contribute to MA association.

MA: trimer vs monomer

In the case of HIV-1, the -myrMA structure was resolved both by NMR [110] [111] and x-ray crystallography [72], while the +myrMA structure was resolved by NMR only [169]. HIV-1 -myrMA (as well as Simian immunodeficiency virus, but neither Equine Infectious Anemia Virus nor MLV MAs) crystallizes as trimers, while it appeared as a monomer under NMR conditions. The overall structure is conserved between +myr and -myrMA, but there are some differences notably in the putative trimerization region and in the first α helix. NMR structural studies confirmed that the myristate group can adopt sequestered and exposed conformations even in the isolated MA protein and in the absence of membranes [149]. Structural and biophysical studies on HIV-1 MA revealed that the exposure of the myristate group is modulated by several factors including protein concentration, oligomerization, pH, and the presence of the capsid. The exposure of the myristate group requires minimal conformational changes in the MA structure [65].

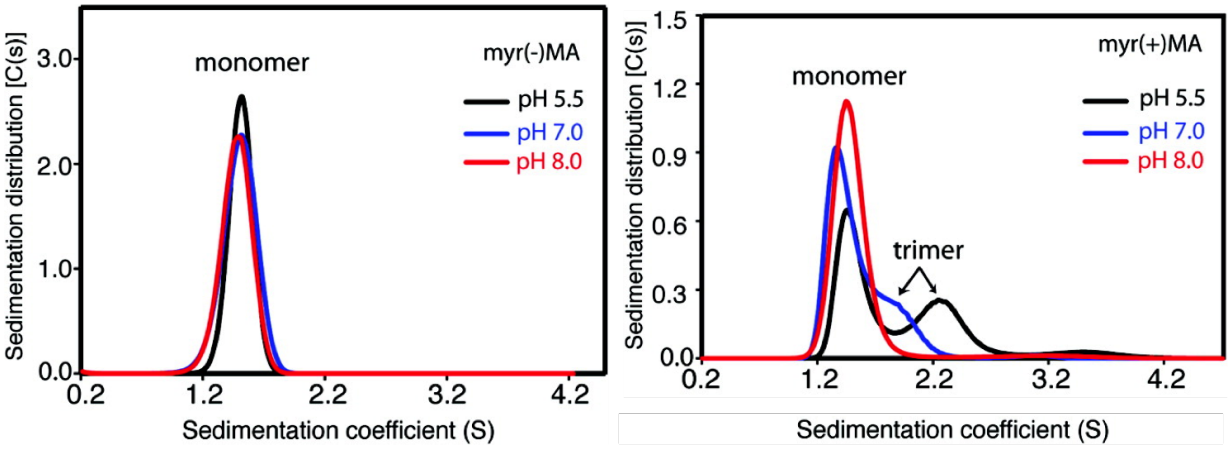

Figure 5.2: Sedimentation coefficient distribution, c(s), obtained from the sedimentation profiles for +myrMA (left) and -myrMA (right) as a function of pH. -myrMA is monomeric for the pH ranges tested while +myrMA is purely monomeric only at pH 8.0 and exists in a monomer-trimer equilibrium below that pH. Figure adapted from [55]

Equilibrium between two conformations of HIV-1 +myrMA in solution correlates with the state of myristoyl [193] and [169]. In the monomeric form, the myristate moiety is sequestrated inside the hydrophobic pocket of the protein. The other conformation has the myristate group exposed and tends to assemble in trimers [169]. In particular, high concentration of MA promotes trimerization and stabilizes the exposure of the myristate group.

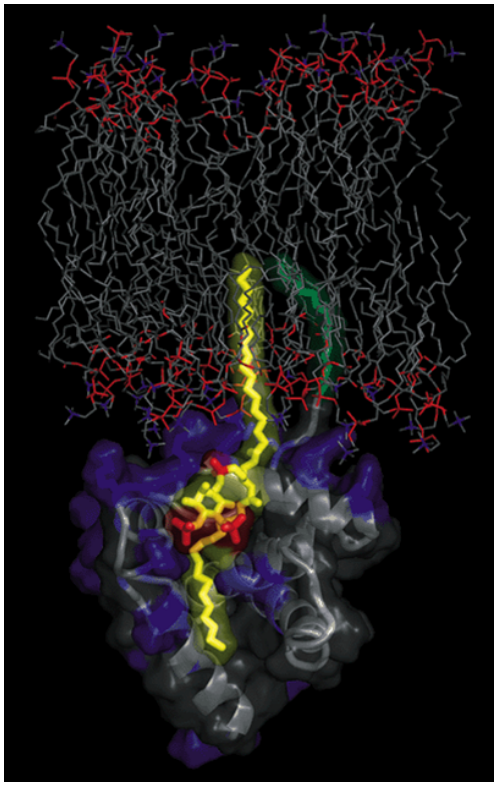

Figure 5.3: Model for MA membrane association based on NMR studies. Basic residues (blue) interact with acidic phospholpids (red) while PI(4,5)P_2 (yellow) inositol ring packs towards MA. The interaction between PI(4,5)P_2 and MA induces conformational changes that trigger the exposure of myristoyl (green) followed by the flip of the unsaturated chain of PI(4,5)P_2 towards the hydrophobic pocket vacated by the myristate upon membrane insertion. Figure from [149]

Many other elements also influence the monomer-trimer equilibrium. As shown by analytical centrifugation studies of high-order assembly of the +myrMA protein in solution, high concentration of MA promotes trimerization [169] [188]. Another parameter that seems to influence the monomer-trimer transition is pH, as shown recently [55]. High pH stabilizes the monomeric MA form, while acidification favors myristate exposure and thus trimer formation. MA trimers were also identified in 2D crystals on lipid membranes [2], but whether MA-MA interactions play a role in the membrane association of full-length Gag remains unclear.

Model of MA association to PI(4,5)P_2- containing membranes

The most accepted model for MA binding to membranes, depicted in Figure 5.3, is based on NMR structural studies. Those measurements probed the MA interaction with truncated PI(4,5)P_2, soluble, to avoid aggregation and signal broadening [149]. PI(4,5)P_2 inositol ring interacts with the highly basic region of MA. It was also suggested that PI(4,5)P_2 triggers myristate exposure from a sequestered state within the dissolved protein [149] followed by a flip of PI(4,5)P_2 unsaturated chain towards an MA hydrophobic pocket, a mechanism that might further enhance the affinity of Gag to lipid rafts.

The structural basis of MA-membrane association is still disputed [178] [178]. NMR studies propose that MA binding to bilayers is governed by a trio of interactions in which the myristate group and the acyl chains of PIP_2 and PS/PE/PC [178] anchor Gag to the membrane. The lipid environment, either micelles or bicelles, was sufficient to trigger myristate group exposure, no $PI(4,5)P_2$ is required [178]. Coarse grained simulations, however, predict inositol ring binding to MA basic patch residues exactly in the same way as described by the NMR studies, but observed no flip of the $PI(4,5)P_2$ acyl chain towards the protein hydrophobic cavity [178]. The model of MA association with the membrane needs further investigation. MA interaction with full-length PIP_2 within the context of lipid membrane bilayers is a step towards clarification of the structural basis of +myrMA association to lipid membranes and will be addressed in Chapter 7.

5.2.2 Conformational Reorganization of HIV-1 Gag at the membrane

Neutron reflectometry measurements probed the conditions under which HIV-1 Gag association to membranes is compact [39], as it is in free solution and VLPs [38], or extended, as it is in immature virions [59] [10]. Model membranes in combination with neutron reflectometry were used to characterize the structural reorganization of HIV-1 Gag at the membrane. The contributions of protein-protein, protein-lipid, and protein-nucleic acid interactions to the extension of the protein were investigated. NR showed that HIV-1 Gag conformation at the membrane depends on molecular context [39], see Figure 5.4. In the absence of nucleic acid, Gag adopts a compact conformation on the membrane with similar dimension of Gags in VLPs [38]. However, exposure of this compact, membrane-bound Gag layer to nucleic acid triggers an extension of the protein to $\approx$ 180 Åfrom the membrane surface, which is approximately the length of the Gag shell in immature virions [59] [10]. Rinsing with a high salt buffer recovers the Gag compact structure. Neither electrostatic interaction between PS lipids and Gag, nor Gag-Gag protein (probably due to low protein-density coverage) were able to trigger HIV-1 Gag extension on its own.

The flexibility of HIV-1 Gag linkers allow the MA and NC domains interact simultaneously with the membrane. In the presence of both membranes and nucleic acid, each of the domains binds its preferred target, MA binds to the membrane and nucleic acid binds to NC, promoting the protein extension. Flexibility of these linkers may be important for controlling molecular reorganization during assembly. Gag species that contain stiffer linkers, MLV and RSV, and mutants that completely lack those linker regions are probed in Chapter 8.

5.3 A comparison between HIV-1, MLV and RSV Gag protein properties

5.3.1 Gag assembly with RNA and packing in immature virus

Gag alone is sufficient for assembly of immature virus-like particles in mammalian cells. The assembled particles are spherical, with a diameter of approximately 100 nm. The Gag molecules are extended rods in the assembled particles, with its N-terminal binding to the membrane and its c-terminus interacting with RNA. These rods are $\sim$ 20 nm long and only 2-3 nm wide. In vitro

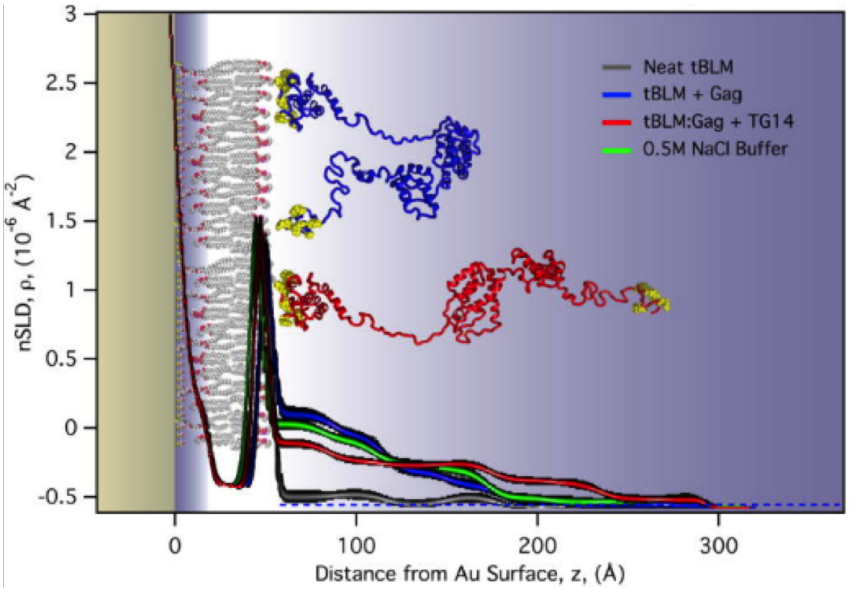

Figure 5.4: HIV-1 Gag conformational changes. In the absence of nucleic acid, Gag adopts a compact conformation at the membrane. Once membrane-bound Gag is exposed to RNA it becomes extended. Both membrane and genome binding are required for HIV-Gag adopting an extended conformation. Figure adapted from [39]

Gag assembles into virus-like particles (VLPs) in the presence of RNA. Those particles closely resemble the structures of viruses assembled in vivo except for the fact that they lack the lipid membrane envelope.

HIV-1. Although Gag assembles into full-size particles in vivo [59], the recombinant HIV-1 Gag assembles into VLPs that are only $\sim$ 25-30 nm in diameter, 3 times smaller than the actual size of the virion. The thickness of Gag protein shell is only 70 Å [38]. VLPs of the correct size are obtained if inositol pentaphosphate (IP5) is added to the assembly reaction [16].

MLV. In cells, immature MLV particles are very similar in overall structure and organization to immature HIV-1 particles Gag. In contrast to HIV-1, MLV Gags form full-size particles $\sim$ 200 Åthick in vitro upon the addition of nucleic acid alone [40], similar to that of immature VLPs assembled in cells [190].

RSV. Cryo-electron microscopy previously determined the lateral and radial arrangement of Gag in vivo and in vitro for assembled RSV particles. The assembled VLPs in vitro and in cells [17] showed the characteristic morphology and size of immature retroviruses [191].

5.3.2 Solution properties of Gag

The similarity in immature retroviral virus packing might suggest similarities in the overall structural properties of Gag proteins, but that is not the case for HIV-1, RSV and MLV.

HIV-1. Hydrodynamic studies on the monomeric HIV-1 Gag protein showed that it is highly flexible, as confirmed by small-angle neutron scattering (SANS) experiments [38]. Atomic-level structures of individual domains within Gag have previously been determined, but these domains are connected in Gag by flexible linkers. Gag models were constructed based on the known structures of individual domains, and each model was tested computationally for its agreement with the experimental hydrodynamic and SANS data. The only models consistent with the data were those in which Gag was folded over, with its N-terminal matrix domain near its C-terminal nucleocapsid domain in agreement with the in vitro assembly studies [39]. Since Gag is a rod-shaped molecule in the assembled immature virion, these findings imply that Gag undergoes a major conformational change upon virus assembly. MLV and RSV Gag solution properties are very distinct from HIV-1 Gag.

MLV. In solution, MLV Gag was analyzed by small angle x-ray scattering (SAXS), which suggests Gag is extended rather than compact [40]. MLV Gag has approximately similar dimensions, $\sim$ 191 Å, to that of Gag in the immature MLV VLPs. In fact, the crystal structure of the MA domain and the CA domain fits well into the molecular envelope of full-length Gag generated by SAXS. The conformational difference adopted by Gag of distinct retrovirus species is due to the linker regions that connect the domains. MLV Gag has a notable sequence feature that consist of a run of prolines between MA and CA domains, which can form polyproline helices and thus contribute to the rigidity and extended conformation of the protein in solution.

RSV. Unlike HIV-1 and similar to MLV Gag, hydrodynamic studies and SAXS measurements led to the conclusion that RSV Gag is extended but flexible in solution [44]. RSV Gag contains several disordered linkers, and Kratky analysis of SAXS data reveal the protein to be extremely flexible in solution. RSV Gag by virtue of its flexibility can sample many conformations, including compact ones for example when it interacts with membranes [44].
A comparison of the structural properties of membrane-bound Gag from viruses from different genera may give insight into common underlying mechanisms of assembly.

Chapter 6

Membrane Binding of HIV-1 Matrix Protein: Dependence on Bilayer Composition and Protein Lipidation

6.1 Synopsis

In this chapter, we use surface plasmon resonance (SPR) spectroscopy on synthetic solid-supported bilayers (tethered bilayer lipid membranes, stBLMs) to parse protein membrane interactions into their components. The lipidic composition of stBLMs can be precisely controlled as discussed in chapter 4, and in particular, membrane signals such as PI(4,5)P_2 can be incorporated in the context of the lipid membrane.

Using SPR on stBLMs, we assess the specific roles of electrostatic, hydrophobic and lipid-specific contributions to viral assembly at the membrane surface. With this tool, we aim to understand the mechanisms that lead to the recruitment of specific lipids into the viral shell. The impact of protein myristoylation is evaluated in a quantitative comparison of the binding of non-myristoylated (-myr) and myristoylated (+myr) protein to these model membranes, and the role of cholesterol (chol) is assessed in promoting protein affinity to the bilayer. Our results show that MA binds to the membrane through a combination of specific and non-specific interactions. We determine the hydrophobic and electrostatic contributions to the non-specific protein binding to charged membranes and show that these contributions are not additive in their total free energy.

Electrostatic attraction and hydrophobic interaction are sufficient to stably anchor MA at the membrane. While electrostatic interactions alone only lead to weak binding of -myrMA, myristoylation increases protein affinity to the bilayer significantly. Both chol and PI(4,5)P_2 affect MA membrane binding dramatically. In the presence of only PI(4,5)P_2, -myrMA and +myrMA affinities were larger than those found for PS containing membranes at similar surface charge densities. In the absence of PI(4,5)P_2, chol increases protein affinity to membranes only for the myristoylated protein. In particular, a combination of chol and PI(4,5)P_2 increases membrane binding of -myrMA and +myrMA to a similar extent, which casts doubts on the proposed chain-swap mechanism [149] in which a PI(4,5)P_2 acyl replaces sequestered myristoyl on the protein upon binding. The molecular level details reported here provide a better understanding of the

lipid interactions of MA and their implications for proper Gag membrane association and viral particle assembly.

6.2 Materials

6.2.1 Lipids

1,2-dioleoyl-sn-glycero-3-phosphocholine (DOPC), 1,2-dioleoyl -sn- glycero-3-phospho-L-serine (DOPS), cholesterol (extracted from ovine wool), L--phosphatidylinositol-4,5-bisphosphate (brain extract; PI(4,5)P_2) and soy-PI were purchased from Avanti Polar Lipids.

6.2.2 Protein expression and purification

Standard laboratory chemicals, culture media, 1-tridecanecarboxylic acid (myristic acid), isopropyl-β-D-thio-galactopyranoside (IPTG), phenylmethylsulphonylfluoride (PMSF), β-mercaptoethanol (β-ME), and tris(2-carboxyethyl)phosphine-hydrochloride (TCEP) were purchased from Sigma Chemical (St. Louis, MO). Protease inhibitor cocktail set I-Calbiochem was from EMD Millipore (Billerica, MA). TALON metal affinity resin was from Clontech Laboratories Inc. (Mountain View, CA). SDS-PAGE supplies were from Bio-Rad (Hercules, CA). Columns for protein purification were from GE Health Care Life Sciences.

Non-myristoylated MA was provided by Sid Datta at the National Cancer Institute (NCI) while myristoylated MA was prepared by Ioannis Karageorgos at the Institute for Bioscience Biotechnology Research (IBBR) according to the following protocol. Matrix proteins were expressed in BL21 (DE3) pLysS cells transfected with the PET 3XC vector. For the production of myrMA, cells were induced at 37°C for 4 hours with 1 mM IPTG, and lysed in buffer A (20 mM Tris HCl, pH 7.4, 10 mM βME and 1 mM PMSF) with 150 mM NaCl. After centrifugation at 12,000g for 15 min to remove cellular debris, the protein was fractionated from the lysate by taking a 40-70% ammonium sulfate saturation cut. The protein was dialyzed against buffer A with 150 mM NaCl. Ammonium sulfate was added to 40% saturation and the solution chromatographed on a butyl Sepharose column. Fractions containing the protein were dialyzed against buffer A with 50 mM NaCl, and chromatographed on an SP Sepharose column. The purified protein was stored in buffer A with 150 mM NaCl and 10% glycerol, and chromatographed on a Superdex 75 gel filtration column before use.

For the expression of +myrMA, cells were grown to OD_{600} = 0.4 with shaking (250 rpm) at 37 °C, then supplemented with myristic acid at a concentration of 10 mg/L and kept growing to OD_{600} = 0.8. At this point, protein expression was induced by adding IPTG to a concentration of 1 mM and the cells cultivated at 30 °C overnight. Cells were harvested by centrifugation at 6,000×g for 15 min at 4 °C, washed with PBS, and held frozen at 80 °C. Five grams (wet weight) of cells were resuspended in 30 mL lysis buffer B (20 mM Tris, 300 mM NaCl, 10 % glycerol, 1 mM PMSF, 1 protease inhibitor mixture set I-Calbiochem, 1 mM TCEP, pH 7.4) and disrupted on ice by sonication. The cell lysate was centrifuged at 10,000g for 30 min at 4 °C and the protein purified by immobilized metal affinity chromatography (IMAC) using the TALON metal

affinity resin. Monomeric MA was separated by size exclusion chromatography on a Superdex 75 10/30 GL column using an KTAPurifier system (Amersham Pharmacia Biotechnology).

6.3 Results

The association of Gag with the plasma membrane (PM) of the host is a complex process in terms of molecular interactions that drive it and lead to the formation of the Gag lattice on the viral membrane in the immature virus. Multiple binding motifs contribute to this process, and here we try to disentangle the contribution of those motifs that relate to the MA domain electrostatic interaction of MAs cationic patch with acidic membranes, hydrophobic interaction of the myristate with the bilayer, and specific interactions with the PM lipid signal, PI(4,5)P_2. In this approach, we deliberately forgo the role of homotypic protein-protein interactions.

By varying membrane compositions and quantifying the affinities of non-myristoylated and myristoylated MA protein at a standardized buffer composition (50 mM NaCl, 10 mM $NaPO_4$ at pH 7.4) by SPR, this study seeks to disentangle the contributions of the physical interactions that lead to MA membrane binding. The lipid compositions were chosen to resemble the major lipid components of the membrane at which viral assembly is initiated, i.e., the inner leaflet of the PM, previously discussed in Chapter 2. However, because phosphatidylethanolamine (PE) at high concentration in our hands does not form stable stBLMs, we use DOPC as the majority component. In this backdrop of DOPC, we investigated the role of DOPS, cholesterol (chol) and PI(4,5)P_2, the major functional lipid resident in the inner PM. In order to characterize the impact of the myristate group and lipid composition on HIV-1 matrix membrane association we systematically studied the interactions of -myrMA and +myrMA with multi-component stBLMs.

6.3.1 Myristoylation increases the MA membrane affinity by over an order of magnitude on PS-containing stBLMs

Independent of myristoylation, binding of MA to stBLMs composed only of DOPC was below the detection limit, but protein binding can be easily observed at PS concentrations of 10 mol% and up. The binding isotherms of -myrMA and +myrMA to DOPC stBLMs that contained various levels of DOPS are shown in Fig. 6.1. As observed earlier [123], electrostatic interactions alone are sufficient to attract -myrMA to the bilayer surface (panel A), and variations in PS concentration led to significant differences both in affinity (K_d) and protein loading (R_∞). At high PS concentrations ($>$ 40 mol%), protein loading approached a value expected for a densely packed protein monolayer ($R_\infty \approx 60$). However, affinities overall remained low, even on stBLM at 100% PS (diamonds in panel A), K_d did not fall below 10 μM for -myrMA. For low-affinity isotherms, full binding curves were not measured due to limitations in available amounts of protein.

In particular, +myrMA showed higher affinities to PS concentration in the bilayer. Binding isotherms were well separated when the PS concentration is increased by 10 mol% between 10% and 40% . While protein loading of the membrane was similar for +myrMA and -myrMA at comparable PS concentrations (see binding curves on 40% DOPS in panels A and B, as well as panel D), the affinity of +myrMA is about one order of magnitude larger than that of -myrMA

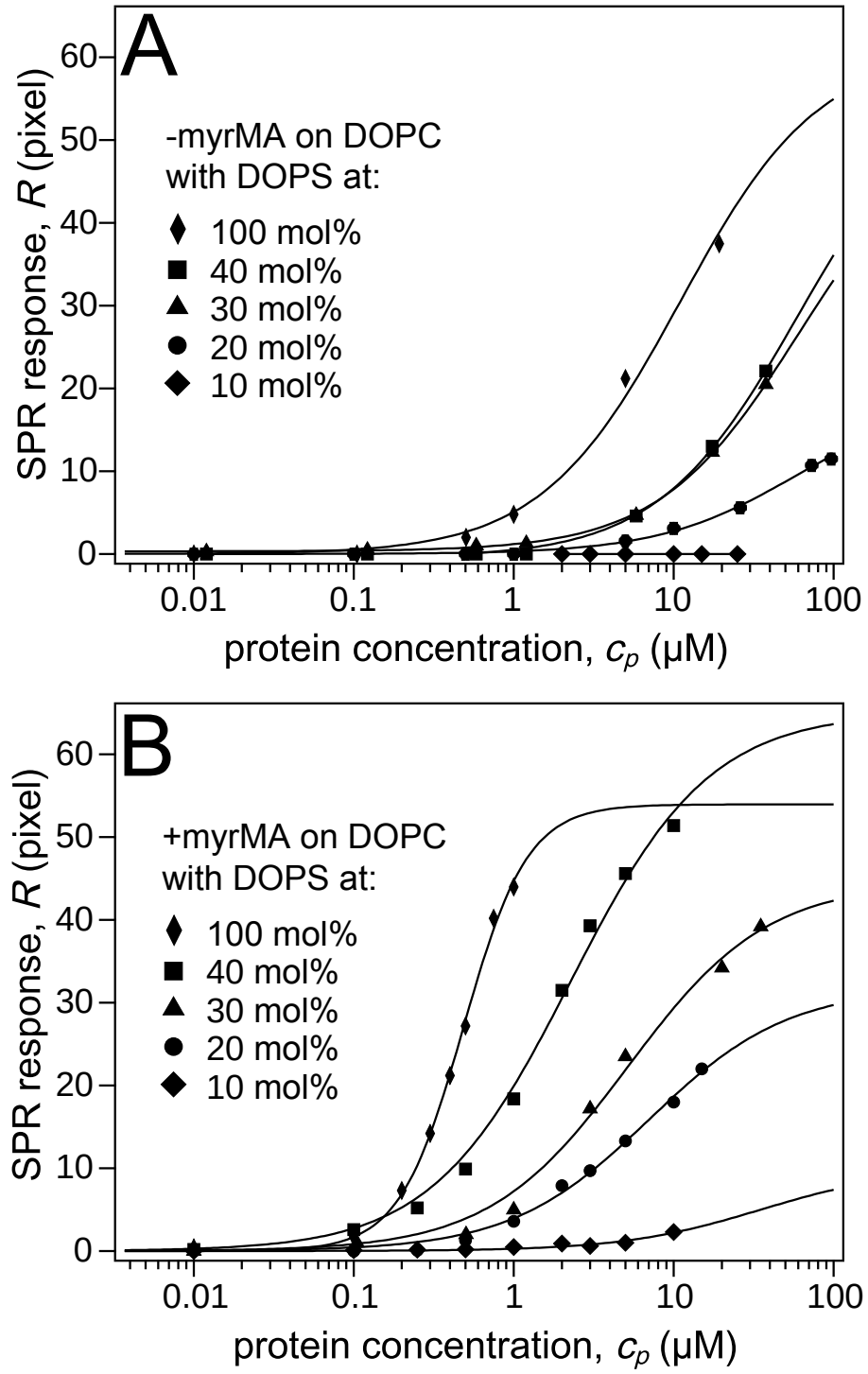

Figure 6.1: Comparison of -myrMA and +myrMA binding to stBLMs that contain DOPC and DOPS. Buffer: 10 mM $NaHPO_4$, 50 mM NaCl, pH 7.4. (A) Representative SPR curves of -myr MA binding, analyzed using the Langmuir model. (B) Representative SPR curves for +myrMA. Binding to 100% DOPS stBLMs showed significant deviations from a Langmuir isotherm and was analyzed with the Hill model, yielding a Hill coefficient of N $\approx$ 2. For low-affinity isotherms, it was not possible to measure full binding curves due to limitations in available amounts of protein.

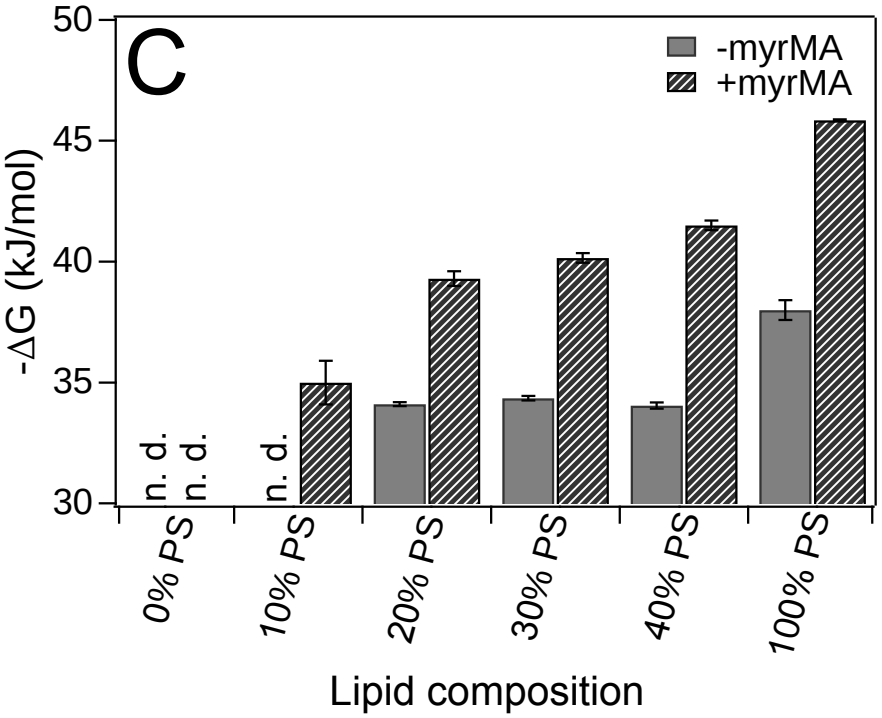

Figure 6.2: Free binding energies ΔG determined from binding isotherms from the data shown in Figure 6.1.

under comparable conditions, representing substantial $\Delta\Delta G$ (ΔG_{+myrMA} - ΔG_{-myrMA}) values that increase with increasing PS content of the bilayer, as shown in Fig. 6.2, where a factor of 10 in K_d accounts for a free energy difference, $\Delta\Delta G \approx 8$ kJ/mol. A summary of these results is compiled in Table 6.1.

The dependence of protein surface density on PS concentration can be rationalized by a simple model based on the probability that MA encounters a certain number of anionic PS molecules when interacting with MA footprint A_f, on the membrane. Assuming that a minimum number of electrostatic contacts is required for stably binding the protein to the membrane and that lipid diffusion is negligible, this probability is proportional to the experimentally observed protein load on the membrane, R_∞. Although oversimplified, this model describes the increase of protein surface density at different PS concentrations in the membrane surprisingly well, Fig. 6.3, predicting that three PS lipids interact directly with each MA in ligating the protein to the surface. The model also predicted that the MA footprint covers $\approx$ 12 lipids in the membrane, in agreement with straightforward calculations based on MA cross section [123] and the area per lipid ($\approx$ 70 Å^2 per molecule). This simplistic model is a first step towards a more robust description of protein loading as a function of lipid concentration and it will replaced in the future by a binding model rooted in thermodynamics.

The results presented in this section show that myristoylation makes a substantial contribution to MA membrane binding, as expected from liposome flotation assays [37]. The strength of our experimental approach - the quantitative assessment of protein affinity to the membrane and protein accumulation at its surface - affords a direct determination of free energy changes (Fig.

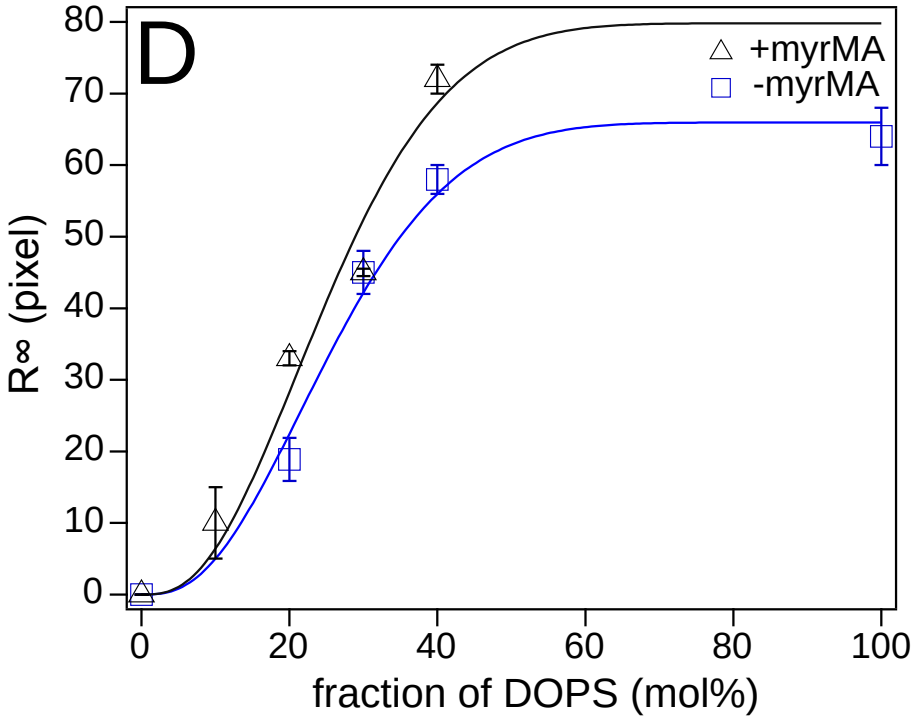

Figure 6.3: Saturation protein surface densities, R_∞. The solid line is a model, indicating saturation of the equilibrium protein load for stBLMs containing more than $\approx$ 40 mol% DOPS. The R_∞ value for +myrMA binding to a 100% DOPS stBLM is excluded from the plot, since it was determined using a different binding model.

6.2) and an estimate of the stoichiometry of interactions (Fig. 6.3). Thereby, the results in Fig. 6.1-6.3 will serve as a backdrop for investigations of membranes of progressively higher complexity.

6.3.2 Cholesterol affects +myrMA targeting to charged membranes

Cholesterol by itself does not engage directly in interactions between Gag and the membrane. Yet, cholesterol has been demonstrated to affect Gag membrane binding strongly [45]. To understand this apparent contradiction, we note that cholesterol influences the physical properties of membranes and their organization [52], most prominently in terms of the formation of cholesterol-enriched membrane domains [101] [135]. These changes are likely to affect Gag binding. To investigate the impact of cholesterol on MA membrane binding quantitatively, various amounts of cholesterol were introduced into DOPC stBLMs with a constant amount of DOPS. The results in Fig. 6.4A show only a small change in affinity of -myrMA in comparison to cholesterol-free stBLMs. For +myrMA, Fig. 6.4B, cholesterol increased the membrane affinity modestly, by a factor of $\approx$ 2.5, when compared to 30 mol% PS-only containing membranes, without significant differences for cholesterol concentrations between 10 mol% and 30 mol%.

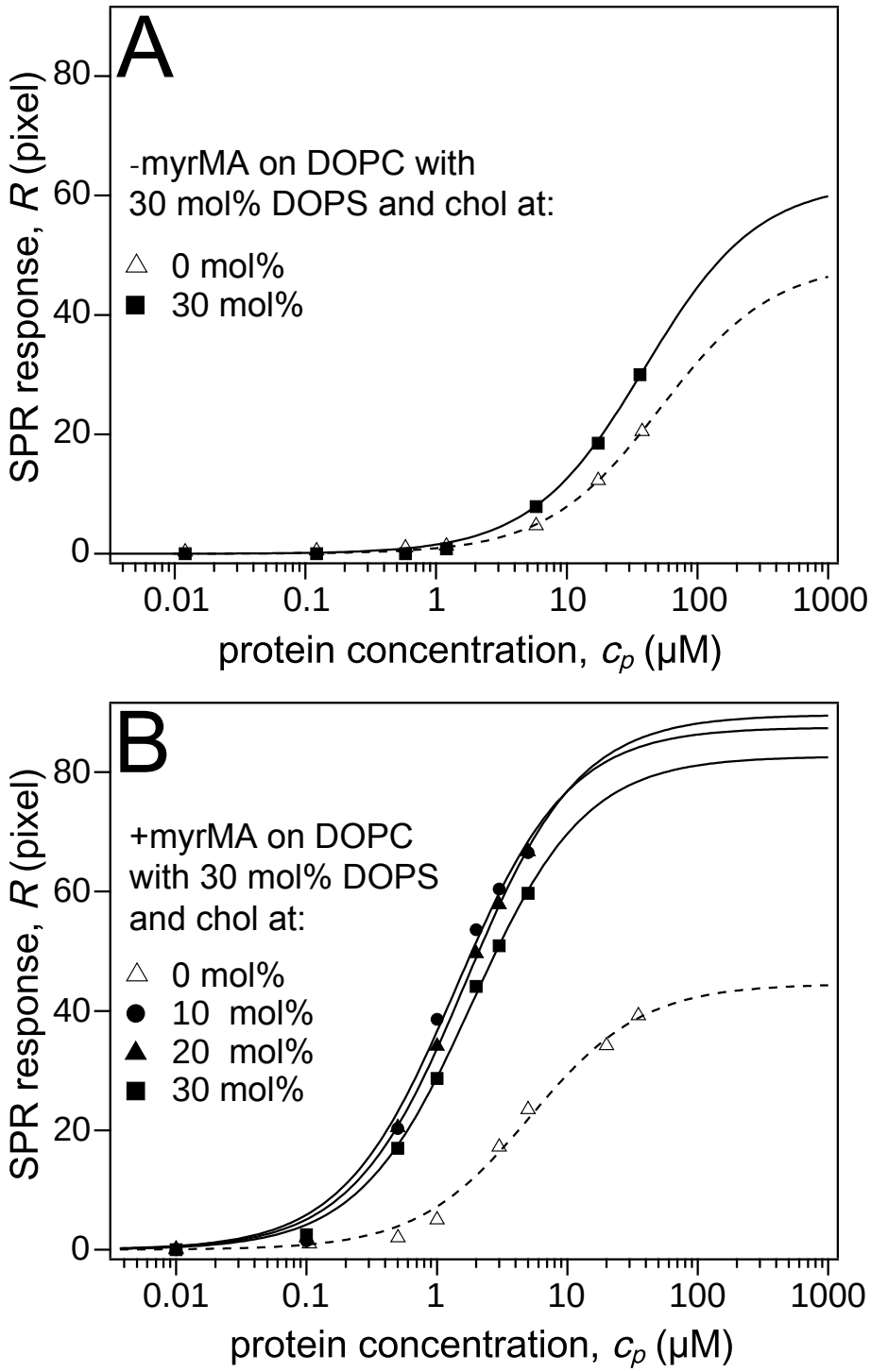

Figure 6.4: Myristoylation enhances MA binding to cholesterol-containing membranes. Cholesterol was incorporated in stBLMs containing DOPC and 30 mol% DOPS, bathed in 50 mM NaCl, 10 mM $NaHPO_4$ pH 7.4. (A) -myrMA adsorption isotherm at 30 mol% cholesterol. (B) +myrMA adsorption isotherms at various cholesterol concentrations between 10 mol% and 30 mol%.

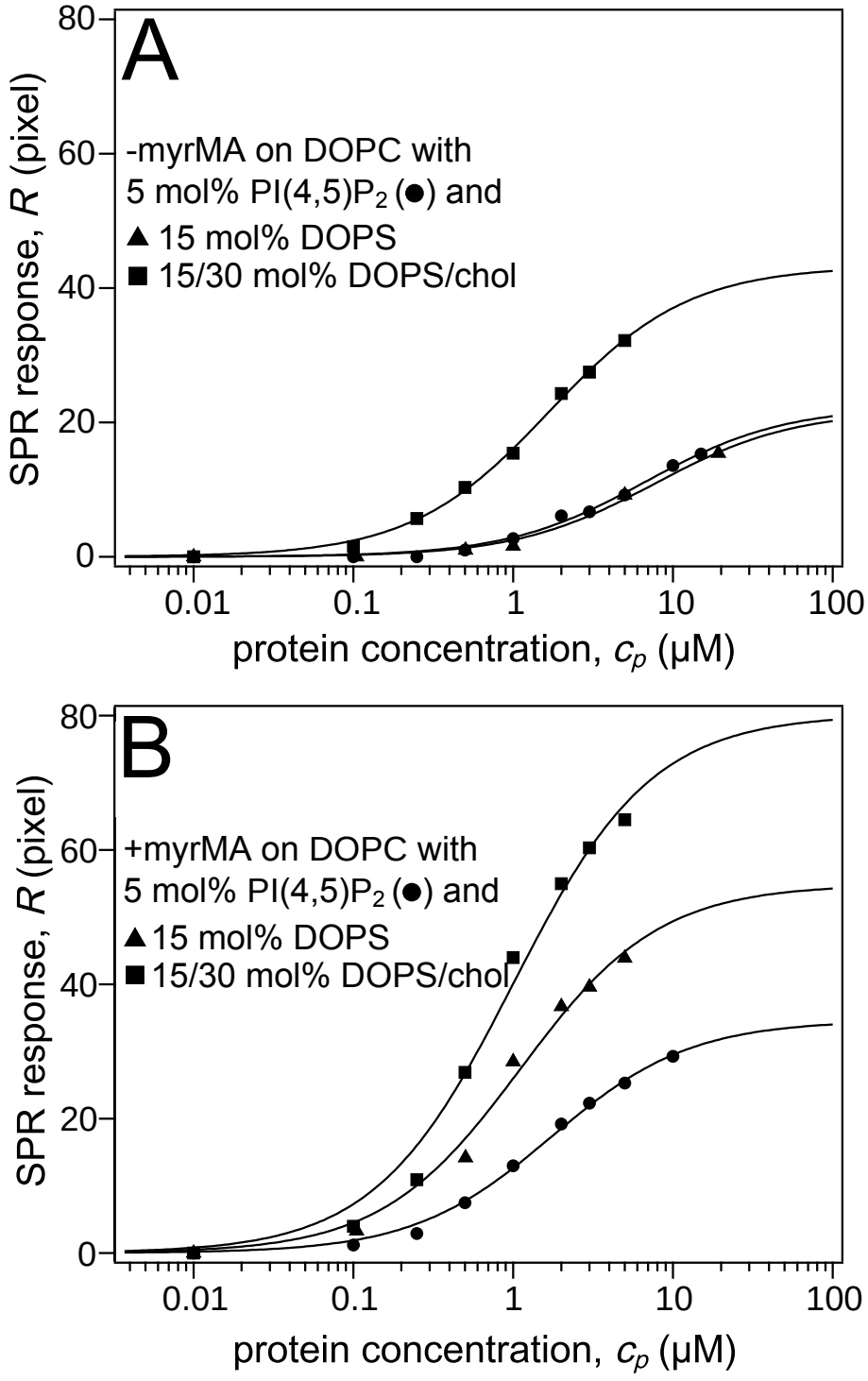

Figure 6.5: Cholesterol enhances MA binding in the presence of PI(4,5)P_2. Exemplary SPR response curves for (A) -myrMA and (B) +myrMA binding to mixed stBLMs containing constant amounts PI(4,5)P_2, bathed in 50 mM NaCl, pH 7.4, in the presence of 15 mol% DOPS and 30 mol% cholesterol

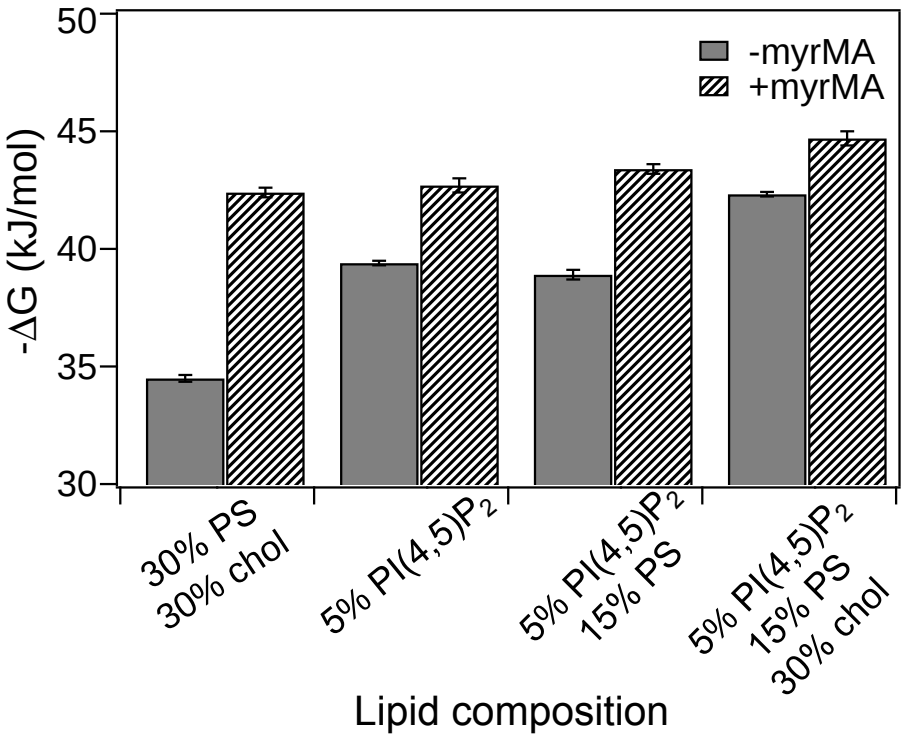

Figure 6.6: Free binding energies of MA to stBLMs derived from the data such as those shown in Figs. 6.7 and 6.8.

The protein load at saturation increased for both proteins, and in particular the membrane load of +myrMA almost doubled due to the presence of cholesterol in DOPC/DOPS membranes. These results show that cholesterol by itself does not contribute to -myrMA affinity for membranes that attract the protein through electrostatic interactions. However, the +myrMA binding to the DOPC/DOPS/chol membrane surface is largely affected when compared to the -myrMA, which suggests that cholesterol facilitates membrane insertion of the myristate.

6.3.3 Cholesterol and PI(4,5)P_2 enhance MA membrane affinity cooperatively

PI(4,5)P_2 is the major lipid signal that distinguishes the mammalian PM from other internal membranes. HIV Gag has a well-defined binding pocket for this phosphatidylinositide in its MA domain [149]. It is therefore generally assumed that PI(4,5)P_2 provides the main signal that directs HIV Gag to the PM as the place of productive assembly. However, quantitative data that characterize the binding of HIV-1 MA to PI(4,5)P_2 are scarce, in particular for +myrMA. We were therefore interested to investigate protein binding to PI(4,5)P_2-containing membranes, specifically in the context of the other membrane components investigated above. Figure 5.5 reports the interaction of MA with membranes that contain PI(4,5)P_2. For DOPC with PI(4,5)P_2 only, the membrane affinity of -myrMA increased almost by a factor of 10 over that observed on a bilayer that contains DOPS at a similar surface charge density. For +myrMA, the increase

was more than a factor of 3. The protein coverage remained about the same in both situations. The addition of PS to a PI(4,5)P_2-containing membrane had no effect on -myrMA membrane binding (Fig. 6.5 A) and resulted only in a moderate increase of the protein load, but not affinity, for +myrMA (Fig. 6.5 B). On the other hand, adding cholesterol makes a substantial difference in protein binding to membranes that contain both DOPS and PI(4,5)P_2. Membrane affinities increased moderately by factors of ≈ 4 and ≈ 2, for -myrMA and +myrMA, respectively, but the impact on the protein load was pronounced. Figure 6.6 summarizes the results on MA membrane binding to cholesterol and PI(4,5)P_2 containing membranes in terms of free binding energies, ΔG.

The results reported in this section for PI(4,5)P_2-containing membranes and membranes that contain both the phosphatidylinositide and cholesterol show convincingly that there is a pronounced synergy between the two membrane components. Neither PI(4,5)P_2 nor cholesterol by themselves increase HIV MA membrane binding notably, but in combination, they boost both binding affinity, i.e., free energy gained from binding, and protein accumulation at the surface. The aggregate of results reported in Fig. 6.2 and 6.6 and Table 6.1 show that the difference in ΔG for membrane binding of +myrMA between the fully complex bilayer that contains DOPC, DOPS, PI(4,5)P_2 and cholesterol and the simple binary DOPC/DOPS bilayer that contains charged lipid in physiological concentration ($\approx 10\%$) is about 10 kJ/mol or about 10% the strength of a covalent bond. Neither of the physical interactions measured separately comes close to this result by itself, and cholesterol is apparently required to merge the individual contributions into an aggregate interaction that shows the high binding avidity that we measure for the complex membrane.

6.3.4 +myrMA binds preferentially to PS-containing membranes as compared to PI-containing membranes

Phosphatidylinositol (PI) is the second most frequent acidic component of the inner PM after PS and, in contrast to PS, is underrepresented in the viral shell where it only appears in trace amounts [3]. However, because PI has the same charge effective as PS, it provides a control to determine whether the modest enrichment of PS in the viral shell, reported in [12], is entirely of electrostatic origin. If that were true, one would expect that binding of MA to PI-containing membranes is significantly reduced from that observed for PS-containing membranes. The results of such measurements (Fig. 6.7) show that the affinity of +myrMA to PI-containing stBLMs was lower, by $\approx 50\%$, than that observed for DOPC/DOPS membranes of equivalent composition, and the protein load was only marginally reduced. For stBLMs that contained PI(4,5)P_2 in addition to PI, we observed a larger reduction in protein load after substituting PS with PI, but the membrane affinity of the protein was also only moderately reduced. The results of this control measurement show that electrostatic interactions of the MA protein are similar with PS and PI, thus suggesting that differential mixing of the lipids into the domain structure within the biological membrane, rather than differing physical interactions, are responsible for their distinct enrichment characteristics in the assembled viral protein/membrane shell.

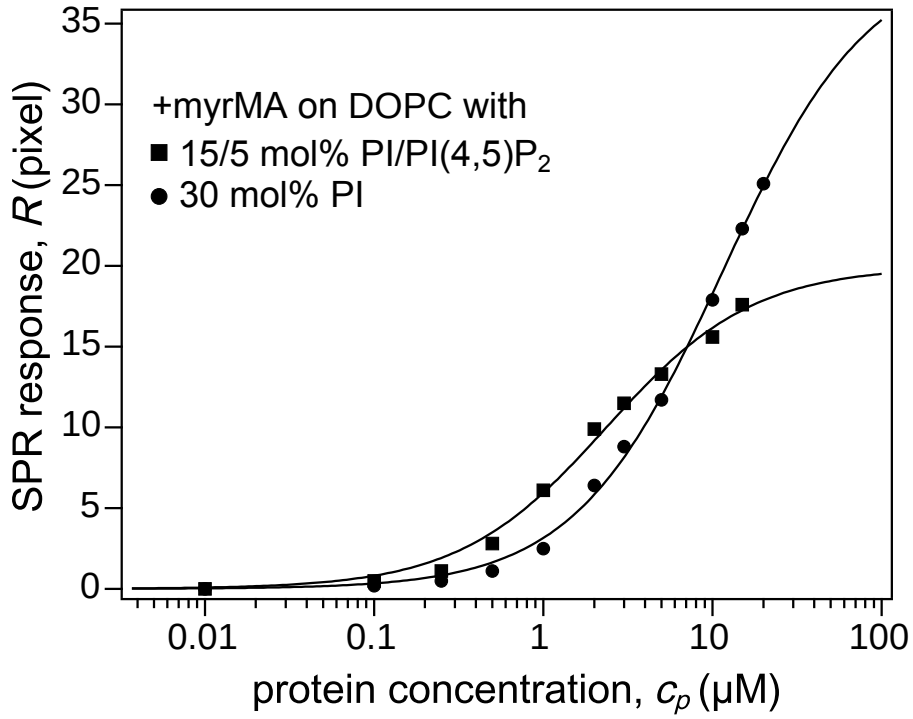

Figure 6.7: Myristoylated MA favors interaction with PS-containing membranes over that with PI-containing membranes. SPR binding curves of +myrMA to stBLMs containing DOPC and PI with or without $PI(4,5)P_2$ at equivalent surface charge densities of the membranes bathed in 50 mM NaCl, pH 7.4.

6.4 Discussion

The HIV-1 matrix protein is the domain of the Gag polyprotein which interacts with the membrane envelope of the proteinaceous capsid lattice in the assembled, immature virus particle. Since this membrane envelope is acquired from the plasma membrane of the host cell during budding, it contains lipids and proteins found in the PM [25] [98]. In this context, it is well known that specific lipids, in particular cholesterol, phosphatidylserine and sphingomyelin, are enriched in the viral membrane envelope while PC and PI are under-represented [21], resulting in the unique composition of the viral lipidome [3] [12] [21]. While the Gag nucleocapsid (NC) domain can compete with MA for association with the acidic surface of the inner PM, thus ligating Gag to the membrane surface in a U-shaped conformation [85], it dissociates from the lipid upon exposure to nucleic acid [38]. The membrane-bound polyprotein thus assumes an extended conformation on the bilayer surface that promotes lateral interactions between the capsid domains, leading to the formation of the two-dimensional protein lattice that defines the immature capsid [59] [167]. A decisive step in this supramolecular self-assembly process that is determined by the atomistic details of the protein/membrane interface of the viral shell is thus the interaction of MA with the inner PM surface. The myristate is essential for targeting Gag to the plasma membrane in vivo [13] [63] [128] [146], as mutation of the N-terminal glycine completely blocks budding and membrane localization of Gag. Myristoylation also plays a crucial role on the assembly of infectious virus particles [193], as there is no assembly observed in

Table 6.1: Best-fit parameters obtained from the Langmuir model for data shown in Figs. 6.1, 6.4, 6.5 and 6.7

	-myrMA		+myrMA	
membrane composition	$K_d(\mu M)$	R_∞ (pixels)	$K_d(\mu M)$	R_∞ (pixels)
100% DOPC	n.d	n.d.	n.d.	n.d.
DOPC:DOPS 90:10	n.d.	n.d.	40 ± 15	10 ± 5
DOPC:DOPS 80:20	57 ± 2	18.9 ± 0.8	7.0 ± 0.9	33 ± 1
DOPC:DOPS 70:30	52 ± 2	45 ± 3	5.0 ± 0.4	45.0 ± 0.5
DOPC:DOPS 60:40	59 ± 3	58 ± 2	2.9 ± 0.2	72 ± 2
100%DOPS	12 ± 2	64 ± 4	0.5 ± 0.1	54 ± 1
DOPC:DOPS:chol 40:30:30	48 ± 3	68 ± 1	2.1 ± 0.1	83.7 ± 0.6
DOPC:PI(4,5)P2 95:05	6.7 ± 0.4	22.3 ± 0.7	1.8 ± 0.2	34.8 ± 0.3
DOPC:DOPS:PI(4,5)P2 85:15:05	8.2 ± 0.7	25.9 ± 0.7	1.4 ± 0.1	40.2 ± 0.7
DOPC:DOPS:PI(4,5)P2:chol 50:15:5:30	2.1 ± 0.1	43.6 ± 0.7	0.8 ± 0.1	80 ± 5
DOPC:PI 70:30	n.d.	n.d.	11.5 ± 0.9	39 ± 1
DOPC:PI:PI(4,5)P2 85:15:05	n.d.	n.d.	2.4 ± 0.2	20 ± 1

the cytoplasm in vivo at otherwise productive levels of Gag that lack the myristate [128].

Roles of membrane charge and protein lipidation. Binding of -myrMA to PS-containing membranes is enabled by electrostatic interactions between the charges on the protein and the anionic membrane [128]. A cationic patch on the surface of MA formed by Arg-4, Lys-26, Lys-27, Lys-30, Lys-32, and Arg-39 was shown by neutron reflection to dive into the surface of the anionic bilayer at a distance where it can directly interact with membrane headgroups [78]. Protein myristoylation adds an additional hydrophobic component to the interaction, as the myristate can insert into the hydrocarbon core of the membrane. However, the myristate increases MA membrane association in the absence of either cholesterol or PI(4,5)P_2 from the membrane. On pure PC/PS bilayers, MA affinity differs by a factor of ≈ 10. ($\Delta\Delta G \approx 6$ kJ/mol) between the myristoylated and non-myristoylated proteins, in qualitatively agreement with vesicle flotation assays [36]. Distinct from the flotation assays, our SPR results determined dissociation constants that are two orders of magnitude lower ($K_d \approx 5$ μM and ≈ 50 μM, respectively, for +myrMA and myrMA), consistent with the tendency of floatation assays to underestimate the affinities of protein to liposomes [64].

The observed gain in free binding energy, $\Delta\Delta G \approx 6$ kJ/mol, of +myrMA over myrMA is much smaller than that expected from inserting individual myristoyl chains from solution into a lipid membrane, estimated to yield ≈ 48 kJ/mol. Several effects could reduce the free binding energy: (1) Transfer of the myristoyl from its hydrophobic sequestration within the dissolved protein into the bilayer is likely associated with a lower enthalpy change than transfer of a free fatty acid from aqueous solution. (2) Not the entire myristoyl group may insert, as it has been previously proposed in a different molecular context. (3) A myristoyl membrane anchor further reduces the bound proteins entropy compared to the non-lipidated species, as recently shown for the membrane-bound, myristoylated GRASP domain.

While the gain in binding energy conferred by the myristate on PI(4,5)P_2-free membranes may be smaller than expected, our results show clearly that MA interaction with PI(4,5)P_2 is not a requirement to trigger myristate exposure at the PM, as previously concluded [149]. Indeed, they agree with recent NMR studies which suggested that the myristate is readily exposed on MA bound to bicelles or micelles that lack PI(4,5)P_2 [178]. We also observe that the gain in free binding energy of -myrMA depends only weakly on the PS content (20-40 mol%) of the membrane while it increases systematically for +myrMA.

Role of PI(4,5)P_2. Although the interaction between MA and PI(4,5)P_2 has already been investigated by a variety of biophysical techniques, quantitative binding data of the protein to this lipid signal in the context of bilayer membranes are still scarce [179] and data measured out of the membrane context tend to underestimate affinities. For example, solution NMR studies reported a dissociation constant of $K_d \approx 150$ μM for myristoylated HIV-1 MA with soluble and 4 carbons acyl chain PI(4,5)P_2, di-C4-PI(4,5)P_2, and a slightly higher affinity to di-C8-PI(4,5)P_2 [149]. A recent SPR investigation in which tetra-phosphorylated inositol, IP4, was immobilized on the sensor chip and competitive binding with pre-equilibrated MA/di-C8-PI(4,5)P_2 was determined, reported a dissociation constant of +myrMA to dissolved di-C8-PI(4,5)P_2 of $K_d \approx 5$ μM [5]. These earlier results, all performed without a membrane, are thereby lower than the SPR results reported here by factors of 100, which suggests that the membrane context is essential for obtaining thermodynamic data.

The addition of 5 mol% PI(4,5)P_2 to DOPC stBLMs resulted in binding affinities of -myrMA and +myrMA larger than those to DOPC with 30 mol% DOPS (Table 6.1). Assuming an effective charge between -3*e* and -4*e* for PI(4,5)P_2 at physiological pH [116], the charge density of a membrane surface containing 5 mol% PI(4,5)P_2 is lower than that brought about by 30 mol% DOPS, showing that PI(4,5)P_2 binding to MA invokes a mechanism that goes beyond electrostatic interaction. This is not surprising, as it is well established that MA binds to dissolved short-chain PI(4,5)P_2 in a specific manner (56). For both -myrMA and +myrMA, the protein load at saturation on stBLMs that contain 5 mol% PI(4,5)P_2 equals that on 20 mol% DOPS. When MA binds to a membrane that contains 20 mol% DOPS, on average ≈ 2.4 DOPS lipids are within the protein footprint on the bilayer, as the footprint area is about $12\times$ the area of a lipid molecule, which is in the range of 68-73 $\mathring{A}^2$ for monounsaturated lipids [94]. From the quantification of the protein load on the bilayers it then follows that the average number of PI(4,5)P_2 molecules bound per MA in the 5 mol% PI(4,5)P_2 stBLM does not exceed two.

When increasing the complexity of the membrane from a binary DOPC/DOPS bilayer to a DOPC/DOPS/ PI(4,5)P_2 system, no significant affinity changes for -myrMA and +myrMA in comparison to 5 mol% PI(4,5)P_2 was observed (Table 6.1). The protein load at saturation, R_∞, remained constant for -myrMA and increased for +myrMA. An interpretation remains difficult due to the lack of a comprehensive PC/PS/PI(4,5)P_2 phase diagram. However, we point out that both -myrMA and +myrMA SPR isotherms on 15 mol% DOPS + 5 mol% PI(4,5)P_2 in DOPC are simple additions of the individual SPR curves on 15 mol% DOPS and 5 mol% PI(4,5)P_2 in the DOPC background. If nothing else, this argues for a lack of cooperative effects between DOPS and PI(4,5)P_2 binding, and it is interesting to speculate that this results from a lack of mixing of PI(4,5)P_2 and DOPS on the length scale of the footprint of the MA protein on the bilayer. Our comparative measurements of +myrMA adsorption to bilayers that contained PI instead of PS

with or without PI(4,5)P_2 did not reveal any major differences. This would suggest that PS and PI should be similarly enriched in the viral shell if electrostatic attraction contributes to lipidomic selection. The fact that PS is moderately over-represented while PI is underrepresented in the viral shell [3] [21], however, suggests that PS preferentially incorporates into cholesterol-rich domains that are enriched in PI(4,5)P_2, while PI does not.

Role of cholesterol. There is no known physical mechanism that promotes direct interactions between membrane-associated Gag and cholesterol. Moreover, neutron reflection studies of HIV Gag on phospholipid membranes showed that the protein associates with the bilayer only peripherally, interacting with the phospholipid headgroups but not the hydrophobic membrane core [123]. Yet, it was also shown that Gag interaction with bilayers is sensitive to the composition of the interior of the bilayer, and in particular to the presence of cholesterol [45]. In the results presented here, the largest differences between +myrMA and -myrMA binding affinities were observed on bilayers that contain PS and cholesterol (left-hand bars in Fig. 6.6). These arise because the affinity of myrMA on DOPC/DOPS stBLMs is insensitive to cholesterol whereas the affinity of +myrMA increases significantly in the presence of cholesterol. For both MA proteins, we also observed a significant increase in the protein load at saturation, by $\approx 50\%$ for -myrMA and by almost 100% for +myrMA. This shows that the binding of both the myristoylated and unmyristoylated proteins to PS-containing membranes is affected by cholesterol, despite the lack of an affinity change for -myrMA, and points to the hydrocarbon region of the lipid bilayer as the origin of these effects. It is well established that cholesterol condenses fluid bilayers by changing lipid packing [42] [76] [136]. However, the observed increases in protein density at the membrane are much larger than the cholesterol-induced increase in lipid density. Therefore, different mechanisms must contribute to rationalize the observed results.

The cholesterol-driven increase in binding affinity of +myr MA could be aided by a compatibility effect that may help the myristate insert in the hydrophobic membrane core composed of unsaturated oleoyl chains in the stBLMs under study. The sterol backbone of cholesterol is asymmetrically substituted with methyls that emerge on one face of the ring system, denoted α, rendering this face rough on the atomistic scale, whereas the β-face, which lacks such substitutions, is smooth [137]. MD simulations suggested a substantial impact of this asymmetry on the binding of cholesterol to saturated (α-face) and unsaturated (β-face) lipid chain [137] and the orientation of the sterol backbone within the bilayer [142]. In the light of these results, we speculate that cholesterol is essential to mediate insertion of the saturated myristate into the unsaturated DOPC matrix of the bilayer core. Of course, biological membranes do not consist of pure lipid species, but rather of complex mixtures of lipidic components that may segregate locally into distinct domains, driven by a tendency of cholesterol to associate preferentially with saturated chains [161]. Our results show that the myristoylated MA protein has a predilection to associate with cholesterol-rich membrane regions, and it is likely to help recruit such patches into the viral membrane shell. It has been shown that myristate substitution with an unsaturated analogue blocks Gag association with detergent-resistant membranes [100], suggesting that the myristate is a key driver for Gag association with lipid rafts. Our results are consistent with this conclusion and explain in vivo results which showed that redistribution of cholesterol from the PM to late endosomes causes relocation of assembly [100] and that cholesterol depletion disrupts Gag binding to membrane rafts [131] [129].

Although cholesterol does not affect the affinity of -myrMA binding to DOPC/DOPS stBLMs, it does increase the affinity significantly to membranes that contain DOPC, DOPS and PI(4,5)P_2. For PI(4,5)P_2-free membranes in particular, this increase is even larger for -myrMA than for +myrMA (Table 6.1). In experimental studies of its effects on lipid packing, cholesterol has been shown to increase the average headgroup-to-headgroup distance for DOPC-containing membranes [136]. It is therefore reasonable to assume that MA has better access to the PI(4,5)P_2 headgroup in the presence of cholesterol. Moreover, recent MD simulations suggested that MA may induce lateral segregation of PI(4,5)P_2 into domains [24]. On the other hand, it was experimentally shown that cholesterol helps stabilize PI(4,5)P_2 lipid clusters [45] [83], which rationalizes the cooperativity of cholesterol and PI(4,5)P_2 in attracting MA to the membrane, as observed in our data. Our results are also consistent with the finding that PI(4,5)P_2 is enriched in the viral envelope in comparison to host cell membranes [21] and compatible with the idea that Gag triggers the formation of PI(4,5)P_2-enriched domains instead of associating with preexisting microdomains [74] [88]. Thereby, a coherent understanding of the roles of molecular interactions emerges that is consistent with the hypothesis that Gag membrane binding depends on cholesterol-rich lipid rafts and triggers local enrichment of its preferential interaction partners, most notably PI(4,5)P_2, in its membrane-protein shell.

6.5 Conclusions

The quantitative binding measurements reported here provide a consolidated picture of how MA interacts with various major components of the PM and the role of its N-terminal lipidation in the overall process. Our comparative study of -myrMA and +myrMA association with well-defined membrane models of progressively higher compositional complexity shows that the various membrane components act synergistically in their interaction with the MA protein, which may explain their selective recruitment into the viral membrane shell. We found that myristoylation affects MA membrane association only modestly in the absence of either cholesterol or PI(4,5)P_2 from the membrane. On pure PC/PS bilayers, MA affinity differs by a factor of 10 between the myristoylated and unmyristoylated protein: $K_d \approx 5$ μM vs. ≈ 50 μM. In its trend, this result is in agreement with vesicle flotation assays [36]. However, our measurements with SPR on stBLMs quantify the affinity with a half-point concentration that is two orders of magnitude lower than those observed with flotation assays [36] [37] [65]. The observation that myristoylated MA binds substantially better to PI(4,5)P_2-free bilayers than myrMA implies further that PI(4,5)P_2 in not required for triggering myristate exposure, as previously concluded [149].

We then observed that cholesterol facilitates the interaction of the myristate with the target membrane and of PI(4,5)P_2 with the protein. Electrostatic attraction and hydrophobic interaction suffice to stably anchor MA at the membrane. While electrostatic interactions alone only lead to weak binding of myrMA, even at low ionic strength (50 mM NaCl), myristoylation increases protein affinity to the bilayer, and both cholesterol and PI(4,5)P_2 augment MA membrane binding significantly. It thus appears that cholesterol promotes access of the protein to the membrane. In the absence of PI(4,5)P_2, cholesterol increases protein affinity to membranes only for the myristoylated protein, consistent with its role to compatibilize saturated and unsaturated membrane components, as shown in MD simulations [24]. In combination, cholesterol and PI(4,5)P_2 in-

crease membrane binding of -myrMA and +myrMA to a similar extent, which indicates that cholesterol particularly facilitates MA access to the phosphatidylinositol headgroup and casts doubts on the proposed chain-swapping mechanism in which a PI(4,5)P_2 acyl chain has been suggested to replace sequestered myristate within the protein upon binding [149]. Overall, the molecular level details reported here provide a better understanding of the lipid interactions of MA and their implications for proper Gag membrane association, lipid recruitment to the viral shell and viral particle assembly.

Chapter 7

pH Dependent Membrane Reorganization Induced upon HIV-1 MA Binding

7.1 Background

Besides establishing the factors that control the association of MA with membranes, another aim of this study is to determine how the membrane lipid composition and myristoylation would impact the orientation of +mryMA membrane bound structure and compare to -myrMA [123]. The results for the non-lipidated construct show that even in the absence of lipid-specific (no PI(4,5)P_2 contained in the stBLM) and hydrophobic (no myristate on the protein) interactions, MA binds in an orientation suitable for downstream assembly of the viral particle, i.e. with its C-terminal end oriented away from the membrane. Electrostatic steering, albeit weak, pre-dispose MA for subsequent anchoring to the membrane via specific binding to PI(4,5)P_2 and myristate insertion.

Neutron reflectometry experiments were performed to probe the impact of the myristoyl and lipid components on MA orientation. The SPR experiments optimized the experimental conditions for the neutron measurements. +myrMA structure on a DOPC:DOPS 70:30 stBLM was first characterized aiming to identify the effect of the myristate group on MA orientation. Neutron reflectometry is extremely sensitive on the normal direction of plane of the bilayer being able to capture the depth profile of the protein layers. As a result of the +myrMA NR experiments, instead of having the size of a monolayer of MA of $\sim$ 50 Å, the protein profile extended over 200 Åaway from the membrane, as shown in Figure 7.1. Various other lipid compositions were tested as well as different protein concentrations to verify whether the overlayer formation was particular to a lipid composition, or concentration dependent. The analysis of all NR measurements revealed extra density of material at the membrane interface. Protein may aggregate at the membrane or membrane undergoes reconstruction upon protein binding.

Even though a good fit (χ^2 =1.56) was obtained using the traditional spline fit, it failed to obtain a structural model in agreement with both, the H_2O and the D_2O data. The protein layer was fit using a nSLD(z) in which the scattering length density is allowed to vary along the normal direction of the membrane surface [189]. For the nSLD(z) spline model, the CVO profile as well as the nSLD profile varies along z, as described in Chapter 3. The nSLD(z) spline was set up to

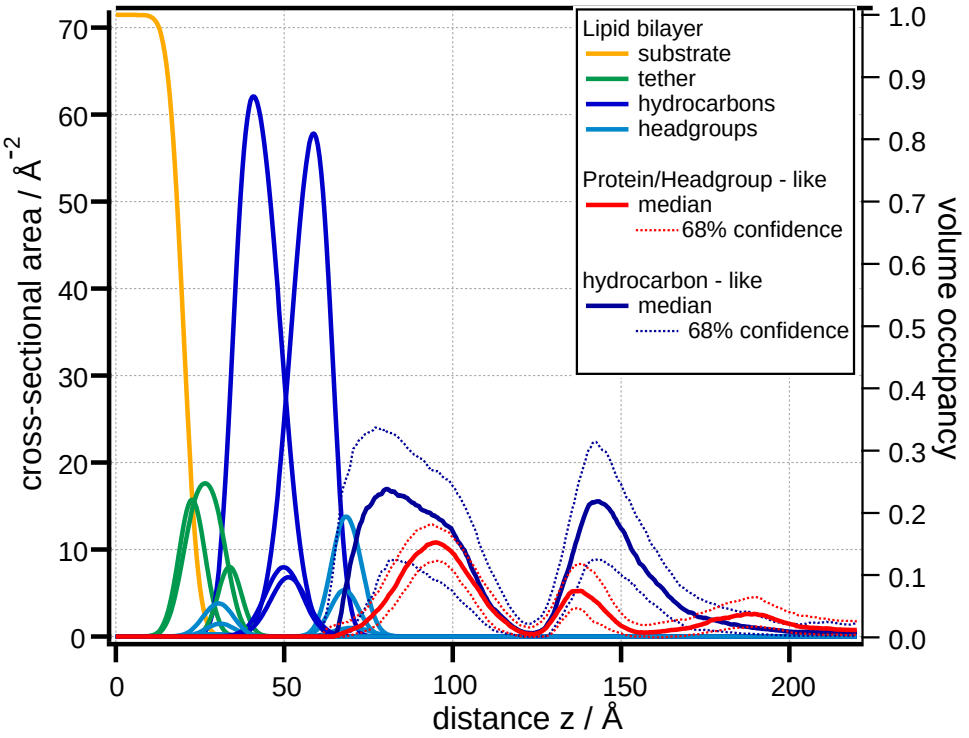

Figure 7.1: NR profile of +myrMA at pH 7.4 shows the presence of overlayers. Simplified molecular distributions for each organic interface layer of the DOPC/DOPS stBLM and +myrMA obtained from the best fit of reflectivity data to the spline fit model. The median protein envelope is shown with its associated 68% confidence intervals (red). Volume occupancy is indicated on the right axis. For comparison, median protein envelope of the hydrocarbon-like material (blue) is also shown.

contain protein and a second unknown molecule to determine the composition of the overlayers. EDTA and glycerol were set as possible molecules contributing to the overlayer profile but no good fit was achieved. An excellent fit was obtained when the SLD of hydrocarbon material was used (See Figure 7.1). Briefly, the profile is decomposed into two envelopes: one containing protein distribution alone (red) and a hydrocarbon-like one (blue). The extra density may be interpreted as a result of protein-lipid complex formation, suggesting that +myrMA, once bound to the membrane, disturbs the lipid organization. Having a lipid-like contribution to the overlayer profile suggests membrane remodeling upon +myrMA interaction, a scenario further investigated by electron microscopy.

To define the next steps in the progress of structural charcaterization of +myrMA by neutron reflection, experimental conditions that would allow the maintainance of planar bilayers required for the NR experiments were carefully investigated. As a first step, a detailed analysis of the SPR experiments was carried out. For example, the protein surface density, R_∞, see Table 7.1 for the parameters, hinted for excessive amount of protein at the membrane. At specific membrane compositions the values obtained for protein coverage were not consistent with the values expected for a monolayer of protein. A monolayer of protein covering 100% of the surface would be equivalent to 60 pixels, assuming +myrMA maximum cross section to be the same as of -myrMA at an specific orientation, A_{CS} = 756 Å [123]. Clearly membranes containing high

content of anionic lipids or cholesterol had $R_\infty > 60$. Those results may reflect two different scenarios: 1) +myrMA indeed aggregates at the interface inducing membrane reconstruction 2) +myrMA packs more efficiently, possibly as trimers, in the presence of cholesterol and higher contents of PS which allows more protein to adsorb at the interface.

Based on the SPR studies, NR experimental conditions were adapted to address the aggregation issue. Since surface charge density may contribute to the aggregates formation, charge density was reduced. That did not lead to the removal of the extra density of material accumulated at the interface (data not shown). Even when the R_∞ values were consistent with a monolayer of MA, NR showed that the overlayers still occurred. Therefore R_∞ is not a good indicator of extra density material at the membrane. In the NR experiments, small protein concentrations were used, without success, as an attempt to prevent the overlayers. Shorter time protein incubations ($\sim$ 30 min instead of 6h) followed by a rinse resulted in low protein coverage undetectable by NR resolution. Those studies suggested that the origin of the overlayers was not associated with lipid composition, surface charge density or protein concentration.

Another possible origin of the extra material at the membrane interface could be related to protein oligomerization, impurities or protein modification. The protein sample was carefully investigated, starting with its purification process. Protein purification involves many steps but as sample yield needs to be high, the number of columns was minimized. Affinity column and size exclusion column were used to purify +myrMA without compromising protein quality. After purification +myrMA was characterized by mass spectrometry for weight and presence of other species. Only single specie with molecular weight equivalent to +myrMA (MW15745 Da) was detected. Dynamic light scattering was used to investigate the propensity of +myrMA to form aggregates in solution. +myrMA was monitored over time ($\sim$ 7h) and as a function of concentration ($c_p \sim 20$ μM). The size distribution for small molecules obtained by DLS is not precise and rather provides a qualitative assessment for the presence of higher order oligomeric structures. +myrMA was stable as a homogeneous distribution of particles with size $\sim$2 nm, consistent with the monomer size, suggesting the overlayers detected by NR were triggered by protein exposure to the lipid membrane.

Membrane reconstruction does not invalidate the SPR results obtained in Chapter 6. The SPR and neutron experiments are measured in different times scales, few hours vs days. Besides that, aggregation at the interface has a typical behavior at the SPR, the signal increases linearly over time and does not reach equilibration. Therefore, any indication of aggregation would be evident from SPR titration curves. Under the experimental conditions and time course of the SPR experiments presented in Chapter 6, aggregates contributions to th SPR signal were none or minimal.

7.2 Evidence for membrane remodeling

7.2.1 +myrMA binding correlates with membrane impairment

EIS was used to assess lipid bilayer quality in response to +myrMA binding. Figure 7.2 shows the Cole-Cole plots of a DOPC:DOPS 70:30 stBLM before (R_{def} = 50 $k\Omega cm^2$) and after +myrMA incubation (R_{def} = 5 $k\Omega cm^2$). Moderate changes in the bilayer resistance and capacitance are

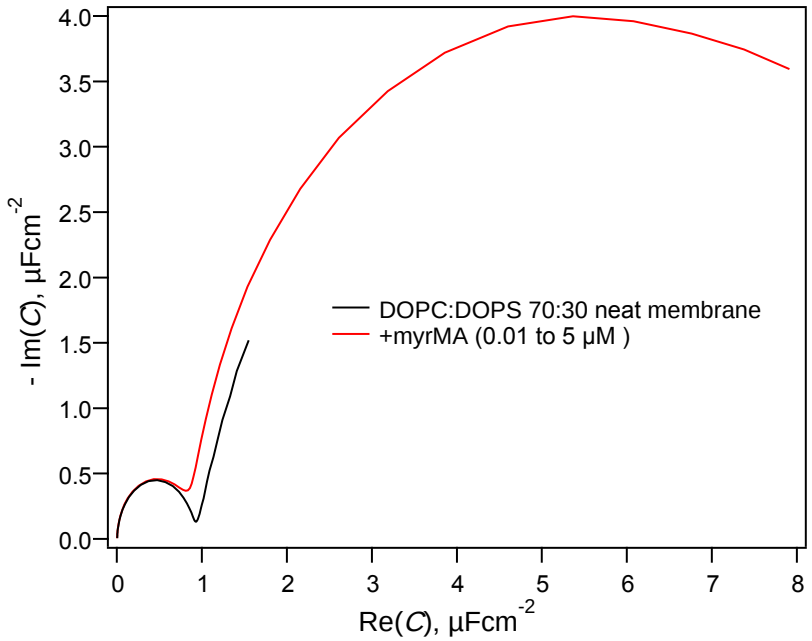

Figure 7.2: Membrane undergoes reconstruction upon +myrMA interaction. Cole-Cole plot of DOPC:DOPS 70:30 stBLM on HC18:βME 30:70 as prepared (black) and after +myrMA concentration series ranging from 0.01 to 5 μM (red). Tail length is proportional to defect-density. Upon protein interaction with the membrane, the bilayer capacitance resembled a SAM spectrum. Its resistance decreased to values below the quality standards adopted for defect-free stBLMs ($R_{def} << 100$ kΩcm^2). Other protein incubation experiments on membrane of different lipid compositions showed similar disturbances of the bilayer membrane.

evident and were observed for all lipid compositions investigated by SPR. The effect of +myrMA on the bilayer electrical parameters can be interpreted as impairment of the lipid bilayer or increase in defect-rich density regions. Previous studies have proposed that packing defects in the membrane promote further protein-membrane interactions by providing additional binding sites to the protein [160] [66]. In fact, +myrMA binds with high affinity to hydrophobic substrates and is thus associate to stBLM defects that have the hydrophobic tether exposed.

Furthermore, after SPR binding assays +myrMA does not completely dissociate from the interface after rinsing (data not shown). Virtually every SPR experiment shows some fraction of irreversibly associated protein. In Chapter 6, it was shown that the myristoyl enhances MA affinity to the lipid membrane which may result in further anchoring of MA into the lipid bilayer, which may result in much slower off-rates, hours instead of minutes. That could explain why incomplete dissociation is observed for +myrMA in the time frame of the measurements.

7.2.2 Membrane remodeling observed on DOPS vesicles

Electron microscopy (EM) was employed to visualize vesicle morphology reconstruction upon the addition of +myrMA. NR suggested that +myrMA binding was responsible for structural changes at the lipid membrane. EM was used to assess membrane remodeling as a response

to +myrMA binding. The EM measurements were performed by Zhiping Jiang at the National Institute of Health (NIH). As a control, micrographs of 100% DOPS vesicles were taken in the absence of +myrMA, see Figure 7.3 A,C. As +myrMA is added to the 100% DOPS vesicles, deformation and mild tubulation occur, see Figure 7.3B). As a control, images of only +myrMA were taken 7.3D, small aggregates were identified. No vesicle remodeling was apparent for +myrMA and POPC:POPS 70:30 suspension few minutes after being mixed as shown in Figure 7.3E. After incubating overnight, Figure 7.3F, another set of images were taken mimicking the incubation time at neutron measurements. Even though no signs of membrane remodeling were detected, huge protein aggregates were found in the vicinity of the liposomes. Aggregates were much more discernible than the ones observed for protein only. Furthermore, pure POPC vesicles when exposed to +myrMA did not show any signs of remodeling or protein aggregation at the interface (data not shown), strongly suggesting the membrane remodeling has an electrostatic origin.

7.3 Targeting the origin of membrane reshaping

In order to track the origin of membrane remodeling a systematic study of the experimental conditions was performed, see section 7.2 for details, which included careful purification of myristoylated protein (passing through multiple columns), detailed inspection of protein purity and optimization of a set of experimental parameters, none of which reverted the effects of +myrMA binding onto the lipid membranes. Minimization of membrane reconstruction may facilitate the structural characterization of +myrMA at lipid membrane interfaces by NR.

7.3.1 Ionic strength effect

The presence of extra density at the stBLM interface detected by NR had its lipid nature revealed by refined modeling of the NR data and was confirmed experimentally by EM images which also suggested membrane remodeling was charge induced. Ionic strength of the buffers was raised in order to screen interactions of electrostatic origin and thus avoid membrane reorganization. Increasing the ionic strength from 50 mM NaCl to 100 mM NaCl had an impact on the dissociation equilibrium constant as expected due to screening effects. For membranes containing PS-only, affinity was 8 times lower (K_d = 35 μM for 30 mol% PS , K_d = 16 μM for 40 mol% PS) and almost 2 times lower for PI(4,5)P_2 containing membranes (K_d = 3 μM). However, high ionic strengths hardly affected the protein surface density, see Table 7.1. NR experiments need to be done at high salts to verify whether the extra layers of materials would still be present. This information cannot be implied from the protein surface coverage values obtained from the SPR measurements.

7.3.2 pH effect

While in solution, myristate exposure is modulated by pH [55], resulting in oligomer formation upon exposure or sequestration of the myristate group, see Section 5.2.1 for more detailed discussion.

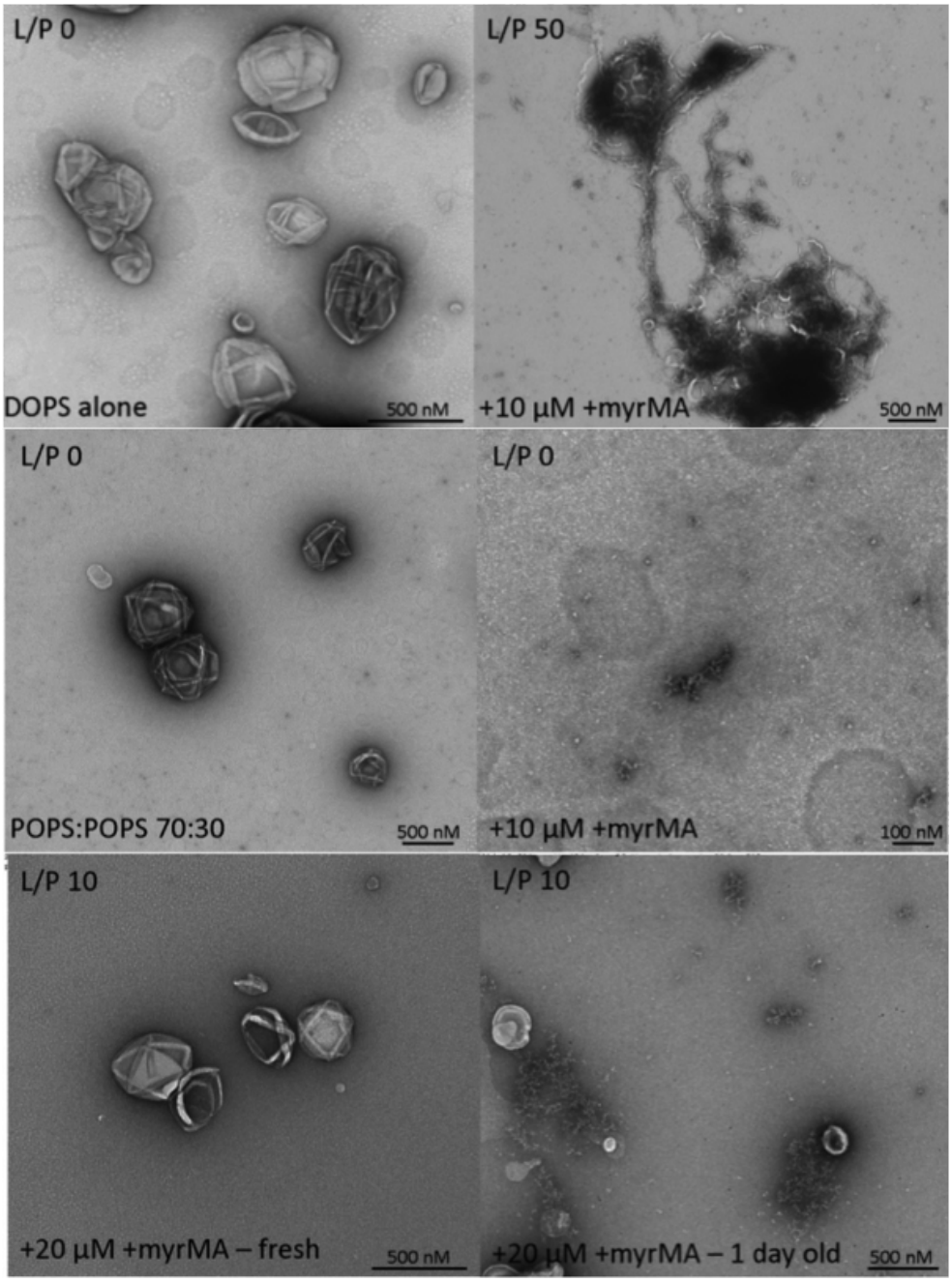

Figure 7.3: Electron microscopy images of PS containing vesicles remodeled by +myrMA at pH 7.4. (A) DOPS vesicles ([DOPS] = 0.5 mM), upon the addition of (B) 10M +myrMA. (C) POPC:POPS 70:30 vesicles ([POPS] = 0.5mM]) and (D) 10μM +myrMA control. POPC:POPS 70:30 vesicles incubated with 20μM of +myrMA for (E) 20 min and (F) after overnight incubation. Lipid-to-protein molar ratios (L/P) are stated in the individual micrographs. Measurements were performed at RT. Length of the scale bar is 500 nm. Micrographs of pure DOPS vesicles at pH 7.4 for control (right). Deformation and mild tubulation can be observed in pure DOPS vesicles but not in the mixed vesicles.

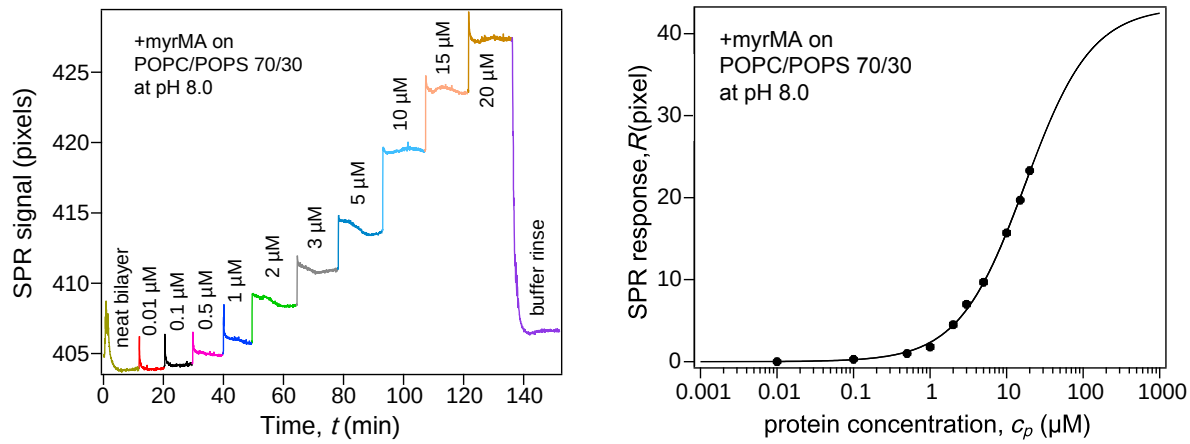

Figure 7.4: Binding of +myrMA on POPC:POPS 70:30 stBLM at pH 8.0. (A) Raw SPR data. Each spike indicates an injection with an increased concentration of protein. A final buffer rinse completely removes the adsorbed protein (B) Langmuir isotherm generated from the equilibrium raw data shows +myrMA affinity to PS-containing membrane is weaker at pH 8.0

To investigate the effect of pH on +myrMA binding to membranes, a set of experiments was performed at higher pH. pH was increased from 7.4 to 8.0 which inhibits the formation of +myrMA trimers in solution [55], favoring the MA monomeric state and thus sequestration of the myristoyl as discussed is Chapter 6.

SPR experiments

SPR experiments were conducted at pH 8.0 on POPC:POPS 70:30 stBLMs as a preliminary screening and for comparison to +myrMA binding at pH 7.4. Raising the pH negatively affects HIV-1 +myrMA binding to membranes by a factor of 5 (K_d = 18 μM). Changes in pH can affect protein charge. MA pI is 9.2 and an increase in pH results in MA net charge reduction. At pH 8.0, +myrMA affinity to PS containing membranes was reduced and buffer rinse removed all protein from the interface, see Figure 7.4. Complete dissociation of +myrMA characterizes reversible binding as opposed to the SPR binding experiments performed at pH 7.4, that showed only partial removal of protein from the membrane surface. The protein surface density $R_\infty \approx 45$ pixels, the same coverage obtained at pH 7.4 on DOPC:DOPS 70:30 stBLMs. At pH 8.0, +myrMA shows lower affinity to PI(4,5)P_2 containing membranes but it is only slightly affected by incorporation of cholesterol. Table 7.1 summarizes the best fit parameters obtained for +myrMA binding to various membranes compositions either at high salt concentration or pH 8.0.

EIS experiments

EIS measurements were carried out before and after +myrMA was added to the DOPC:DOPS 70:30 stBLM during SPR measurements. The impedance spectrum shows that the bilayer remains intact after the last protein concentration is added (Figure 7.5). EIS measurements showed

Table 7.1: Summary of +myrMA SPR experiments best-fit parameters obtained from the Langmuir model at 100 mM NaCl salt concentration and pH 8.0. The experiments were just performed once.

membrane composition	ionic strength	pH	K_d (μM)	R_∞ (pixel)
DOPC:DOPS 60:40	100 mM NaCl	7.4	12±2	70±3
DOPC:DOPS 70:30	100 mM NaCl	7.4	35±1	60±1
POPC:POPS 70:30	50 mM NaCl	8.0	18±1	43±2
POPC:PI(4,5)P_2 95:05	100 mM NaCl	7.4	3±1	35±1
POPC:PI(4,5)P_2 95:05	50 mM NaCl	8.0	10±1	74±2
POPC:PI(4,5)P_2:chol 67.5:2.5:30	50 mM NaCl	8.0	7±1	104±4

that membrane quality was not affected by +myrMA binding. Capacitance after +myrMA incubation is slightly larger than the neat bilayer which suggests membrane thinning due to protein association. Resistance was unaffected, $R_{def} > 200$ kΩcm^2 before and after the +myrMA incubation. The EIS spectra indicate that binding of +myrMA to membranes at pH 8.0 does not create defect-rich density regions on the membrane nor induces extreme membrane remodeling.

Neutron experiments

To confirm the absence of overlayers at pH to 8.0, NR experiments were performed. At pH 8.0, +myrMA complete binding reversibility is achieved within minutes and membrane reconstruction can be minimized. The +myrMA structure was probed on a deuterated lipid bilayer d-31POPC:POPS 70:30. Deuterated POPC lipids were chosen to confirm the hydrocarbon nature of the overlayers if no clean structure of +myrMA could be achieved. Incubation of +myrMA at 1 and 10 μM was measured on the d-31POPC:POPS 70:30 stBLM. A control fit of the bilayer was performed to check for remaining vesicles at the interface. At 1μM no protein was detected at the interface. At 10 μM changes in the reflectivity curves at two different contrasts, H_2O and D_2O, were observed revealing the presence of protein adsorbed at the membrane. Figure 7.6 shows +myrMA nSLD profiles at pH 8.0. The protein layer thickness is consistent with a MA monolayer ($\approx$ 50Å). Protein profile slightly overlaps with the outer leaflet headgroup. Experiments were repeated on non-deuterated membranes DOPC:DOPS 70:30 and similar profile was achieved (data not shown).

The spatial association and orientation of +myrMA on the stBLM is based on the +myrMA NMR structure. The orientation probability analysis is not conclusive on the most probable orientation of +myrMA at the interface and still needs further refinement. The crystal structure envelope matches almost completely the free-form spline protein envelope and within uncertainties the protein envelopes are the same. The protein envelopes outside the lipid membrane are indistinguishable, suggesting that the globular core of matrix remains folded upon membrane association. The spline fit of +myrMA shows greater density penetrating the headgroup region of the outer leaflet compared to the orientation fit based on the NMR structure. Lipid reorganization could contribute to the differences in the density profiles or the crystal structure and the membrane bound structure are different. At pH 8.0, minimal membrane reconstruction upon +myrMA binding can still happen. We recently speculate that the extra density on the headgroup region is promoted by the binding of sodium ions to the negatively charged lipid headgroups. MA binding

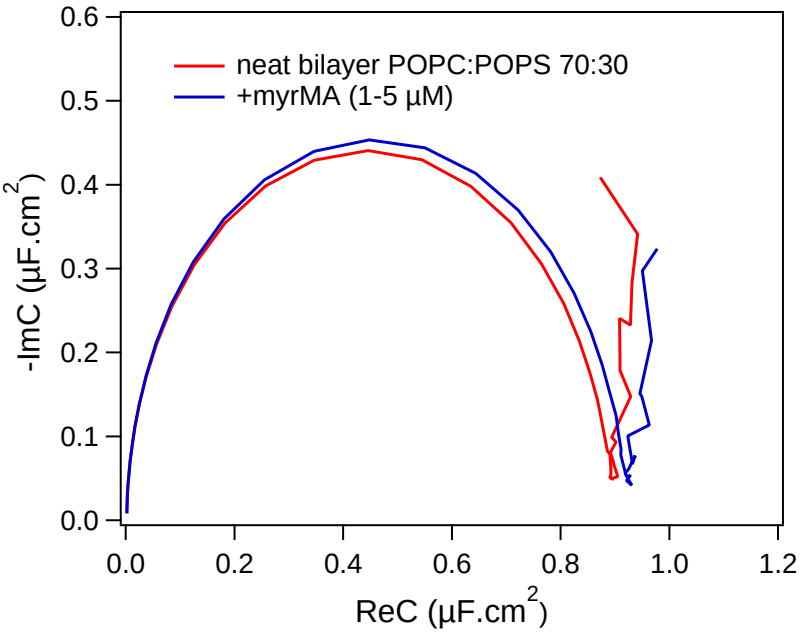

Figure 7.5: Lipid membrane is minimally affected by +myrMA binding at pH 8.0. Cole-Cole plots of an stBLM POPC:POPS 70:30 as prepared (red trace) and after being incubated with +myrMA at 5 μM (blue trace). Upon protein interaction with the membrane, the bilayer capacitance increases slightly and its resistance remains the same or slightly improves, $R_{def} > 200$ kΩcm^2.

as demonstrated throughout this chapter induces the remodeling of lipid membranes.

7.4 Discussion

The N-terminal matrix domain of the HIV-1 Gag binds Gag to the membrane. Electrostatic interaction between MA basic patch residues and membrane anionic lipids, myristoyl effect and lipid specific were dissected and quantified in Chapter 6. The characterization of matrix membrane-bound structure and its dependence on lipid composition and protein lipidation is also important. The lipid-binding of -myrMA was experimentally established by NR measurements [123]. -myrMA was found to bind peripherally to the lipid bilayer and electrostatic interactions are sufficient to define a favorable orientation of -myrMA on the membrane. The influence of the myristoyl on defining a new lipid binding interface or provide a more stable anchoring of the protein to the membrane was thus tested. Surprisingly, overlayers extending more than 200 Åaway from the membrane were observed. Refined modeling of the neutron data revealed the hydrocarbon nature of the overlayers, suggesting membrane reconstruction was triggered by +myrMA binding. EIS suggested membrane remodeling which was later confirmed by EM, strengthening the membrane reconstruction hypothesis.

SPR binding studies and EM images showed that +myrMA has a reduced affinity for, and does induce membrane reconstruction, vesicles composed of 30 mol% PS. Membrane remodeling is a complex process that involves many steps from binding to membrane reconstruction. The

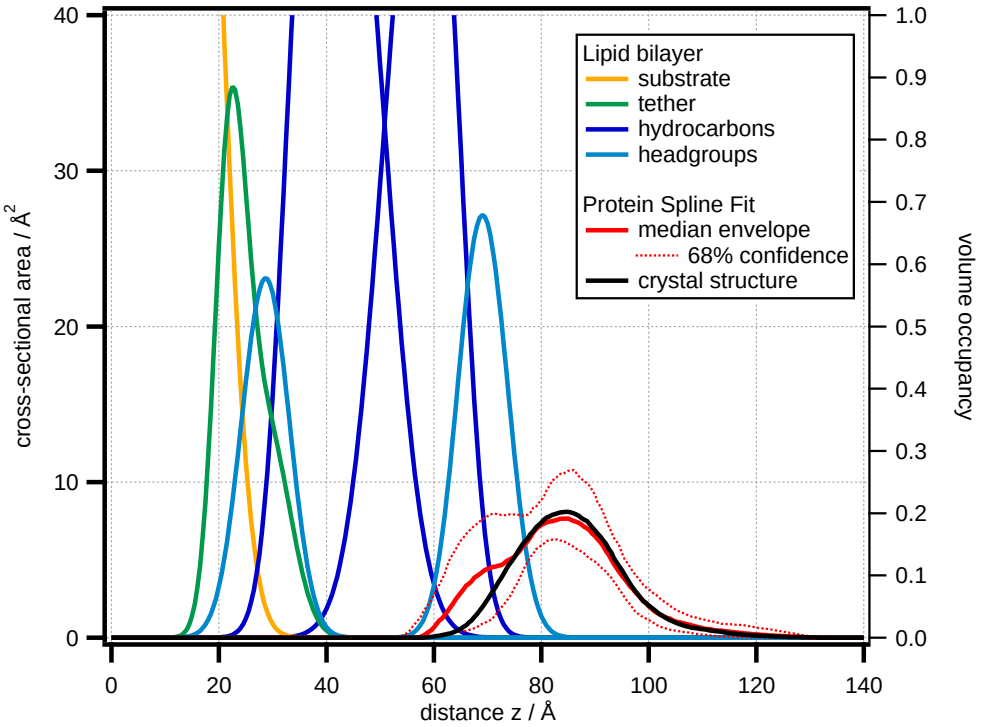

Figure 7.6: +myrMA monolayer at pH 8.0. Molecular distributions for each component of the d-31POPC/POPS 70/30 stBLM are zoomed in to emphasize the protein layer distribution. 10 μM +myrMA profile obtained from the best fit of reflectivity data to the spline fit model. The median protein envelope is shown with its associated 68% confidence intervals (red trace). Volume occupancy is indicated on the right axis. No overlayers are detected. A comparison of the median orientation fit using MA NMR structure is shown (black trace).

difference in the results between the pure DOPS vesicles where remodeling was observed and the PC:PS mixture where only protein aggregates were detected may be correlated to differences in the binding affinities or density of protein bound. +myrMA binds to pure DOPS membranes 10$\times$ tighter than to DOPC:DOPS 70:30 stBLMs and 100$\times$ tighter than pure DOPC stBLMs, see Table 6.1.

SPR and vesicle studies imply that membrane reorganization is charge induced. A pH increase from 7.4 to 8.0 resulted in the removal of the extra layers, as evidenced by NR. Further experiments at different pHs and lipid membrane compositions need to be carried out in order to better comprehend how pH and myristoylation regulates well-behaved +myrMA binding to membranes.

Chapter 8

Conformational Differences in Membrane Bound Retroviral Gag

8.1 Background

Gag is the major structural component for the assembly of new retroviral particles in infected host cells. Cryo-EM studies of immature virions indicated Gag molecules pack laterally on the plasma membrane in long extended conformational states. All Gag proteins contain structured domains: matrix (MA), capsid (CA) and nucleocapsid (NC), that are separated by linker regions that can be either flexible as in HIV-1 or rigid as in RSV and MLV.

A multitude of molecular interactions is involved in membrane association resulting in complex molecular reorganizations. The Gag polyprotein through MA, viral genome and PM domains of unique lipid composition interact in the course of viral assembly to form a highly organized, uniform layer of Gag protein and nucleic acid on the lipid membrane. Previous work by showed HIV-1 Gag can undergo large conformational changes depending on its biochemical environment, transitioning from a compact to extended conformation from simultaneously binding both the membrane and nucleic acid [39]. In contrast to HIV-1 Gag, SAXS experiments show MLV and RSV are always extended in and highly flexible in solution [40] [44].

To test whether and how the unstructured regions contribute to assembly, MLV and RSV Gag and its mutants counterpart, where the linker that connects the MA and CA domain is deleted, were investigated. These studies have the potential to establish a functional role for the disordered linker regions in retroviral Gag that may rely in preventing unproductive assembly processes in the host cytosol or on the membrane in the absence of viral genome.

8.2 Rous Sarcoma Virus (RSV)

8.2.1 Constructs

Rous sarcoma virus (RSV) Gag protein truncation mutants of Gag were purified by Rob Dick at Cornell University. Membrane binding affinities and structure were characterized by SPR and NR respectively. RSV Gag is a naturally unmyristoylated protein. RSV Δ flex carries an internal

deletion from residue 104 to 220, thus removing the putative flexible region, which appears to be unstructured by crystallography or by secondary structure predictions. MA is the 155-residue domain of RSV responsible for targeting the plasma membrane and MBD stands for membrane binding domain and spans the first 86 amino acids of MA n-terminus [177], which includes the basic residues that form a basic patch on a surface-exposed region of the protein, similarly to other retroviral species.

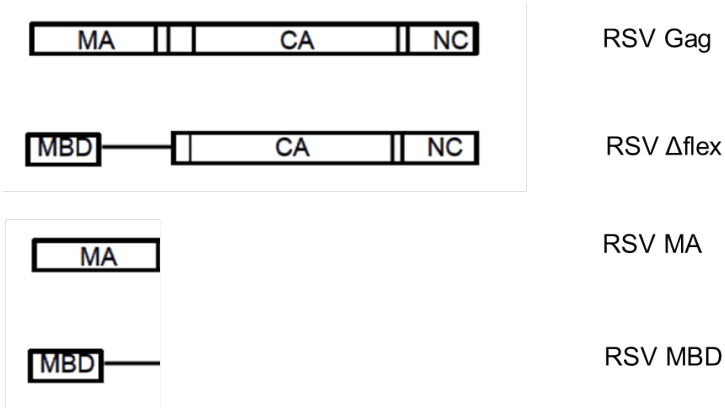

Figure 8.1: Schematic representation of RSV Gag constructs

8.2.2 Membrane binding

Quantitative assessments of the strength of membrane binding for the constructs shown in Figure 8.1 were determined by SPR at 50 mM NaCl, 20 mM Tris at pH 8.0.

MA

Although MA among retroviruses has a very low homology in sequence, their structures are very similar. RSV MA is naturally unmyristoylated and, unlike HIV MA, has no known defined PI(4,5)P_2 binding pocket. Since RSV MA lacks myristoylation, the exposed basic patch is responsible for primarily mediating membrane binding during assembly. The structural similarity between the RSV MA and those of other retroviruses suggests that RSV Gag may interact with acidic phospholipids in the inner leaflet of the plasma membrane via electrostatic interactions.

SPR experiments were carried out at stBLMs of various compositions to determine lipid composition influence on RSV MA membrane association. MA is completely removed from the DOPC/DOPS 70:30 membrane when protein-free buffer is flowed into the system, see Figure 8.2. RSV MA binding is well described by a Langmuir model, best fit parameters for the various compositions tested can be found on Table 8.1. MA binding to stBLMs containing PS as the anionic lipid providing electrostatics is in tenth of μM range. We also quantified the SPR responses for MA with stBLMs containing 2% PI(4,5)P_2, in the background of the same PS composition, DOPC/DOPS/PI(4,5)P_2 68/30/2, aiming to learn about specificity between PI(4,5)P_2 and MA. The added PI(4,5)P_2 increased the affinity of MA by almost an order of magnitude. Finally, incorporation of 30% cholesterol did not enhance the affinity of MA.

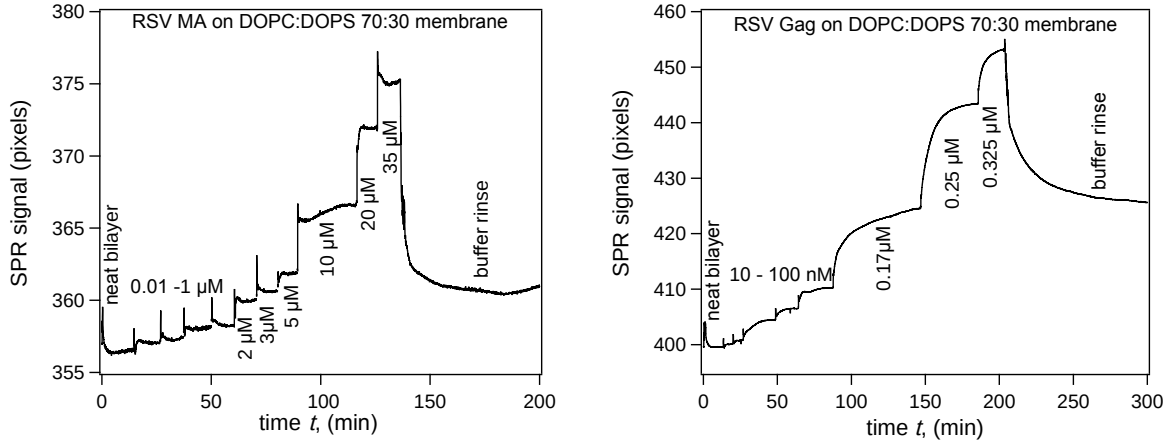

Figure 8.2: Examples of SPR binding curves (raw data) of MA and Gag to DOPC/DOPS (70/30) stBLMs. Neat bilayer is exposed to increasing protein concentrations. Plateaus correspond to equilibrium responses at given protein concentrations, followed by a final rinse. Gag remains bound to the membrane after rinsed with buffer while MA is almost completely removed.

MBD

RSV MA comparably with the other MAs has a globular structure and a floppy disordered region formed by the last 50 aminoacids. The functional membrane binding region of RSV Gag correspond to the first 87 amino acids of MA [177] [125], which therefore was labeled the membrane binding domain (MBD). Even small deletions in the MBD block assembly and budding [177]. The MBD has a net charge of +4 at a neutral pH, and although the charges are not clustered in the primary amino acid sequence, the solution structure reveals that several basic residues form a patch on the surface of the protein [112]. RSV MBD binding to anionic membranes containing 30 mol% was initially investigated (data not shown). Very high protein concentrations ($>$ 100 μM) were added to the stBLMs in order to reach membrane binding saturation. MBD data was fitted with a langmuir model, which predicted, with huge uncertainties, a K_d of $\sim$ 270 μM. Such a high K_d value was unexpected. MBD includes MA basic patch residue, which involved in membrane binding and therefore the calculated affinity was expected to be similar to that obtained for RSV MA. This result indicates that the lack of the unstructured region of MA may influence negatively the binding of MBD to membranes. Further test of the binding of MBD to membranes of different lipid compositions were not performed due to the high amounts of protein required.

Gag

RSV Gag is naturally unmyristoylated which makes it an ideal model for studying electrostatic interactions involved in protein membrane association.

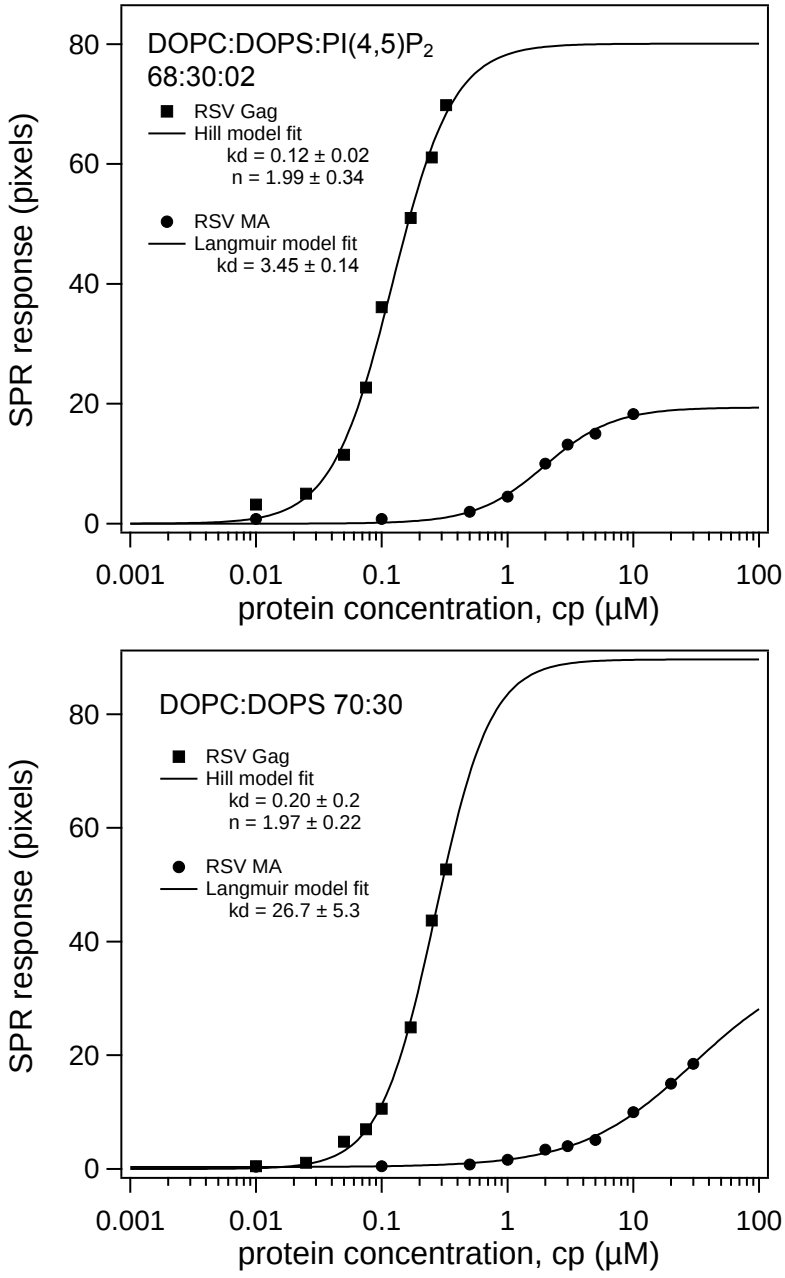

Figure 8.3: Affinity was quantified in 50mM NaCl at pH 8 to stBLMs at a fixed PS concentration of 30%.Gag (squares) and MA (circles) binding quantification to DOPC/DOPS stBLMS either with (red) or without (black) 2% $PI(4,5)P_2$. Langmuir isotherm well described MA data. In contrast, Gag data was fitted with Hill equation to model its cooperative membrane binding behavior. Measurements were repeated at least two times

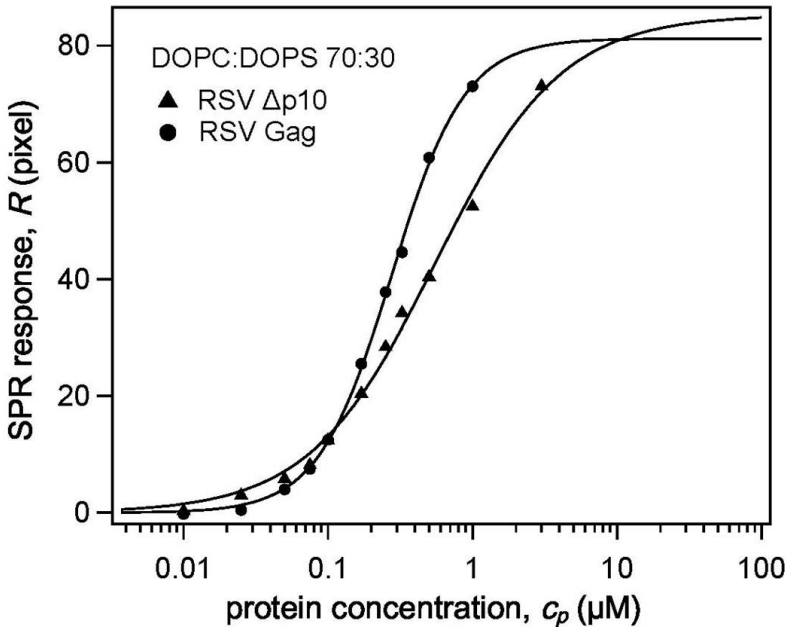

Figure 8.4: Affinity was quantified in 50mM NaCl at pH 8 to stBLMs at a fixed PS concentration of 30%. Gag (circles) and Δflex (triangles) binding quantification to DOPC:DOPS 70:30 stBLMS. Langmuir isotherm well described the Δflex. In contrast, Gag data was fitted with Hill equation to model its cooperative membrane binding behavior. Measurements were repeated at least two times

Both RSV Gag and HIV Gag are sensitive to the highly charged plasma membrane (PM) inner leaflet lipid PI(4,5)P_2 [130] [133] [30] [20] [122] but since RSV MA has no known PI(4,5)P_2 specific binding site, this interaction is believed to have only of electrostatic nature.

The binding affinity of RSV Gag to a stBLM consisting of DOPC/DOPS (70/30) was characterized by surface plasmon resonance (SPR), see Figure 8.3. At Gag concentrations up to 0.5 μM the SPR signal remained stable for several hours, indicating non-specific binding and surface aggregation were not issues at these concentrations. Above 1 μM RSV Gag aggregates as evident by a linear increase on the SPR signal. Protein-free buffer rinse only partially removed the membrane-bound RSV Gag. RSV Gag binding did not follow a Langmuir model and thus had its binding described and quantified by the Hill equation. At 50 mM NaCl, Gag bound tightly and cooperatively to the membrane with a dissociation constant, K_d = 207 nM and a Hill coefficient, n = 2.3. Such as for RSV MA, we also quantified the SPR responses for Gag with stBLMs containing 2% PI(4,5)P_2, in the background of the same PS composition, DOPC/DOPS/PI(4,5)P_2 68/30/02. The added PI(4,5)P_2 increased the affinity of Gag had only a modest effect on Gag affinity (Figure 8.3).Tthe SPR experiments show that PI(4,5)P_2 induced a two-fold decrease in K_d for RSV Gag at 50mM NaCl. We speculate that this effect would be greater at a physiologically relevant ionic strength, but because of slow binding kinetics in conjunction with surface aggregation at elevated concentrations (>1 μM) we were unable to acquire interpretable data for Gag binding to supported bilayers at 150 mM NaCl. The small effect of PI(4,5)P_2 on RSV binding may be explained by the fact that Gag membrane binding involves lattice formation due to lateral protein-protein interactions, presumably mediated by the neighboring capsid domains,

Table 8.1: Best-fit parameters obtained from the Langmuir model and Hill equation for RSV MA and Gag, respectively, membrane binding at different lipid compositions (50 mM NaCl at pH 8.0)

Protein	Lipid composition	$K_d(\mu M)$	$R_\infty(pixels)$	Hill coefficient (N)
RSV MBD	DOPC:DOPS 70:30	$>> 100$	27 ± 5	Langmuir model
RSV MA	DOPC:DOPS 70:30	24 ± 2	40 ± 5	Langmuir model
	DOPC:DOPS:chol 50:30:20	22 ± 3	49 ± 2	Langmuir model
	DOPC:DOPS:PI(4,5)P2 68:30:02	3.9 ± 0.4	31 ± 3	Langmuir model
RSV Gag	DOPC:DOPS 70:30	0.24 ± 0.01	75 ± 3	2
	DOPC:DOPS:chol 50:30:20	0.20 ± 0.01	90 ± 12	3
	DOPC:DOPS:PI(4,5)P2 68:30:02	0.13 ± 0.01	90 ± 12	2
RSV Δflex	DOPC:DOPS 70:30	0.5 ± 0.1	83 ± 10	Langmuir model

rather than only lipid-protein interactions as in the case of MA. A role for the NC domain in mediating Gag-membrane association cannot be neglected. In fact, if NC is not occupied by its preferential binding partner, RNA, it can interact with acid lipids in the plasma membrane. Finally, incorporation of 30% cholesterol did not enhance the affinity either of Gag or of MA (Table 8.1). Furthermore, cooperativity showed to be independent of lipid composition.

The SPR response for MA and for full-length Gag in the presence of DOPC/DOPS (70/30) membranes was different in several respects. First, while MA was removed completely by subsequent rinses with protein-free buffer, full-length Gag remained partially bound to the membrane surface as can be seen in Figure 8.2 . Second, unlike for MA, the SPR response for Gag did not follow a Langmuir model, suggesting collective adsorption that is more appropriately described by the Hill equation (with N≈2). The Hill equation includes a parameter for cooperativity, strongly suggesting that Gag dimerizes upon adsorption to the membrane surface. Third, the estimated membrane affinity of Gag was much greater than the affinity of MA ($K_d \sim$ nM vs. μM, respectively) as depicted in Figure 8.3.

Δflex

In order to understand the role of the unstructured linkers in regulating the structural reorganization of Gag at the membrane, going from compact to extended, we investigated the RSV mutant, Δflex, where the linker between MA and CA is absent, lacking the high flexibility introduced by the linker region. According to in vitro assembly assays those deletion do not prevent Δflex to assemble into VLPs. Moreover SAXS show that those deletions result in more ordered protein.

The SPR binding experiments of Δflex mutant performed on DOPC/DOPS 70/30 aimed to understand how the protein linker influences RSV-membrane coupling. In contrast to RSV Gag that behaves cooperatively at the membrane interface, the binding of Δflex to anionic membranes is well described by a Langmuir isotherm, see Figure 8.4, and therefore shows no sign of cooperativity. The affinity of Δflex was slightly reduced, $K_d \sim 0.5$ μM and the protein density did not change. This finding implies that the deleted region in the Δflex accommodates residues that are involved in the modulation of the cooperative behavior of RSV Gag at the membrane, but cooperativity should have drastic effects on K_d, which is missing.

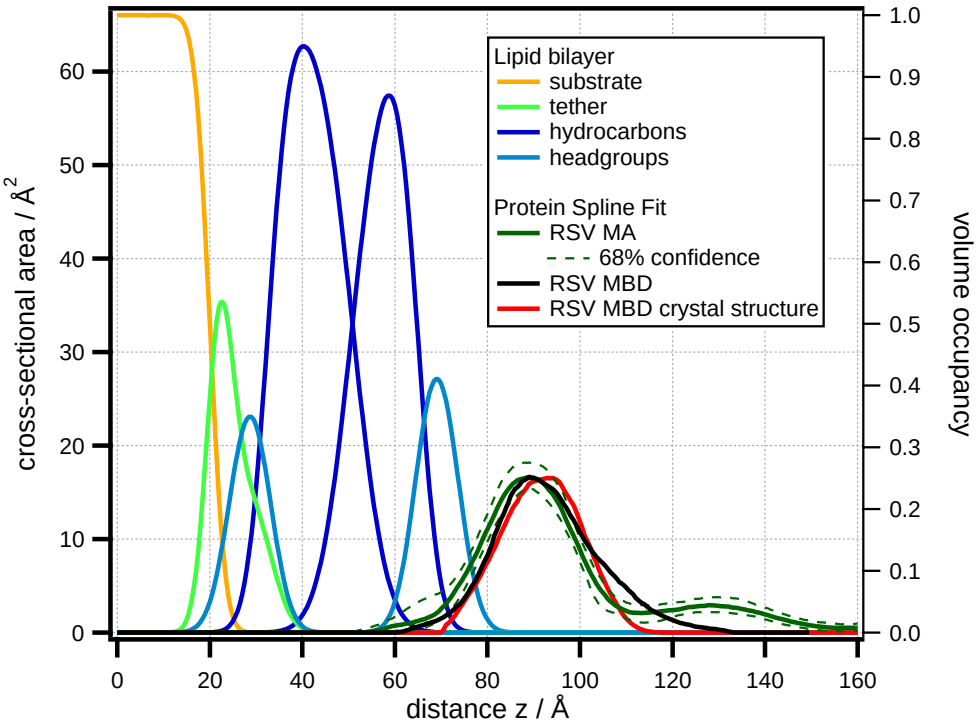

Figure 8.5: nSLD profile of RSV MA profile at 10 μM on DOPC:DOPS 70:30 lipid bilayer as determined by spline method shown in green. Black lines correspond to MBD protein envelope at 50 μM on DOPC:DOPS 70:30 lipid bilayer. Red line represent the best-fit of the nSLD distribution calculated from the MBD crystal structure.

8.2.3 Membrane-bound structure

Quantitative information provided by the SPR experiments was used as a reference for optimal conditions to probe the conformation and structure of RSV Gag constructs when bound to the membrane by NR.

MA

RSV MA bound structure was characterized on DOPC:DOPS 70:30 lipid membranes. The protein envelope shows no overlayers and has dimensions consistent with a monolayer of protein adsorbed at the interface. We observed only minimal penetration of the protein into the lipid headgroup region, indicating that RSV MA interaction with the membrane is purely an interfacial phenomenon. The region of the nSLD attributed to the protein which is proximal to the membrane is well approximated by the putative nSLD distribution derived from the MBD crystal structure. On the distal end of the protein nSLD distribution, at z = 120 - 150 Åfrom the gold surface, we observe extra density that is not matched by the nSLD profile obtained from MBD crystal structure. It is valid to speculate that the unstructured region of RSV MA, not present in the crystal structure, contributes the scattering in that region of the profile, as observed in Figure 8.5. The ultimate step is to compare the orientation fit of MBD crystal structure to ongoing simu-

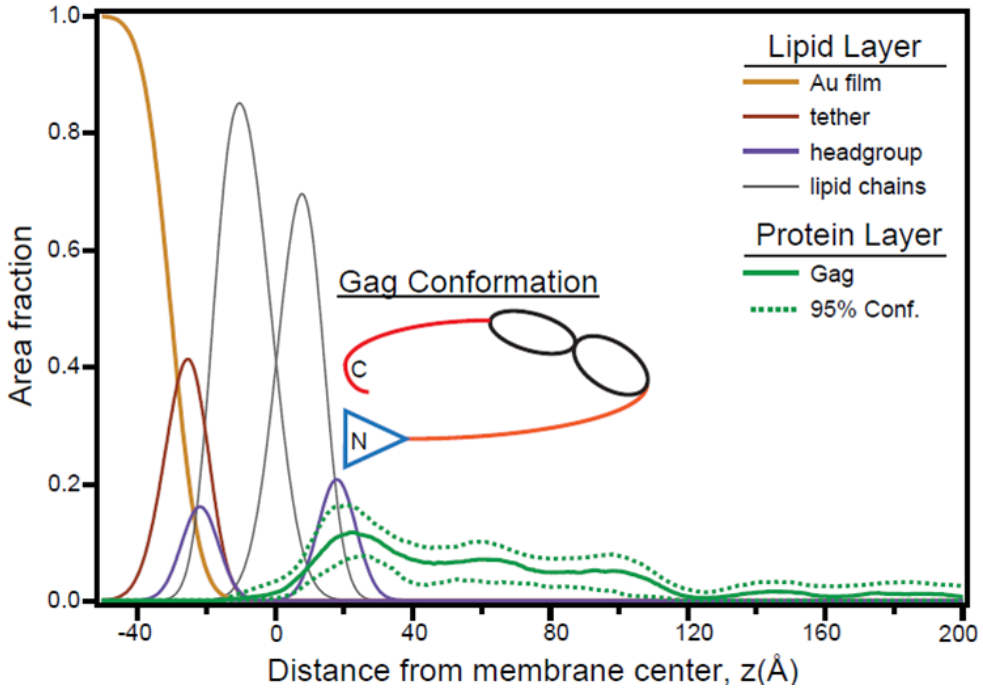

Figure 8.6: RSV Gag is compact at the membrane. Area fraction profile showing the molecular distribution of the lipid layer DOPc:DOPS 70:30 and the RSV Gag protein (solid green curve). 95% confidence bands determined by the fitting procedure are also shown (dashed green curve). An interpretative cartoon is also included.

lations performed by our collaborators from Cornell University. Compared with HIV-1 -myrMA bound structure [123] and location with respect to the membrane, both profiles look very similar, showing slight penetration in the outer leaflet headgroup region.

RSV Gag and Δflex

According to hydrodynamic and SAXS studies purified RSV Gag in solution is extended but highly flexible [44]. ΔFlex mutant showed to be more ordered and therefore less flexible. NR measurements were performed on a stBLM composed of DOPC/DOPS 70/30 for both RSV and ΔFlex at similar concentrations. The protein profile for RVS Gag was embedded within the headgroup region of the membrane and extended ≈100 Åfrom the bilayer. By comparison, the dimensions of RSV Gag in virus-like particles (VLPs) assembled in vitro shows the protein to be extended with a dimension of ≈ 180 Å [17]. Thus RSV Gag is more compact when bound to a membrane than when assembled into immature virus particles such as HIV-1. Surprisingly, the removal of the internal, putatively unstructured segment of Gag, in the protein ΔFlex did not prevent Gag from adopting a folded over conformation at the membrane. The protein profile reveals that RSV ΔFlex spans the membrane almost completely from one leaflet to the other and extends ≈120 Åfrom the membrane. The fact that ΔFlex inserts deeper on the membrane is surprising taking into account that MBD and MA binding makes interfacial contact with the membrane and RSV Gag penetrates only the outer leaflet headgroup of the bilayer. The mechanisms that leads

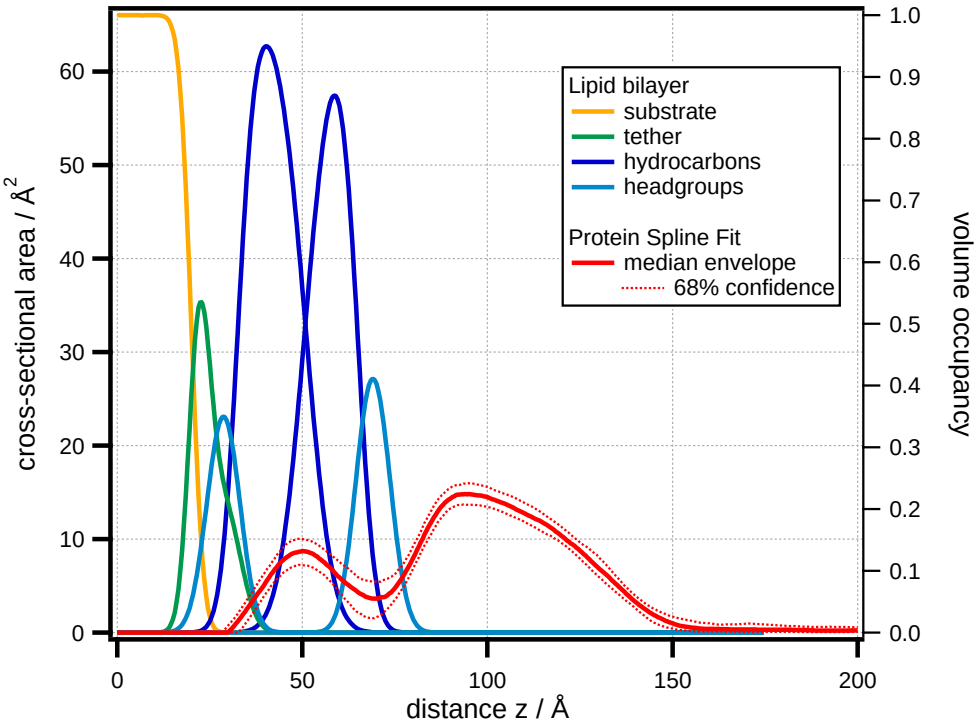

Figure 8.7: Δflex RSV is compact at the membrane. Area fraction profile showing the molecular distribution of the lipid layer DOPC:DOPS 70:30 and the RSV Gag protein (solid red curve).95% confidence bands determined by the fitting procedure are also shown (dashed red curve).

ΔFlex to insert further on the hydrocarbon core still remains unclear.

8.3 Murine Leukemia Virus (MLV)

8.3.1 Constructs

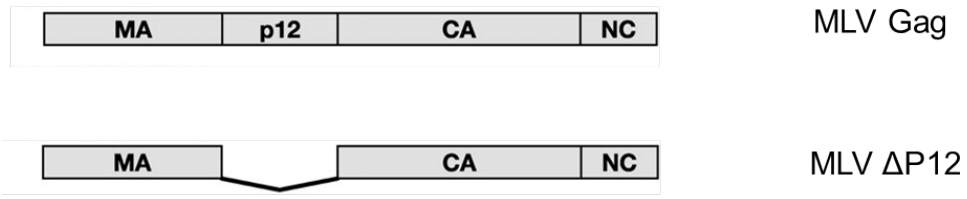

Figure 8.8: Schematic representation of MLV Gag constructs

Murine Leukemia Virus (MLV) Gag protein and its mutant counterpart were provided by our collaborator Sid Datta at the Drug Resistance program at National Cancer Institute. Membrane binding affinities and structure were characterized by SPR and NR respectively. MLV Gag is the full-length non-myristoylated version of the protein. MLV ΔP12 lacks the p12 domain between

MA and CA domains. p12 is an 84 residue unstructured polypeptide, which is located between the N-terminal MA and CA domains, that facilitates viral budding at late stages of the viral life cycle [**?**].

8.3.2 Membrane binding

Quantitative assessment of the strength of membrane binding for the constructs showed in Figure 8.8 was carried out by SPR at 50 mM NaCl at pH 7.4.

Gag and ΔP12

SPR experiments were carried out to quantify binding affinity of MLV Gag and ΔP12 to stBLMs composed of binary mixture DOPC:DOPS at varying amounts of PS. Full-length and truncated version of MLV Gag were both prone to aggregation at protein concentration > 7 μM, thereby limiting the concentration range at we could perform the SPR experiments. That was not an issue when binding was probed at low salt conditions (50 mM NaCl) since MLV binding was in the 1 μM range. At physiological salt conditions, protein aggregation turned out to be an obstacle for determining with precision the dissociation constant for the MLV constructs at anionic membranes. Figure 8.9 shows the binding of MLV to stBLMs with PS concentrations varying from 22.5 to 30 mol%. At 15 mol% PS (data not shown), there was no protein bound up to 7 μM, upper bound concentration above which protein aggregates. At 19 mol% PS (data not shown), MLV Gag binds very poorly ($K_d >> 7$ μM). For PS concentrations above the 20 mol% threshold, we get a K_d of approximately 1 μM with saturation responses R_∞ proportional to the amount of PS present in the bilayer. In the lower PS concentration regime, protein density increases linearly as function of PS concentration. This behavior predicts a R_∞ of zero at 15 mol% PS, minimum threshold of PS present in the bilayer below which no binding is observed. This fact was independently verified by SPR experiments, which confirmed the lack of membrane-bound protein on DOPC/DOPS 85/15 stBLMs.

To support the role of electrostatics in MLV Gag binding, we increased the buffer ionic strength from 50 mM to 100 mM NaCl and tested the affinity of the protein to a stBLM containing 22.5 mol% PS in a DOPC background. Surface coverage was not affected, but the equilibrium constant increased from 1 to 5 μM. Cholesterol influence on MLV Gag binding was also probed. The affinity of the protein to a stBLM was composed of DOPC/DOPS/chol 40/30/30 at 50 mM NaCl was not altered by the presence of cholesterol but the protein surface density increases substantially (Table 8.2). Increase in the protein loading at the membrane, imposed by the presence of cholesterol, was a trend observed for all the Gag proteins investigated. This may be an important mechanism for assembly and still needs to be further pursued.

ΔP12 Gag successfully assembled into full-size particles [40], similar to that of immature VLPs assembled in cells, upon addition of nucleic acid alone despite the linker deletion between MA and CA. Preliminary SAXS measurements suggests ΔP12 is more flexible than MLV Gag but it is still extended in solution. It was pointed out by our collaborators that the reliability of the SAXS data was dubious due to radiation damage, and thus only the first few snapshots could be used in the Kratky analysis.

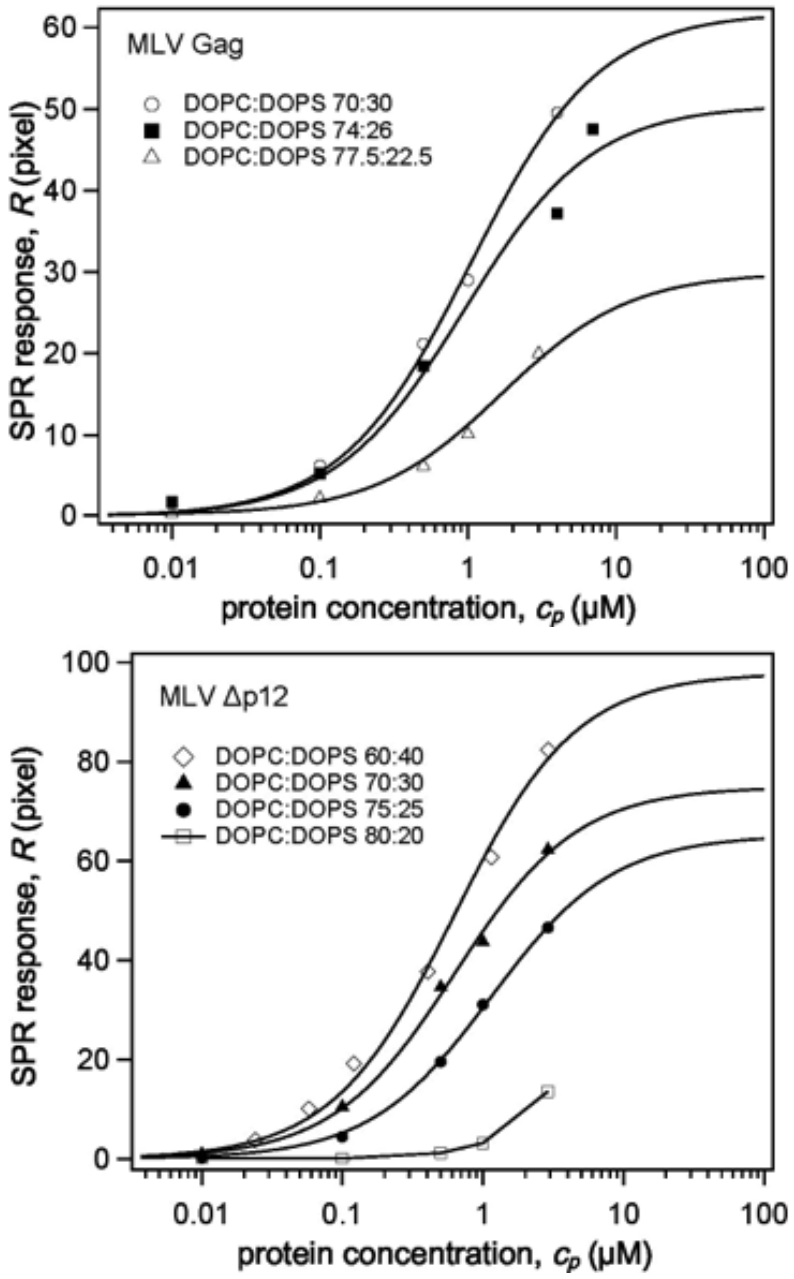

Figure 8.9: Gag membrane-binding is electrostatically driven. Comparison of MLV and ΔP12 binding to stBLMs that contain DOPC and DOPS at varying amounts. (A) Representative SPR curves of MLV binding, analyzed with the Langmuir model. (B) Representative SPR curves for ΔP12.

Table 8.2: Best-fit binding parameters estimated from the Langmuir model for MLV Gag wt and ΔP12 mutant on DOPC:DOPS membranes

Protein	Lipid composition	$K_d(\mu M)$	$R_\infty(pixels)$
MLV Gag	DOPC:DOPS 70:30	1.1 ± 0.2	60 ± 5
	DOPC:DOPS 74:26	1.1 ± 0.1	49 ± 3
	DOPC:DOPS 77.5:22.5	1.7 ± 0.3	30 ± 3
	DOPC:DOPS 81:19	$>>7$	n.d.
	DOPC:DOPS 85:15	no binding	—
MLV ΔP12	DOPC:DOPS 60:40	0.62 ± 0.01	97.8 ± 0.2
	DOPC:DOPS 70:30	0.64 ± 0.02	76 ± 1
	DOPC:DOPS 75:25	1.3 ± 0.1	54 ± 1
	DOPC:DOPS 80:20	$>>3$	—

The mutant ΔP12 was then tested for its binding affinity to stBLMs at PS concentrations varying between 20 and 40 mol%, to address the role of the linker region in MLV Gag binding, as shown in Fig. 8.9. At 20 mol% PS ΔP12 binds poorly up to 3 μM and affinity could not be estimated without surpassing the protein concentration limit imposed by protein aggregation. At PS$>$ 20 mol%, MLV-ΔP12 binding followed a Langmuir model. Moreover, ΔP12 bound to stBLMs in a similar fashion affinity when compared to the wild-type MLV (K_d = 0.6 μM), showing that the linker deletion has little or no impact on membrane binding.

8.3.3 Membrane-bound structure

Both constructs, MLV Gag and MLV-ΔP12, were characterized with neutron reflection (NR) and X-ray reflectivity in order to find out their conformation at the membrane. SAXS measurements revealed that MLV Gag is extended in solution [40] as it is ΔP12. The p12 linker is about 20 Ålong so it would be expected Δp12 dimensions to be shorter by 20 Åwhen compared to the MLV Gag. X-ray data on 100% DPPS lipid monolayer under a surface pressure of 30 mN/m were collected. the wild-type MLV and ΔP12 membrane- bound complexes show very distinct overall structures. Wt MLV Gag extends only 100 Åfrom the membrane surface suggesting that the protein adopts a back-folded conformation. Δp12, on the other hand, is completely extended $\sim$ 220 Å. No insertion in the monolayer was observed for any of the proteins.

In order to probe the Gag constructs conformation structure in more relevant membrane surface charge densities, NR was performed on stBLM containing 30 mol% PS, Figure 8.10. NR and X-ray measurements are in complete agreement with respect to the arrangement of MLV Gag and ΔP12 when bound to the membrane. ΔP12 appeared extended $\sim$ 220 Åand very well ordered on the membrane interface. MLV gag was found to be in a more compact conformation $\sim$ 110 Åbut fully extended in the presence of nucleic acid showing a similar mechanism once observed for HIV-1 Gag.

Wild-type MLV Gag binds membranes in vitro in backfolded conformations, as shown by NR, indicating structural flexibility at some extent of their MA-CA linkers. In contrast, MLV mutant, ΔP12, in which the MA-CA linker has been eliminated, binds the membrane in an extended conformation. Comparative analysis of the SPR data between these two constructs

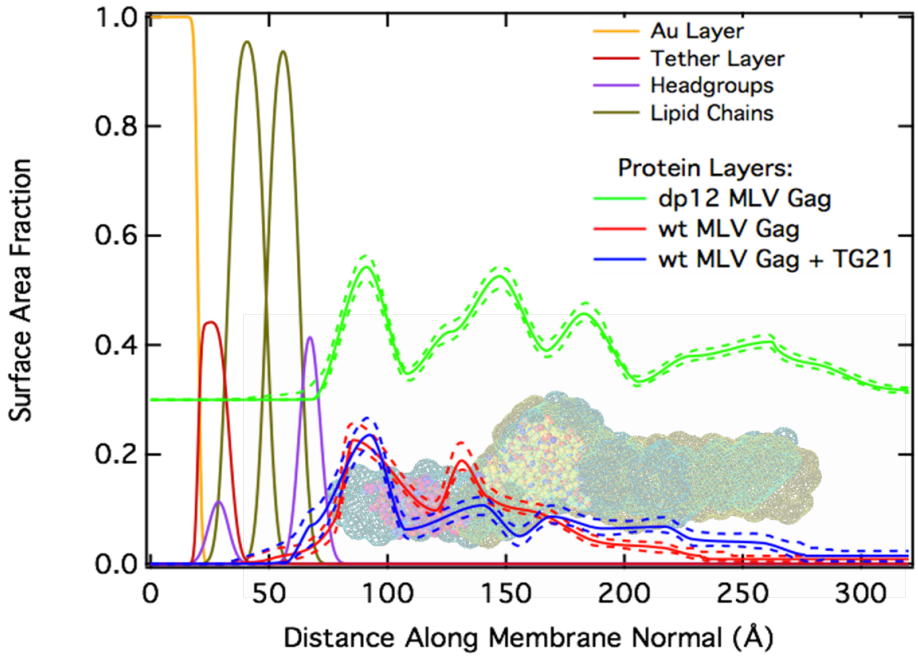

Figure 8.10: MLV Gag is compact at the membrane while ΔP12 is extended. Area fraction profile showing the molecular distribution of the lipid layer DOPC:DOPS 70:30 and the ΔP12 (solid green curve) MLV Gag protein in the absence (solid red curve) and presence of nucleic acid (solid blue curve). 95% confidence bands determined by the fitting procedure are also shown (dashed curves). MLV envelope generated by SAXS is also included.

confirmed similar membrane binding affinity. However, both neutron and X-ray reflectivity measurements showed significant structural differences.

8.4 Discussion

Several Gag-membrane associated complexes were investigated and the main results from their comparison follow below

RSV vs HIV-1 MA

The first immediate result that emerges from this comparison is that overall the naturally unmyristoylated RSV MA membrane binding association with model membranes depends similarly on lipid composition, both qualitatively and quantitatively, as non-myristoylated HIV-1 MA. Cholesterol has no effect in binding affinity but increases protein density at the membrane. PIP_2 increases affinity by at least 7 times. Moreover, the membrane affinities of both HIV-1 -myrMA an RSV MA are in the μM range.

Membrane bound structure of RSV MA and HIV-1 -myrMA and location with respect to

the membranes look very similar. Protein association is strictly interfacial only showing few Angstroms penetration in the outer leaflet headgroup region. Preliminary fits of HIV-1 +myrMA on the other shows deeper penetration on the headgroup which can be attributed to the presence of the myristoyl moiety. Myristoylation seems to be responsible for stably anchoring the protein to the bilayer, as presumed.

RSV vs MLV vs HIV-1 Gag

RSV full-length Gag have nanomolar range affinity to membranes Measurements of membrane-bound Gag conformations by neutron reflectometry (NR) showed that RSV an+ d MLV like HIV-1 Gag do not extend far from the bilayer, consistent with a compact Gag structure. The membrane-bound Gag conformation was interpreted to result from both MA and NC domains simultaneously interacting with the bilayer [44] such as seem to be the case for HIV-1 Gag [38]. Even though MLV and RSV behaves as an extended rod in solution, the linkers are stiffer than HIV-1 but flexible enough to allow both MA and NC domains to interact with the charged membrane. In one model of HIV Gag-membrane interaction, derived from NR measurements, if NC is not occupied by nucleic acid, it freely interacts with a negatively charged membrane. This interaction would result in a Gag configuration that is unfavorable for multimerization. The same is true for RSV Gag, the folded conformation adopted at the membrane interface does not favor lateral interaction among Gag neighbor molecules regulated by the capsid domain, which at first goes against the results observed by SPR. Those measurements predict cooperative behavior interpreted to arise from protein-protein interaction. The divergence between SPR and NR RSV data can be explained by the requirement of critical surface coverage to promote interaction among Gag neighbor molecules. MLV Gag on other hand shows no sign of cooperativity but neutron data shows that extension of Gag on the membrane can be driven by nucleic acid. Once Gag is at the membrane, NC goes to its preferential interaction with RNA and extends the protein in a mechanism that seems to be common among retroviruses. Wild-type Gags show a backfolded conformation in the absence of nucleic acid. That conformation does not favor productive lattice formation. Not all the interactions or components needed to trigger extension are involved: multimerization, critical surface coverage, PIP_2 or nucleic acid are some of the possibilities.

Linker deletion effect

Linker deletion does affect neither RSV nor MLV Gag binding affinity, although it alters RSV Gag binding mode. Cooperative behavior is absent in the Δflex mutant. The linker region seems to be involved in regulating RSV gag multimerization. Linker regions are responsible for Gag flexibility, Kratky plots confirm mutants are less flexible than wild-type Gags Gag structures probed by neutron reflection show distinct conformations at the membrane. Mutant of MLV, ΔP12, but not RSV, Δflex, Gag is extended. For MLV Gag, the deletion of the p12 domain resulted in the loss of Gag ability to adopt compact conformation when bound to lipid bilayer which needs further investigation.

Here, we aimed at revealing molecular-scale structures of full-length and truncated forms of

membrane-associated Gag to understand the complex mechanism of membrane coupling. We quantified dynamic aspects of protein association with bilayers and nucleic acids, that drive the polyproteins subsequent reorganization which results the dense, laterally assembled membrane-Gag-nucleic acid complex required for productive viral shell formation.

Chapter 9

Endolysin PlyC Mechanism for Plasma Membrane Translocation: Entry Point Revealed

In this final chapter the molecular basis of PlyC binding to the mammalian plasma membrane is investigated. PlyC structural features are addressed in section 9.3. Quantitative studies using stBLMs with well-defined lipid compositions were investigated in section 9.2.1 and 9.2.2. Assessment of lipid membrane quality by EIS and PlyC localization at the membrane by NR were characterized in sectiond 9.2.3 and 9.2.4.

9.1 Introduction

Opportunistic human pathogens, such as Streptococcus pyogenes, cause a broad spectrum of diseases, ranging from pharyngitis to pneumonia, by colonizing the skin and mucosal surface. Intriguingly, the PlyC holoenzyme is not only an extremely potent lysin specific for streptococci, but it also lyses pathogens within mammalian cells in culture if applied exogeneously. This implies that the endolysin recognizes and binds to the bacterial plasma membrane and peptidoglycan cell wall components. PlyC also has the unique and inherent ability to penetrate into mammalian cells and retain bacteriolitic activity in the intracellular environment. PlyC gains cell entry apparently without inflicting damage, and is internalized into the cytoplasm where it targets streptococci in the perinuclear region.

For this process, the lysin must also specifically bind to mammalian plasma membrane (PM) components and transgress into the cytosol. Here, we investigate this specificity in the context of target membranes, quantify PlyCB affinity to model membranes as a function of bilayer composition and characterize the structure of the protein-membrane complex. This is relevant for a variety of potential PlyC applications. (1) After invasion of their mammalian hosts, staphylococci and streptococci frequently evade the host immune system and antibiotic treatment by internalizing into epithelial cells, enabling them to subsequently repopulate and recolonize surrounding cells and tissues after clearance of the antibiotic agent. In these situations, PlyC may provide a novel therapeutic opportunity against refractory infections. (2) The ability of PlyCB to

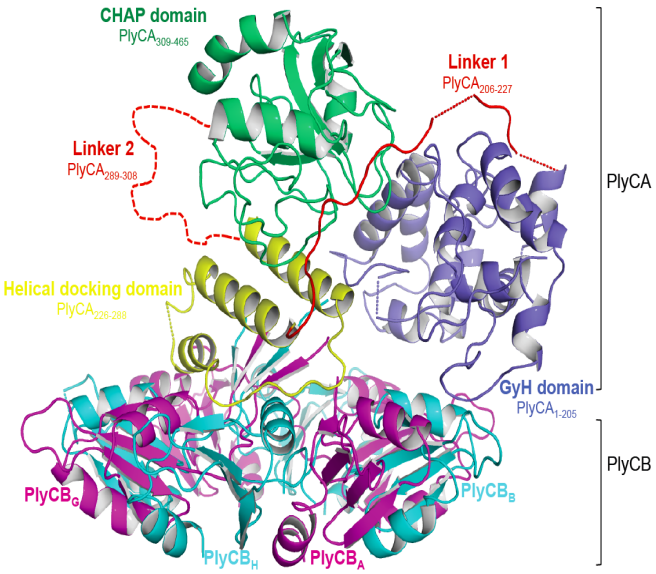

Figure 9.1: PlyC crystal structure. PlyC is composed by two subunits connected by a flexible linker: PLyCA the catalytic domain and PlyCB the bacteria cell wall biding domain

transgress the mammalian PM barrier could be used for shuttling other protein therapeutics that might replace PlyCA, the catalytic domain of PlyC, as a payload.

In binding studies to model membranes with well-defined lipid compositions, we show that the interaction of PlyCB with purely zwitterionic membranes is negligible. On the other hand, the protein interacts strongly with membranes that contain phosphatidylserine (PS) above a concentration threshold and much weaker with other anionic lipids, suggesting specificity for PS. Furthermore, a point mutant, PlyCB-R66E, that lacks the ability to translocate membranes has likewise lost affinity for PS. With neutron reflection from stBLMs, two distinct PlyCB membrane-association modes are observed. Depending on PS membrane concentration, PlyCB is either peripherally associated or deeply inserted into the bilayer, essentially spanning the membrane. The finding that PlyCB interaction with the PM depends on PS suggests that cells under a variety of pathologic stresses that promote PS externalization may be particularly amenable for PlyCB targeting and invasion, adding further value to the therapeutic potential of this potent endolysin.

The endolysin PlyC from bacteriophage C1, was first characterized by Fischetti and coworkers [126]. Endolysins from bacteriophage that infect Gram-positive bacteria are generally between 25-40 kDa in size, composed of two or more domains, and are the product of a single coding gene [126]. PlyC, unlike the other endolysins, is uniquely composed of two separate gene products, PlyCA and PlyCB. Described in terms of its crystal structure [115], consists of two components, a single enzymatic domain termed PlyCA non-covalently linked to a ring-shaped octameric assembly of PlyCB with a molecular weight of 62.9 kDa that alone is sufficient to target the bacterial cell wall.

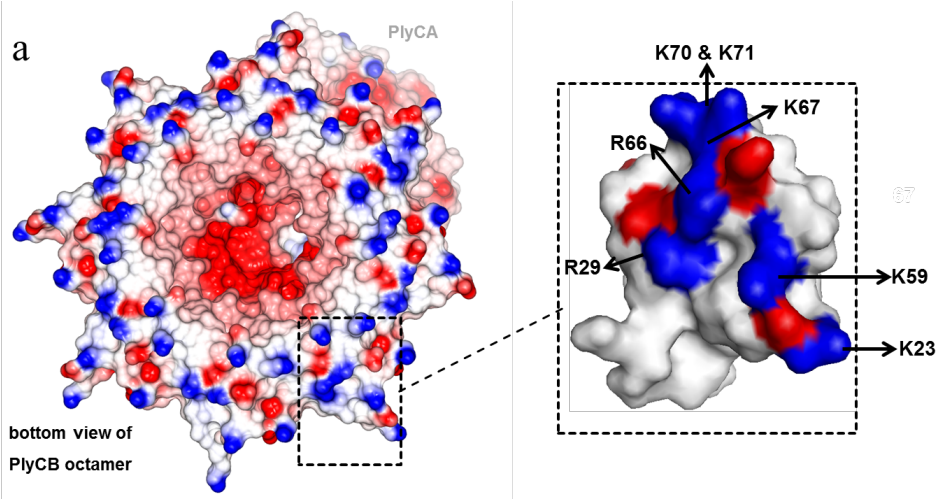

Figure 9.2: Electrostatic surface potential PlyCB binding domain. The protein surface is color-coded according to electrostatic potential: positive and negative charges are shown in blue and red, respectively. The enlarged view at the right shows a binding pocket structure, which is composed of several cationic residues. The pocket has been identified as crucial for specific phospholipid binding and initiating PlyC internalization into mammalian cells.

9.1.1 PlyCB electrostatic map

Further studies determined that internalization is specific to one of the PlyC subunits. PlyCB is the domain responsible for mediating the translocation of the PlyC holoenzyme across the plasma membrane. The PlyC crystal structure provided key insights into the origin of PlyCB-membrane interactions. At neutral pH, the PlyCB octamer net charge is positive (pI = 8.5), and its solvent accessible surface contains 48 cationic residues, two arginine and four lysine on each monomer. Cationic amino acid patches frequently promote membrane adhesion and may result in membrane penetration. As previously mentioned, PlyCB possesses the intrinsic capacity to internalize in eukaryotic cells. The cationic residues, lysines and arginines, are the key elements that mediate binding and interaction with the plasma membrane. Also described is a cationic binding pocket on the surface-active interface of PlyCB, on which Arg66 is one of the critical residues for lipid binding. To explore the roles of cationic residues in PlyC binding, site direct-mutant PlyCB-R66E, which has an arginine replaced by a glutamine, and has lost its ability to directly translocate the PM, was also probed.

9.2 Results

9.2.1 PlyCB binding to stBLMs containing anionic lipids shows specificity for PS

A phosphoinositide array indicated that PlyCB associates with anionic lipids, preferentially PA and PS suggesting that the binding has elements of specificity and it is not driven purely by electrostatics. SPR experiments were carried out on mixed stBLMs containing various anionic

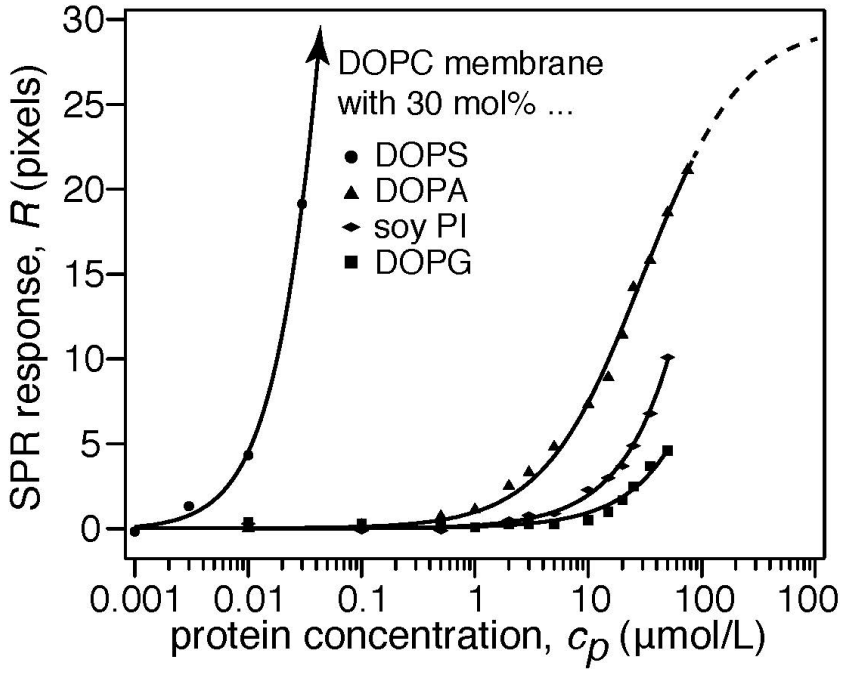

Figure 9.3: Affinity of wt PlycB to negatively charged tethered lipid bilayer membranes containing neutral DOPC and anionic lipids at 30 mol% under physiologically relevant conditions (150 mM NaCl at pH 7.4). The isotherm for DOPC:DOPS = 70:30 is only partially shown. Data at cp $>$ 10 μM were corrected for protein contributions to the optical index of the buffer. Buffer rinses following protein incubations removed bound PlyCB from PG, PI and PA-containing membranes. PlyCB binds poorly to PA, PG and PI (phosphatidic acid, phosphatidylglycerol and phosphatidylinositol - membrane lipids that bear the same charge as phosphatidylserine but have slightly distinct molecular structures). The much stronger protein adsorption to PS shows clearly the specificity of PlyCB to this plasma membrane lipid

lipids (PS, PG, PI and PA) in a background of DOPC. After forming the stBLMs and characterizing them with EIS, PlyCB in PBS (pH 7.4) at 150 mmol/L NaCl was injected into the sample chamber at concentrations between 0.01 and 50 μmol/L. Control experiments with PlyCB on pure DOPC stBLMs showed no detectable protein binding. Figure 9.3 shows an exemplary SPR result and summarizes results obtained with a constant concentration of 30 mol% anionic lipid in DOPC-based stBLMs. PlyCB binds poorly to PG and PI (equilibrium binding constant, K_d $>>$ 10 μmol/L), and shows only low affinity to PA (K_d = 26.9 $\pm$ 2.9 μmol/L), as observed in Fig. 9.3. In all these cases, rinsing the membranes with protein-free buffer after protein binding reverts the SPR signal to baseline as seen in Figure 9.4A. Figure 9.3 also shows a (partial) adsorption isotherm of PlyCB to a DOPC:DOPS stBLM at 30 mol% anionic lipid which visualizes clearly how much stronger the protein binds to PS. Here, binding is observed starting from $c_p \approx$ 10 nmol/L and results in an R_∞ value that far exceeds that observed with PA ($\sim$ 180 ng/cm^2).

9.2.2 PlyCB membrane affinity depends on PS concentration

Figure 9.5 shows the binding of PlyCB to stBLMs with PS concentrations between 10 and 30 mol%. At PS $>$ 20 mol%, the adsorption isotherms no longer followed simple Langmuir be-

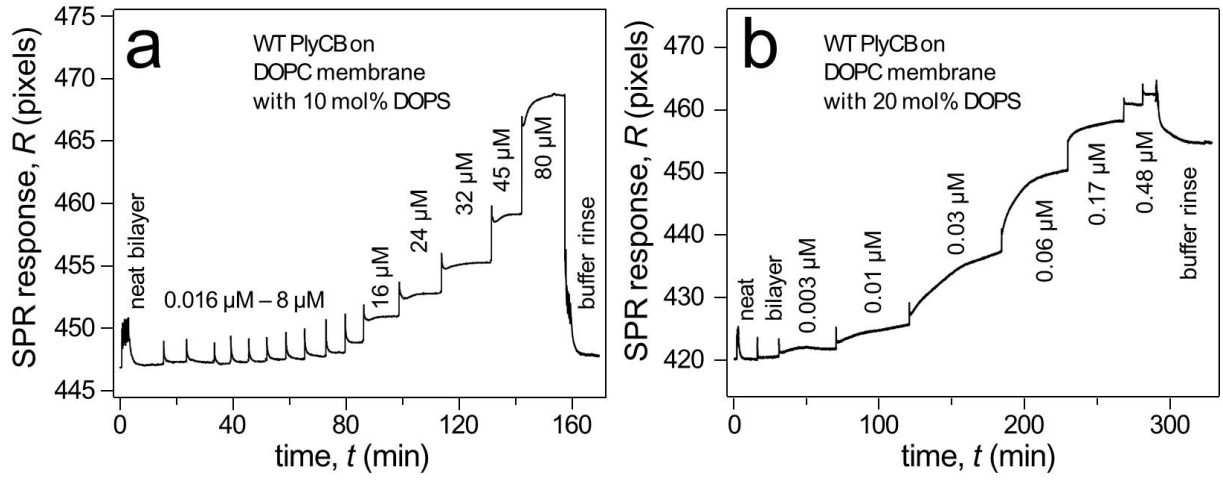

Figure 9.4: Binding of PlyCB to stBLMs with 10 and 20 mol% DOPS, respectively. Each spike indicates an injection with an increased concentration of protein. A final buffer rinse removes the adsorbed protein quantitatively on 10 mol% PS, but only partially on 20 mol% PS, indicating that the association of the protein with the membrane surface may differ depending on PS concentration

havior but were well described by Hill functions with N $>$ 1 (Table 9.1). On membranes that contained 30 mol% PS, both the affinity of the protein (K_d = 40 $\pm$ 10 nmol/L) and its surface density ($R_\infty \approx$ 400 ng/cm^2) were very high. In fact, R_∞ is larger, by a factor of $\approx$ 2, than expected for a densely packed protein monolayer in which the PlyCB units are aligned with their putative membrane-binding interface on the bilayer. Buffer rinses of stBLMs that contained PS at $>$ 15 mol% removed the bound protein only partially (Figure 9.4B). While membrane binding of PlyCB is extremely strong at high PS concentration, its affinity decreases rapidly at lower PS content. Figure 9.5 shows that bilayers with 20 mol% PS show similar characteristics to membranes at 30 mol% (k_d = 40 nmol/L). However, at 15 mol% PS, K_d increases to $\approx$ 0.5 μmol/L, and at 10 mol% PS, bilayers have essentially lost their affinity for phosphatidylserine. At the same time, protein binding has lost its collective character, as adsorption isotherms at 15 mol% PS, but not at higher PS concentrations, are well described by a Langmuir adsorption process (N = 1). Moreover, adsorbed protein is washed off completely by buffer rinses of membranes with low PS content. However, PlyCB is progressively more retained as PS contents increases. We therefore observe a threshold behavior of PlyCB binding to PS-containing bilayers where membranes at PS concentrations $>$ 15 mol% behave distinctly different from membranes at $<$ 15 mol%.

The fact that PlyCB binds strongly to PS-containing bilayers at concentrations $>$ 15 mol% when compared to membranes containing anionic lipids at the same charge density, implies that both electrostatic attraction and specific binding contribute to PlyCB interaction with the membrane. To test whether an electrostatic component of the interaction can be provided by a distinct lipid than PS, with the same charge but differing in headgroup geometry, we measured the affinity of the protein to an stBLM that was composed of PC:PA:PS = 7:2:1 (Fig. 9.6). We observed that the binding was much stronger in this case ($K_d \approx$ 1.2 μ mol/L) than to membranes

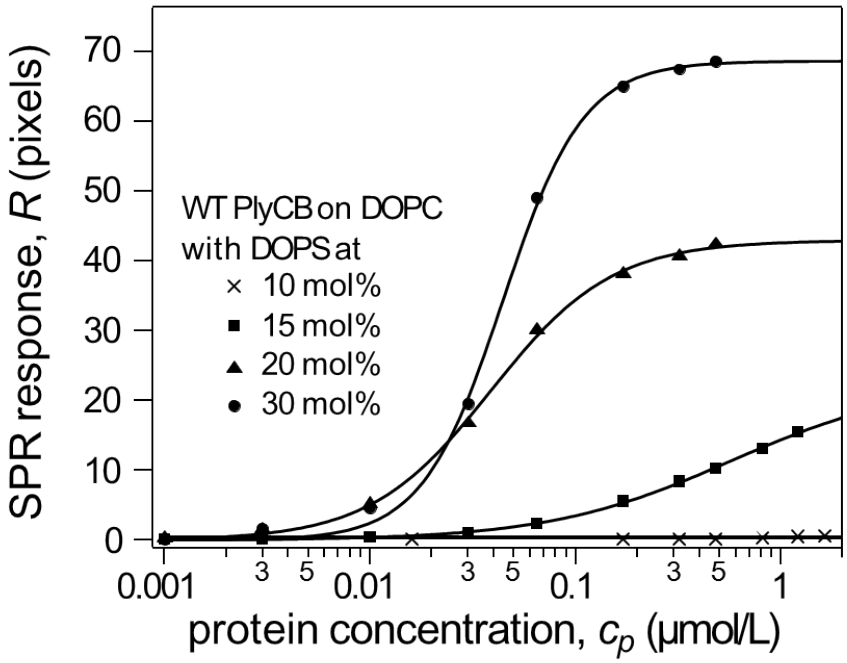

Figure 9.5: Roles of specific interaction of PlyCB with PS and electrostatic interaction in membrane binding. Affinity of PlyCB in 150 mM NaCl at pH 7.4 to stBLMs that contain DOPC and DOPS. (A) wt PlyCB binding to binary membranes with DOPC and various concentrations of DOPS. Inset presents an exemplary data set (20 mol% DOPS) and shows that PlyCB protein remains bound to the membrane after a buffer rinse. A similar resistence to washoff of the protein is observed with 30 mol% PS in the bilayer.

with 10 mol% of PS or 30 mol% PA as the only anionic lipid, but not as strong as to stBLMs containing 20 mol% PS. As for the weak binding to membranes containing only PA as anionic lipid, a simple Langmuir isotherm describes the binding well. The affinity and surface coverage of PlyCB to the ternary PC:PA:PS 7:2:1 is similar to the DOPC:DOPS 85:15 system. However, once you rinse the system with protein-free buffer most of the protein remains at the interface which indicates PlyCB might insert on the membrane at those condition

To establish the minimum amount of PS required to maintain PlyCB high affinity to the membranes, the amounts of PS were systematically decreased and replaced with PA, keeping the total charge density constant at 30 mol%. At 2.5mol% PS PlyCB has lost its affinity to the system, the K_d values are similar to 30 mol% PA-only membrane. Experiments also showed that PlyCB binds poorly to membranes containing 10%PS only and 30 mol% of either PI or PG. Binding of PlyCB to ternary membranes containing 10%PS and 20% PG or PI increases significantly ($K_d \sim 11$ μM for PG and ~ 20 μM for PI) see Table 9.1 for values. At 2.5 mol% PS the binding is negligible such as it is when you have 30 mol % PG. All the protein adsorbed is removed from the interface after buffer rinse when PS content is below or equal to 2.5 mol%.

To confirm PS specificity of PlyCB interaction with the membrane, we tested the mutant PlyCB-R66E, which lacks the ability to translocate the plasma membrane, for its affinity to stBLMs. In the mutant, an Arg residue in a cationic patch on the putative membrane binding interface, identified as critical for PlyC membrane transgression, is replaced with a Glu, reversing

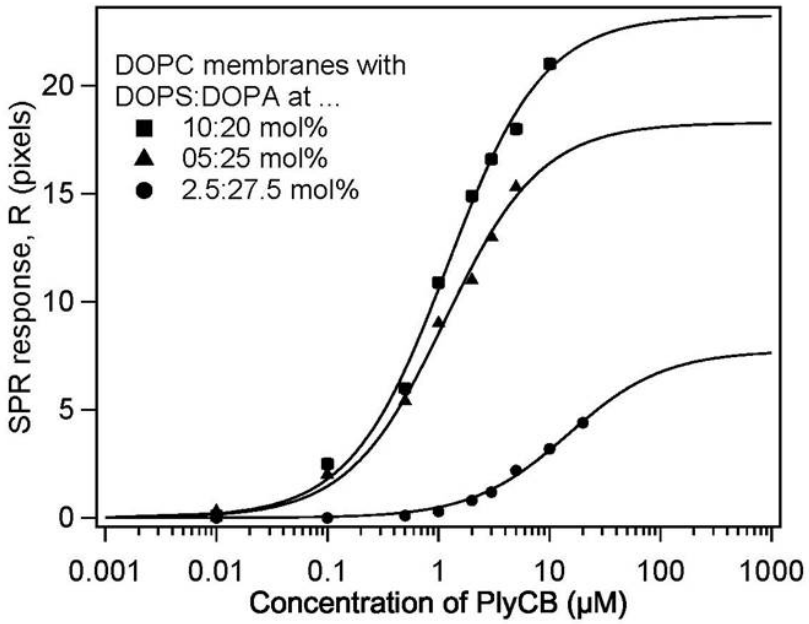

Figure 9.6: WT PlyCB binding to a ternary membranes composed of DOPC:DOPA:DOPS, systematically replacing PS by PA. Both electrostatic attraction and specific interaction contribute to PlyCB interaction to the membranes. At 2.5 mol% PS PlyCB lost its high affinity

the charge at this position. As shown in Fig. 9.7, PlyCB essentially loses its affinity for a membrane with 30 mol% PS, a composition to which wt PlyCB binds with high affinity and avidity

9.2.3 Membrane response to PlyCB binding

EIS was used to assess bilayer quality and monitor changes in its electrochemical characteristics - bilayer resistance and capacitance - in response to PlyCB binding. Figure 9.9 shows exemplary Cole-Cole plots of an stBLM (DOPC:DOPS = 70:30) before and after protein incubation (480 nmol/L PlyCB). This data shows that PlyCB association with the bilayer affects the structural integrity of the membrane only minimally. In particular, it is interesting to note that the resistivity of the bilayer remains high, even after the protein inserts into the membrane (as shown by NR below). EIS was systematically recorded as a function of protein concentration for DOPC stBLMs containing 15 and 30 mol% DOPS. In addition, a control experiment was performed with PlyCB-R66E on DOPC:DOPS = 7:3. In concentration ranges near the half-saturation concentrations, both wt PlyCB on PC:PS = 85:15 and PlyCB-R66E on PC:PS = 7:3 showed no significant changes in membrane capacitance and resistance (data not shown). While capacitances did not change at all (less than $\pm$ 1%) for c_p up to 1.2 μmol/L (PlyCB on PC:PS = 85:15) and c_p up to 50 μmol/L (PlyCB-R66E on PC:PS = 7:3), resistances dropped by $\approx$10% (1.2 μM PlyCB on PC:PS = 85:15) and $<$ 5% (50 μM PlyCB-R66E on PC:PS = 7:3). For wt PlyCB on PC:PS = 7:3, we detected small changes of the membrane parameters. The capacitance increases by $\approx$ 4% and the resistance drops by $\approx$ 25% at c_p = 480 nmol/L. However, this reduction left the

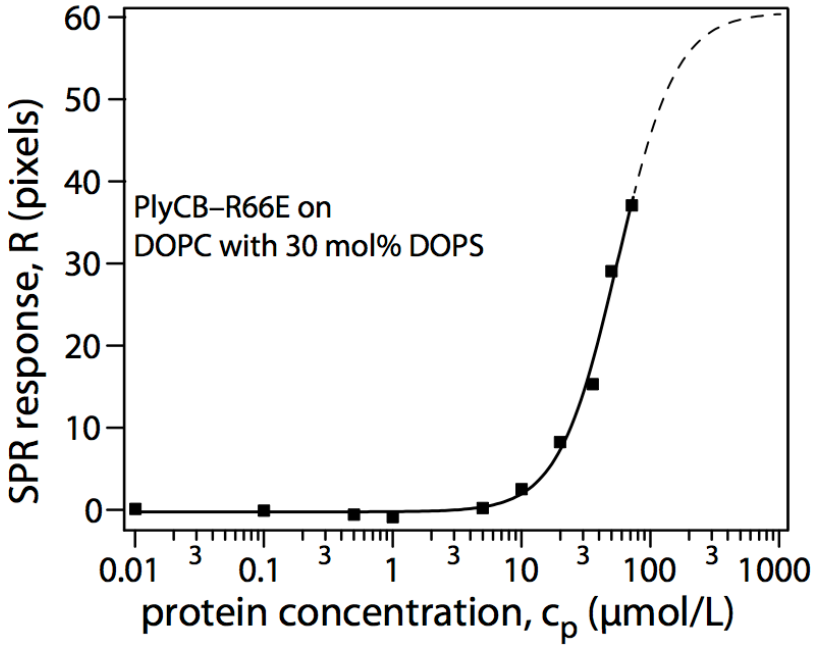

Figure 9.7: PlyCB-R66E binding to a binary stBLM containing DOPC with 30 mol% DOPS. Data at $c_p > 10$ μM were corrected for protein contributions to the optical index of the buffer

membrane still at a resistance of 100 kΩcm^2.

9.2.4 PlyCB localization at PS-containing membranes depends on PS concentration

In view of these SPR results, the localization of PlyCB with respect to the membrane as a function of PS concentration was characterized with neutron reflection (NR). Initial measurements prior to protein incubation confirmed the EIS results in suggesting that all stBLMs contain high-quality lipid membranes. Subsequently, neutron data were collected at multiple protein concentrations and, eventually, after a final rinse with protein-free buffer. In order to obtain high densities of the protein at the membrane surfaces, protein concentrations were chosen near the saturation of the Langmuir isotherms presented in Fig. 9.4. Each of the measurements was performed at multiple isotopic water compositions of the buffer. This contrast-variation approach permits the determination of unique bilayer-protein complex structures, as shown earlier [158] [156] [113] [69], in terms of one-dimensional lipid/protein distributions as a function of the distance from the interface, z, which we refer to as component volume occupancy (CVO) profiles [68] [124]. Figure 9.10 illustrates how the PlyCB-membrane complexes at saturating concentrations on PC/PS stBLMs show distinctly different overall structures on 15 and 30 mol% DOPS. At 15 mol% PS, PlyCB forms a diffuse layer of protein that extends at least 200 Åout from the membrane surface (Fig. 9.10a: 5 μmol/L PlyCB in the buffer that baths the membrane). However, while the lateral protein density is highest near the membrane surface, it remains low at any z. Importantly, the NR experiments shows that protein insertion into the membrane is negligible. Overall, the CVO

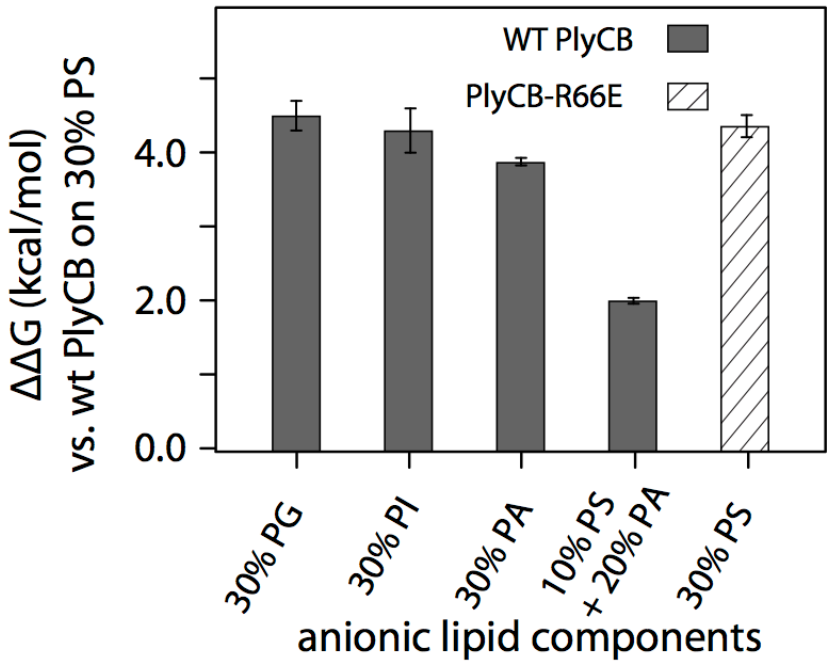

Figure 9.8: Summary of protein affinities, displayed as differences in Free Energy of membrane binding $\Delta G = k_B T \ln K_d$, for membranes with 30 mol% anionic lipids of various compositions as indicated with respect to WT PlyCB on 30 mol% PS. This graph visualizes that the binding of WT protein to PG, PI or PA is much weaker than to PS (positive deviations of $\Delta\Delta G$ indicate lower affinities) and that a low concentration of PS with a larger concentration of PA restores some of the protein binding. Similarly, the R66E mutant of PlyCB binds to 30 mol% PS with a similarly low affinity as that of WT PlyCB to 30 mol% PI

profile suggests that PlyCB at this saturating concentration forms an open-mesh network of protein on the membrane surface that has a thickness of $\approx$ 20 nm, and does not penetrate the bilayer. Following a rinse with protein-free buffer, we observed that this diffuse protein layer essentially remained attached to the interface, although some protein was lost (data not shown). At high DOPS concentration, PlyCB associates with stBLMs in a different complex. Figure 4B shows the CVO profile of the protein on DOPC:DOPS 70:30 at c_p = 600 nmol/L. At this concentration, the protein is deeply inserted in the membrane and spans across its entire thickness, headgroup to headgroup. More protein is superficially adsorbed and forms a CVO peak at a distance of $\approx$ 20 Åabove the membrane surface. Flushing the membrane with protein-free buffer removed this adsorbed protein, as shown in Fig. 9.10C. The CVO profile after the flush shows that the PlyCB protein retained within the membrane is almost symmetrically distributed across the tethered bilayer and occupies up to 10% of the bilayer volume. The protein CVOs shown in Fig. 9.10 for stBLMs in contact with protein-containing solutions extend beyond the size of a single PlyCB octamer, and were modeled by continuous spline-based distributions. The CVO profiles shown in Fig. 9.10A, in particular, indicates a compact protein layer within the membrane which can be related to the known crystal structure of PlyC [115]. Using the PlyCB structure, we interpreted the NR data also by combining a continuous distribution of bilayer components [156] with the

Table 9.1: Best-fit parameters from fitting Hill equation to SPR data shown in Fig. 9.3, 9.5 .

Protein	Lipid composition	K_d (μM)	R_∞ (ng/cm^2)	N
wt PlyCB	DOPC:DOPG 70:30	$>>$ 50	n.d	n.d.
	DOPC:soy PI 70:30	$>$50	n.d	n.d.
	DOPC:DOPA 70:30	26.9 $\pm$2.9	170 $\pm$ 8	(Langmuir fit)
	DOPC:DOPS 90:10	$>>$ 50	n.d.	n.d.
	DOPC:DOPS 85:15	0.49 $\pm$0.02	128.8 $\pm$2.7	1.0 $\pm$0.1
	DOPC:DOPS 80:20	0.04 $\pm$0.01	251.7 $\pm$0.4	1.5 $\pm$0.1
	DOPC:DOPS 70:30	0.04 $\pm$0.01	402.5 $\pm$2.5	2.2 $\pm$0.2
	DOPC:DOPA:DOPS 70:20:10	1.2 $\pm$0.1	134.6 $\pm$1.2	(Langmuir fit)
	DOPC:DOPA:DOPS 70:25:05	1.1 $\pm$0.1	104.6 $\pm$1.2	(Langmuir fit)
	DOPC:DOPA:DOPS 70:27.5:2.5	17 $\pm$3	48 $\pm$4	(Langmuir fit)
	DOPC:DOPG:DOPS 70:20:10	11.2 $\pm$0.5	96 $\pm$3	(Langmuir fit)
	DOPC:DOPG:DOPS 70:25:5	15.4 $\pm$1.0	54 $\pm$1.8	(Langmuir fit)
	DOPC:DOPG:DOPS 70:27.5:2.5	no binding	—	—
	DOPC:soyPI:DOPS 70:20:10	17.4 $\pm$1.2	102 $\pm$6	(Langmuir fit)
PlyCB-R66E	DOPC:DOPS 70:30	62.2 $\pm$ 22.2	331 $\pm$72	2.0 $\pm$0.05

crystal structure by optimizing the distance and orientation of the protein at the membrane, as described in Chapter 3. This rigid body modeling approach resembled the protein distribution determined with the spline fit very well (black trace in Fig. 9.10A), which suggests that the inserted protein spans the bilayer at a well-defined angle which leads to a match with the bilayer thickness. Data resampling was performed to determine the most likely orientation angle of the protein within the bilayer and its distribution, see Chapter 3 for more details. Only two Euler angles are relevant in the rigid body rotation, which were chosen to be the inclination θ of the eight-fold symmetry axis against the membrane normal and the rotation γ of the toroidal protein body around this symmetry axis. The distribution of these angles show that most likely PlyCB orientation forms high angles at the membrane, inclination angle θ is slightly larger than 60. Not surprisingly, ϕ is equally distributed along the arc defined by θ, reflecting the eight-fold symmetry of the toroidal PlyCB protein body (Figure 9.12). A second interpretation, also in agreement with the protein envelope obtained by the spline fit, consists of two PlyCB stacked in the bilayer.

9.3 Discussion

Internalization of PlyC is initiated by structural interactions between a cationic pocket on PlyCB and phospholipids of the plasma membrane as indicated by phospholipid screening assays. Our results suggest a model for PlyC interaction with plasma membranes in which a cationic binding groove on the protein surface is a central determinant of successful internalization. We propose that PlyC internalization initiates as membrane binding through electrostatic interaction and specific ligation with PS. Our SPR binding studies show that PS plays an eminent role in PlyCB membrane binding and may be the cellular ligand that mediates protein binding to the plasma membrane. In semi-quantitative terms, this result is echoed in Rosetta protein-ligand docking

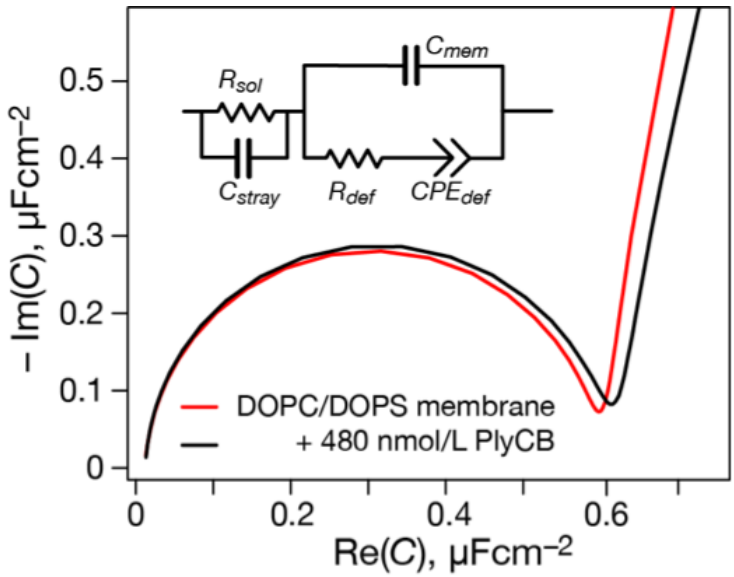

Figure 9.9: PlyCB membrane binding distorts bilayer integrity only minimally. Raw EIS spectra (Cole-Cole plots) of an stBLM (DOPC:DOPS = 7:3) as prepared (red) and after incubation with 480 nmol/L PlyCB (black trace). While the EIS spectra were measured between 10 kHz and 1 Hz, the spectra shown here cover only the range, 10 kHz to 13.6 Hz in order to visualize the capacitive semi-circles well. Upon protein interaction with the membrane, the bilayer capacitance increases slightly and its resistivity decreases by $\approx$ 25%, as determined by fitting to the ECM shown in the inset. Other protein incubation experiments showed even less disturbances of the bilayer membrane than those in this graph.

models. For PS and PE, only distinguished through the seryl carboxyl, the results for lipids with truncated fatty acid chains suggest that PS has a lower interface energy ($>$ 3.5 kcal/mol) than that of PE.

We note that the docking calculations performed by our collaborators are consistent with the experimental PlyCB-membrane binding data, even though the agreement could be fortuitous if various approximations in the docking analysis compensate. Indeed, the free energy difference between docked PS and PE compares well with the difference in ΔG observed between PlyCB binding to PS-containing membranes and to membranes without this specific phospholipid ligand. PlyC binding to purely zwitterionic membranes is weak and has not been thoroughly studied, but the binding to non-specific anionic lipids or the binding of PlyCB-R66E to PS are good proxies which both show Δ ΔG values around 4 kcal/mol (Fig. 9.8), which is of the same order of magnitude as the docking result, while somewhat oversimplified, capture the essence of the specificity observed for PS lipid. The failure of PlyCB-R66E to bind tightly to PS membranes relies on the fact that the mutation is a response to conformational changes in the PlyCB pocket, that can no longer accommodate the PS-headgroup geometry.

PS is an important component of eukaryotic cellular membranes preferentially found on the inner plasma membrane leaflet. Disruption of membrane asymmetry is known to follow apoptosis. On the other hand, recent studies [173] [154] show that membrane inversion is not unique for cell death, and some viruses, such as the vesicular stomatitis virus, utilize PS as the cellular receptor [18] It is therefore plausible that PS can also act as a receptor for PlyC, even more so as

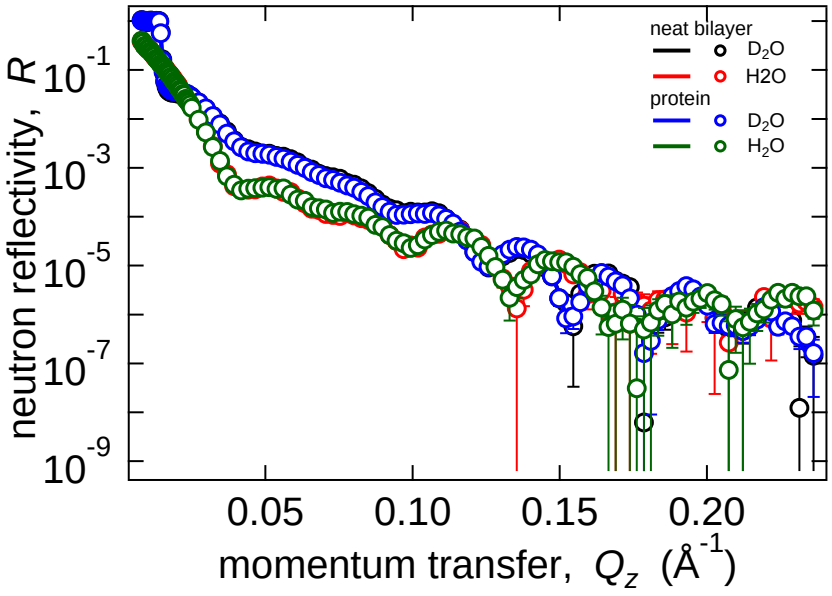

Figure 9.10: Neutron reflectivity raw data for DOPC:DOPS 70:30 neat stBLM (black and red) and in contact with 600 nM of PlyCB (blue and green) in H_2O and D_2O contrasts

PS equilibration across the plasma membrane is more likely for cells stressed by pathogen invasion. In another cell biological analogy, annexin A5 binds PS reversibly in a calcium-dependent manner and is often used as a marker for apoptosis. PlyC might penetrate cells in a similar mechanism, as PlyCB possesses eight potential PS binding sites, each on the outer surface of the octamer. While further experimental evidence is required, it is tempting to speculate that parallels between the PS-driven membrane interaction of annexins and PlyC may produce membrane invaginations that lead to PlyC endocytosis.

Finally, the identification of PlyCB as the shuttle that catalyzes cellular entry of the catalytic PlyCA subunit opens the possibility for molecular engineering to fuse distinct cargos onto the PlyCB scaffold for delivery into mammalian cells.

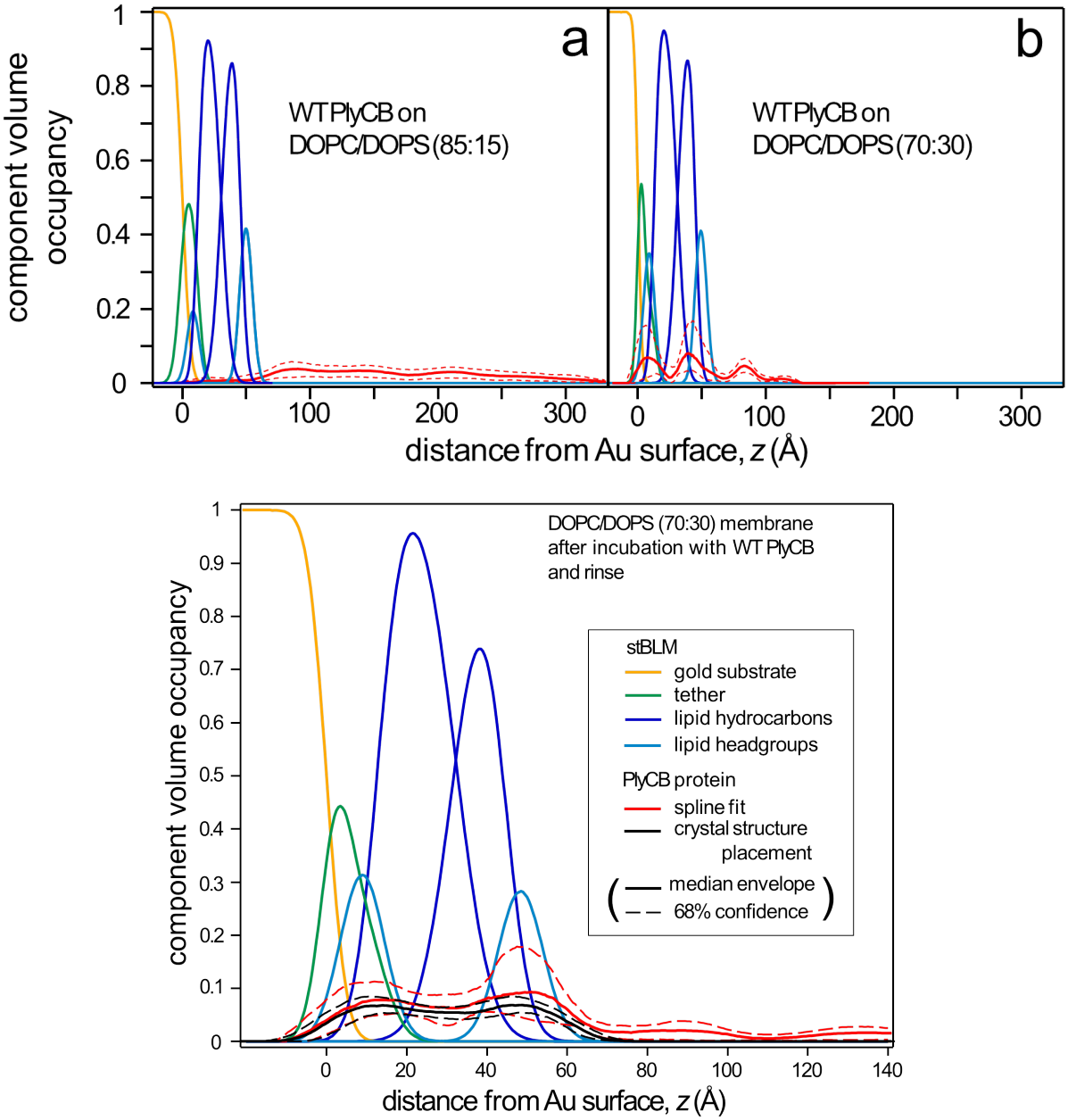

Figure 9.11: PlyCB forms distinct membraneprotein complexes at high and low PS content of the bilayer. CVO profiles of membrane-bound PlyCB on DOPC stBLMs containing (a) 15 mol% and (b,c) 30 mol% DOPS. Neutron reflection experiments were performed on neat bilayers and on bilayers in contact with protein-containing solutions (5 μM and 600 nM in panels a and b, respectively), and co-refined. While the CVO profile in (a) shows accumulation of protein outside the bilayer, but no incorporation into the membrane, the protein inserts deeply into the PS-rich bilayer, as indicated by the CVO profiles in panel b. The same stBLM DOPC:DOPS 70:30 as in after a buffer rinse. Only the structures of the stBLMs in the presence of PlyCB protein are shown. The CVO profile shows the protein remains deeply inserted into the PS-rich bilayer even after rinse (red trace). The loosely associated protein from the membrane surface was removed. Comparison of the median orientation fit using PlyCB crystal structure is shown with its associated 68% confidence intervals(black trace)

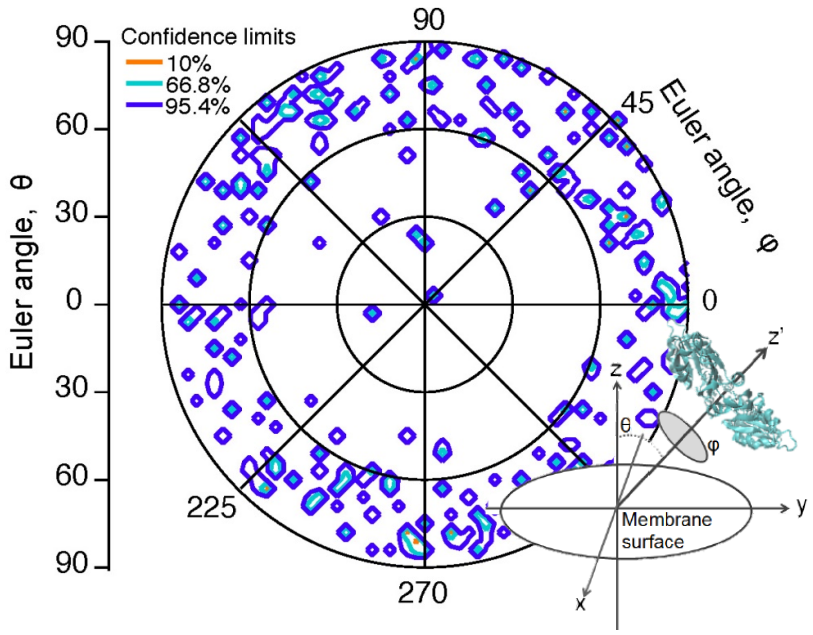

Figure 9.12: Probability distribution of PlyCB orientations (θ,ϕ) with respect to the DOPC:DOPS 70:30 bilayer normal. The most likely distribution of PlyCB inclination angle θ is larger than 60 and ϕ is equally distributed along the arc defined by θ, reflecting the symmetry of PlyCB.

Bibliography

[1] A. Alfadhli and E. Barklis. The roles of lipids and nucleic acids in HIV-1 assembly. *Front. Microbiol.*, 5:253, jan 2014. 1.1, 1.1.1

[2] A. Alfadhli, R. L. Barklis, and E. Barklis. HIV-1 matrix organizes as a hexamer of trimers on membranes containing phosphatidylinositol-(4,5)-bisphosphate. *Virology*, 387(2):466–72, may 2009. 5.2.1

[3] R. C. Aloia, F. C. Jensen, C. C. Curtain, P. W. Mobley, and L. M. Gordon. Lipid composition and fluidity of the human immunodeficiency virus. *Proc. Natl. Acad. Sci. U. S. A.*, 85(3):900–4, feb 1988. 5.2.1, 5.2.1, 6.3.4, 6.4

[4] S. Amir Reza, A. S. M. Noor, and M. M. Moksin. *Plasmonics - Principles and Applications*. InTech, 2012. (document), 3.6

[5] K. Anraku, R. Fukuda, N. Takamune, S. Misumi, Y. Okamoto, M. Otsuka, and M. Fujita. Highly sensitive analysis of the interaction between HIV-1 Gag and phosphoinositide derivatives based on surface plasmon resonance. *Biochemistry*, 49(25):5109–16, jun 2010. 5.2.1, 6.4

[6] S. J. Attwood, Y. Choi, and Z. Leonenko. Preparation of DOPC and DPPC Supported Planar Lipid Bilayers for Atomic Force Microscopy and Atomic Force Spectroscopy. *Int. J. Mol. Sci.*, 14(2):3514–39, jan 2013. 4.3

[7] S. Barer, Robert Joseph, editor. *Refractometry of living cells. Part I. Basic principles*. Department of Human Anatomy, Oxford, 1955. 3.2.5

[8] Y. Barsukov and J. R. Macdonald, editors. *Imepdancy spectroscopy: Theory, Experiment, and Applications*. John Wiley Sons, Inc., Hoboken,NJ, 2005. 3.1.2

[9] J. Benesch, A. Askendal, and P. Tengvall. Quantification of adsorbed human serum albumin at solid interfaces: a comparison between radioimmunoassay (RIA) and simple null ellipsometry. *Colloids Surfaces B Biointerfaces*, 18(2):71–81, aug 2000. 3.2.5

[10] J. A. G. Briggs, M. C. Johnson, M. N. Simon, S. D. Fuller, and V. M. Vogt. Cryo-electron microscopy reveals conserved and divergent features of gag packing in immature particles of Rous sarcoma virus and human immunodeficiency virus. *J. Mol. Biol.*, 355(1):157–68, jan 2006. 5.1, 5.2.2

[11] R. E. Brown and H. L. Brockman. Using monomolecular films to characterize lipid lateral interactions. *Methods Mol. Biol.*, 398:41–58, jan 2007. 2.2.1

[12] B. Brügger, B. Glass, P. Haberkant, I. Leibrecht, F. T. Wieland, and H.-G. Kräusslich. The HIV lipidome: a raft with an unusual composition. *Proc. Natl. Acad. Sci. U. S. A.*, 103(8):2641–6, feb 2006. 5.2.1, 5.2.1, 6.3.4, 6.4

[13] M. Bryant and L. Ratner. Myristoylation-dependent replication and assembly of human immunodeficiency virus 1. *Proc. Natl. Acad. Sci. U. S. A.*, 87(2):523–7, jan 1990. 6.4

[14] R. Budvytyte, G. Valincius, G. Niaura, V. Voiciuk, M. Mickevicius, H. Chapman, H.-Z. Goh, P. Shekhar, F. Heinrich, S. Shenoy, M. Lösche, and D. J. Vanderah. Structure and properties of tethered bilayer lipid membranes with unsaturated anchor molecules. *Langmuir*, 29(27):8645–56, jul 2013. 2.2.3, 2.2.4, 4.3, 4.5

[15] D. L. Bush and V. M. Vogt. In Vitro Assembly of Retroviruses. *Annu. Rev. Virol.*, 1(1):561–580, nov 2014. 1.1

[16] S. Campbell, R. J. Fisher, E. M. Towler, S. Fox, H. J. Issaq, T. Wolfe, L. R. Phillips, and a. Rein. Modulation of HIV-like particle assembly in vitro by inositol phosphates. *Proc. Natl. Acad. Sci. U. S. A.*, 98(19):10875–9, sep 2001. 5.3.1

[17] S. Campbell and V. M. Vogt. In vitro assembly of virus-like particles with Rous sarcoma virus Gag deletion mutants: identification of the p10 domain as a morphological determinant in the formation of spherical particles. *J. Virol.*, 71(6):4425–35, jun 1997. 5.3.1, 8.2.3

[18] F. A. Carneiro, P. A. Lapido-Loureiro, S. M. Cordo, F. Stauffer, G. Weissmüller, M. L. Bianconi, M. A. Juliano, L. Juliano, P. M. Bisch, A. T. Da Poian, and Poian. Probing the interaction between vesicular stomatitis virus and phosphatidylserine. *Eur. Biophys. J.*, 35(2):145–54, jan 2006. 9.3

[19] E. Catmull and R. Rom. *Computer Aided Geometric Design*. Elsevier, 1974. 3.3.5

[20] J. Chan, R. a. Dick, and V. M. Vogt. Rous sarcoma virus gag has no specific requirement for phosphatidylinositol-(4,5)-bisphosphate for plasma membrane association in vivo or for liposome interaction in vitro. *J. Virol.*, 85(20):10851–60, oct 2011. 8.2.2

[21] R. Chan, P. D. Uchil, J. Jin, G. Shui, D. E. Ott, W. Mothes, and M. R. Wenk. Retroviruses human immunodeficiency virus and murine leukemia virus are enriched in phosphoinositides. *J. Virol.*, 82(22):11228–38, nov 2008. 5.2.1, 6.4

[22] Y.-H. M. Chan and S. G. Boxer. Model membrane systems and their applications. *Curr. Opin. Chem. Biol.*, 11(6):581–7, dec 2007. 1, 4.1

[23] K. S. Chang, C. Chou, and C. H. Lin. Focused-beam attenuated total-reflection technique on absorptive film in Kretschmann's configuration. *Appl. Opt.*, 32(16):2957–62, jun 1993. 3.2.2

[24] L. Charlier, M. Louet, L. Chaloin, P. Fuchs, J. Martinez, D. Muriaux, C. Favard, and N. Floquet. Coarse-grained simulations of the HIV-1 matrix protein anchoring: revisiting its assembly on membrane domains. *Biophys. J.*, 106(3):577–85, feb 2014. 6.4, 6.5

[25] E. Chertova, O. Chertov, L. V. Coren, J. D. Roser, C. M. Trubey, J. W. Bess, R. C. Sowder, E. Barsov, B. L. Hood, R. J. Fisher, K. Nagashima, T. P. Conrads, T. D. Veenstra, J. D.

Lifson, and D. E. Ott. Proteomic and biochemical analysis of purified human immunodeficiency virus type 1 produced from infected monocyte-derived macrophages. *J. Virol.*, 80(18):9039–52, sep 2006. 6.4

[26] N. J. Cho, S. J. Cho, K. H. Cheong, J. S. Glenn, and C. W. Frank. Employing an amphipathic viral peptide to create a lipid bilayer on Au and TiO2. *J. Am. Chem. Soc.*, 129(33):10050–1, aug 2007. 4.2.2

[27] N. J. Cho, S. J. Cho, J. O. Hardesty, J. S. Glenn, and C. W. Frank. Creation of lipid partitions by deposition of amphipathic viral peptides. *Langmuir*, 23(21):10855–63, oct 2007. 4.2.2

[28] N.-J. Cho, G. Wang, M. Edvardsson, J. S. Glenn, F. Hook, and C. W. Frank. Alpha-helical peptide-induced vesicle rupture revealing new insight into the vesicle fusion process as monitored in situ by quartz crystal microbalance-dissipation and reflectometry. *Anal. Chem.*, 81(12):4752–61, jun 2009. 4.2.2

[29] G. Choi, S. Park, B. Choi, S. Hong, J. Lee, E. Hunter, and S. S. Rhee. Identification of a Cytoplasmic Targeting/Retention Signal in a Retroviral Gag Polyprotein. *J. Virol.*, 73(7):5431–5437, jul 1999. 1.1

[30] V. Chukkapalli, I. B. Hogue, V. Boyko, W.-S. Hu, and A. Ono. Interaction between the human immunodeficiency virus type 1 Gag matrix domain and phosphatidylinositol-(4,5)-bisphosphate is essential for efficient gag membrane binding. *J. Virol.*, 82(5):2405–17, mar 2008. 8.2.2

[31] J. M. Coffin, S. H. Hughes, and H. E. Varmus. Retroviruses, 1997. 5.1

[32] B. A. Cornell, V. L. Braach-Maksvytis, L. G. King, P. D. Osman, B. Raguse, L. Wieczorek, and R. J. Pace. A biosensor that uses ion-channel switches. *Nature*, 387(6633):580–3, jun 1997. 4.2

[33] R. Cseh and R. Benz. Interaction of phloretin with lipid monolayers: relationship between

structural changes and dipole potential change. *Biophys. J.*, 77(3):1477–88, sep 1999. 2.2.1

[34] I. Czolkos, A. Jesorka, and O. Orwar. Molecular phospholipid films on solid supports. *Soft Matter*, 7(10):4562, may 2011. 2.2

[35] D. L. Daleke. Regulation of phospholipid asymmetry in the erythrocyte membrane. *Curr. Opin. Hematol.*, 15(3):191–5, may 2008. 2.1.1

[36] A. K. Dalton, D. Ako-Adjei, P. S. Murray, D. Murray, and V. M. Vogt. Electrostatic interactions drive membrane association of the human immunodeficiency virus type 1 Gag MA domain. *J. Virol.*, 81(12):6434–45, jun 2007. 5.2.1, 6.4, 6.5

[37] A. K. Dalton, P. S. Murray, D. Murray, and V. M. Vogt. Biochemical characterization of rous sarcoma virus MA protein interaction with membranes. *J. Virol.*, 79(10):6227–38, may 2005. 6.3.1, 6.5

[38] S. A. K. Datta, J. E. Curtis, W. Ratcliff, P. K. Clark, R. M. Crist, J. Lebowitz, S. Krueger, and A. Rein. Conformation of the HIV-1 Gag protein in solution. *J. Mol. Biol.*, 365(3):812–24, jan 2007. 5.2.2, 5.3.1, 5.3.2, 6.4, 8.4

[39] S. A. K. Datta, F. Heinrich, S. Raghunandan, S. Krueger, J. E. Curtis, A. Rein, and H. Nanda. HIV-1 Gag extension: conformational changes require simultaneous interaction with membrane and nucleic acid. *J. Mol. Biol.*, 406(2):205–14, feb 2011. (document), 1, 2.3.2, 5.2.2, 5.4, 5.3.2, 8.1

[40] S. A. K. Datta, X. Zuo, P. K. Clark, S. J. Campbell, Y.-X. Wang, and A. Rein. Solution properties of murine leukemia virus gag protein: differences from HIV-1 gag. *J. Virol.*, 85(23):12733–41, dec 2011. 5.3.1, 5.3.2, 8.1, 8.3.2, 8.3.3

[41] A. de Marco, N. E. Davey, P. Ulbrich, J. M. Phillips, V. Lux, J. D. Riches, T. Fuzik, T. Ruml, H.-G. Kräusslich, V. M. Vogt, and J. A. G. Briggs. Conserved and variable features of Gag structure and arrangement in immature retrovirus particles. *J. Virol.*,

84(22):11729–36, nov 2010. 5.1

[42] F. de Meyer and B. Smit. Effect of cholesterol on the structure of a phospholipid bilayer. *Proc. Natl. Acad. Sci. U. S. A.*, 106(10):3654–8, mar 2009. 6.4

[43] P. F. Devaux and A. Zachowski. Maintenance and consequences of membrane phospholipid asymmetry. *Chem. Phys. Lipids*, 73(1-2):107–120, sep 1994. 2.1.1

[44] R. A. Dick, S. A. K. Datta, H. Nanda, X. Fang, Y. Wen, M. Barros, Y.-X. Wang, A. Rein, and V. M. Vogt. Hydrodynamic and Membrane Binding Properties of Purified Rous Sarcoma Virus Gag Protein. *J. Virol.*, 89(20):10371–82, oct 2015. 5.3.2, 8.1, 8.2.3, 8.4

[45] R. A. Dick, S. L. Goh, G. W. Feigenson, and V. M. Vogt. HIV-1 Gag protein can sense the cholesterol and acyl chain environment in model membranes. *Proc. Natl. Acad. Sci. U. S. A.*, 109(46):18761–6, nov 2012. 6.3.2, 6.4

[46] B. R. Dorvel, H. M. Keizer, D. Fine, J. Vuorinen, A. Dodabalapur, and R. S. Duran. Formation of tethered bilayer lipid membranes on gold surfaces: QCM-Z and AFM study. *Langmuir*, 23(13):7344–55, jun 2007. 2.2.3, 4.1

[47] M. Eeman and M. Deleu. From biological membranes to biomimetic model membranes, 2010. 2.2

[48] L. S. Ehrlich, S. Fong, S. Scarlata, G. Zybarth, and C. Carter. Partitioning of HIV-1 Gag and Gag-related proteins to membranes. *Biochemistry*, 35(13):3933–43, apr 1996. 5.2.1

[49] D. M. Engelman. Membranes are more mosaic than fluid. *Nature*, 438(7068):578–80, dec 2005. 2.1.1

[50] A. Erbe, R. J. Bushby, S. D. Evans, and L. J. C. Jeuken. Tethered bilayer lipid membranes studied by simultaneous attenuated total reflectance infrared spectroscopy and electrochemical impedance spectroscopy. *J. Phys. Chem. B*, 111(13):3515–24, apr 2007. 2.2.4

[51] B. Fadeel and D. Xue. The ins and outs of phospholipid asymmetry in the plasma membrane: roles in health and disease. *Crit. Rev. Biochem. Mol. Biol.*, 44(5):264–77, 2009.

2.1.1

[52] G. W. Feigenson. Phase boundaries and biological membranes. *Annu. Rev. Biophys. Biomol. Struct.*, 36:63–77, jan 2007. 6.3.2

[53] V. A. Fischetti. Bacteriophage lysins as effective antibacterials. *Curr. Opin. Microbiol.*, 11(5):393–400, oct 2008. 1.2

[54] V. A. Fischetti. Bacteriophage endolysins: a novel anti-infective to control Gram-positive pathogens. *Int. J. Med. Microbiol.*, 300(6):357–62, aug 2010. 1.2

[55] E. L. Fledderman, K. Fujii, R. H. Ghanam, K. Waki, P. E. Prevelige, E. O. Freed, and J. S. Saad. Myristate exposure in the human immunodeficiency virus type 1 matrix protein is modulated by pH. *Biochemistry*, 49(44):9551–62, nov 2010. (document), 5.2, 5.2.1, 7.3.2, 7.3.2

[56] E. O. Freed. HIV-1 gag proteins: diverse functions in the virus life cycle. *Virology*, 251(1):1–15, nov 1998. 5.1

[57] E. O. Freed. HIV-1 assembly, release and maturation. *Nat. Rev. Microbiol.*, 13(8):484–496, jun 2015. 1.1, 5.1

[58] F. N. Fritsch and R. E. Carlson. Monotone Piecewise Cubic Interpolation. *SIAM J. Numer. Anal.*, 17(2):238–246, apr 1980. 3.3.5

[59] S. D. Fuller, T. Wilk, B. E. Gowen, H.-G. Kräusslich, and V. M. Vogt. Cryo-electron microscopy reveals ordered domains in the immature HIV-1 particle. *Curr. Biol.*, 7(10):729–738, oct 1997. 5.1, 5.2.2, 5.3.1, 6.4

[60] G. Gaines. *Insoluble monolayers at liquid-gas interfaces*. Interscience Publishers, New York, 1966. 2.2.1

[61] H. Gao, J. Feng, G. A. Luo, A. L. Ottova, and H. Ti Tien. Some Electrochemical Features of Supported Bilayer Lipid Membranes. *Electroanalysis*, 13(1):49–53, jan 2001. 2.2.3

[62] R. B. Gennis. *Biomembranes*. Springer Advanced Texts in Chemistry. Springer New York,

New York, NY, 1989. 2.1.1

[63] H. G. Göttlinger, J. G. Sodroski, and W. A. Haseltine. Role of capsid precursor processing and myristoylation in morphogenesis and infectivity of human immunodeficiency virus type 1. *Proc. Natl. Acad. Sci. U. S. A.*, 86(15):5781–5, aug 1989. 6.4

[64] E. Hamard-Peron, F. Juillard, J. S. Saad, C. Roy, P. Roingeard, M. F. Summers, J.-L. Darlix, C. Picart, and D. Muriaux. Targeting of Murine Leukemia Virus Gag to the Plasma Membrane Is Mediated by PI(4,5)P2/PS and a Polybasic Region in the Matrix. *J. Virol.*, 84(1):503–515, oct 2009. 6.4

[65] E. Hamard-Peron and D. Muriaux. Retroviral matrix and lipids, the intimate interaction. *Retrovirology*, 8(1):15, jan 2011. 5.2.1, 5.2.1, 6.5

[66] N. S. Hatzakis, V. K. Bhatia, J. Larsen, K. L. Madsen, P.-Y. Bolinger, A. H. Kunding, J. Castillo, U. Gether, P. Hedegård, and D. Stamou. How curved membranes recruit amphipathic helices and protein anchoring motifs. *Nat. Chem. Biol.*, 5(11):835–41, nov 2009. 7.2.1

[67] T. Heimburg. *Thermal Biophysics of Membranes*. Tutorials in Biophysics. Wiley-VCH Verlag GmbH & Co. KGaA, Weinheim, Germany, jul 2007. 2.1.1

[68] F. Heinrich and M. Lösche. Zooming in on disordered systems: neutron reflection studies of proteins associated with fluid membranes. *Biochim. Biophys. Acta*, 1838(9):2341–9, sep 2014. 2.3.2, 9.2.4

[69] F. Heinrich, H. Nanda, H. Z. Goh, C. Bachert, M. Lösche, and A. D. Linstedt. Myristoylation restricts orientation of the GRASP domain on membranes and promotes membrane tethering. *J. Biol. Chem.*, 289(14):9683–91, apr 2014. 2.3.1, 3.3.5, 3.3.5, 9.2.4

[70] F. Heinrich, T. Ng, D. J. Vanderah, P. Shekhar, M. Mihailescu, H. Nanda, and M. Lösche. A new lipid anchor for sparsely tethered bilayer lipid membranes. *Langmuir*, 25(7):4219–29, apr 2009. 2.2.4, 2.2.4, 3.1.4, 4.3, 4.4.1

[71] Heinz Raether. *Surface Plasmons on Smooth and Rough Surfaces and on Gratings*, volume 111 of *Springer Tracts in Modern Physics*. Springer Berlin Heidelberg, 1988. 3.2.1

[72] C. P. Hill, D. Worthylake, D. P. Bancroft, a. M. Christensen, and W. I. Sundquist. Crystal structures of the trimeric human immunodeficiency virus type 1 matrix protein: implications for membrane association and assembly. *Proc. Natl. Acad. Sci. U. S. A.*, 93(7):3099–104, apr 1996. 5.2.1, 5.2.1

[73] A. Hinderliter and S. May. Cooperative adsorption of proteins onto lipid membranes. *J. Phys. Condens. Matter*, 18(28):S1257–70, jul 2006. 3.2.5

[74] I. B. Hogue, J. R. Grover, F. Soheilian, K. Nagashima, and A. Ono. Gag induces the coalescence of clustered lipid rafts and tetraspanin-enriched microdomains at HIV-1 assembly sites on the plasma membrane. *J. Virol.*, 85(19):9749–66, oct 2011. 5.2.1, 6.4

[75] W.-C. Hung, M.-T. Lee, F.-Y. Chen, and H. W. Huang. The condensing effect of cholesterol in lipid bilayers. *Biophys. J.*, 92(11):3960–7, jun 2007. 2.1.1

[76] W.-C. Hung, M.-T. Lee, F.-Y. Chen, and H. W. Huang. The condensing effect of cholesterol in lipid bilayers. *Biophys. J.*, 92(11):3960–7, jun 2007. 6.4

[77] I. Iacovache, M. Bischofberger, and F. G. van der Goot. Structure and assembly of pore-forming proteins. *Curr. Opin. Struct. Biol.*, 20(2):241–6, apr 2010. 1

[78] J. N. Israelachvili, D. J. Mitchell, and B. W. Ninham. Theory of self-assembly of hydrocarbon amphiphiles into micelles and bilayers. *J. Chem. Soc. Faraday Trans. 2*, 72:1525, jan 1976. 6.4

[79] F. Jaehnig, K. Harlos, H. Vogel, and H. Eibl. Electrostatic interactions at charged lipid membranes. Electrostatically induced tilt. *Biochemistry*, 18(8):1459–1468, apr 1979. 4.5

[80] M. K. Jain. Biomembranes: Molecular structure and function. *Cell*, 58(5):813–814, sep 1989. 2.1.1

[81] K. C. Jambo, D. H. Banda, A. M. Kankwatira, N. Sukumar, T. J. Allain, R. S. Heyderman,

D. G. Russell, and H. C. Mwandumba. Small alveolar macrophages are infected preferentially by HIV and exhibit impaired phagocytic function. *Mucosal Immunol.*, 7(5):1116–26, sep 2014. 5.2.1

[82] J. Jass, T. Tjärnhage, and G. Puu. From liposomes to supported, planar bilayer structures on hydrophilic and hydrophobic surfaces: an atomic force microscopy study. *Biophys. J.*, 79(6):3153–63, dec 2000. 1, 4.1

[83] Z. Jiang, R. E. Redfern, Y. Isler, A. H. Ross, and A. Gericke. Cholesterol stabilizes fluid phosphoinositide domains. *Chem. Phys. Lipids*, 182:52–61, sep 2014. 6.4

[84] C. A. Keller and B. Kasemo. Surface specific kinetics of lipid vesicle adsorption measured with a quartz crystal microbalance. *Biophys. J.*, 75(3):1397–1402, sep 1998. 4.5

[85] N. Kempf, V. Postupalenko, S. Bora, P. Didier, Y. Arntz, H. de Rocquigny, and Y. Mély. The HIV-1 nucleocapsid protein recruits negatively charged lipids to ensure its optimal binding to lipid membranes. *J. Virol.*, 89(3):1756–67, feb 2015. 6.4

[86] M. W. Kendig. Nonlinear Current Response of Electrochemical Systems. *J. Electrochem. Soc.*, 131(12):2777, dec 1984. 3.1.2

[87] M. S. Kent, J. K. Murton, D. Y. Sasaki, S. Satija, B. Akgun, H. Nanda, J. E. Curtis, J. Majewski, C. R. Morgan, and J. R. Engen. Neutron reflectometry study of the conformation of HIV Nef bound to lipid membranes. *Biophys. J.*, 99(6):1940–8, sep 2010. 2.3.2

[88] A. Kerviel, A. Thomas, L. Chaloin, C. Favard, and D. Muriaux. Virus assembly and plasma membrane domains: which came first? *Virus Res.*, 171(2):332–40, feb 2013. 6.4

[89] M. S. Khan, N. S. Dosoky, and J. D. Williams. Engineering lipid bilayer membranes for protein studies. *Int. J. Mol. Sci.*, 14(11):21561–97, jan 2013. 2.2.3

[90] B. J. Kirby, P. A. Kienzle, B. B. Maranville, N. F. Berk, J. Krycka, F. Heinrich, and C. F. Majkrzak. Phase-sensitive specular neutron reflectometry for imaging the nanometer scale composition depth profile of thin-film materials. *Curr. Opin. Colloid Interface Sci.*,

17(1):44–53, feb 2012. 3.3.5

[91] M. M. Kozlov. Biophysics: Joint effort bends membrane. *Nature*, 463(7280):439–40, jan 2010. 2.1.1

[92] E. Kretschmann. Die Bestimmung optischer Konstanten von Metallen durch Anregung von Oberflchenplasmaschwingungen. *Zeitschrift fr Phys.*, 241(4):313–324, aug 1971. 3.2.1

[93] G. Krishna, J. Schulte, B. A. Cornell, R. J. Pace, and P. D. Osman. Tethered Bilayer Membranes Containing Ionic Reservoirs: Selectivity and Conductance. *Langmuir*, 19(6):2294–2305, mar 2003. 3.1.4

[94] N. Kučerka, S. Tristram-Nagle, and J. F. Nagle. Structure of Fully Hydrated Fluid Phase Lipid Bilayers with Monounsaturated Chains. *J. Membr. Biol.*, 208(3):193–202, apr 2006. 6.4

[95] R. Lahdo and L. De La Fournière-Bessueille. Insertion of the amyloid precursor protein into lipid monolayers: effects of cholesterol and apolipoprotein E. *Biochem. J.*, 382(Pt 3):987–94, sep 2004. 2.2.1

[96] M. Leslie. A lifeline for lipid rafts? *J. Cell Biol.*, 202(1):3–3, jul 2013. 2.1.1

[97] R. N. A. H. Lewis and R. N. McElhaney. Membrane lipid phase transitions and phase organization studied by Fourier transform infrared spectroscopy. *Biochim. Biophys. Acta*, 1828(10):2347–58, oct 2013. 2.1.1

[98] M. E. Linde, D. R. Colquhoun, C. Ubaida Mohien, T. Kole, V. Aquino, R. Cotter, N. Edwards, J. E. K. Hildreth, and D. R. Graham. The conserved set of host proteins incorporated into HIV-1 virions suggests a common egress pathway in multiple cell types. *J. Proteome Res.*, 12(5):2045–54, may 2013. 6.4

[99] R. Lindner and H. Y. Naim. Domains in biological membranes. *Exp. Cell Res.*, 315(17):2871–8, oct 2009. 2.1.1, 2.1.1

[100] O. W. Lindwasser and M. D. Resh. Myristoylation as a target for inhibiting HIV assembly: unsaturated fatty acids block viral budding. *Proc. Natl. Acad. Sci. U. S. A.*, 99(20):13037–42, oct 2002. 6.4

[101] D. Lingwood and K. Simons. Lipid rafts as a membrane-organizing principle. *Science*, 327(5961):46–50, jan 2010. 6.3.2

[102] J. Lipkowski. Building biomimetic membrane at a gold electrode surface. *Phys. Chem. Chem. Phys.*, 12(42):13874–87, nov 2010. 2.2

[103] H. Lodish, A. Berk, S. L. Zipursky, P. Matsudaira, D. Baltimore, and J. Darnell. Biomembranes: Structural Organization and Basic Functions, 2000. 1, 2.1.1

[104] N. Lukoyanova, S. C. Kondos, I. Farabella, R. H. P. Law, C. F. Reboul, T. T. Caradoc-Davies, B. A. Spicer, O. Kleifeld, D. A. K. Traore, S. M. Ekkel, I. Voskoboinik, J. A. Trapani, T. Hatfaludi, K. Oliver, E. M. Hotze, R. K. Tweten, J. C. Whisstock, M. Topf, H. R. Saibil, and M. A. Dunstone. Conformational changes during pore formation by the perforin-related protein pleurotolysin. *PLoS Biol.*, 13(2):e1002049, feb 2015. 1

[105] G. Ma and H. C. Allen. DPPC Langmuir monolayer at the air-water interface: probing the tail and head groups by vibrational sum frequency generation spectroscopy. *Langmuir*, 22(12):5341–9, jun 2006. 2.2.1

[106] R. Machán and M. Hof. Lipid diffusion in planar membranes investigated by fluorescence correlation spectroscopy. *Biochim. Biophys. Acta*, 1798(7):1377–91, jul 2010. 2.2.3

[107] A. I. Magee and I. Parmryd. Detergent-resistant membranes and the protein composition of lipid rafts. *Genome Biol.*, 4(11):234, jan 2003. 2.1.1

[108] C. F. Majkrzak, N. F. Berk, S. Krueger, J. A. Dura, M. Tarek, D. Tobias, V. Silin, C. W. Meuse, J. Woodward, and A. L. Plant. First-principles determination of hybrid bilayer membrane structure by phase-sensitive neutron reflectometry. *Biophys. J.*, 79(6):3330–40, dec 2000. 3.3.4

[109] C. Mariani, M. Desdouits, C. Favard, P. Benaroch, and D. M. Muriaux. Role of Gag and lipids during HIV-1 assembly in CD4(+) T cells and macrophages. *Front. Microbiol.*, 5:312, jan 2014. 5.2.1

[110] M. A. Massiah, M. R. Starich, C. Paschall, M. F. Summers, A. M. Christensen, and W. I. Sundquist. Three-dimensional structure of the human immunodeficiency virus type 1 matrix protein. *J. Mol. Biol.*, 244(2):198–223, nov 1994. 5.2.1

[111] S. Matthews, P. Barlow, J. Boyd, G. Barton, R. Russell, H. Mills, M. Cunningham, N. Meyers, N. Burns, and N. Clark. Structural similarity between the p17 matrix protein of HIV-1 and interferon-gamma. *Nature*, 370(6491):666–8, aug 1994. 5.2.1

[112] J. M. McDonnell, D. Fushman, S. M. Cahill, W. Zhou, A. Wolven, C. B. Wilson, T. D. Nelle, M. D. Resh, J. Wills, and D. Cowburn. Solution structure and dynamics of the bioactive retroviral M domain from Rous sarcoma virus. *J. Mol. Biol.*, 279(4):921–8, jun 1998. 8.2.2

[113] D. J. McGillivray, G. Valincius, F. Heinrich, J. W. F. Robertson, D. J. Vanderah, W. Febo-Ayala, I. Ignatjev, M. Lösche, and J. J. Kasianowicz. Structure of Functional Staphylococcus aureus α-Hemolysin Channels in Tethered Bilayer Lipid Membranes. *Biophys. J.*, 96(4):1547–1553, feb 2009. 2.2.4, 9.2.4

[114] D. J. McGillivray, G. Valincius, D. J. Vanderah, W. Febo-Ayala, J. T. Woodward, F. Heinrich, J. J. Kasianowicz, and M. Lösche. Molecular-scale structural and functional characterization of sparsely tethered bilayer lipid membranes. *Biointerphases*, 2(1):21–33, mar 2007. 2.2.3, 2.2.4, 2.2.4, 3.1.3, 3.1.4, 4.3, 4.4.1

[115] S. McGowan, A. M. Buckle, M. S. Mitchell, J. T. Hoopes, D. T. Gallagher, R. D. Heselpoth, Y. Shen, C. F. Reboul, R. H. P. Law, V. A. Fischetti, J. C. Whisstock, and D. C. Nelson. X-ray crystal structure of the streptococcal specific phage lysin PlyC. *Proc. Natl. Acad. Sci. U. S. A.*, 109(31):12752–7, jul 2012. 9.1, 9.2.4

[116] S. McLaughlin, J. Wang, A. Gambhir, and D. Murray. PIP(2) and proteins: interactions, organization, and information flow. *Annu. Rev. Biophys. Biomol. Struct.*, 31:151–75, jan 2002. 4.5, 6.4

[117] T. T. Mills, J. Huang, G. W. Feigenson, and J. F. Nagle. Effects of cholesterol and unsaturated DOPC lipid on chain packing of saturated gel-phase DPPC bilayers. *Gen. Physiol. Biophys.*, 28(2):126–39, jun 2009. 2.1.1

[118] H. Möhwald. Phospholipid and phospholipid-protein monolayers at the air/water interface. *Annu. Rev. Phys. Chem.*, 41:441–76, jan 1990. 2.2.1

[119] S. Munro. Lipid Rafts. *Cell*, 115(4):377–388, nov 2003. 2.1.1

[120] P. S. Murray, Z. Li, J. Wang, C. L. Tang, B. Honig, and D. Murray. ostatic homology: models for membrane binding function throughout the viral life cycle.Retroviral matrix domains share electr. *Structure*, 13(10):1521–31, oct 2005. 5.2.1

[121] P. S. Murray, Z. Li, J. Wang, C. L. Tang, B. Honig, and D. Murray. Retroviral matrix domains share electrostatic homology: models for membrane binding function throughout the viral life cycle. *Structure*, 13(10):1521–31, oct 2005. 5.2.1

[122] S. Nadaraia-Hoke, D. V. Bann, T. L. Lochmann, N. Gudleski-O'Regan, and L. J. Parent. Alterations in the MA and NC domains modulate phosphoinositide-dependent plasma membrane localization of the Rous sarcoma virus Gag protein. *J. Virol.*, 87(6):3609–15, mar 2013. 8.2.2

[123] H. Nanda, S. A. K. Datta, F. Heinrich, M. Lösche, A. Rein, S. Krueger, and J. E. Curtis. Electrostatic interactions and binding orientation of HIV-1 matrix studied by neutron reflectivity. *Biophys. J.*, 99(8):2516–24, oct 2010. 2.2.4, 2.3.2, 3.3.5, 6.3.1, 6.3.1, 6.4, 7.1, 7.1, 7.4, 8.2.3

[124] H. Nanda, F. Heinrich, and M. Lösche. Membrane association of the PTEN tumor suppressor: Neutron scattering and MD simulations reveal the structure of proteinmembrane

complexes. *Methods*, 77-78:136–146, may 2015. 2.3.2, 9.2.4

[125] T. D. Nelle and J. W. Wills. A large region within the Rous sarcoma virus matrix protein is dispensable for budding and infectivity. *J. Virol.*, 70(4):2269–76, apr 1996. 8.2.2

[126] D. Nelson, R. Schuch, P. Chahales, S. Zhu, and V. a. Fischetti. PlyC: a multimeric bacteriophage lysin. *Proc. Natl. Acad. Sci. U. S. A.*, 103(28):10765–70, jul 2006. 9.1

[127] S. Nisole and A. Saïb. Early steps of retrovirus replicative cycle. *Retrovirology*, 1(1):9, jan 2004. 5.1

[128] I. P. O'Carroll, R. M. Crist, J. Mirro, D. Harvin, F. Soheilian, A. Kamata, K. Nagashima, and A. Rein. Functional redundancy in HIV-1 viral particle assembly. *J. Virol.*, 86(23):12991–6, dec 2012. 6.4

[129] A. Ono. Relationships between plasma membrane microdomains and HIV-1 assembly. *Biol. Cell*, 102(6):335–50, jun 2010. 5.2.1, 6.4

[130] A. Ono, S. D. Ablan, S. J. Lockett, K. Nagashima, and E. O. Freed. Phosphatidylinositol (4,5) bisphosphate regulates HIV-1 Gag targeting to the plasma membrane. *Proc. Natl. Acad. Sci. U. S. A.*, 101(41):14889–94, oct 2004. 8.2.2

[131] a. Ono and E. O. Freed. Plasma membrane rafts play a critical role in HIV-1 assembly and release. *Proc. Natl. Acad. Sci. U. S. A.*, 98(24):13925–30, nov 2001. 5.2.1, 6.4

[132] A. Ono, J. M. Orenstein, and E. O. Freed. Role of the Gag matrix domain in targeting human immunodeficiency virus type 1 assembly. *J. Virol.*, 74(6):2855–66, mar 2000. 5.2.1

[133] A. Ono, A. A. Waheed, A. Joshi, and E. O. Freed. Association of human immunodeficiency virus type 1 gag with membrane does not require highly basic sequences in the nucleocapsid: use of a novel Gag multimerization assay. *J. Virol.*, 79(22):14131–40, nov 2005. 8.2.2

[134] A. Otto. Excitation of nonradiative surface plasma waves in silver by the method of

frustrated total reflection. *Zeitschrift fr Phys.*, 216(4):398–410, aug 1968. 3.2.1

[135] J. Pan, T. T. Mills, S. Tristram-Nagle, and J. F. Nagle. Cholesterol perturbs lipid bilayers nonuniversally. *Phys. Rev. Lett.*, 100(19):198103, may 2008. 2.1.1, 6.3.2

[136] J. Pan, S. Tristram-Nagle, and J. Nagle. Effect of cholesterol on structural and mechanical properties of membranes depends on lipid chain saturation. *Phys. Rev. E*, 80(2):021931, aug 2009. 2.1.1, 6.4

[137] S. A. Pandit, S.-W. Chiu, E. Jakobsson, A. Grama, and H. L. Scott. Cholesterol packing around lipids with saturated and unsaturated chains: a simulation study. *Langmuir*, 24(13):6858–65, jun 2008. 6.4

[138] L. G. Parratt. Surface Studies of Solids by Total Reflection of X-Rays. *Phys. Rev.*, 95(2):359–369, jul 1954. 3.3.2

[139] C. Peetla, A. Stine, and V. Labhasetwar. Biophysical interactions with model lipid membranes: applications in drug discovery and drug delivery. *Mol. Pharm.*, 6(5):1264–76, jan 2009. (document), 2.3

[140] J. Penfold. Neutron reflectivity and soft condensed matter. *Curr. Opin. Colloid Interface Sci.*, 7(1-2):139–147, mar 2002. 3.3.1

[141] R. Phillips, T. Ursell, P. Wiggins, and P. Sens. Emerging roles for lipids in shaping membrane-protein function. *Nature*, 459(7245):379–85, may 2009. 2.1.1

[142] S. Pöyry, T. Róg, M. Karttunen, and I. Vattulainen. Significance of cholesterol methyl groups. *J. Phys. Chem. B*, 112(10):2922–9, mar 2008. 6.4

[143] W. H. Press. *Numerical Recipes 3rd Edition: The Art of Scientific Computing*. Cambridge University Press, 2007. 3.3.5

[144] G. Puu and I. Gustafson. Planar lipid bilayers on solid supports from liposomes factors of importance for kinetics and stability. *Biochim. Biophys. Acta - Biomembr.*, 1327(2):149–161, jul 1997. 4.3

[145] E. Reimhult, F. Höök, and B. Kasemo. Intact Vesicle Adsorption and Supported Biomembrane Formation from Vesicles in Solution: Influence of Surface Chemistry, Vesicle Size, Temperature, and Osmotic Pressure . *Langmuir*, 19(5):1681–1691, mar 2003. 4.5

[146] A. Rein, M. R. McClure, N. R. Rice, R. B. Luftig, and A. M. Schultz. Myristylation site in Pr65gag is essential for virus particle formation by Moloney murine leukemia virus. *Proc. Natl. Acad. Sci. U. S. A.*, 83(19):7246–50, oct 1986. 6.4

[147] M. D. Resh. Fatty acylation of proteins: new insights into membrane targeting of myristoylated and palmitoylated proteins. *Biochim. Biophys. Acta*, 1451(1):1–16, aug 1999. 5.2.1

[148] J. D. Robertson. The molecular structure and contact relationships of cell membranes. *Prog. Biophys. Mol. Biol.*, 10:343–418, jan 1960. 2.1.1

[149] J. S. Saad, J. Miller, J. Tai, A. Kim, R. H. Ghanam, and M. F. Summers. Structural basis for targeting HIV-1 Gag proteins to the plasma membrane for virus assembly. *Proc. Natl. Acad. Sci. U. S. A.*, 103(30):11364–9, jul 2006. (document), 5.2.1, 5.2.1, 5.2.1, 5.3, 5.2.1, 6.1, 6.3.3, 6.4, 6.5

[150] E. Sackmann. Supported Membranes: Scientific and Practical Applications. *Science (80).*, 271(5245):43–48, jan 1996. 2.2, 2.2.4

[151] J. R. Sambles, G. W. Bradbery, and F. Yang. Optical excitation of surface plasmons: An introduction. *Contemp. Phys.*, 32(3):173–183, may 1991. 3.2.1

[152] R. B. M. Schasfoort and A. J. Tudos, editors. *Handbook of Surface Plasmon Resonance*. Royal Society of Chemistry, Cambridge, 2008. (document), 3.2.2, 3.5, 3.2.2, 3.2.5

[153] P. Schuck. Use of surface plasmon resonance to probe the equilibrium and dynamic aspects of interactions between biological macromolecules. *Annu. Rev. Biophys. Biomol. Struct.*, 26:541–66, jan 1997. 3.2.1

[154] K. Segawa, J. Suzuki, and S. Nagata. Constitutive exposure of phosphatidylserine on

viable cells. *Proc. Natl. Acad. Sci. U. S. A.*, 108(48):19246–51, nov 2011. 9.3

[155] A. P. Serro, A. Carapeto, G. Paiva, J. P. S. Farinha, R. Colaço, and B. Saramago. Formation of an intact liposome layer adsorbed on oxidized gold confirmed by three complementary techniques: QCM-D, AFM and confocal fluorescence microscopy. *Surf. Interface Anal.*, 44(4):426–433, apr 2012. 2.2.3

[156] P. Shekhar, H. Nanda, M. Lösche, and F. Heinrich. Continuous distribution model for the investigation of complex molecular architectures near interfaces with scattering techniques. *J. Appl. Phys.*, 110(10):102216–10221612, nov 2011. 3.3.5, 3.3.5, 9.2.4

[157] S. Shenoy, R. Moldovan, J. Fitzpatrick, D. J. Vanderah, M. Deserno, and M. Lösche. In-plane homogeneity and lipid dynamics in tethered bilayer lipid membranes (tBLMs). *Soft Matter*, 2010(6):1263–1274, jan 2010. 2.2.3, 2.2.4, 2.2.4, 4.1

[158] S. Shenoy, P. Shekhar, F. Heinrich, M.-C. Daou, A. Gericke, A. H. Ross, and M. Lösche. Membrane association of the PTEN tumor suppressor: molecular details of the protein-membrane complex from SPR binding studies and neutron reflection. *PLoS One*, 7(4):e32591, jan 2012. 2.3.2, 3.2.5, 3.3.5, 9.2.4

[159] S. S. Shenoy, H. Nanda, and M. Lösche. Membrane association of the PTEN tumor suppressor: electrostatic interaction with phosphatidylserine-containing bilayers and regulatory role of the C-terminal tail. *J. Struct. Biol.*, 180(3):394–408, dec 2012. 1, 2.3.2

[160] V. V. Shvadchak, L. J. Falomir-Lockhart, D. A. Yushchenko, and T. M. Jovin. Specificity and kinetics of alpha-synuclein binding to model membranes determined with fluorescent excited state intramolecular proton transfer (ESIPT) probe. *J. Biol. Chem.*, 286(15):13023–32, apr 2011. 7.2.1

[161] K. Simons and R. Ehehalt. Cholesterol, lipid rafts, and disease. *J. Clin. Invest.*, 110(5):597–603, sep 2002. 6.4

[162] K. Simons and E. Ikonen. Functional rafts in cell membranes. *Nature*, 387(6633):569–72,

jun 1997. 2.1.1, 2.1.1

[163] K. Simons and J. L. Sampaio. Membrane organization and lipid rafts. *Cold Spring Harb. Perspect. Biol.*, 3(10):a004697, oct 2011. 2.1.1

[164] K. Simons and G. van Meer. Lipid sorting in epithelial cells. *Biochemistry*, 27(17):6197–202, aug 1988. 2.1.1

[165] S. J. Singer and G. L. Nicolson. The fluid mosaic model of the structure of cell membranes. *Science*, 175(4023):720–31, feb 1972. 2.1.1

[166] E. Stansell, R. Apkarian, S. Haubova, W. E. Diehl, E. M. Tytler, and E. Hunter. Basic residues in the Mason-Pfizer monkey virus gag matrix domain regulate intracellular trafficking and capsid-membrane interactions. *J. Virol.*, 81(17):8977–88, sep 2007. 1.1

[167] W. I. Sundquist and H.-G. Kräusslich. HIV-1 assembly, budding, and maturation. *Cold Spring Harb. Perspect. Med.*, 2(7):a006924, jul 2012. 1.1, 5.1, 6.4

[168] L. K. Tamm and H. M. McConnell. Supported phospholipid bilayers. *Biophys. J.*, 47(1):105–13, jan 1985. 1, 3.1.4

[169] C. Tang, E. Loeliger, P. Luncsford, I. Kinde, D. Beckett, and M. F. Summers. Entropic switch regulates myristate exposure in the HIV-1 matrix protein. *Proc. Natl. Acad. Sci. U. S. A.*, 101(2):517–22, jan 2004. 5.2.1, 5.2.1

[170] K. Tawa and K. Morigaki. Substrate-supported phospholipid membranes studied by surface plasmon resonance and surface plasmon fluorescence spectroscopy. *Biophys. J.*, 89(4):2750–8, oct 2005. 2.2.3

[171] G. Valincius, D. J. McGillivray, W. Febo-Ayala, D. J. Vanderah, J. J. Kasianowicz, and M. Lösche. Enzyme activity to augment the characterization of tethered bilayer membranes. *J. Phys. Chem. B*, 110(21):10213–6, jun 2006. 3.1.3

[172] G. Valincius, T. Meškauskas, and F. Ivanauskas. Electrochemical impedance spectroscopy of tethered bilayer membranes. *Langmuir*, 28(1):977–90, jan 2012. 3.1.1

[173] S. M. van den Eijnde, M. J. van den Hoff, C. P. Reutelingsperger, W. L. van Heerde, M. E. Henfling, C. Vermeij-Keers, B. Schutte, M. Borgers, and F. C. Ramaekers. Transient expression of phosphatidylserine at cell-cell contact areas is required for myotube formation. *J. Cell Sci.*, 114(Pt 20):3631–42, oct 2001. 9.3

[174] G. van Meer, D. R. Voelker, and G. W. Feigenson. Membrane lipids: where they are and how they behave. *Nat. Rev. Mol. Cell Biol.*, 9(2):112–24, feb 2008. (document), 1, 1.2, 2.1.1, 2.2, 2.1.1, 5.2.1

[175] D. J. Vanderah, R. S. Gates, V. Silin, D. N. Zeiger, J. T. Woodward, C. W. Meuse, G. Valincius, and B. Nickel. Isostructural Self-Assembled Monolayers. 1. Octadecyl 1-Thiaoligo(ethylene oxides). *Langmuir*, 19(7):2612–2620, apr 2003. 3.1.3

[176] N. Verdaguer, S. Corbalan-Garcia, W. F. Ochoa, I. Fita, and J. C. Gómez-Fernández. Ca(2+) bridges the C2 membrane-binding domain of protein kinase Calpha directly to phosphatidylserine. *EMBO J.*, 18(22):6329–38, nov 1999. 2.3.1

[177] M. F. Verderame, T. D. Nelle, and J. W. Wills. The membrane-binding domain of the Rous sarcoma virus Gag protein. *J. Virol.*, 70(4):2664–8, apr 1996. 8.2.1, 8.2.2

[178] J. Vlach and J. S. Saad. Trio engagement via plasma membrane phospholipids and the myristoyl moiety governs HIV-1 matrix binding to bilayers. *Proc. Natl. Acad. Sci. U. S. A.*, 110(9):3525–30, feb 2013. 5.2.1, 6.4

[179] J. Vlach and J. S. Saad. Structural and molecular determinants of HIV-1 Gag binding to the plasma membrane. *Front. Microbiol.*, 6:232, jan 2015. 6.4

[180] M. L. Wagner and L. K. Tamm. Tethered Polymer-Supported Planar Lipid Bilayers for Reconstitution of Integral Membrane Proteins: Silane-Polyethyleneglycol-Lipid as a Cushion and Covalent Linker. *Biophys. J.*, 79(3):1400–1414, sep 2000. 1, 2.2

[181] X. Wang, M. M. Shindel, S.-W. Wang, and R. Ragan. Elucidating driving forces for liposome rupture: external perturbations and chemical affinity. *Langmuir*, 28(19):7417–

27, may 2012. 4.1, 4.5

[182] A. Watts, K. Harlos, and D. Marsh. Charge-induced tilt in ordered-phase phosphatidylglycerol bilayers Evidence from x-ray diffraction. *Biochim. Biophys. Acta - Biomembr.*, 645(1):91–96, jun 1981. 4.5

[183] K. Weise, D. Huster, S. Kapoor, G. Triola, H. Waldmann, and R. Winter. Gibbs energy determinants of lipoprotein insertion into lipid membranes: the case study of Ras proteins. *Faraday Discuss.*, 161:549–61; discussion 563–89, jan 2013. 3.2.5

[184] J. N. Weiss. The Hill equation revisited: uses and misuses. *FASEB J.*, 11(11):835–41, sep 1997. 3.2.5

[185] O. Wesoowska, K. Michalak, J. Maniewska, and A. B. Hendrich. Giant unilamellar vesicles - a perfect tool to visualize phase separation and lipid rafts in model systems. *Acta Biochim. Pol.*, 56(1):33–9, jan 2009. 2.2.2

[186] S. H. White and W. C. Wimley. Membrane protein folding and stability: physical principles. *Annu. Rev. Biophys. Biomol. Struct.*, 28:319–65, jan 1999. 1

[187] M. Wu, E. Maier, R. Benz, and R. E. W. Hancock. Mechanism of Interaction of Different Classes of Cationic Antimicrobial Peptides with Planar Bilayers and with the Cytoplasmic Membrane of Escherichia coli . *Biochemistry*, 38(22):7235–7242, jun 1999. 2.2.4

[188] Z. Wu, J. Alexandratos, B. Ericksen, J. Lubkowski, R. C. Gallo, and W. Lu. Total chemical synthesis of N-myristoylated HIV-1 matrix protein p17: structural and mechanistic implications of p17 myristoylation. *Proc. Natl. Acad. Sci. U. S. A.*, 101(32):11587–92, aug 2004. 5.2.1

[189] T. L. Yap, Z. Jiang, F. Heinrich, J. M. Gruschus, C. M. Pfefferkorn, M. Barros, J. E. Curtis, E. Sidransky, and J. C. Lee. Structural features of membrane-bound glucocerebrosidase and α-synuclein probed by neutron reflectometry and fluorescence spectroscopy. *J. Biol. Chem.*, 290(2):744–54, jan 2015. 3.3.5, 7.1

[190] M. Yeager, E. M. Wilson-Kubalek, S. G. Weiner, P. O. Brown, and A. Rein. Supramolecular organization of immature and mature murine leukemia virus revealed by electron cryo-microscopy: implications for retroviral assembly mechanisms. *Proc. Natl. Acad. Sci. U. S. A.*, 95(13):7299–304, jun 1998. 5.3.1

[191] F. Yu, S. M. Joshi, Y. M. Ma, R. L. Kingston, M. N. Simon, and V. M. Vogt. Characterization of Rous sarcoma virus Gag particles assembled in vitro. *J. Virol.*, 75(6):2753–64, mar 2001. 5.3.1

[192] W. Zhou, L. J. Parent, J. W. Wills, and M. D. Resh. Identification of a membrane-binding domain within the amino-terminal region of human immunodeficiency virus type 1 Gag protein which interacts with acidic phospholipids. *J. Virol.*, 68(4):2556–69, apr 1994. 5.2.1

[193] W. Zhou and M. D. Resh. Differential membrane binding of the human immunodeficiency virus type 1 matrix protein. *J. Virol.*, 70(12):8540–8, dec 1996. 5.2.1, 6.4

[194] J. Zimmerberg and K. Gawrisch. The physical chemistry of biological membranes. *Nat. Chem. Biol.*, 2(11):564–7, nov 2006. 2.1.1